

NORTHWESTERN UNIVERSITY

MOF-Based Catalysts for the Tandem Reaction of
Hydrogen Peroxide Generation and Oxidation

A DISSERTATION

SUBMITTED TO THE GRADUATE SCHOOL
IN PARTIAL FULFILLMENT OF THE REQUIREMENTS

for the degree

DOCTOR OF PHILOSOPHY

Field of Chemistry

By

Rungmai Limvorapitux

EVANSTON, ILLINOIS

September 2019

© Copyright by Rungmai Limvorapitux 2019

All Rights Reserved

ABSTRACT

MOF-Based Catalysts for the Tandem Reaction of Hydrogen Peroxide Generation and Oxidation

Rungmai Limvorapitux

Oxidation is an important process in synthesizing a broad range of useful products such as polymers, pharmaceuticals, and fine chemicals. While H_2O_2 is a highly attractive oxidant for oxidative chemistry due to its high percentage of oxygen and environmentally friendly water byproduct, it is often used in excess due to its intrinsic instability. At large scales, the transportation of the highly concentrated H_2O_2 also poses high operational costs and safety concerns. Thus, the one-pot [H_2O_2 generation + oxidation] tandem reaction has become an important strategy to utilize this green oxidant more efficiently and economically. To implement this approach, this thesis focuses on the development of tandem catalysts that can generate H_2O_2 directly from H_2 and O_2 and consume this oxidant immediately in the subsequent oxidation.

Two metal species, noble-metal nanoparticles (NPs) and Mo^{VI} complexes, were employed to catalyze each reaction step in the [H_2O_2 generation + alkene oxidation] tandem reaction. Specifically, a UiO-66- NH_2 metal-organic framework (MOF) crystal with encapsulated NPs in its core and anchored Mo^{VI} species on its surface, has been developed for this purpose. The use of this dually functionalized core-shell catalyst in the [H_2O_2 generation + alkene oxidation] tandem reaction resulted in a significant enhancement of the epoxide productivity as opposed to a physical mixture of two singly functionalized catalysts. In addition, the encapsulation of the NPs inside the

MOF crystal can suppress an alkene-hydrogenation side reaction, leading to a higher selectivity for the epoxide product.

To demonstrate how matched reaction rates can improve the efficiency of H_2O_2 consumption, the alkene-oxidation step was then replaced by a faster sulfide-oxidation reaction. The bare MOF with open-coordination sites on its nodes was found to be catalytically active for sulfide oxidation, and the incorporation of V^{IV} species on those sites further enhances the consumption of H_2O_2 . A new reactor configuration was developed to measure the reaction rates of sulfide oxidation and H_2O_2 generation, enabling for both rates to be further tuned for efficient consumption of H_2O_2 in our tandem reaction.

ACKNOWLEDGEMENTS

I express my sincere gratitude to Prof. SonBinh Nguyen, my graduate advisor, for his mentorship throughout my graduate career. His dedication in time and effort has prepared me to become a good scientist, who thinks critically, asks good questions, and does meaningful work. The 4-year plan that he asked me to work on during my first year helped me significantly in framing this thesis work. Beyond scientific knowledge, his extraordinary guidance equipped me with invaluable skills in collaboration, technical writing, and presentation. I would like to also extend my gratitude to my committee members, Profs. Joseph Hupp, Ken Poeppelmeier, and Regan Thomson for their invaluable insights every step along my Ph.D. journey.

This thesis could not have been successfully completed without the help from my brilliant collaborators. First, I want to acknowledge Prof. Chia-Kuang Tsung and his team—Prof. Lien-Yang Chou, Dr. Allison Young, and Mr. Victor Lo—at Boston College. I am glad that a discussion during your visit led to our fruitful collaboration. Second, I want to thank Prof. Randall Snurr, Dr. Haoyuan Chen, and Mr. Matthew Mendonca for their computational modeling that helped elucidate the mechanism of my catalysts. Third, I want to acknowledge Prof. Eric Weitz and Dr. Weiqiang Wu for the great opportunity to learn about IR. Last, I want to thank Prof. Neil Schweitzer for setting up reactors and teaching me many useful engineering skills.

I am grateful for my lab members, especially Dr. Cornelius Audu, Dr. Lily Mao, Dr. Bill Hong, Dr. Sanjiban Chakraborty, Dr. Sergio Garibay, Dr. Yonghwi Kim, Mengtan Liu, Ananya Agrawal, Matthew Du, Jessica Beard, Jean Chang, Fred Zhang, Zhizhi Kong, Dr. Cloud Chang, Tori Seto, and Max Sigal, for their kind help and support throughout my graduate career. I am

thankful for learning how to synthesize MOFs when I started working in the lab from Zachary Meinhart. A special thank you goes to Dr. Giang Nguyen, who trained me in catalysis research and always provided helpful academic and non-academic guidance even after she graduated.

For the past 5 years at Northwestern University, I couldn't imagine myself without many good companions outside my research lab. Among those, I would like to especially thank Papis Wongchaisuwat, Silvia Clement-Lam, Sabina Puspita, Yoes Kenawas, Wara Urwasi, Allison Wustrow, Tik Sathisuksanoh, and Air Prasomsri for their great friendship, kind support, and helpful advice during my Ph.D. candidacy. I am also blessed to have a great time with my Thai buddies—Art Sakulsom, May Laohaviraphab, Gong Chanthawijaikul, Pom Chirakija, Wave Ngampruetikorn, Knot Patana-anake, Ping Rochanavibhata, Eng Mahawattanangul, and Note Wattanasirichaigoon. They made my weekends and holidays full of good food, nonstop laughs, and unforgettable memories.

I am lucky to have family members—Teng, Paew, Tom, Ta, and Aunt Qwan in particular—that always believe in me, respect my decisions, and support my dreams. Despite infrequent meetups and only a handful of video calls per year, I always feel their love and care, which tremendously motivate me to move forward. I also have been fortunate to meet Kevin, who has committed to editing this thesis with his faded memory of chemistry. His all-around support and encouragement have brought me to this successful phase in my life.

To close this thesis, I am grateful for my experience at Northwestern University as a Ph.D. student. I hope to use the knowledge and skills I gained throughout my academic career to continue doing impactful work. I would like to always remember that “when the going gets tough, the tough get going” (Joseph P. Kennedy).

TABLE OF CONTENTS

ABSTRACT	3
ACKNOWLEDGMENTS	5
TABLE OF CONTENTS	7
LIST OF TABLES	10
LIST OF FIGURES	12
LIST OF SCHEMES	20
Chapter 1 Introduction to one-pot tandem reactions and the design of tandem catalysts	21
1.1 One-pot tandem reactions	22
1.2 Design of catalysts for tandem reactions	24
1.3 The [H ₂ O ₂ generation + oxidation] tandem reaction	25
1.4 MOFs as support for tandem catalysts.....	27
1.5 Thesis overview	28
Chapter 2 Coupling molecular and nanoparticle catalysts on single metal-organic framework microcrystals for the [H₂O₂ generation + selective alkene oxidation] tandem reaction	31
2.1 Introduction.....	32
2.2 Background and motivation.....	32
2.3 Synthesis of MOF-based catalysts	35
2.4 Activities of NP-containing catalysts for H ₂ O ₂ production	39
2.5 Activities of (sal)Mo-functionalized catalysts for alkene oxidation.....	41
2.6 Activities and selectivities of MOF-based catalysts in tandem reaction	43
2.7 The advantages of coupling NP and molecular catalysts on the same MOF microcrystal.....	46

	8
2.8 Conclusion	50
2.9 Experimental.....	51
Chapter 3 Elucidating the mechanism of the UiO-66-catalyzed sulfide oxidation: activity and selectivity enhancements through changes in the node coordination environment and solvent	89
3.1 Introduction.....	90
3.2 Background and motivation.....	90
3.3 Synthesis and characterization of the UiO-66 derivative	93
3.4 Selection of reaction system	95
3.5 Activity of the catalysts and computational study	96
3.6 Inhibition by CH ₃ OH and the possibility of forming H-bonding networks at the Zr ₆ -oxo-hydroxo nodes	104
3.7 Recyclability of BzOH-UiO-66 and decap-UiO-66	106
3.8 Conclusion	107
3.9 Experimental.....	108
Chapter 4 Developing metal-organic framework catalysts for the efficient consumption of H₂O₂ in the [H₂O₂ generation + sulfide oxidation] tandem reaction	147
4.1 Introduction.....	148
4.2 Selection of UiO-66-based catalyst for sulfide oxidation.....	148
4.3 Measurements of H ₂ O ₂ -consumption rate in sulfide oxidation	153
4.4 Measurements of H ₂ O ₂ -generation rate	155
4.5 [H ₂ O ₂ generation + sulfide oxidation] tandem reaction.....	158
4.6 Conclusion	159
4.7 Experimental.....	160
Chapter 5 Epilogue	177

5.1 General conclusions about the work described in this thesis.....	178
5.2 MOFs with larger pore size for better mass transportation and more catalyst loading.....	179
5.3 Tandem reaction in the gas phase to eliminate solvent and simplify separation	180
5.4 Last remarks.....	182
REFERENCES	183
CURRICULUM VITAE	200

LIST OF TABLES

Table 2.1	The NP sizes, NP loadings, and Mo loadings for UiO-66-NH ₂ derivatives.	37
Table 2.2	The catalytic activity of MOF-based catalysts in H ₂ O ₂ generation.	40
Table 2.3	The oxidation of <i>cis</i> -cyclooctene with H ₂ O ₂ in 7/3 v/v CH ₃ OH/H ₂ O. ^c	42
Table 2.4	Hy/Ox ratios and Ox productivities for Br-COE in the presence of different types of MOF catalysts. ^e	44
Table 2.5	Hy/Ox ratios and Ox productivities for 4-methylstyrene in the presence of different types of MOF catalysts. ^e	45
Table 2.6	Oxidation productivity for <i>cis</i> -cyclooctene in the presence of different types of MOF catalysts. ^d	47
Table 2.7	Preparative data, pore, and surface properties of UiO-66-NH₂ and its derivatives before catalysis.	63
Table 2.8	Preparative data, pore, and surface properties of MOFs after catalysis.	63
Table 2.9	Relative comparison of H ₂ O ₂ decomposition in the presence of different MOF materials as measured by the H ₂ O ₂ concentration remained from a standard sample after being stirred for 6 h.	78
Table 2.10	H ₂ O ₂ concentration and productivity data for the generation of H ₂ O ₂ from H ₂ and O ₂ using different catalysts.	78
Table 2.11	Yield and oxidation productivity for the oxidation of <i>cis</i> -cyclooctene using different catalysts.	80
Table 2.12	Yield and oxidation productivity for the oxidation of <i>cis</i> -cyclooctene using UiO-66-sal(Mo) and the leached Mo.	81
Table 2.13	Concentration of products, Hy/Ox ratios, and Ox productivities for Br-COE in the presence of different types of MOF catalysts.	82
Table 2.14	Concentration of products, Hy/Ox ratios, and Ox productivities for 4-methylstyrene in the presence of different types of MOF catalysts.	83
Table 2.15	Concentration of products, Hy/Ox ratios, and Ox productivity for <i>cis</i> -cyclooctene in the presence of different types of MOF catalysts.	84

		11
Table 2.16	Amount of metal leaching from each catalyst after catalysis.	85
Table 2.17	Amount of Mo catalyst and oxidation productivity in the UiO-66-sal(Mo) -catalyzed oxidation of <i>cis</i> -cyclooctene using H ₂ O ₂ .	86
Table 2.18	Amount of Mo catalyst and oxidation productivity in the Pd@UiO-66-sal(Mo) -catalyzed [H ₂ O ₂ generation + <i>cis</i> -cyclooctene oxidation] tandem reaction.	87
Table 3.1	Composition of the three UiO-66 MOF derivatives and the Zr ₆ -oxo-hydroxo cluster used in this work.	94
Table 3.2	Initial rates for the MOF-catalyzed oxidations of sulfide and sulfoxide in CH ₃ OH, starting directly with each individual substrate.	100
Table 3.3	Computed binding free energies at 298 K and equilibrium binding constants of different solvents and reactants to the Zr ₆ -oxo-hydroxo node.	104
Table 3.4	Formula and BET area of materials.	118
Table 3.5	Catalysts used in the reaction.	124
Table 3.6	Amount of Zr leached out into solution after each cycle.	133
Table 3.7	Relative enthalpy values (ΔH , kJ/mol) for the various species in the oxidation of methyl phenyl sulfide without catalyst (corresponding to the “Uncatalyzed” profile in Figure 3.2).	134
Table 3.8	Relative enthalpy values (ΔH , kJ/mol) for the various species in the oxidation of methyl phenyl sulfide by the Zr ₆ -oxo-hydroxo cluster node of UiO-66 (corresponding to the “Node of UiO-66” profile in Figure 3.2).	134
Table 3.9	Binding enthalpies of three different solvents and substrates to the Zr ₆ -oxo-hydroxo cluster node of UiO-66.	134
Table 4.1	Catalytic activity of MOF-based catalysts in the oxidation of methyl phenyl sulfide with H ₂ O ₂ in the CH ₃ OH/H ₂ O (7/3 v/v) solvent mixture.	151
Table 4.2	Amount of metal loading and BET area of UiO-66-NH₂ and its derivatives.	170
Table 4.3	H ₂ O ₂ generation at different amount of Pd NPs loading.	175
Table 4.4	MOFs used in the [H ₂ O ₂ generation + sulfide oxidation] tandem reaction.	176

LIST OF FIGURES

Figure 1.1	Conventional stepwise synthesis and one-pot reaction.	22
Figure 1.2	Examples of one-pot reactions with high efficiency.	23
Figure 1.3	A two-step concurrent tandem reaction.	24
Figure 1.4	The [H ₂ O ₂ generation + oxidation] tandem reaction.	26
Figure 1.5	A proposed dually functionalized core-shell platform for [H ₂ O ₂ generation + oxidation] tandem reaction, where the catalyst for the first reaction step is located inside the support and is surrounded by the catalyst for the second reaction step.	27
Figure 1.6	The incorporation of catalyst species into MOFs at their inorganic nodes, at their organic linkers, or inside their pores.	28
Figure 1.7	A dually functionalized core-shell MOF catalyst and its catalytic activity in the [H ₂ O ₂ generation + oxidation] tandem reaction.	29
Figure 1.8	Node of UiO-66 MOFs and their catalytic activities in sulfide oxidation.	29
Figure 1.9	[H ₂ O ₂ generation + sulfide oxidation] tandem reaction with efficient consumption of H ₂ O ₂ .	30
Figure 2.1	A schematic illustration of a dually functionalized MOF catalyst for the [H ₂ O ₂ generation + selective alkene oxidation] tandem reaction. The Pd NPs are encapsulated inside the MOF microcrystal, whose surfaces are functionalized with sal(Mo) moieties.	35
Figure 2.2	TEM images of the MOF materials before catalysis. To guide the readers' eyes, the position of some of the NPs on the MOF microcrystals for Pd-PVP/UiO-66-sal(Mo) and Pd/UiO-66-sal(Mo) have been indicated with white arrows. Comparing the TEM images of these samples to that of Pd@UiO-66-sal(Mo) suggests two different types of NP distributions. The NPs in the Pd@UiO-66-sal(Mo) sample are positioned throughout the middle part of the crystals because most of them are fully encapsulated inside the MOF crystals.	38
Figure 2.3	Left: A calibration curve for H ₂ O ₂ concentration constructed from titrating against a 5 mM Ti(SO ₄) ₂ solution. Right: Photo of mixtures of 5 mM Ti(SO ₄) ₂ solution (1 mL) and H ₂ O ₂ standard solution (1 mL) at different concentrations (Left to right: 2, 1, 0.5, 0.25, and 0 mM).	62

- Figure 2.4** N₂ isotherms for **UiO-66-NH₂** and its derivative before catalysis. Left: MOFs before ligand modification and Mo incorporation. Right: MOFs after ligand modification and Mo incorporation. Close symbols: adsorption; open symbols: desorption. 64
- Figure 2.5** Photos of the MOF materials. First row: MOFs before ligand modification and Mo incorporation. Second row: MOFs after ligand modification and Mo incorporation. 64
- Figure 2.6** PXRD patterns of **UiO-66-NH₂** and its modified derivatives before ligand modification and Mo incorporation. The unchanged PXRD pattern of the MOFs after incorporation of Au NPs and Pd NPs suggests that the modification did not alter the main crystallinity of the host framework. The peak ~38° in **Au/UiO-66-NH₂** pattern represents the (111) planes of the Au NPs.⁶⁰ 65
- Figure 2.7** PXRD patterns of the MOFs after ligand modification and Mo incorporation. The unchanged PXRD pattern of the MOFs after incorporation with Mo complex suggests that the modification did not alter the main crystallinity of the host framework. 65
- Figure 2.8** PXRD patterns of the MOFs after catalysis. As suggested by this data, the MOFs are still crystalline after being used in each reaction. 66
- Figure 2.9** FT-IR spectra of **UiO-66-NH₂** and its derivatives before ligand modification and Mo incorporation. 66
- Figure 2.10** FT-IR spectra of the MOFs after ligand modification and Mo incorporation, clearly showing the presences of Mo=O (~930 cm⁻¹) and O-O (~890 cm⁻¹) groups.⁹³ 67
- Figure 2.11** FT-IR spectra of the MOFs after catalysis. The spectra suggested that there are some Mo complex coordinate to the MOFs since the bands at ~930 cm⁻¹ and ~890 cm⁻¹ still remain. 67
- Figure 2.12** TEM images of the MOF materials after catalysis. To guide the readers' eyes, the position of some of the NPs on the MOF microcrystals for **Pd-PVP/UiO-66-sal(Mo)** have been indicated with white arrows. Comparing the TEM images of these samples to that of **Pd@UiO-66-sal(Mo)**, suggests two different types of NP distributions. The NPs in the **Pd@UiO-66-sal(Mo)** sample are positioned throughout the middle part of the crystals because most of them are fully encapsulated inside the MOF crystals. We note in passing that while TEM imaging can contrast the relative differences between **Pd@UiO-66-(sal)Mo** and **Pd/UiO-66-(sal)Mo**, with the former

having the majority of the NPs encapsulated in the MOF crystals, it is difficult to absolutely prove that there are no NPs on the exterior surfaces. This is the same situation with 3D tomography, which can demonstrate that the majority of the NPs are in the MOF crystal⁹⁴ but cannot conclusively exclude the probability that there are few small NPs on exterior surfaces because these NPs are difficult to identify in 3D tomography images. Similarly, XPS analysis is not unambiguous. Due to their low-density, porous nature, the inelastic mean free-paths of the electron signals coming from MOF materials in an XPS experiment are longer than commonly observed. Thus, more signals will come from deeper inside the MOF microcrystals, making XPS less surface-sensitive and impractical for distinguishing if the NPs are on the exterior surfaces or inside the crystals. For instance, a previous report⁹⁵ shows that even when the majority of the NPs are encapsulated in the MOF crystals instead of on their surfaces, the elemental signatures due to these NPs were still detectable by XPS.

68

Figure 2.13 Reusability and reproducibility data for **Pd@UiO-66-NH₂** in catalytic H₂O₂ generation. For each cycle, the catalyst is recovered from the previous cycle, taking into account the amount of lost catalyst. The H₂O₂ productivity of the MOF catalyst decreased to 50-60% after the 3rd cycle. This experiment was repeated 2 times (Experiments 1 and 2). Based on the data in Table 2.16, **Pd@UiO-66-NH₂** was selected for these reusability/reproducibility tests due to its lowest tendency to leach Pd.

80

Figure 2.14 Epoxide-formation profiles to assess the activity of the leached Mo from the **UiO-66-sal(Mo)**-catalyzed oxidation of *cis*-cyclooctene using H₂O₂. Two identical experiments were set up where the **UiO-66-sal(Mo)** catalyst was exposed to a reaction media containing a 1:1 molar ratio of substrate and H₂O₂ (mimic our standard benchtop reaction conditions) for 2 h before one was subjected to the filtration test. Epoxide concentrations were monitored for both the unfiltered reaction (blue line) and the filtrate (red line) using GC-FID. The lines are only included as visual guides. See also Table 2.17.

85

Figure 2.15 Epoxide-formation profiles to assess the activity of the leached Mo from the **Pd@UiO-66-sal(Mo)**-catalyzed [H₂O₂ generation + *cis*-cyclooctene oxidation] tandem reaction. An experiment with the **Pd@UiO-66-sal(Mo)** catalyst were set up under our standard tandem reaction conditions and carried out for 2 h before being stopped and subjected to the filtration test. Additional H₂O₂ was added to the filtrate and the epoxide concentration was monitored using GC-FID. For comparison, epoxide concentration data for the standard (unfiltered) tandem reaction using **Pd@UiO-66-sal(Mo)** were also included (blue line). The lines are only included as visual guides. See also Table 2.18.

86

- Figure 2.16** Estimated smallest dimension for 5-bromo-1-cyclooctene (5.23 Å, left) and 4-methylstyrene (4.22 Å, right). 87
- Figure 3.1** The conversion (a) and selectivity (b) profiles in the catalytic oxidation of methyl phenyl sulfide in CH₃OH using H₂O₂ as the oxidant. All reactions were carried out with a 100:100:1 molar ratio of sulfide:H₂O₂:Zr₆-oxo-hydroxo clusters. See Figures 3.17-3.19 for catalysis data that extend up to 9 h. 97
- Figure 3.2** The computed free-energy profiles for the catalytic oxidation of methyl phenyl sulfide using H₂O₂ as the oxidant without catalyst (black) and with a Zr₆-oxo-hydroxo cluster possessing *one* [μ_1 -OH + μ_1 -OH₂] open site as a model for an “uncapped” node of UiO-66 (blue). To reduce system size in our node model, the capping acid modulator is HCOOH and all benzene rings in the BDC linker are replaced with hydrogen atoms. The system is essentially a (Zr₆(μ_3 -O)₄(μ_3 -OH)₄(OOCH)₁₁) node. Free energies were calculated at 298 K and are reported in kJ/mol. Results were calculated using the PCM solvation model for CH₃OH for both the uncatalyzed and the catalyzed reactions. In the current figure, only a few selected hydrogen bonds are shown for the transition states to reduce the complexity in the drawings. The reader should note that the simplified depictions of isolated μ_1 -OH and μ_1 -OH₂ sites are only used in this scheme for clarity. Hydrogen bonds do exist between adjacent μ_1 -OH and μ_1 -OH₂ sites, as well as with H-bond-capable solvent molecules; thus, isolated μ_1 -species are probably unlikely, as discussed in later sections. For detailed illustrations of the hydrogen-bonded species, see Figure 3.29 as well as the structures shown in Section 3.9. 98
- Figure 3.3** The conversion profile in the catalytic oxidation of methyl phenyl sulfoxide in CH₃OH using H₂O₂ as the oxidant. All reactions were carried out with a 100:100:1 molar ratio of methyl phenyl sulfoxide:H₂O₂:Zr₆-oxo-hydroxo node. 99
- Figure 3.4** The conversion (a) and selectivity (b) profiles in the catalytic oxidation of methyl phenyl sulfide using H₂O₂ as the oxidant and **BzOH-UiO-66** as the catalyst in three different solvents. All reactions were carried out with a 100:100:1 molar ratio of methyl phenyl sulfide:H₂O₂:Zr₆-oxo-hydroxo node. 101
- Figure 3.5** Optimized structure of the [Zr- μ_1 -OH + Zr- μ_1 -O=S(CH₃)Ph] product intermediate. White, grey, red, yellow, and cyan spheres represent H, C, O, S, and Zr atoms, respectively. 104

- Figure 3.6** Plots of the concentration ratio of BDC, BzOH, and HCOOH to the MA internal standard versus the integration ratio of the signals for the analytes (BDC, BzOH, and HCOOH) to MA. 117
- Figure 3.7** The ^1H NMR spectra of: a) digested **BzOH-UiO-66** batch 1 and b) digested **BzOH-UiO-66** batch 2 in $\text{DMSO-}d_6$. 119
- Figure 3.8** The ^1H NMR spectrum of: a) digested **decap-UiO-66** batch 1 and b) digested **decap-UiO-66** batch 2 in $\text{DMSO-}d_6$. 120
- Figure 3.9** The ^1H NMR spectrum of digested **HCOOH-UiO-66** in $\text{DMSO-}d_6$. 121
- Figure 3.10** The ^1H NMR spectrum of digested isolated Zr_6 -oxo-hydroxo cluster in $\text{DMSO-}d_6$. 121
- Figure 3.11** PXRD patterns for UiO-66 MOFs used in this study. 122
- Figure 3.12** N_2 isotherms for UiO-66 MOFs used in this study. Close symbols: adsorption; open symbols: desorption. 122
- Figure 3.13** Top row: Representative SEM images of three UiO-66 MOFs used in this study. Bottom row: The corresponding SEM-derived particle-size-distribution profile for each of the MOF samples; each profile was constructed based on measurements of >100 particles. 123
- Figure 3.14** Product-formation profiles (product vs conversion (a) and product vs time (b)) in the catalytic oxidation of methyl phenyl sulfide in CH_3OH using H_2O_2 (1 equiv) as the oxidant. For convenience, product = sulfoxide + sulfone. 126
- Figure 3.15** Product-formation profiles (product vs conversion (a) and product vs time (b)) in the catalytic oxidation of methyl phenyl sulfoxide in CH_3OH using H_2O_2 (1 equiv) as the oxidant. 126
- Figure 3.16** Product-formation profiles in the uncatalyzed oxidation of methyl phenyl sulfide in CH_3OH using BzOOH (~ 0.8 equiv) as an oxidant. 127
- Figure 3.17** Product-formation profiles (9 h, product vs time) in the catalytic oxidation of methyl phenyl sulfide in CH_3OH using H_2O_2 (1 equiv) as the oxidant. For convenience, product = sulfoxide + sulfone. 128
- Figure 3.18** Product-formation profiles (9 h, product vs conversion) in the catalytic oxidation of methyl phenyl sulfide in CH_3OH using H_2O_2 (1 equiv) as the oxidant. For convenience, product = sulfoxide + sulfone. 128

		17
Figure 3.19	Selectivity profiles (9 h) in the catalytic oxidation of methyl phenyl sulfide in CH ₃ OH using H ₂ O ₂ (1 equiv) as the oxidant.	129
Figure 3.20	Product-formation profiles (product vs conversion (a) and product vs time (b)) in the catalytic oxidation of methyl phenyl sulfide using H ₂ O ₂ as the oxidant and BzOH-UiO-66 as the catalyst in three different solvents. For convenience, product = sulfoxide + sulfone.	129
Figure 3.21	Product-formation profiles in the catalytic oxidation of methyl phenyl sulfide in CH ₃ OH using H ₂ O ₂ (1 equiv) as the oxidant and BzOH-UiO-66 batch 2 as the catalyst. Five cycles were carried out. For convenience, product = sulfoxide + sulfone.	130
Figure 3.22	Selectivity profiles in the catalytic oxidation of methyl phenyl sulfide in CH ₃ OH using H ₂ O ₂ (1 equiv) as the oxidant and BzOH-UiO-66 batch 2 as the catalyst. Five cycles were carried out.	130
Figure 3.23	Product-formation profiles in the catalytic oxidation of methyl phenyl sulfide in CH ₃ OH using H ₂ O ₂ (1 equiv) as the oxidant and decap-UiO-66 as the catalyst. The materials used in this study came from BzOH-UiO-66 batch 2. Five cycles were carried out. For convenience, product = sulfoxide + sulfone.	131
Figure 3.24	Selectivity profiles in the catalytic oxidation of methyl phenyl sulfide in CH ₃ OH using H ₂ O ₂ (1 equiv) as the oxidant and decap-UiO-66 as the catalyst. The materials used in this study came from BzOH-UiO-66 batch 2. Five cycles were carried out.	131
Figure 3.25	PXRD patterns for BzOH-UiO-66 batch 2 before and after catalysis.	132
Figure 3.26	PXRD patterns for decap-UiO-66 batch 2 before and after catalysis.	132
Figure 3.27	SEM images of UiO-66 MOFs after cycles 4 (top panels) and 5 (bottom panels) of catalysis. While there is no visible changes in morphology, the broadening of the PXRD profiles shown in Figures 3.25-3.26 suggest some loss of crystallinity.	133
Figure 3.28	Two possible Langmuir-Hinshelwood-type reaction mechanisms of sulfoxide oxidation obtained from DFT calculations.	135
Figure 3.29	Top: A structural drawing of the Zr-μ ₁ -OOH species shown in Figure 3.2. Bottom: Outcome of an attempt to carry out geometry optimization of the 3-member Zr(η ² -O ₂) peroxy ring proposed by Faccioli <i>et al.</i> ¹¹⁰	136

Figure 4.1	Proposed core-shell catalyst for the [H ₂ O ₂ generation + sulfide oxidation] tandem reaction.	148
Figure 4.2	The conversion profiles in the catalytic oxidation of methyl phenyl sulfide at room temperature in the CH ₃ OH/H ₂ O (7/3 v/v) solvent mixture using H ₂ O ₂ as the oxidant. All reactions were carried out with a 100:100:1 molar ratio of sulfide:H ₂ O ₂ :metalloporphyrin.	150
Figure 4.3	Conversion profiles in the oxidation of methyl phenyl sulfide using H ₂ O ₂ in the CH ₃ OH/H ₂ O (7/3 v/v) solvent mixture.	153
Figure 4.4	Previous and new reaction setups for sulfide oxidation reaction (see Section 4.7 for details and photo of an actual setup).	154
Figure 4.5	The rate profile in the oxidation of methyl phenyl sulfide at different flow rates using V-UiO-66-NH₂ catalyst (~0.05 mg V).	154
Figure 4.6	The rates of methyl phenyl sulfide oxidation at different concentration of H ₂ O ₂ using V-UiO-66-NH₂ catalyst (~0.1 mg V).	155
Figure 4.7	Previous and new reaction setups for H ₂ O ₂ generation and [H ₂ O ₂ generation + oxidation] tandem reaction (see Section 4.7 for details and photo of an actual setup).	156
Figure 4.8	The H ₂ O ₂ -generation profiles of 3 trials using Pd@UiO-66-NH₂ catalyst (~0.3 mg Pd).	157
Figure 4.9	The methyl phenyl sulfoxide profile for the [H ₂ O ₂ generation + sulfide oxidation] tandem reaction using a physical mixture of Pd@UiO-66-NH₂ (~0.3 mg Pd) + V-UiO-66-NH₂ (~0.1 mg V) catalysts.	158
Figure 4.10	The methyl phenyl sulfoxide profile for the [H ₂ O ₂ generation + sulfide oxidation] tandem reaction using a physical mixture of Pd@UiO-66-NH₂ (~0.15 mg Pd) + V-UiO-66-NH₂ (~0.1 mg V) catalysts.	158
Figure 4.11	The methyl phenyl sulfoxide profile for the [H ₂ O ₂ generation + sulfide oxidation] tandem reaction using a Pd@V-UiO-66-NH₂ (~0.03 mg Pd and ~0.2 mg V) catalyst.	159
Figure 4.12	Reaction setup for rate measurement of the sulfide oxidation.	163
Figure 4.13	Reaction setup to measure the rate of the H ₂ O ₂ generation and the [H ₂ O ₂ generation + sulfide oxidation] tandem reaction.	164

- Figure 4.14** Plots of the concentration of methyl phenyl sulfide and methyl phenyl sulfoxide versus their areas of intergration. 165
- Figure 4.15** Left: A calibration curve for H₂O₂ concentration constructed from titrating against a FOX reagent. Right: Photo of mixtures of FOX reagent (50 μL) and H₂O₂ standard solution (950 μL) at different concentrations. 169
- Figure 4.16** N₂ isotherms for **UiO-66-NH₂** and its derivatives. Close symbols: adsorption; open symbols: desorption. 170
- Figure 4.17** PXRD patterns of **UiO-66-NH₂** and its derivatives. 171
- Figure 4.18** SEM images of **UiO-66-NH₂** and its derivatives. 171
- Figure 5.1** The organic linkers (left to right) of UiO-67, UiO-68, PCN-222, and PCN-229 MOFs. 180
- Figure 5.2** Two potential oxidation-focused tandem reactions in the gas phase. (a) [H₂O₂ generation + propene epoxidation] tandem reaction. (b) [H₂O₂ generation + benzene oxidation] tandem reaction. 181

LIST OF SCHEMES

Scheme 2.1	A schematic of the reaction manifolds for the [H ₂ O ₂ generation + alkene oxidation] tandem reaction. ^a	33
Scheme 2.2	The catalytic activity of MOF-based catalysts in H ₂ O ₂ generation.	36
Scheme 3.1	The UiO-66-catalyzed oxidation of sulfide with H ₂ O ₂ oxidant.	92
Scheme 3.2	The synthesis of the three isomorphous UiO-66 materials used in this work (left panel) and a proposal for the conversion of a Zr-μ ₁ -OH species in the open sites into active Zr-μ ₁ -OOH species (right panel). For simplicity, only one Zr ₆ -oxo-hydroxo node of each UiO-66 sample is shown here.	94
Scheme 3.3	Proposed interactions of the open sites on the nodes of UiO-66 MOFs with different solvents and substrates. In CH ₃ CN and CH ₂ Cl ₂ (bottom right quadrant), the [Zr-μ ₁ -OH + Zr-μ ₁ -O=S(CH ₃)Ph] product intermediate can form and produce more sulfone. In CH ₃ OH, the reaction can be slowed down due to formation of several CH ₃ OH-solvated species (left side; the species shown in the bottom left were proposed by Caratelli <i>et al.</i> ^{129, 161}) that “siphon off” the Zr-μ ₁ -OOH active species. In addition, [Zr-μ ₁ -OH + Zr-μ ₁ -O(CH ₃)H] species would predominate in the reaction mixture, reducing the formation of sulfone. Finally, as more product is made, product inhibition may occur (top left and top right) in polar solvents and under low-oxidant conditions such as those chosen for this study.	103
Scheme 4.1	Possible paths for Mo ^{VI} leaching from UiO-66-sal(Mo) . For simplicity, only one organic linker is shown here.	149
Scheme 4.2	Synthesis of UiO-66-por(Fe) . For simplicity, only one organic linker is shown here.	151
Scheme 4.3	Synthesis of V-UiO-66-NH₂ . For simplicity, only one Zr node is shown here.	152

Chapter 1

Introduction to one-pot tandem reactions and the design of tandem catalysts

1.1 One-pot tandem reactions

The synthesis of fine chemicals and industrially important intermediates often requires a series of reactions to be carried out in different vessels and for the products from each reaction to be separated and purified (Figure 1.1, top). To reduce time, energy, cost, and material losses associated with these separations and purifications, two or more reactions can be combined into a single operation (Figure 1.1, bottom).¹ The *in-situ*-generated compound (in this scenario, compound C is called an “intermediate”) from the first reaction step serves as a starting material for the subsequent reaction step. This one-pot strategy² has been implemented in the syntheses of a broad range of organic compounds³ and polymers.⁴

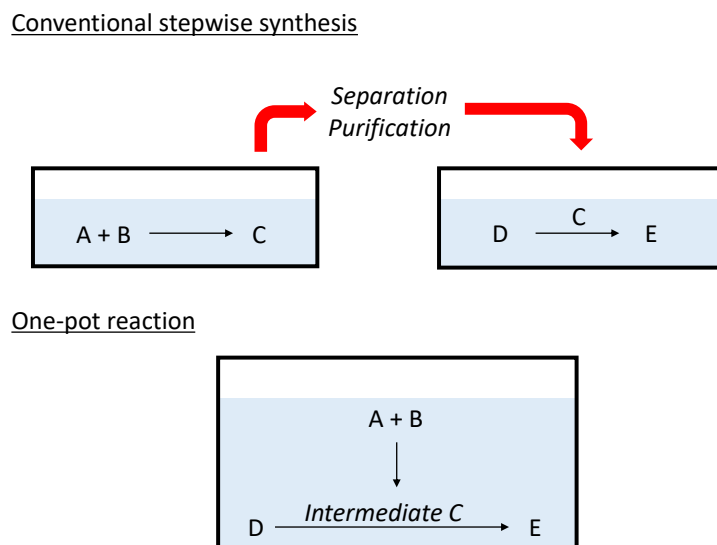


Figure 1.1 Conventional stepwise synthesis and one-pot reaction.

One-pot reactions provide the most benefit when their multistep reactions have the following characteristics (Figure 1.2):⁵

- (1) Unstable reaction intermediates that can decompose if they are not rapidly consumed.

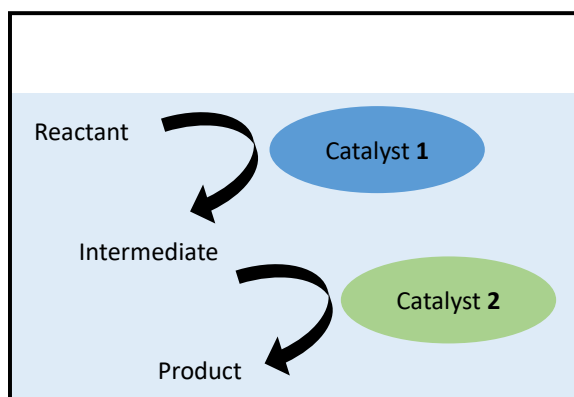


Figure 1.3 A two-step concurrent tandem reaction.

1.2 Design of catalysts for tandem reactions

Due to the coexistence of all components (reagents, intermediates, catalysts, and solvents) in the same reaction volume, the design and selection of catalysts **1** and **2** in tandem reactions are more challenging compared to those in conventional stepwise syntheses. The first consideration involves utilization of reagents in the correct sequence by catalysts **1** and **2** to prevent side reactions that can generate waste and complicate the purification of the final product.⁸ Second, these two catalysts need to have good stabilities and activities under the desired operating parameters (e.g., solvents, temperature, and pressure).⁹ To fulfill the aforementioned criteria, one approach is to control the location and environment of catalysts **1** and **2** by incorporating them on solid supports.¹⁰ These solid supports also allow for the separation and potential recycling of catalysts after the reaction.

The distance between catalysts **1** and **2** on the support can be controlled, in which the simplest system involves a physical mixture of individually supported catalysts **1** and **2**. For example, Huang *et al.* immobilized enzyme and sulfonic functional groups on separate

mesoporous silica supports and combined them to catalyze the [glucose isomerization + dehydration] tandem reaction.¹¹ In another example, Yamada *et al.* demonstrated that the distance between two catalysts can be shortened to less than 10 nm in their bilayer Pt-CeO₂ and Pt-SiO₂ catalyst.¹² Interestingly, they found that these materials yielded higher catalytic activities than a physical mixture of Pt-CeO₂ and Pt-SiO₂ in the [CH₃OH decomposition + ethylene hydroformylation] tandem reaction.¹²

The aforementioned study implies that it is important to optimize the distance between catalysts **1** and **2** for good results in the tandem reactions. As shown above, the greater the distance between the two catalysts, the longer it takes for the mass transport of the intermediate to occur.¹³ This can result in a low concentration of intermediate during the second step, which decreases catalytic activity. On the other hand, if the two catalysts are too close to each other, some side reactions may occur. For example, Zečević *et al.* found that a close distance between Pt and zeolite catalysts in the [alkane dehydrogenation + alkane hydrocracking] tandem reaction caused an undesired secondary cracking reaction.¹⁴

1.3 The [H₂O₂ generation + oxidation] tandem reaction

We envisioned that the synthesis of oxidized compounds, which have a broad utilization,¹ is a potential multistep process that would benefit from being carried out in a tandem fashion. Due to low selectivities from O₂,¹⁵⁻¹⁶ H₂O₂ is the next-most environmentally friendly oxidant for oxidation. It has a high percentage of active oxygen (47 wt %) and only produces water as a byproduct.¹⁷⁻¹⁸ Although H₂O₂ has been successfully used in industrial settings,¹⁹ it is not stable and readily decomposes at moderate temperatures,²⁰ resulting in the need for superstoichiometric usage.²¹ In addition, the storage and transportation of H₂O₂ can also pose safety concerns and high

operational costs.¹⁹ A strategy that can overcome these problems is to generate H₂O₂ from H₂ and O₂ and use it *in-situ* for the oxidation in a tandem fashion (Figure 1.4).¹⁹

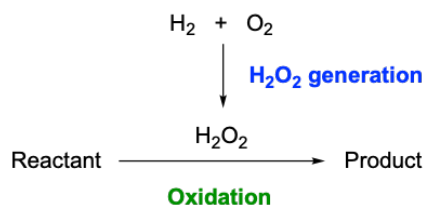


Figure 1.4 The [H₂O₂ generation + oxidation] tandem reaction.

In this thesis, we focused on the development of a catalyst system for the [H₂O₂ generation + oxidation] tandem reaction. For the first reaction step, H₂O₂ can be directly generated from H₂ and O₂ gases in the presence of Pd, Pt, or Au catalysts.²²⁻²⁴ These noble-metal catalysts, either as ions or nanoparticles (NPs), have been deposited on many types of supports, such as metal oxides, zeolites, membrane materials, and metal-organic frameworks (MOFs).^{23, 25} For the second oxidation step, a broad range of transition metal complexes that are known to form active oxo and peroxy species in the presence of H₂O₂ can be used.²⁶ Indeed, heterogeneous analogues of these complexes have been shown to facilitate the oxidations of organic compounds such as alcohols, sulfides, alkenes, and alkanes.¹⁸

To efficiently consume the *in-situ*-generated H₂O₂ in the [H₂O₂ generation + oxidation] tandem reaction, we deemed it necessary to have a short diffusion distance between the two catalytic species. In addition, a catalyst support that can “entrap” H₂O₂ is preferred as it can enhance the local concentration of H₂O₂ around the oxidation catalyst. We envisioned that the simplest design for achieving these two criteria is a dually functionalized core-shell platform (Figure 1.5). Here, the H₂O₂-generating catalyst is encapsulated inside a porous support whose surface is functionalized with oxidation catalysts.

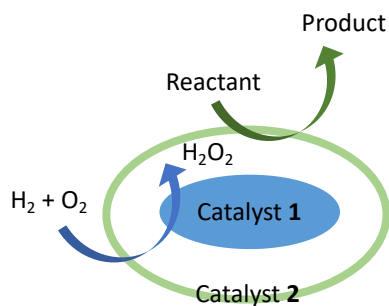


Figure 1.5 A proposed dually functionalized core-shell platform for [H₂O₂ generation + oxidation] tandem reaction, where the catalyst for the first reaction step is located inside the support and is surrounded by the catalyst for the second reaction step.

1.4 MOFs as support for tandem catalysts

To design the aforementioned dually functionalized core-shell platform, we considered MOFs to be an ideal support for employing two catalytic species for our [H₂O₂ generation + oxidation] tandem reaction. MOFs are crystalline materials comprised of inorganic nodes and organic linkers (Figure 1.6) that can be modified to accommodate a broad range of physical and chemical features for catalysis.²⁷ Specifically, for our purpose, the pore size of MOFs can be tuned to allow for good diffusion of H₂ and O₂ gases to catalyst **1** at the core, which is an important criterion in developing core-shell catalysts.²⁸ In addition, MOFs can be made with catalytic species at their inorganic nodes, at their organic linkers, or inside their pores (Figure 1.6).²⁹⁻³⁰ For example, Zhao *et al.* have synthesized the core-shell Pd@IRMOF-3 catalyst, where Pd NPs are located inside the IRMOF-3 MOF.³¹ The catalyst has shown high activity and selectivity of the desired product in the [Knoevenagel condensation + hydrogenation] tandem reaction.³¹

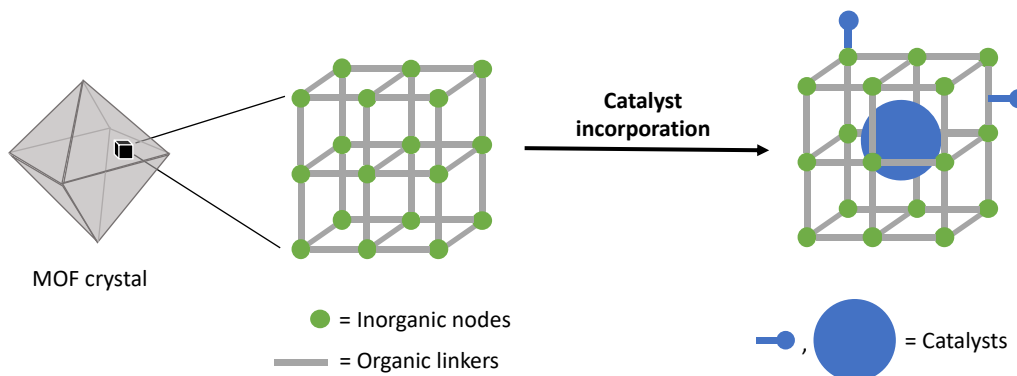


Figure 1.6 The incorporation of catalyst species into MOFs at their inorganic nodes, at their organic linkers, or inside their pores.

1.5 Thesis overview

The work in this thesis focuses on the development of dually functionalized core-shell UiO-66 MOF³²⁻³⁵ catalyst that efficiently generate and use H₂O₂ intermediate in the [H₂O₂ generation + oxidation] tandem reaction. As outlined thus far, chapter 2 demonstrated the advantages of using a UiO-66 MOF crystal to encapsulate Pd NPs and to anchor Mo^{VI} species on its surface, to catalyze H₂O₂ generation and alkene oxidation, respectively (Figure 1.7). Due to the close proximity of the two catalysts, this dually functionalized **Pd@UiO-66-sal(Mo)** catalyst exhibited higher productivities for the desired epoxide products in comparison to a physical mixture of two singly functionalized MOFs. Notably, it can also enhance the selectivity for the epoxide product by suppressing alkene-hydrogenation side reactions.

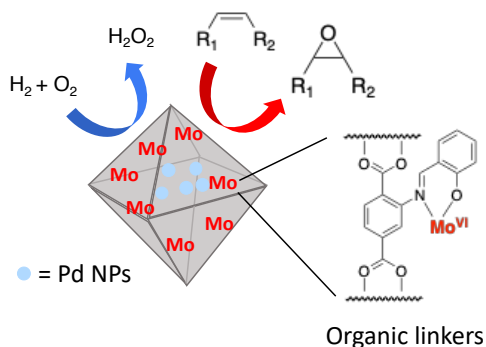


Figure 1.7 A dually functionalized core-shell MOF catalyst and its catalytic activity in the [H₂O₂ generation + oxidation] tandem reaction.

In chapter 3, we focused on improving the efficiency of H₂O₂ consumption in the [H₂O₂ generation + oxidation] tandem reaction by increasing the rate of the oxidation step. The oxidation of sulfide was chosen as the second reaction step due to its faster reaction rate compared to that of alkene epoxidation (Figure 1.8). UiO-66 MOF was developed with more open-coordination sites on their nodes and the resulting **decap-UiO-66** MOF exhibited an enhancement in the catalytic activity for sulfide oxidation. The kinetic studies and computational modeling of our UiO-66 catalysts allow us to elucidate their mechanism in sulfide oxidation and further provide a guideline to improve the catalytic activities of the UiO-66 material.

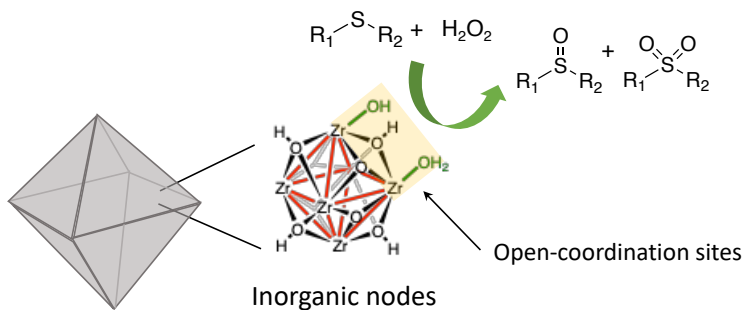


Figure 1.8 Node of UiO-66 MOFs and their catalytic activities in sulfide oxidation.

In chapter 4, we demonstrated that incorporating V^{IV} species onto the open-coordination sites of **UiO-66-NH₂** nodes can further increase the rate of sulfide oxidation. In addition, we developed a new reactor configuration that can carry out the rate study of **V-UiO-66-NH₂** catalyst in sulfide oxidation, providing a target rate for H_2O_2 generation in our tandem reaction (Figure 1.9). After measuring the initial rate of H_2O_2 generation, we tuned the reaction by adjusting the loading amount of Pd NPs in the **Pd@UiO-66-NH₂** MOF or the pressure of H_2 and O_2 gas feed. The optimized **Pd@UiO-66-NH₂** can be incorporated with V^{IV} species, yielding a dually functionalized catalyst that can efficiently consume H_2O_2 in [H_2O_2 generation + oxidation] tandem reaction.

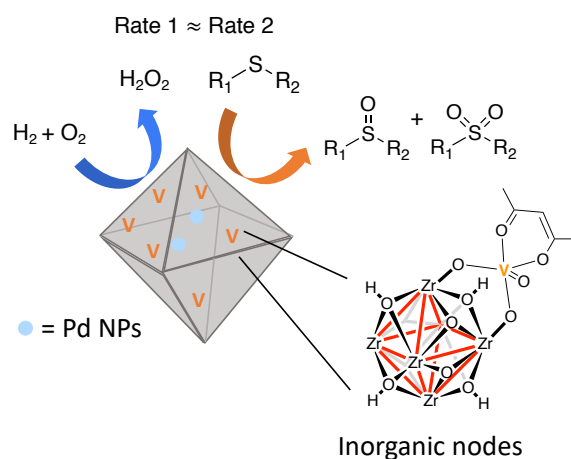


Figure 1.9 [H_2O_2 generation + sulfide oxidation] tandem reaction with efficient consumption of H_2O_2 .

Lastly, chapter 5 offers a summary to the development of dually functionalized UiO-66 MOF for [H_2O_2 generation + oxidation] tandem reaction. In addition, we provide an outlook on the future of catalyst design and applications for the [H_2O_2 generation + oxidation] tandem reaction.

Chapter 2

Coupling molecular and nanoparticle catalysts on single metal-organic framework microcrystals for the [H₂O₂ generation + selective alkene oxidation] tandem reaction

Portions of this chapter appear in the following manuscript: Limvorapitux, R.; Chou, L. Y.;

Young, A. P.; Tsung, C.-K.; Nguyen, S. T., *ACS Catal.* **2017**, *7*, 6691-6698.

2.1 Introduction

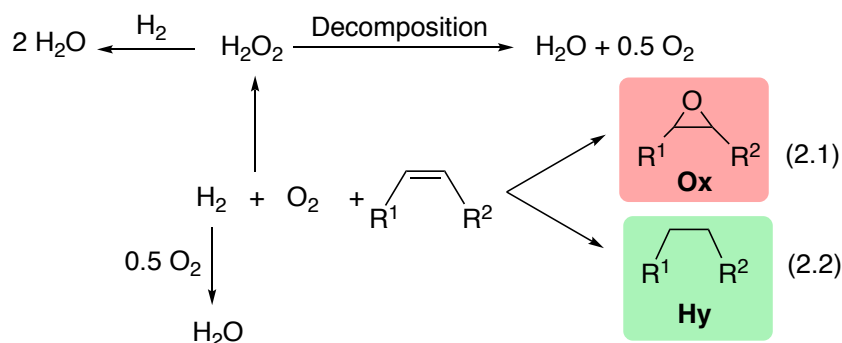
As discussed in chapter 1, combining H_2O_2 generation and oxidation into a tandem reaction can result in a better utilization of the oxidant by eliminating separation, purification, and transportation. In this chapter, we focus on developing a model catalyst, a *dually functionalized MOF*, for this tandem reaction and demonstrate its advantages in the [H_2O_2 generation + alkene oxidation] tandem reaction. First, using the UiO-66 MOF as a catalyst support for two catalyst sites can suppress the alkene-hydrogenation side reaction. Second, the close proximity of two catalysts can enhance the productivity for the epoxide product. Third, the rate of H_2O_2 generation can be tuned for a better utilization of H_2O_2 .

2.2 Background and motivation

Epoxides are key chemical intermediates for the syntheses of many fine chemicals and pharmaceuticals³⁶ and can be synthesized from an alkene in the presence of H_2O_2 . A major commercial success in this area is the use of the titanium silicalite-1 (TS-1) catalyst for the oxidation of propylene by H_2O_2 , as industrially practiced by Dow and BASF in the production of propylene oxide.¹⁹ To couple H_2O_2 generation and alkene oxidation into a tandem reaction (Scheme 2.1, Eq 2.1),¹⁹ two catalysts can be used: one for producing H_2O_2 and the other for the subsequent oxidation step. Given that H_2O_2 can safely be generated from H_2 and O_2 gases in the presence of Pd or Au nanoparticles (NPs) (see Section 2.9 for further safety discussion),²²⁻²⁴ these NP catalysts are highly attractive candidates for the H_2O_2 -generating step. As an example, Au/TS-1 catalysts have been extensively examined as tandem catalysts for gas-phase propylene epoxidation^{37,38,39} where the Au NPs serve as the primary catalyst for H_2O_2 generation and Au-Ti sites are the main active species for oxidation.⁴⁰ Unfortunately, the noble-metal NPs are also

known to be active catalysts for alkene hydrogenation (Scheme 2.1, Eq 2.2),⁴¹⁻⁴² and it is this secondary pathway that can significantly decrease the overall selectivity towards the desired epoxide product.⁴³⁻⁴⁶ Thus, incorporating a strategy that can suppress the alkene-hydrogenation pathway in NP-catalyzed H₂O₂-generation would be highly attractive for increasing epoxide selectivity in a [H₂O₂ generation + alkene oxidation] tandem reaction.

Scheme 2.1 A schematic of the reaction manifolds for the [H₂O₂ generation + alkene oxidation] tandem reaction.^a



^aWe note in passing that the NPs used in this tandem scheme can also catalyze other side reactions such as combustion of hydrogen, hydrogenation of H₂O₂, and decomposition of H₂O₂ (left side of the scheme), all of which can reduce the selectivity toward H₂O₂ generation.²³

Although current efforts to couple H₂O₂ generation and alkene oxidations have been focused primarily on gas-phase reactions via flow processes with simple alkenes such as propylene,^{19, 47-49} we are interested in the possibility of extending this concept to liquid-phase reactions⁴³ that can encompass a wider scope of alkene substrates. However, carrying out such reactions in solution, particularly for batch processes, requires that we address two challenging criteria. First, the two different types of catalysts need to be deployed within a close proximity to decrease the degree of diffusion and decomposition of H₂O₂. Second, as described above, an additional selectivity screen would be necessary to prevent the hydrogenation side reaction. Using

microcrystals of metal-organic frameworks (MOFs) as a platform to host and couple two different catalysts could be an ideal strategy to fulfill these criteria, given recent reports on the controlled positioning of several different catalysts into MOF crystals^{30, 50-53} and the demonstration that molecular-size selectivity can be achieved in MOF-based catalysts.⁵⁴⁻⁵⁶

In this chapter, we report a dually functionalized catalyst system based on MOFs to demonstrate the concept for [H₂O₂ generation + selective alkene oxidation] tandem reaction (Figure 2.1). The metal NPs are encapsulated within microcrystals of UiO-66-NH₂ MOF, whose surfaces are modified with a (sal)Mo^{VI} (sal = salicylaldimine) molecular epoxidation catalyst. The MOF aperture is large enough to allow the small H₂ and O₂ gases to reach the encapsulated NP catalysts to generate H₂O₂, which is then released into the reaction media. At the same time, this “gated window” aperture⁵⁷ can prevent the larger alkene substrate from coming into contact with the NPs to undergo the undesirable hydrogenation. In such a scenario, the alkene-oxidation catalyst moieties are most effective when positioned at the surface of the MOF microcrystals, where they can mediate the oxidation of the alkene substrate using the *in-situ*-generated H₂O₂. In such manners, the MOF crystal acts as a molecular-size “gatekeeper” that allows the dual catalyst functionalities to accomplish the desired [H₂O₂ generation + alkene oxidation] tandem reaction with minimal alkene hydrogenation. In addition, such a catalyst combination in one microcrystal will produce the desired epoxide product at a higher productivity than the corresponding physical mixture of two singly modified catalysts (i.e., a MOF-encapsulated NP catalyst and a MOF-supported (sal)Mo catalyst) due to the close proximity of the two catalyst species.

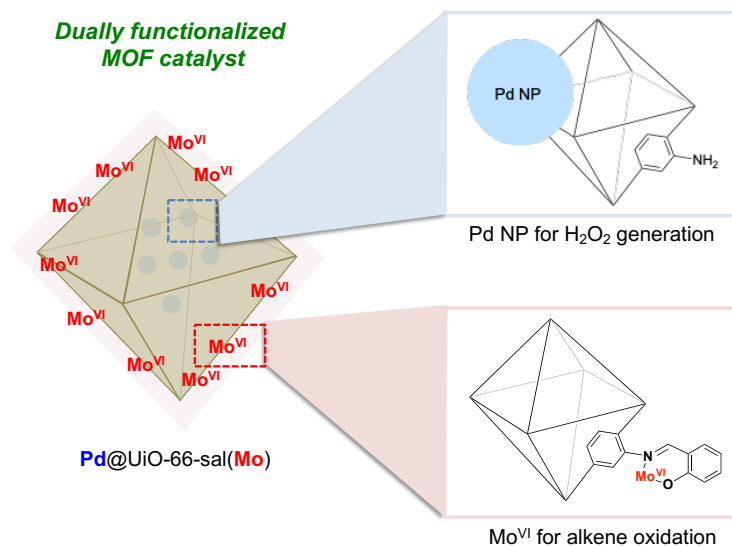
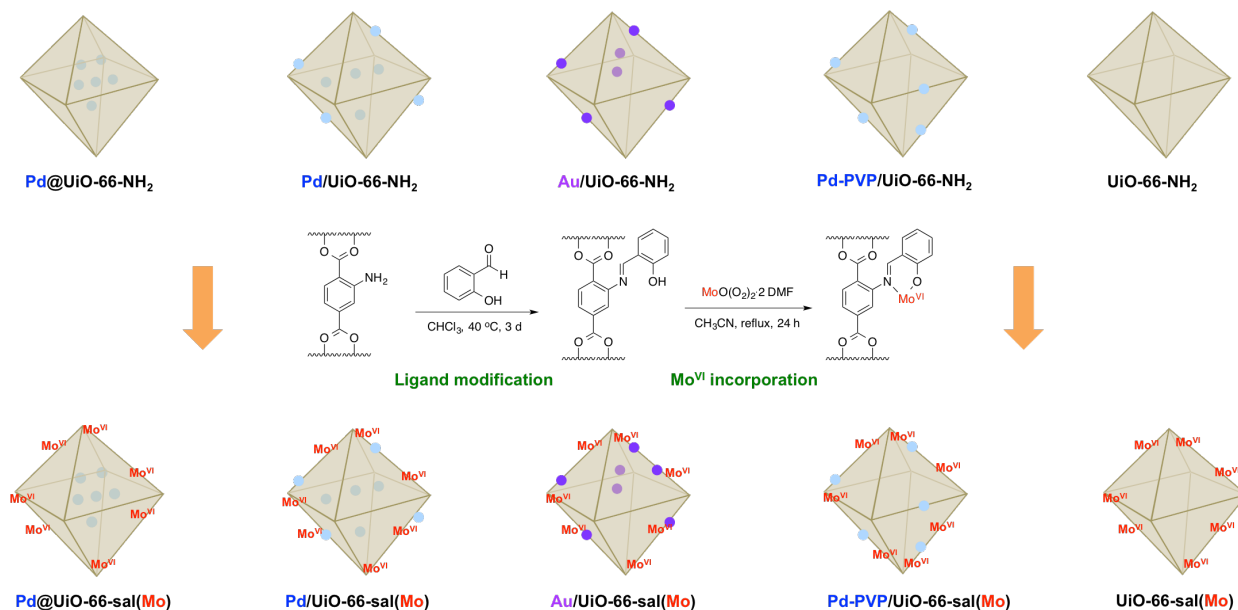


Figure 2.1 A schematic illustration of a dually functionalized MOF catalyst for the [H₂O₂ generation + selective alkene oxidation] tandem reaction. The Pd NPs are encapsulated inside the MOF microcrystal, whose surfaces are functionalized with sal(Mo) moieties.

2.3 Synthesis of MOF-based catalysts

As the MOF support of choice, we selected the UiO-66 series, which has the proper aperture size and excellent stability in protic media,³³⁻³⁵ to encapsulate noble-metal NPs^{29, 51, 58-60} and to be functionalized with molecular catalysts.⁶¹⁻⁶⁴ Encapsulation of Pd and Au NPs inside UiO-66 crystals still allows easy access for H₂ and O₂ through the ~6 Å aperture³² of the MOF and the subsequent release of H₂O₂ while selectively excluding larger alkene substrates such as *cis*-cyclooctene. For the molecular alkene-oxidation catalyst, we chose (sal)Mo, a moiety that has been tethered onto **UiO-66-NH₂** and has shown activity towards the epoxidation of *cis*-cyclooctene in the presence of H₂O₂,⁶² albeit at elevated temperature.

Scheme 2.2 The catalytic activity of MOF-based catalysts in H₂O₂ generation.



As shown in Scheme 2.2, **Pd@UiO-66-NH₂**, in which Pd NPs are encapsulated inside MOF crystals, are synthesized via a *de novo* method modified from a previous report⁶⁵ (see Section 2.9 for the synthesis procedure and for the characterization data). This material is then post-synthetically functionalized with salicylaldehyde and MoO(O₂)₂·2 DMF to create the dually functionalized **Pd@UiO-66-sal(Mo)** MOF in two steps,⁶² as confirmed by ICP-OES (Table 2.1) and FT-IR (Figures 2.9-2.10). The PXRD patterns of the modified MOFs indicated that the materials remained crystalline (Figures 2.6-2.7). TEM analysis confirmed the presence of encapsulated Pd NPs (6.1 ± 0.9 nm) throughout the MOF microcrystals (550 nm) (Figure 2.2). The decrease in the BET surface areas⁶²⁻⁶⁴ compared to that of **Pd@UiO-66-NH₂** was consistent with the sal(Mo) modification, which added mass and partially blocked the pores of the surface layers of the MOF crystals (Table 2.7, entries 2 and 8). To elucidate the effects of the individual catalyst components, we also synthesized two other materials (Scheme 2.2): 1) **Pd/UiO-66-NH₂**, where the NPs were formed via a wetness-impregnation method⁶⁶ so that Pd NPs are distributed

both inside the MOF crystals and on their exterior surfaces; 2) **Pd-PVP/UiO-66-NH₂**, where the PVP-capped Pd NPs⁶⁷ were first synthesized in colloidal solution and then attached to only the exterior surface of the MOF crystals.

Table 2.1 The NP sizes, NP loadings, and Mo loadings for UiO-66-NH₂ derivatives.

Catalyst	NP size (nm)	NP loading (wt %) ^a	Mo loading (wt %)
Pd@UiO-66-NH₂	-	3.2	-
Pd/UiO-66-NH₂	-	6.2	-
Au/UiO-66-NH₂	-	6.6	-
Pd-PVP/UiO-66-NH₂	-	2.5-3.3 ^b	-
Pd@UiO-66-sal(Mo)	6.1 ± 0.9	1.7	16
Pd/UiO-66-sal(Mo)	4.9 ± 1.0	2.4	17
Au/UiO-66-sal(Mo)	9.1 ± 2.8	4.3	16
Pd-PVP/UiO-66-sal(Mo)	3.6 ± 1.1	1.4	17
UiO-66-sal(Mo)	-	-	16-18 ^b

^aAfter the modification of amine ligand and the incorporation of Mo complex, the NP loadings in wt % decreased due to an increase in the total mass of catalyst (see Section 2.9 for the supporting calculation). ^bThe range of loading is from experimental variations over two batches.

While we initially set out to examine compositions that comprise either Pd or Au NPs, which are known to have very different activities for H₂O₂ generation, preliminary experiments suggested that synthesizing **Au@UiO-66-NH₂** material via a *de novo* method is difficult to achieve. As such, we adapted a double-solvent/H₂-reduction method⁶⁰ to synthesize **Au/UiO-66-NH₂** as an alternative, where the Au NPs are distributed mainly inside the MOF crystals, albeit with a small amount on the exterior surfaces. Comparing to the **UiO-66-NH₂**, all three classes of NP-containing MOFs still maintained good porosities and showed persistence of crystallinities as shown by BET area measurements (Table 2.7, entries 4-6) and PXRD analysis (Figure 2.6), respectively.

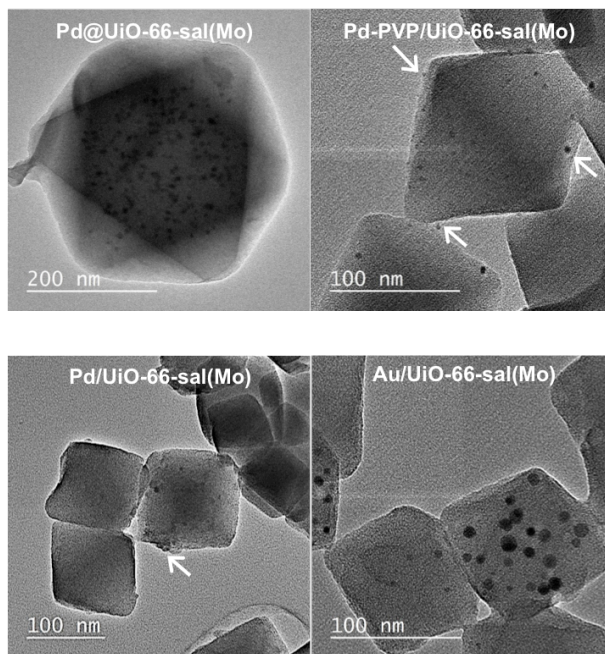


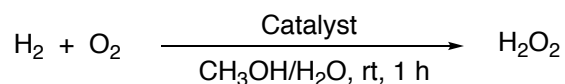
Figure 2.2 TEM images of the MOF materials before catalysis. To guide the readers' eyes, the position of some of the NPs on the MOF microcrystals for **Pd-PVP/UiO-66-sal(Mo)** and **Pd/UiO-66-sal(Mo)** have been indicated with white arrows. Comparing the TEM images of these samples to that of **Pd@UiO-66-sal(Mo)** suggests two different types of NP distributions. The NPs in the **Pd@UiO-66-sal(Mo)** sample are positioned throughout the middle part of the crystals because most of them are fully encapsulated inside the MOF crystals.

To evaluate the effect of the relative positioning of the two catalyst components, the (sal)Mo derivatives **Pd/UiO-66-sal(Mo)**, **Au/UiO-66-sal(Mo)**, **Pd-PVP/UiO-66-sal(Mo)**, and **UiO-66-sal(Mo)** were synthesized from the corresponding amino-functionalized derivatives. Using the previously discussed two-step post-synthesis modification (Scheme 2.2),⁶² all four materials can be obtained with comparable Mo loadings to that of **Pd@UiO-66-sal(Mo)** (Table 2.1), as indicated by ICP-OES analysis. Transmission FT-IR analysis (Figures 2.9-2.10) again confirmed the incorporation of the (sal)Mo functionalities. The PXRD patterns of these materials (Figures 2.6-2.7) were similar to those of the parent MOFs, indicating the preservation of crystallinity and long-range ordering. TEM images confirmed the presence of the NPs, on/in the

MOF crystals (Figure 2.2). As in the case of **Pd@UiO-66-sal(Mo)**, the BET areas of these four (sal)Mo derivatives decreased proportionately from those of the parent MOFs (Table 2.7).

2.4 Activities of NP-containing catalysts for H₂O₂ production

All catalyst samples and controls were separately tested for their activities towards H₂O₂ production from H₂ and O₂ gases (for the NP-containing catalysts) and alkene oxidation (for the (sal)Mo-containing catalysts). The catalytic generation of H₂O₂ was evaluated using a batch reactor in a 7/3 v/v CH₃OH/H₂O solvent mixture that was reported to be safe and optimal in productivity for this reaction (see Section 2.9 for further safety discussion),⁶⁸⁻⁷⁰ presumably due to a combination of the good solubilities of H₂ and O₂ gases²³ as well as the protic nature of the media.⁷¹ As expected, the control **UiO-66-NH₂** and **UiO-66-sal(Mo)** did not produce any H₂O₂ (Table 2.2, entries 2-3). In contrast, all Pd-containing catalysts were highly active, producing > 200 mol H₂O₂/h/kg_{NP} at room temperature (Table 2.2, entries 4-6), (see Section 2.9 for additional discussion on the effectiveness of the catalysts and their H₂ selectivity). **Au/UiO-66-NH₂** also produced H₂O₂, albeit at a slower rate than the Pd-containing materials (Table 2.2, cf. entries 7 and 5), consistent with literature reports.⁶⁸⁻⁷⁰

Table 2.2 The catalytic activity of MOF-based catalysts in H₂O₂ generation.

Entry	Catalyst	NPs (mg)	H ₂ O ₂ ^a (mM)	H ₂ O ₂ productivity ^a (mol/h/kg _{NP})
1	-	-	0	0
2	UiO-66-NH₂ ^b	-	0	0
3	UiO-66-sal(Mo) ^c	-	0	0
4	Pd@UiO-66-NH₂	0.5	7.0 ± 0.8	273 ± 31
5	Pd/UiO-66-NH₂	0.5	6.3 ± 0.3	248 ± 12
6	Pd-PVP/UiO-66-NH₂	0.5	6.6 ± 0.7	259 ± 28
7	Au/UiO-66-NH₂	2.6 ^d	0.3 ± 0.3	12 ± 10
8	Pd@UiO-66-NH₂ ^e	0.5	1.9 ± 0.1	12 ± 0.5

Reaction conditions: 5 vol % H₂/CO₂ (250 psig), 25 vol % O₂/CO₂ (100 psig), CH₃OH (14 mL), and H₂O (6 mL). ^aThe amount of H₂O₂ generated was determined by colorimetric titration with a 5 mM Ti(SO₄)₂ indicator solution. ^b15 mg of catalyst was used. ^c27 mg of catalyst was used. ^dA much-higher amount of Au NPs was needed to generate enough H₂O₂ to be detectable by the colorimetric titration. ^eThe reaction was conducted for 6 h.

Interestingly, the H₂O₂-generation activity of **Pd@UiO-66-NH₂** slowly degraded over time:⁷² the composite catalyst was only half as active after 3 cycles (Figure 2.13). Consistent with this behavior was the slight decrease in the H₂O₂ productivity exhibited by **Pd/UiO-66-NH₂** after being exposed to an H₂O₂ solution at room temperature for 6 h (cf. Table 2.2, entry 5 and Table 2.10, entry 4). As the amount of Pd NPs loss after reaction was minimal (~0.2 wt % loss after the 2nd and 3rd cycles; see Table 2.16), we attributed the activity loss to a decrease in active surface sites of the Pd NPs.

Although the encapsulated metal NPs can generate H₂O₂ from H₂ and O₂ gases, they can also cause the decomposition of H₂O₂ (Scheme 2.1), either through a side reaction with the H₂ gas^{70, 73} or by direct decomposition on the surface of the NPs.⁷³ These decomposition processes can be quite significant in solution, particularly for batch processes: when the **Pd@UiO-66-NH₂**

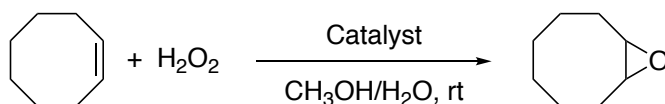
catalyst was employed in the H₂O₂-generation experiment for 6 h, instead of our standard 1 h experiment, the measured level of H₂O₂ productivity dropped by 20 times (Table 2.2, cf. entries 4 and 8). Similar results were observed for **Pd/UiO-66-NH₂** (cf. Table 2.2, entry 5 and Table 2.10, entry 3). Partially supporting the hypothesis that H₂O₂ can also undergo decomposition on the surface of the NPs was the observation that a commercial H₂O₂ solution undergoes more decomposition when being exposed to **Pd/UiO-66-NH₂** in comparison to **UiO-66-NH₂** (Table 2.9, cf. entries 2 and 3). These observations reinforce the necessity for positioning the (sal)Mo moiety in close proximity to the NP catalyst: the generated H₂O₂ is most efficiently used *in-situ* for the next step before the decomposition.

2.5 Activities of (sal)Mo-functionalized catalysts for alkene oxidation

As expected, our (sal)Mo-functionalized MOF composites were active towards the catalytic epoxidation of *cis*-cyclooctene with aqueous H₂O₂. In a 7/3 v/v CH₃OH/H₂O media, the same solvent mixture used in the H₂O₂ generation, **UiO-66-(sal)Mo** successfully produced cyclooctene oxide as the only oxidation product from *cis*-cyclooctene and H₂O₂. Unfortunately, when the reaction time was lengthened from 6 to 18 h, the oxidation productivity decreased (Table 2.3, cf. entries 3 and 4). ICP-OES analysis of the reaction solution after 6 h, where H₂O₂ is still present based on a colorimetric strip test, showed significant leaching (~80%) of Mo from the support (Table 2.16, entry 4), which could contribute to the observed loss in activity and a lower productivity overtime. However, a separate control experiment where **UiO-66-(sal)Mo** was exposed to a 7/3 v/v CH₃OH/H₂O solution of *cis*-cyclooctene over 6 h without stirring showed only 17% loss of Mo content (Table 2.12, entry 2), suggesting that the solvent system alone does not cause significant decomposition of the (sal)Mo moiety. Addition of H₂O₂ to the filtrate of this

solution results in minimal per-Mo oxidation productivity compared to the **UiO-66-(sal)Mo** (Table 2.12, cf. entries 1 vs 2), suggesting that the leached Mo species is not as active as the supported (sal)Mo moieties.

Table 2.3 The oxidation of *cis*-cyclooctene with H₂O₂ in 7/3 v/v CH₃OH/H₂O.^c



Entry	Catalyst	Amount (mg)	Time (h)	Oxidation ^a productivity ^b (mmol/h/kg _{cat})
1	-	0	18	0
2	UiO-66-NH₂	15	6	0
3	UiO-66-sal(Mo)	15	6	25 ± 2.5
4	UiO-66-sal(Mo)	15	18	18 ± 2.5

Reaction conditions: *cis*-cyclooctene (0.06 mmol), 30 wt % H₂O₂ (0.06 mmol), CH₃OH (7 mL), and H₂O (3 mL). ^aProductivity of epoxide was determined by GC-FID against an internal standard. ^bThe error bar was calculated based on the average of standard deviation from all runs. ^cFor additional yield and conversion data, see Table 2.11.

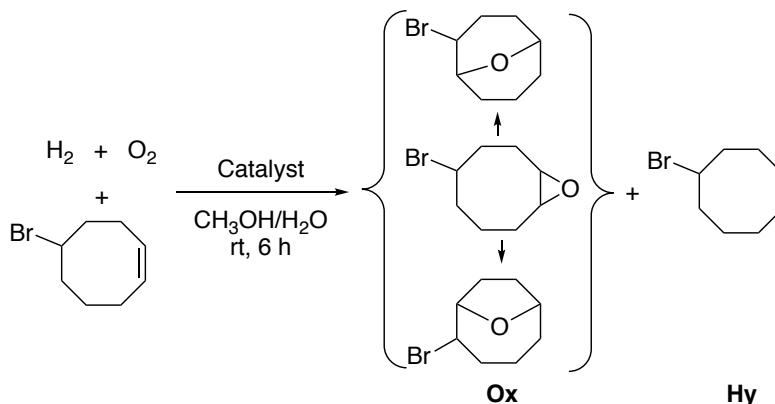
Together, the aforementioned data support the hypothesis that the loss of Mo species from the (sal)Mo-functionalized MOF is a primary cause for the deactivation of the epoxidation catalyst. This loss is most likely due to the presence of H₂O₂, although stirring may also accelerate the leaching by breaking up some of the more-fragile MOF crystals. As these complications would decrease the overall epoxide productivity in our systems, comparison of catalytic capabilities among the catalysts in this study are best made when the losses of Mo are similar. As expected, no epoxide was observed with the parent **UiO-66-NH₂** MOF (Table 2.3, entry 2). Given that our MOF-supported NPs and (sal)Mo catalyst components are capable of carrying out their respective catalytic functions at room temperature, we proceeded to elucidate their combined effect in the tandem reaction 2.1 (Scheme 2.1).

2.6 Activities and selectivities of MOF-based catalysts in tandem reaction

To minimize catalyst deactivation while still being able to obtain a detectable amount of epoxide, the tandem reaction 2.1 (Scheme 2.1) was first carried out using a physical mixture of MOF-supported NPs and (sal)Mo in the batch reactor. In addition, we selected 5-bromo-1-cyclooctene (Br-COE, smallest dimension ~ 5.23 Å, Figure 2.16) and 4-methylstyrene (smallest dimension ~ 4.22 Å, Figure 2.16) as the alkene substrates to test the hypothesis that the pore aperture of UiO-66-NH₂ (~ 6 Å³²) can exclude the larger alkene from coming to contact with the encapsulated NPs in MOFs. These substrates were also selected because their hydrogenated products have low volatility, thus minimizing the loss of these alkane byproducts during reactor sampling and allowing for more-accurate analysis of the hydrogenation pathway.

As expected, subjecting Br-COE to our catalytic conditions in the presence of the [Pd@UiO-66-NH₂ + UiO-66-(sal)Mo] catalyst combination, where Pd NPs are *encapsulated within the MOF crystals*, afforded a product mixture with a low molar ratio of hydrogenation and oxidation products (Hy/Ox) (Table 2.4, entry 1). In contrast, the [Pd-PVP/UiO-66-NH₂ + UiO-66-(sal)Mo] combination, where the Pd NPs *mostly resided on the surface of MOF crystals*, yielded a product mixture with a 6-fold-higher Hy/Ox ratio (Table 2.4, entry 2). Given the similar oxidation productivities for these two cases (Table 2.4, cf. entries 1 and 2), the lower Hy/Ox product ratio observed for the first can be attributed to the ability of the UiO-66 pore aperture in selectively sieving out Br-COE and preventing it from coming into contact with the encapsulated Pd NPs inside the Pd@UiO-66-NH₂ crystals. Not surprisingly, this low Hy/Ox ratio was preserved when the dually functionalized Pd@UiO-66-(sal)Mo MOF catalyst was used (Table 2.4, cf. entries 1 and 3).

Table 2.4 Hy/Ox ratios and Ox productivities for Br-COE in the presence of different types of MOF catalysts.^e



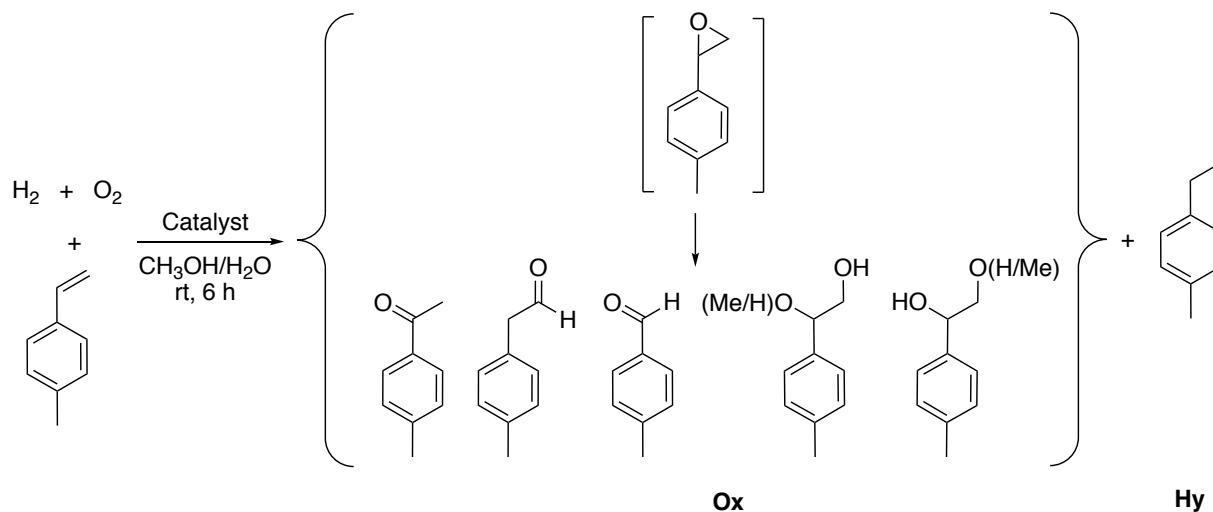
Entry	Catalyst	Hy/Ox ^a ratio ^b	Ox ^a productivity ^c (mmol/h/kg _{NP})
1	Pd@UiO-66-NH₂ + UiO-66-(sal)Mo	0.91 ± 0.28	191 ± 48
2 ^d	Pd-PVP/UiO-66-NH₂ + UiO-66-(sal)Mo	5.5 ± 1.7	211 ± 48
3	Pd@UiO-66-(sal)Mo	0.94 ± 0.29	206 ± 48

Reaction conditions: 5 vol % H₂/CO₂ (250 psig), 25 vol % O₂/CO₂ (100 psig), Br-COE (0.05 mmol), CH₃OH (14 mL), and H₂O (6 mL). The catalyst comprises 0.51 mg of NPs and 4.8 mg of Mo by weight. ^aThe oxidation (Ox) product comprises epoxide-rearranged compounds and was determined by GC-FID with an internal standard method. ^bThe error bar was proportionally calculated as a percentage of the Hy/Ox ratio based on the average of the percentage standard deviations from the alkane. ^cThe error bar was calculated based on the average of standard deviations from all tries. ^dFor this experiment, Pd-PVP/UiO-66-NH₂ was selected because most of its Pd NPs are located on the exterior surface of MOF crystal, which will provide the best contrast against the Pd@UiO-66-NH₂ in entry 1. ^eSee Table 2.13 for a full set of data and differences in the Hy/Ox ratios between the Pd/UiO-66-NH₂ and Pd-PVP/UiO-66-NH₂ systems.

Further supporting the aforementioned size-selective properties of the UiO-66 support is the much smaller (~1.3 fold) difference in Hy/Ox product ratios observed for 4-methylstyrene when being exposed to the [Pd@UiO-66-NH₂ + UiO-66-(sal)Mo] and [Pd-PVP/UiO-66-NH₂ + UiO-66-(sal)Mo] catalyst combinations, respectively (Table 2.5, cf. entries 1 and 2). While the encapsulated Pd NPs in the first catalyst combination are still less accessible to the 4-methylstyrene

substrate, the smaller size of this alkene would diminish the difference in substrate accessibilities between the two catalyst combinations, especially under similar oxidation productivities.

Table 2.5 Hy/Ox ratios and Ox productivities for 4-methylstyrene in the presence of different types of MOF catalysts.^e



Entry	Catalyst	Hy/Ox ^a ratio ^b	Ox ^a productivity ^c (mmol/h/kg _{NP})
1	Pd@UiO-66-NH₂ + UiO-66-(sal)Mo	22 ± 3	156 ± 22
2 ^d	Pd-PVP/UiO-66-NH₂ + UiO-66-(sal)Mo	29 ± 4	184 ± 22
3	Pd@UiO-66-(sal)Mo	10 ± 1	234 ± 22

Reaction conditions: 5 vol % H₂/CO₂ (250 psig), 25 vol % O₂/CO₂ (100 psig), 4-methylstyrene (0.05 mmol), CH₃OH (14 mL), and H₂O (6 mL). The catalyst comprises 0.68 mg of NPs and 4.8 mg of Mo by weight. ^aThe oxidation (Ox) product comprises epoxide-rearranged compounds (4-methylphenylacetaldehyde, 4-methylacetophenone, and minor epoxide ring-opening compounds) as well as other styrene-based oxidation products (4-methylbenzaldehyde) and was determined by GC-FID with an internal standard method. While the epoxide is not directly observed given the protic nature of the solvent mixture, the major rearranged products were verified as derivable from the epoxide by an independent experiment (See Section 2.9). ^bThe error bar was proportionally calculated as a percentage of the Hy/Ox ratio based on the average of the percentage standard deviations from the Ox products. ^cThe error bar was calculated based on the average of standard deviations from all runs. ^dFor this experiment, Pd-PVP/UiO-66-NH₂ was selected because most of its Pd NPs are located on the exterior surface of MOF crystal, which will provide the best contrast against the Pd@UiO-66-NH₂ in entry 1. ^eSee Table 2.14 for a full set of data and differences in the Hy/Ox ratios between the Pd/UiO-66-NH₂ and Pd-PVP/UiO-66-NH₂ systems.

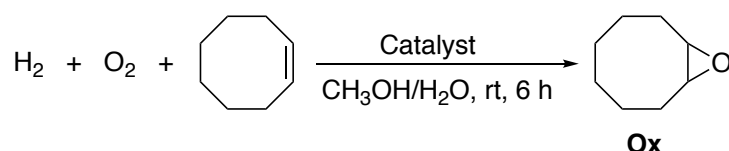
It is worth noting that the similar oxidation productivities for all the catalyst combinations in Table 2.4 can be attributed to a combination of two factors: the alkene oxidation step being rate-limiting and the low reactivity of the Br-COE substrate. Both of these can be inferred from the much larger H₂O₂ productivities (Table 2.2, unit = mol/h/kg_{NP} = 31.2 × mol/h/kg_{cat} for **Pd@UiO-66-NH₂**) in comparison to the epoxidation productivities for **UiO-66-(sal)Mo** (Table 2.3, unit = mmol/h/kg_{cat} = 0.16 × mmol/h/kg_{Mo}) and those from the tandem reaction (Table 2.4, unit = mmol/h/kg_{NP}). While the (sal)Mo moieties in the dually functionalized catalyst may experience a higher local H₂O₂ concentration by being close to the encapsulated Pd NPs, this advantage is greatly diminished if Br-COE is not converted to the epoxide fast enough. As a result, the oxidation productivities for all three-catalyst combinations do not appear to greatly differ, with most of the generated H₂O₂ diffusing into the solution. Together, these observations underline the importance of properly matching the rates of the different active sites in our tandem catalyst. This concept is demonstrated in the next section, where we employ the more-reactive substrate *cis*-cyclooctene to better accentuate the difference between the dually functionalized catalyst and the physical mixtures of the two singly functionalized catalysts.

2.7 The advantages of coupling NP and molecular catalysts on the same MOF microcrystal

To maximize the capability of our dually functionalized catalyst for epoxide generation, the tandem reaction 2.1 (Scheme 2.1) was carried out with *cis*-cyclooctene, which is more reactive than both Br-COE and 4-methylstyrene in epoxidation and whose epoxide is also more stable than the corresponding epoxides of both of these substrates. As anticipated, the singly functionalized catalyst controls do not show any cyclooctene epoxidation activity under our tandem reaction conditions (Table 2.6, entries 1-3 and 6). In addition, the absolute values for *cis*-cyclooctene

oxidation productivities by **Pd@UiO-66-(sal)Mo** and the [**Pd@UiO-66-NH₂** + **UiO-66-sal(Mo)**] physical mixture (Table 2.6, entries 5 and 4) are higher than the corresponding data for both 4-methylstyrene (Table 2.5, entries 3 and 1) and Br-COE (Table 2.4, entries 3 and 1), confirming that it is a much better substrate for H₂O₂ utilization.

Table 2.6 Oxidation productivity for *cis*-cyclooctene in the presence of different types of MOF catalysts.^d



Entry	Catalyst	NPs (mg)	Mo (mg)	Ox ^a productivity ^b (mmol/h/kg _{NP})
1	-	-	-	0
2	UiO-66-sal-Mo	-	4.8	0
3	Pd@UiO-66-NH₂	0.5	-	0
4	Pd@UiO-66-NH₂ + UiO-66-sal(Mo)	0.5	4.8	570 ± 64
5	Pd@UiO-66-sal(Mo)	0.5	4.8	828 ± 64
6	Pd/UiO-66-NH₂	0.5	-	0
7	Pd/UiO-66-NH₂ + UiO-66-sal(Mo)	0.7	4.8	493 ± 120
8	Pd/UiO-66-(sal)Mo	0.7	4.8	599 ± 120
9	Au/UiO-66-NH₂	2.6	-	2 ± 0.24 ^c
10	Au/UiO-66-NH₂ + UiO-66-sal(Mo)	2.6	9.6	2.5 ± 0.24
11	Au/UiO-66-(sal)Mo	2.6	9.6	26 ± 0.24

Reaction conditions: 5 vol % H₂/CO₂ (250 psig), 25 vol % O₂/CO₂ (100 psig), *cis*-cyclooctene (0.12 mmol), CH₃OH (14 mL), and H₂O (6 mL). ^aAmount of products and productivity were determined by GC-FID against an internal standard. ^bThe error bar was calculated by averaging standard deviations from all tries for each catalyst system. ^cWhile a small amount of cyclooctene oxide can be observed in the presence of the **Au/UiO-66-NH₂** control, this is not surprising because Au NPs are known to be active for alkene epoxidation with O₂ and TBHP.⁷⁴⁻⁷⁵ ^dSee Table 2.15 for a full set of data that includes the Pd-PVP system and the **Hy/Ox** ratios for all four tandem catalyst systems in this study.

Consistent with the results shown in Table 2.5, **Pd@UiO-66-(sal)Mo** exhibited higher oxidation productivity (~1.5 times) for *cis*-cyclooctene in comparison to the [**Pd@UiO-66-NH₂** + **UiO-66-sal(Mo)**] physical mixture (Table 2.6, cf. entries 5 and 4). These data reinforce our initial hypothesis that the *close proximity of two catalysts* increases product ratio in the tandem reaction: the closer the two catalysts, the higher the concentration of H₂O₂ around the sal(Mo) groups and the more effective the epoxidation. Because H₂O₂ is generated within the MOF crystal, as it diffuses out it is more likely to be consumed by the (sal)Mo moieties on the crystal surface to produce the epoxide. Similar observations have recently been reported by Yamashita and coworkers for a Pd@Ti-HSS yolk-shell nanostructured catalyst used in a [H₂O₂ generation + sulfide oxidation] tandem reaction.⁷⁶ While the alkene oxidation step is still rate-limiting for **Pd@UiO-66-(sal)Mo**, the (sal)Mo moieties can epoxidize the more-active *cis*-cyclooctene substrate faster, leading to a more effective usage of the H₂O₂ oxidant compared to that in the Br-COE case.

The advantage of having the Pd NPs completely encapsulated inside the UiO-66 crystal is also quite clear. **Pd@UiO-66-(sal)Mo** afforded a more effective utilization of the generated H₂O₂ oxidant than **Pd/UiO-66-(sal)Mo**, as reflected by the larger oxidation productivity (Table 2.6, cf. entries 5 and 8) under similar H₂O₂ generation per kg_{NP} (Table 2.2, cf. entries 4 and 5). Presumably, much of the H₂O₂ that was generated by the Pd NPs that reside on the surface of the **Pd/UiO-66-(sal)Mo** microcrystals would diffuse away before having a chance to react with the (sal)Mo moiety and the alkene substrate. In addition, the *cis*-cyclooctene substrate in solution will be more likely to undergo hydrogenation reactions with the exposed Pd NPs on the surface of **Pd/UiO-66-sal(Mo)** microcrystals (Table 2.15, cf. the **Hy/Ox** ratios for entries 3 and 6), and this

will decrease the substrate concentration able to undergo epoxidation. Together, these two factors decrease the total oxidation productivity for **Pd/UiO-66-sal(Mo)**, in comparison to **Pd@UiO-66-sal(Mo)**.

While employing *cis*-cyclooctene as a substrate can lead to improved usage of the H₂O₂ oxidant, **Pd@UiO-66-(sal)Mo** is still only ~1.5 times better than the [**Pd@UiO-66-NH₂** + **UiO-66-sal(Mo)**] physical mixture in oxidation productivities (Table 2.6, cf. entries 5 and 4). This small difference may be explained if the Pd NPs are producing H₂O₂ at a faster rate than can be efficiently consumed by the (sal)Mo catalysts and most of the H₂O₂ would diffuse into the solution. In such a scenario, a major portion of the oxidation product would come from the interactions of the (sal)Mo moiety with the H₂O₂ in solution and the oxidation productivities of the two aforementioned catalysts would not be very different. Employing a *slower* H₂O₂-generating catalyst, such as that based on Au NPs (Table 2.2, cf. entries 5 and 7), should then allow for a more-even matching of the two reactions in our tandem reaction 2.1 (Scheme 2.1), resulting in a bigger difference in epoxide productivities between the dually functionalized catalyst and the physical mixture of two singly functionalized catalysts.

Indeed, the advantage of coupling two catalysts in one MOF crystal is most noticeable when comparing **Au/UiO-66-(sal)Mo** and [**Au/UiO-66-NH₂** + **UiO-66-(sal)Mo**] (Table 2.6). The dually functionalized catalyst exhibited an epoxide productivity that is an order of magnitude higher than the corresponding physical mixture (Table 2.6, cf. entries 10 and 11). We attribute this large difference in epoxide productivities observed between the two Au NP-containing catalysts to the slower production of H₂O₂ by Au NPs. As the amount of H₂O₂ being generated in **Au/UiO-66-(sal)Mo** is smaller than that in the Pd analog, the oxidant should have a better chance

of reacting with the (sal)Mo catalyst moiety on the surface of the MOF crystal before diffusing into the solution. In contrast, in the [Au/UiO-66-NH₂ + UiO-66-sal(Mo)] physical mixture, the small amount of H₂O₂ being generated by Au/UiO-66-NH₂ must additionally diffuse into solution before reaching the UiO-66-sal(Mo) catalyst, leading to a large decrease in the effective usage of the oxidant in the epoxidation step.

The aforementioned close-proximity effect, which is much larger for the two Au/UiO-66 systems (10×; Table 2.6, cf. entries 10 and 11) compared to that for the analogous Pd/UiO-66 systems (1.2×; Table 2.6, cf. entries 7 and 8), can indeed be attributed to the large differences in rate of H₂O₂ generation. As the Pd NPs produces H₂O₂ at a much faster rate than Au NPs (Table 2.2, cf. entries 5 and 7), a large portion of the generated H₂O₂ diffuses into the solution, leading to a smaller percentage difference in the oxidant concentrations around the (sal)Mo moiety in Pd/UiO-66-(sal)Mo compared to that in the [Pd/UiO-66-NH₂ + UiO-66-sal(Mo)] physical mixture. This in turn leads to a smaller percentage difference in the two corresponding epoxide productivities.

2.8 Conclusion

We have demonstrated that the controlled positioning and coupling of two different catalysts in one MOF microcrystal can be highly beneficial for the [H₂O₂ generation + alkene oxidation] tandem reaction (Scheme 2.1, Eq 2.1). By encapsulating NP catalysts inside UiO-66-NH₂ microcrystals, we minimize their interactions with the large alkene substrates and reduce side reactions such as alkene hydrogenation in the presence of H₂. In addition, enhanced epoxide productivity is achieved when both the H₂O₂-generating NP and the (sal)Mo epoxidation catalysts are integrated on the same MOF crystal. This colocalization effect can be quite important for the

most effective usage of the relatively unstable H₂O₂ oxidant, especially for the case of Au NP, whose H₂O₂-generation activity is lower than that for the Pd NP analogue. Together, these data suggest that the close positioning and good activity-matching between the two-active species in the support as well as the substrate are both important for the improvement in tandem catalysis.

While these issues will be addressed in chapters 3 and 4, we note herein that the use of MOF as a controllable platform for the close co-deployment of different catalysts that can act in concert in a molecular-like scale is a promising venue for integrating biocatalytic concepts into abiotic platform, akin to cascade reactions in multi-enzyme processes.⁷⁷⁻⁷⁹ Successful implementation of such a concept can allow for the spatial separation of incompatible reactants,⁸⁰ allowing for the development of novel tandem reactions with high selectivity and efficiency.

2.9 Experimental

2.9.1 Materials and methods

Unless otherwise stated, all reagents were used as received. Zirconium chloride was purchased from Strem Chemicals, Inc. (Newburyport, MA). 2-Aminoterephthalic acid, hydrogen peroxide, *m*-chloroperbenzoic acid, hydrobromic acid solution 33 wt % in acetic acid, *cis*-cyclooctene, 1,5-cyclooctadiene, naphthalene, H₂AuCl₄·3H₂O, MoO₃, PdCl₂, Na₂PdCl₄, L-ascorbic acid, polyvinylpyrrolidone, potassium bromide, and ICP standards (gold, palladium, molybdenum and zirconium) were purchased from Sigma-Aldrich Co., LLC. (St. Louis, MI). Salicylaldehyde was purchased from Acros Organic, part of Thermo Fisher Scientific (Morris, NJ). Potassium chloride was purchased from Fisher Scientific, Inc. (Pittsburg, PA). Concentrated sulfuric acid and glacial acetic acid were purchased from VWR Scientific, LLC (Chicago, IL). Deuterated dimethylsulfoxide (DMSO-*d*₆, 99%), deuterated chloroform (CDCl₃, 99.8%) and deuterated

sulfuric acid (D_2SO_4 , 96–98% solution in D_2O) were purchased from Cambridge Isotope Laboratories, Inc. (Tewksbury, MA). Ultrapure deionized (DI) H_2O (18.2 $M\Omega\cdot cm$ resistivity) was obtained from a Millipore Milli-Q Biocel A10 instrument (Millipore Inc., Billerica, MA). Solvents were purchased from either Sigma-Aldrich Co., LLC. (St. Louis, MI) or Fisher Scientific, Inc. (Pittsburg, PA) and used as received.

N_2 gas (Ultra High Purity Grade 5) used for the adsorption and desorption measurements was obtained from Airgas Specialty Gases (Chicago, IL). Gases for H_2 reduction (5 vol % H_2/N_2) and for reaction (5 vol % H_2/CO_2 and 25 vol % O_2/CO_2) were also obtained from Airgas Specialty Gases (Chicago, IL). Dry solvents were prepared by passing HPLC-grade solvents through a Dow-Grubbs solvent system installed by Glass Contours (now JC Meyer Solvent Systems, Laguna Beach, CA, USA). Dry hexane was collected under inert gases, degassed under vacuum, and stored under nitrogen in a Strauss flask prior to use.

N_2 adsorption and desorption isotherms were measured on a Micromeritics Tristar II 3020 (Micromeritics Instrument Corporation, Norcross, GA) at 77 K. Before each run, samples were activated at 120 °C for 24 h under high vacuum on an ASAP 2020 (Micromeritics Instrument Corporation, Norcross, GA) instrument. Between 40-100 mg of sample was used in each measurement and BET surface area was calculated in the region $P/P_0 = 0.005-0.3$. The micropore volumes, micropore surface areas, and external surface areas for all samples were determined using conventional t-plot methods from N_2 adsorption data. For most of the MOFs, the values were selected over the 3.5-5 Å range by fitting the data to the Harkins-Jura thickness equation.⁸¹

Transmission electron microscopy (TEM) images were taken by Prof. Lien-Yang Chou and Dr. Allison Young using a 200 mesh copper grids (Ted Pella, Inc., Redding, CA) on a JEOL JEM2010F run at 200 kV (JEOL USA Inc., Peabody, MA).

Powder X-ray diffraction (PXRD) patterns were recorded on a ATX-G Rigaku X-ray Diffractometer (Rigaku Americas, The Woodlands, TX) equipped with an 18 kW Cu rotating anode, an MLO monochromator, and a high-count-rate scintillation detector. Measurements were made over the range $2^\circ < 2\theta < 50^\circ$ in 0.05° step width with a $3^\circ/\text{min}$ scanning speed.

Inductively coupled plasma optical-emission spectroscopy (ICP-OES) was conducted on a computer-controlled (QTEGRA software v. 2.2) Thermo iCap 7600 Duo ICP-OES (Thermo Fisher Scientific, Waltham, MA) instrument equipped with a SPRINT valve and a CETAC 520ASX autosampler (Teledyne CETAC, Inc., Omaha, NE). MOF samples (~2 mg) were digested in a small amount (1.5 mL) of a mixture of 1/1 v/v conc. HNO_3/HCl by heating in a Biotage SPX microwave reactor (Biotage, Uppsala, Sweden, software version 2.3, build 6250) at 120°C until the solution became clear. The acidic solution was diluted to 25 mL with DI H_2O and analyzed for Pd (324.270 and 340.458 nm), Mo (202.030, 204.598 and 203.844 nm), Au (242.795, 267.595 and 208.209 nm), and Zr (339.198 and 343.823 nm) content as compared to standard solutions.

Absorption spectra of mixture solution were recorded on a Varian Cary 300 Bio UV-vis spectrophotometer (Varian, Inc., Palo Alto, CA) using a masked quartz cell (path length = 10 mm, catalog # 29B-Q-10-MS, Starna cells Inc., Atascadero, CA).

Fourier-transformed infrared (FT-IR) spectroscopy was performed on a Thermo Nicolet Nexus 870 FTIR spectrometer (Thermo Scientific, Waltham, MA), using KBr pellets. Frequencies

are given in reciprocal centimeters (cm^{-1}). The FT-IR spectra were analyzed using EZ Omnic software (Thermo Scientific, Waltham, MA).

^1H NMR and ^{13}C NMR spectra were recorded on a Bruker 500 FT-NMR spectrometer (Bruker Biospin Corp., Billerica, MA, 499.773 MHz). ^1H chemical shifts are reported in ppm from TMS with the residual solvent resonances as internal standards.

Centrifugation was carried out in an Eppendorf Centrifuge 5804 R, Model AG 22331 (Eppendorf AG, Hamburg, Germany) equipped with an F34-6-38 rotor. All centrifugations were carried out at 5000-6000 rpm (3214-4628 g) for 10-20 min.

Gas chromatographic analysis was carried out on an Agilent Technologies 6890N Network GC system (Agilent Technologies, Inc., Santa Clara, CA) equipped with an FID detector. An HP-5 capillary column (30 m \times 320 μm \times 0.25 μm film thickness) was used to analyze *cis*-cyclooctene and 5-bromo-1-cyclooctene substrates. A ZB-624 capillary column (30 m \times 250 μm \times 1.4 μm film thickness) was used to analyze 4-methylstyrene substrate.

GC-MS analysis was carried out on either: 1) a Shimadzu QP2010 GC/MS system (Shimadzu Corp, Kyoto, Japan) equipped with a ZB-624 column (30 m \times 250 μm \times 1.4 μm film thickness) and processed with Shimadzu GCMS solution software version 2.71. Or 2) an Agilent Technologies 6890N Network GC system (Agilent Technologies, Inc., Santa Clara, CA) equipped with an HP-5 capillary column (30 m \times 320 μm \times 0.25 μm film thickness) and processed with Agilent Instrument GCMS software version E.02.02.1431.

Safety caution regarding mixture of H_2 and O_2 gases. Given that a combination of H_2 (flammable gas) and O_2 (oxidizer) in the presence of a metal catalyst has the potential for explosion, solvent choice, gas composition, vol % of each gas, as well as temperature and pressure

of the reaction must be carefully considered before carrying out the experiment. We selected a 7/3 v/v CH₃OH/H₂O solvent mixture that was reported to be safe and optimal in productivity for the H₂O₂ generation.⁶⁸⁻⁷⁰ Regarding the gas composition and vol % of each gas component, CO₂ was chosen as an inert diluent for the H₂/O₂ gas mixtures because its presence narrows down the explosive region of these mixtures more than other inert gases.^{15, 82} For the gas mixture in this study, we chose to combine a 250 psig feed of 5 vol % H₂/CO₂ and a 100 psig feed of 25 vol % O₂/CO₂ to give a final H₂/O₂/CO₂ volume ratio of 3.6/7.1/89.3, which is predicted to be outside of the explosive window.⁸³ Finally, as an increase in temperature and pressure will widen the explosion range,⁸⁴ we conducted our reaction at room temperature and a safe total pressure of 350 psig.

2.9.2 Synthesis of precursor, UiO-66-NH₂ and its derivatives

UiO-66-NH₂. This material was made following a previously reported literature procedure.⁶⁴ In a 250 mL round-bottom flask, ZrCl₄ (0.4 g, 1.7 mmol) was dissolved in DMF (75 mL) by ultra-sonication at 50-60 °C before being combined with glacial acetic acid (2.85 mL, 850 mmol). In a separate 50 mL Erlenmeyer flask, 2-aminoterephthalic acid (0.311 g, 1.7 mmol) was dissolved completely in DMF (25 mL) before being added to the ZrCl₄ solution. The combined mixture was homogenized by swirling before a small amount (0.125 mL) of DI H₂O was added. The tightly capped round-bottom flask was sonicated at 50-60 °C and placed in a 120 °C oil bath under static condition for 24 h. After being cooled to room temperature, the precipitate was collected by centrifugation and washed with DMF (~20 mL) two times each day for two days. The collected materials were then washed and immersed in CH₃OH (~20 mL) three times for one day before being isolated through centrifugation and decantation. The isolated solid was then dried at

120 °C under vacuum to give a light yellow powder (~500 mg) that is then stored at room temperature. Multiple batches of MOFs were synthesized and combined for subsequent use in the syntheses of other MOF catalysts. Characterization data was obtained on the combined materials as detailed in later section.

Pd@UiO-66-NH₂. This material was made by Prof. Lien-Yang Chou and Dr. Allison Young following a previously reported literature procedure⁶⁵ with some modifications in a manner that is similar to the synthesis of **UiO-66-NH₂**. Briefly, Na₂PdCl₄ (2.35 mg, 0.008 mmol) was first dissolved in the DMF (1 mL) that is going to be used in the **UiO-66-NH₂** synthesis. The synthesis of **Pd@UiO-66-NH₂** was then carried out using this DMF solution as described above. After 24 h at 120 °C, the product was collected by centrifugation, washed with DMF (25 mL) two times per day for two days, and immersed in CH₃OH (25 mL) for three additional days. The isolated solid was then dried at 120 °C under vacuum overnight and stored at room temperature before use.

We note that the strategy that we employed herein takes advantage of a recently reported concept⁶⁵ where the NPs are first formed in the MOF-synthesis reaction mixture and then coated by the MOF in the same media. This strategy can dramatically reduce the numbers of NPs on the exterior surface in contrast to conventional wetness-impregnation method,⁸⁵⁻⁸⁷ where the NP particle synthesis is carried out by soaking the MOF crystals in solutions of the metal precursor and then reducing the entrapped metal ions. This difference is apparent when one compares the TEM images of our **Pd@UiO-66-(sal)Mo** (*in-situ* method) and **Pd/UiO-66-(sal)Mo** (wetness-impregnation method) samples (Figure 2.2 for pre-catalysis and Figure 2.11 for post-catalysis).

Pd/UiO-66-NH₂. This material was made by adapting a literature protocol for Pd/MIL-125(Ti).⁶⁶ In a 6 dram vial, 10 mM H₂PdCl₄ solution was prepared by dissolving PdCl₂ (177 mg,

1 mmol) in 0.4 M HCl_{aq} (5 mL, 2 mmol). The solution was heated up to 70 °C until PdCl₂ was completely dissolved, and diluted up to 100 mL with DI H₂O. Activated **UiO-66-NH₂** (200 mg) was dispersed in DI H₂O (40 mL) by ultra-sonication for ~10 min in a separate 100 mL round-bottom flask. The aqueous Pd solution (10 mL) was then added dropwise to the stirring MOF dispersion over a period of 20 min and the resulting mixture was further stirred for 24 h. Then MOFs composite was isolated by centrifugation, dried at 120 °C under vacuum, and reduced in a 5 vol % H₂/N₂ flow at 200 °C for 6 h.

PVP-modified Pd nanoparticles (Pd-PVP). This material was synthesized according to previously reported literature protocol.⁶⁷ Poly(vinylpyrrolidone) (PVP, 105 mg), L-ascorbic acid (60 mg, 0.34 mmol), KBr (75 mg, 0.63 mmol), and KCl (141 mg, 1.9 mmol) were dissolved in DI H₂O (8 mL) in a 50 mL round-bottom flask and the mixture was stirred at 80 °C for 10 min. In a separate 2 dram vial, Na₂PdCl₄ (57 mg, 0.19 mmol) was dissolved in DI H₂O (3 mL) and the aqueous Pd solution was added to pre-prepared PVP solution dropwise under the vigorous stir. The flask was capped and the reaction was stirred at 80 °C for 3 h. The Pd-PVP was collected by centrifugal filter (Amicon Ultra centrifugal filter units, MWCO 10kDa), washed 10 times with DI H₂O to remove excess PVP, and dried at 120 °C under vacuum.

Pd-PVP/UiO-66-NH₂. This material was made by adapting the literature procedure for Pd/ZnO.⁶⁷ All of as-prepared Pd-PVP NPs were dispersed in ethanol (5 mL) in a 6 dram vial. In a separate 100 mL round-bottom flask, **UiO-66-NH₂** (250 mg) was well-dispersed in ethanol (30 mL) by ultra-sonication for ~10 min before being combined with the Pd-PVP in ethanol solution (2.5 mL) under the vigorous stirring. The mixture was stirred continuously for 3 h and the MOFs was isolated by centrifugation. After being washed with ethanol, the MOFs was dried at 120 °C

under vacuum. Two batches of MOF were synthesized and combined for characterization before being used in catalysis.

Au/UiO-66-NH₂. This material was made by adapting the literature procedure for Au/UiO-66.⁶⁰ In a 1 dram vial, HAuCl₄·3H₂O (27.6 mg, 0.07 mmol) was dissolved completely in DI H₂O (160 μL). Activated **UiO-66-NH₂** (200 mg) was added to a separate 100 mL pear-shaped Schlenk flask equipped with a magnetic stir bar. The flask was evacuated and filled with nitrogen gas before dry *n*-hexane (40 mL) was added. The mixture was sonicated for ~20 min until the MOF was well-dispersed in the solvent and set to stir vigorously. The aqueous Au^{III} solution was then added dropwise to the stirring MOF dispersion over a period of 20 min and the resulting mixture was further stirred for 3 h. The reaction was stopped and the composite MOF material was allowed to settle. It was then isolated from the mother liquor by decantation, left in the flask until all the remaining solvent had evaporated, and dried at 120 °C under vacuum. For ease of handling and to make a large-enough quantity for the series of studies, materials from three batches of MOFs were combined and reduced in a 5 vol % H₂/N₂ flow at 200 °C for 6 h.

MoO(O₂)₂·2 DMF. This material was synthesized according to previous reported literature protocol.⁶² In a 100 mL round-bottom flask, MoO₃ (4 g, 0.028 mmol) and H₂O₂ (20 mL, 0.26 mmol) were combined and stirred at 40 °C for 4 h. DMF (4.48 mL, 0.054 mmol) was then added into the flask, and the mixture was stirred for 2 h at room temperature. After that the filtrate was filtered out from the mixture using a disposable syringe equipped with 0.2 μm PTFE syringe filter (VWR International, North American Cat. No. 28145-495). The yellow solution was stored in the refrigerator for 1-2 days before being vacuum-filtered over a Büchner funnel. The collected precipitant was subsequently rinsed several times with ethanol (~10 mL each) over the Büchner

funnel. Finally, the yellow solid was transfer to a watch glass before being covered by another watch glass and dried over Drierite in a glass vacuum desiccator for 24 h.

UiO-66-sal(Mo). This material was made following a literature procedure.⁶² In a 50 mL round-bottom flask, **UiO-66-NH₂** (700 mg) was dispersed in CHCl₃ (15 mL) by ultra-sonication for ~10 min before being combined with salicylaldehyde (700 μ L, 6.6 mmol). The mixture was stirred at 40 °C for three days and the MOFs was collected by centrifugation. The collected MOFs was redispersed in CH₃CN and soaked for ~3 h before being collected by centrifugation and this washing step was repeated five times. Next, in a 250 mL round-bottom flask, the **UiO-66-(sal)** MOF was dispersed in CH₃CN (70 mL) by ultra-sonication for ~10 min before being combined with MoO(O₂)₂·2 DMF (700 mg, 2.2 mmol). The resulting mixture was stirred at reflux for 24 h and the MOFs was collected by centrifugation. The MOFs was redispersed and soaked in CH₃CN (~30 mL) for ~3 h before being collected by centrifugation. This CH₃CN-washing step was repeated 3 times, and then 3 more with ethanol (~30 mL). Finally, the **UiO-66-(sal)Mo** MOF was dried at 120 °C under vacuum overnight and stored at room temperature in a screw-cap vial.

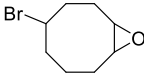
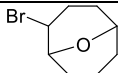
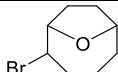
Pd@UiO-66-sal(Mo), Pd/UiO-66-sal(Mo), Pd-PVP/UiO-66-sal(Mo), and Au/UiO-66-sal(Mo) can be prepared by following the synthesis of **UiO-66-sal(Mo)** and replacing **UiO-66-NH₂** with **Pd@UiO-66-NH₂**, **Pd/UiO-66-NH₂**, **Pd-PVP/UiO-66-NH₂**, and **Au/UiO-66-NH₂** to obtain **Pd@UiO-66-sal(Mo)**, **Pd/UiO-66-sal(Mo)**, **Pd-PVP/UiO-66-sal(Mo)**, and **Au/UiO-66-sal(Mo)**, respectively. The amount of the parent MOF material might be varied, but the ratio of reagents were kept the same for all syntheses.

5-bromo-1-cyclooctene (Br-COE). This compound was synthesized according to a previously reported literature protocol⁸⁸ with some modification. In a 100 mL round-bottom flask

equipped with a magnetic stir bar, HBr/acetic acid (13 mL, 0.074 mol) was added in to inhibitor-free 1,5-cyclooctadiene (10 mL, 0.082 mol). The mixture was vigorously stirred for 18 h at room temperature. The reaction mixture was poured into an ice/water mixture, extracted with diethyl ether, washed with NaHCO₃ solution, dried over Na₂SO₄, and filtered over a Büchner funnel. The filtrate was evaporated *in vacuo* and the resulting yellow oil was distilled under vacuum. The collected crude-product distillate (~6 mL) was further purified via flash-column chromatography on silica gel (3 mm × 15 mm; hexanes eluent). Combining the product-containing fractions and removing solvents yielded Br-COE as a light yellow oil.

***m*CPBA epoxidation of Br-COE.** In a 50 mL round-bottom flask equipped with a magnetic stir bar, a solution of Br-COE (1 g, 5.3 mmol) in CH₂Cl₂ (25 mL) was vigorously stirred for 20 min in an ice/water bath. Freshly recrystallized *m*CPBA (910 mg, 5.3 mmol) was added and the resulting mixture was stirred for an additional 20 min during which time a white precipitate formed. The reaction mixture was warmed up to room temperature and stirred for an additional 1.5 h before being filtered through a plug of glass wool to remove the precipitated *m*-chlorobenzoic acid byproduct. The plug was rinsed multiple times with hexanes and the combined filtrate was evaporated to near dryness on a rotary evaporator to give a wet white solid comprising of the oxidized products, *m*-chlorobenzoic acid, and *m*CPBA. This crude material was re-dissolved in a minimum amount of hexanes (~2-3 mL) and purified by flash column chromatography over silica gel (2 cm × 8 cm; hexanes eluent). Careful collection of the eluted materials in 1 mL fractions enables the isolation of epoxide-rich product mixtures. Assignment of mixture components was made using a combination of ¹H NMR, ¹³C NMR, and GC-MS data. NMR data were also

confirmed against simulated values using the online simulator at <https://www.nmrdb.org/>. Critical simulated NMR peaks of the epoxide products from the reaction are listed below.

Compound	¹ H NMR (500 MHz, CDCl ₃)		¹³ C NMR (500 MHz, CDCl ₃)	
	<i>CHBr</i>	<i>Ether HC(O)CH</i>	<i>CHBr</i>	<i>Ether HC(O)CH</i>
				
4-bromo-9-oxabicyclo[6.1.0]nonane			55.6	55.5
<i>cis</i>	4.37	3.10, 3.01		
<i>trans</i>	4.60	3.11, 3.05		
				
2-bromo-9-oxabicyclo[3.3.1]nonane			51.6	77.0, 72.5
<i>cis</i>	4.16	4.19, 3.96		
<i>trans</i>	4.30	4.30, 4.03		
				
2-bromo-9-oxabicyclo[4.2.1]nonane			56.6	82.5, 76.1
<i>cis</i>	4.33	3.89, 3.86		
<i>trans</i>	4.30	4.23, 3.89		

4-methylstyrene oxide. In a 50 mL round-bottom flask equipped with a magnetic stir bar, a solution of 4-methylstyrene (200 mg, 1.7 mmol) in CH₂Cl₂ (15 mL) was vigorously stirred for 20 min in an ice/water bath. Freshly recrystallized *m*CPBA (292 mg, 1.7 mmol) was added and the resulting mixture was stirred for additional 20 min. After that, the reaction mixture was warmed up to room temperature and was stirred for 1.5 h during which time a white precipitate form. The reaction mixture was then filtered through a plug of glass wool to remove the precipitated *m*-chlorobenzoic acid byproduct. The plug was rinsed multiple times with hexanes and the combined filtrate was evaporated to near dryness on a rotary evaporator to give a wet white solid comprising of the oxidized products, *m*-chlorobenzoic acid, and *m*CPBA. This crude materials was re-dissolved in a minimum amount of hexanes (~2-3 mL) and purified by flash-

column chromatography over silica gel (2 cm × 8 cm; hexanes:ethyl acetate = 10:1 v/v eluent). Careful collection of the eluted materials in 1 mL fractions enables the isolation of epoxide-rich product mixtures with minimal contaminations by the 4-methylbenzaldehyde and 4-methylphenylacetaldehyde side products. Assignment of each component was made using a combination of ^1H NMR, and GC-MS data. NMR data were confirmed against reported literature values for 4-methylstyrene oxide,⁸⁹ 4-methylbenzaldehyde,⁹⁰ and 4-methylphenylacetaldehyde.⁹¹

5 mM $\text{Ti}(\text{SO}_4)_2$. This indicator solution was prepared according to a modified previously reported literature protocol.⁹² In a 100 mL round-bottom flask, concentrated H_2SO_4 (11 mL, 200 mmol) was combined with solid TiO_2 (1.2 g, 15 mmol) and the resulting mixture was stirred for 20 h at 120 °C. This mixture was then diluted with DI H_2O (30 mL) and filtered through a fine-fritted funnel. After analysis with ICP-OES, the resulting clear solution (180 mM) was further diluted with enough DI H_2O to obtain a 5 mM TiSO_4 solution that is stored in a 4 °C refrigerator until being used.

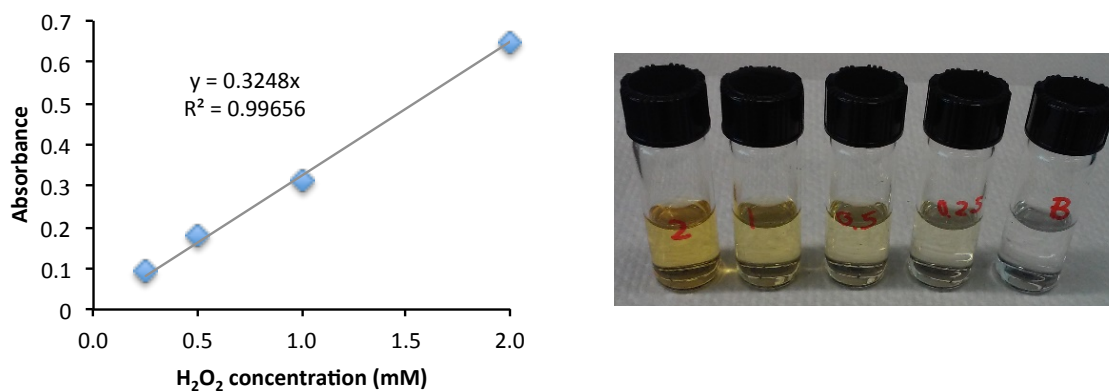


Figure 2.3 Left: A calibration curve for H_2O_2 concentration constructed from titrating against a 5 mM $\text{Ti}(\text{SO}_4)_2$ solution. Right: Photo of mixtures of 5 mM $\text{Ti}(\text{SO}_4)_2$ solution (1 mL) and H_2O_2 standard solution (1 mL) at different concentrations (Left to right: 2, 1, 0.5, 0.25, and 0 mM).

2.9.3 Characterization data of UiO-66-NH₂ and its derivatives

Table 2.7 Preparative data, pore, and surface properties of **UiO-66-NH₂** and its derivatives before catalysis.

Entry	MOFs	NPs (wt %)	Mo (wt %)	BET area (m ² /g)	Total pore volume (cm ³ /g)	Micropore volume (cm ³ /g)	Micropore surface area (m ² /g)	External surface area (m ² /g)
1	UiO-66-NH₂	-	-	1410	0.56	0.46	1250	160
2	Pd@UiO-66-NH₂	3.2	-	1020	0.41	0.37	940	80
3	Pd@UiO-66-NH₂	1.6	-	490	0.41	0.21	390	100
4	Pd/UiO-66-NH₂	6.2	-	1030	0.46	0.39	910	120
5	Au/UiO-66-NH₂	6.6	-	1010	0.40	0.35	910	100
6	Pd-PVP/UiO-66-NH₂	3.3	-	1210	0.48	0.41	1090	120
7	UiO-66-sal(Mo)	-	18	530	0.22	0.18	470	60
8	Pd@UiO-66-sal(Mo)^a	1.7	16	600	0.24	0.20	530	70
9	Pd/UiO-66-sal(Mo)	2.4	17	590	0.25	0.20	510	80
10	Au/UiO-66-sal(Mo)	4.3	16	380	0.16	0.13	330	50
11	Pd-PVP/UiO-66-sal(Mo)	1.4	17	620	0.25	0.21	560	60

^a3.2 wt% Pd@UiO-66-NH₂ (Entry 2) was used as a starting material.

Table 2.8 Preparative data, pore, and surface properties of MOFs after catalysis.

Entry	MOFs	BET area (m ² /g)	Total pore volume (cm ³ /g)	Micropore volume (cm ³ /g)	Micropore surface area (m ² /g)	External surface area (m ² /g)
1	UiO-66-sal(Mo)	420	0.25	0.22	380	40
2	Pd@UiO-66-NH₂ (3.2 wt %)	560	0.32	0.27	480	80
3	Pd@UiO-66-sal(Mo)	590	0.34	0.30	520	70

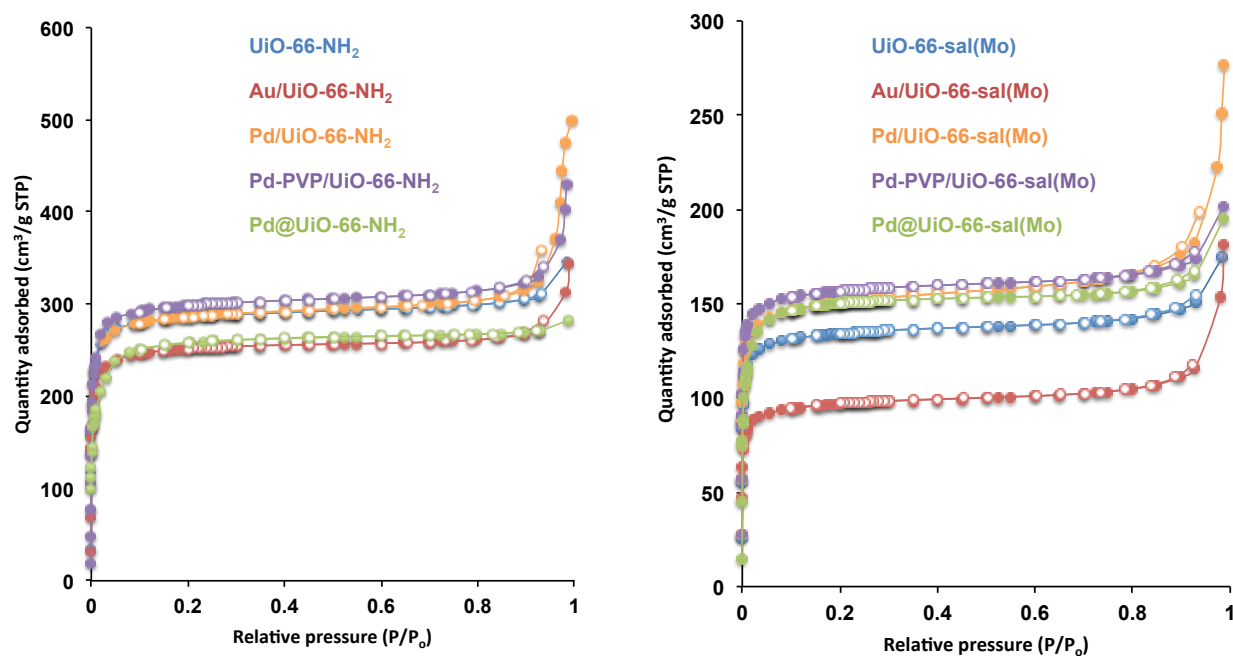


Figure 2.4 N_2 isotherms for UiO-66-NH₂ and its derivative before catalysis. Left: MOFs before ligand modification and Mo incorporation. Right: MOFs after ligand modification and Mo incorporation. Close symbols: adsorption; open symbols: desorption.

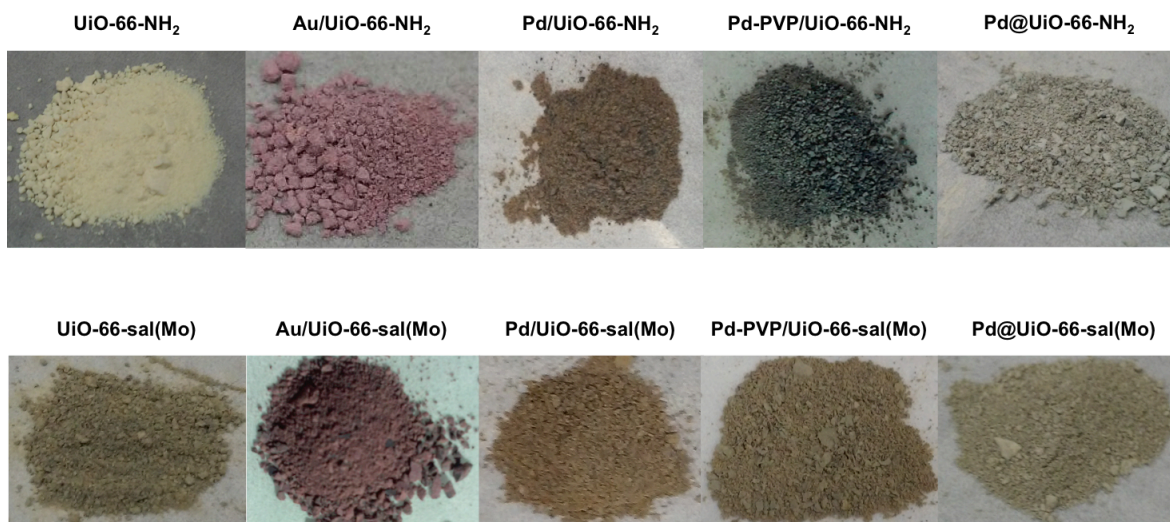


Figure 2.5 Photos of the MOF materials. First row: MOFs before ligand modification and Mo incorporation. Second row: MOFs after ligand modification and Mo incorporation.

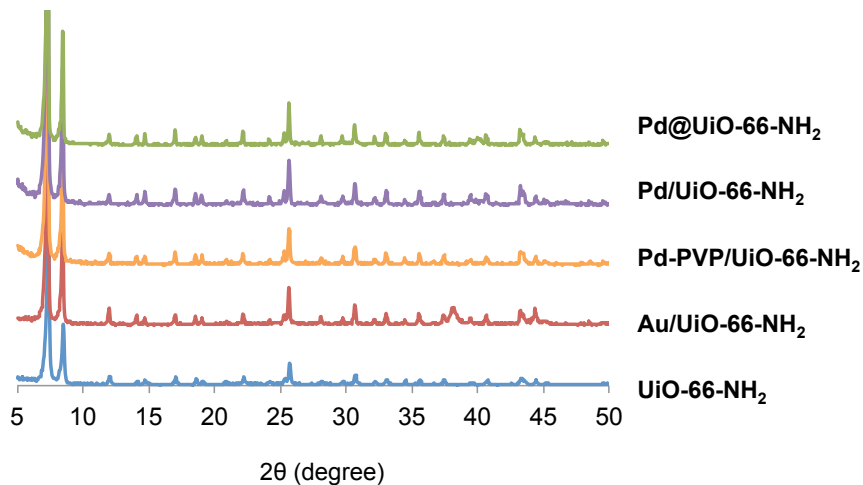


Figure 2.6 PXRD patterns of **UiO-66-NH₂** and its modified derivatives before ligand modification and Mo incorporation. The unchanged PXRD pattern of the MOFs after incorporation of Au NPs and Pd NPs suggests that the modification did not alter the main crystallinity of the host framework. The peak $\sim 38^\circ$ in **Au/UiO-66-NH₂** pattern represents the (111) planes of the Au NPs.⁶⁰

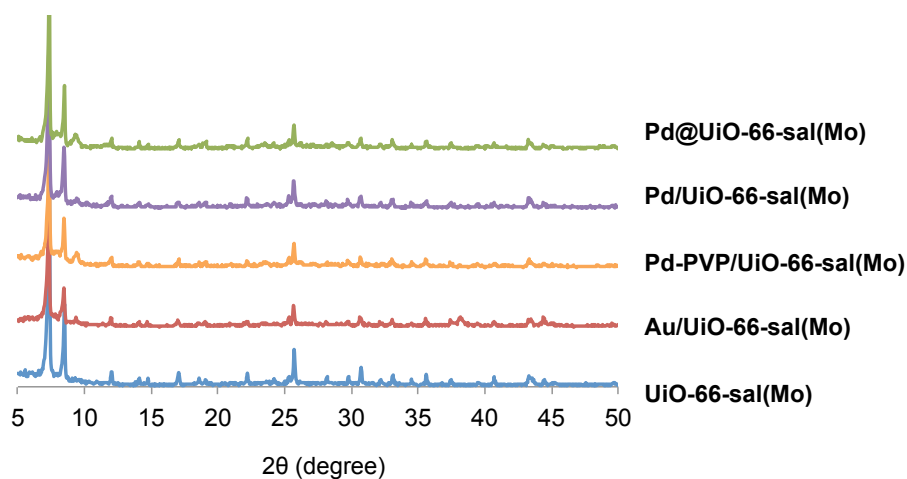


Figure 2.7 PXRD patterns of the MOFs after ligand modification and Mo incorporation. The unchanged PXRD pattern of the MOFs after incorporation with Mo complex suggests that the modification did not alter the main crystallinity of the host framework.

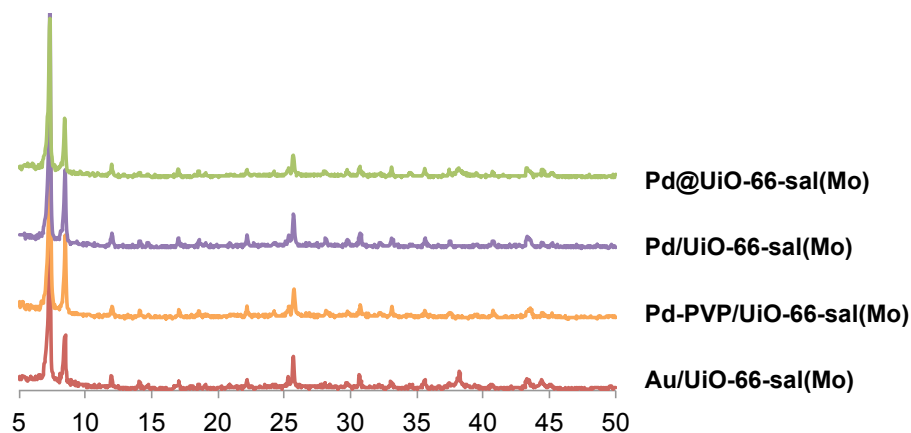


Figure 2.8 PXRD patterns of the MOFs after catalysis. As suggested by this data, the MOFs are still crystalline after being used in each reaction.

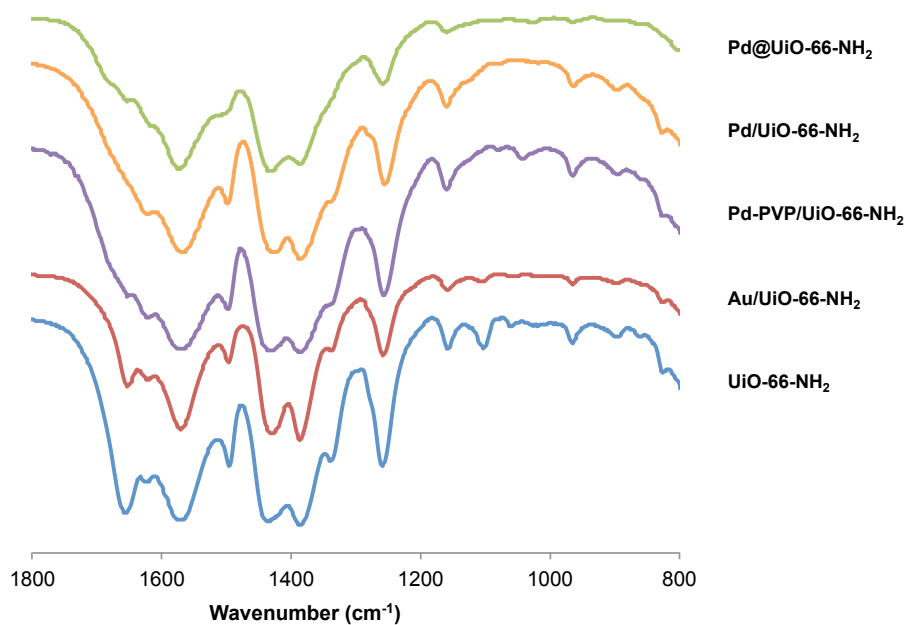


Figure 2.9 FT-IR spectra of UiO-66-NH₂ and its derivatives before ligand modification and Mo incorporation.

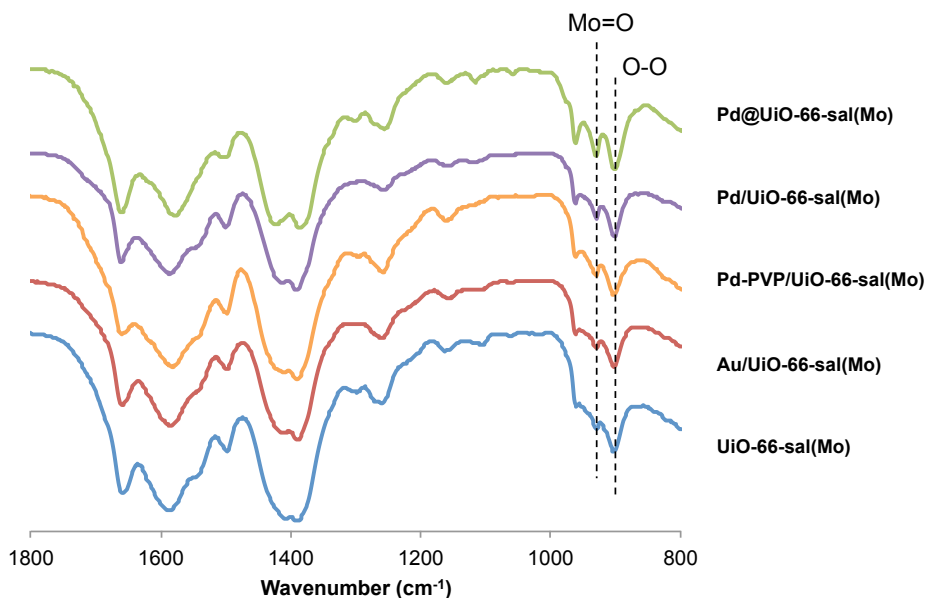


Figure 2.10 FT-IR spectra of the MOFs after ligand modification and Mo incorporation, clearly showing the presences of Mo=O ($\sim 930\text{ cm}^{-1}$) and O-O ($\sim 890\text{ cm}^{-1}$) groups.⁹³

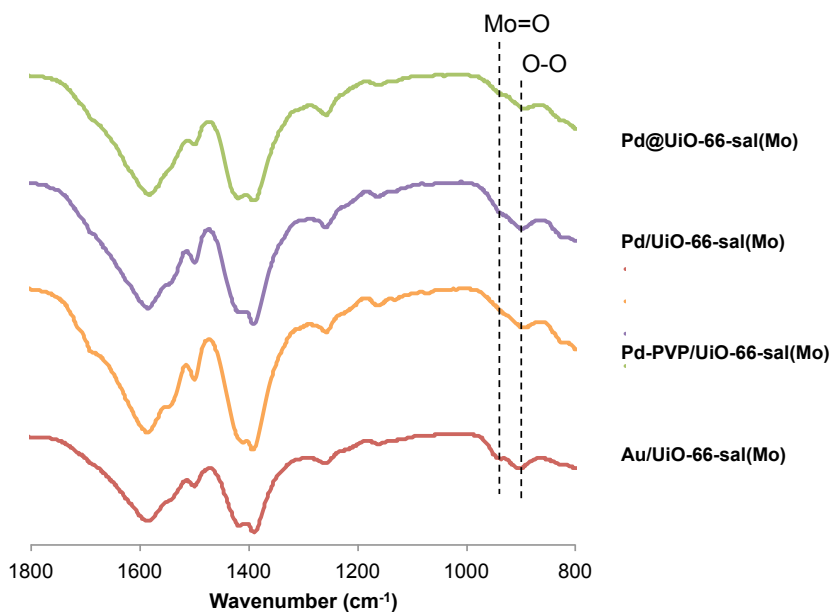


Figure 2.11 FT-IR spectra of the MOFs after catalysis. The spectra suggested that there are some Mo complex coordinate to the MOFs since the bands at $\sim 930\text{ cm}^{-1}$ and $\sim 890\text{ cm}^{-1}$ still remain.

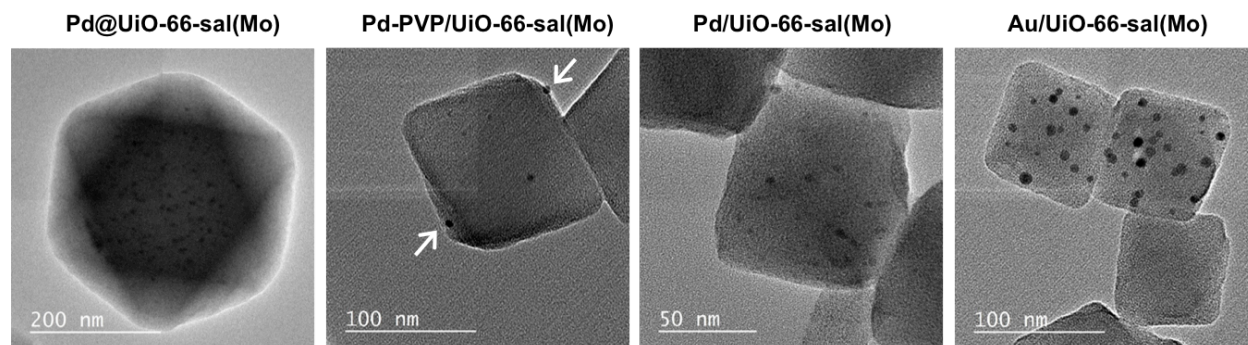


Figure 2.12 TEM images of the MOF materials after catalysis. To guide the readers' eyes, the position of some of the NPs on the MOF microcrystals for **Pd-PVP/UiO-66-sal(Mo)** have been indicated with white arrows. Comparing the TEM images of these samples to that of **Pd@UiO-66-sal(Mo)**, suggests two different types of NP distributions. The NPs in the **Pd@UiO-66-sal(Mo)** sample are positioned throughout the middle part of the crystals because most of them are fully encapsulated inside the MOF crystals. We note in passing that while TEM imaging can contrast the relative differences between **Pd@UiO-66-(sal)Mo** and **Pd/UiO-66-(sal)Mo**, with the former having the majority of the NPs encapsulated in the MOF crystals, it is difficult to absolutely prove that there are no NPs on the exterior surfaces. This is the same situation with 3D tomography, which can demonstrate that the majority of the NPs are in the MOF crystal⁹⁴ but cannot conclusively exclude the probability that there are few small NPs on exterior surfaces because these NPs are difficult to identify in 3D tomography images. Similarly, XPS analysis is not unambiguous. Due to their low-density, porous nature, the inelastic mean free-paths of the electron signals coming from MOF materials in an XPS experiment are longer than commonly observed. Thus, more signals will come from deeper inside the MOF microcrystals, making XPS less surface-sensitive and impractical for distinguishing if the NPs are on the exterior surfaces or inside the crystals. For instance, a previous report⁹⁵ shows that even when the majority of the NPs are encapsulated in the MOF crystals instead of on their surfaces, the elemental signatures due to these NPs were still detectable by XPS.

2.9.4 Evaluation of catalytic activity

Catalytic H₂O₂ generation. The generation of H₂O₂ was carried out in a 50 mL Parr Instruments stainless steel autoclave (model 4590, maximum working pressure of 3000 psig, Parr Instrument, Inc., Moline, IL) equipped with an overhead mechanical stirrer, and thermocouple and pressure gauge for temperature and pressure measurements. In a typical experiment, the autoclave

was charged with catalysts shown in Tables 2.1 and 2.7 (the catalyst loading is adjusted to obtain the weight of NPs indicated in Tables 2.2 and 2.10), 7/3 v/v mixture of CH₃OH (14 mL) and DI H₂O (6 mL). The autoclave was sealed and immersed into an ice-water bath (8-10 °C) or a room-temperature water bath and stirred at 500 rpm. Then the autoclave was sequentially filled with 5 vol % H₂/CO₂ (250 psig) and 25 vol % O₂/CO₂ (100 psig) to give a final hydrogen-to-oxygen ratio of 1:2 at a total pressure of 350 psig. After the experiment has progressed for 30 min, 1 h, or 6 h, the autoclave was vented slowly and an aliquot (2 mL) of the reaction mixture was removed and filtered using a 0.2 μm PTFE syringe filter (VWR International, North American Cat. No. 28145-495) that is attached to a disposable syringe. A portion (1 mL) of the clear filtrate was combined with an aliquot (1 mL) of a 5 mM Ti(SO₄)₂ solution to give a yellow solution that indicates the presence of H₂O₂. Due to the limited range of H₂O₂ detection with 5 mM Ti(SO₄)₂ solution, the filtered aliquot from the experiment using Pd catalysts (100 μL) was diluted 10 times with 7/3 v/v mixture of CH₃OH (630 μL) and DI H₂O (270 μL) before being mixed with an aliquot (1 mL) of 5 mM Ti(SO₄) solution. To analyze the concentration of H₂O₂, the mixture solution was measured the absorbance at ~405 nm using a UV-vis spectrometer. Data are listed in Tables 2.2 and 2.10 (entries 1-3).

Evaluation of H₂O₂ decomposition by MOF materials at room temperature. A 5.9 mM stock solution of H₂O₂ was prepared by adding H₂O₂ (60 μL) to a 7/3 v/v mixture of CH₃OH (70 mL) and DI H₂O (30 mL). In a typical experiment, the MOF material (none, **UiO-66-NH₂**, or **Pd/UiO-66-NH₂**) was added as a solid to a 10-20 mL Biotage microwave vial equipped with a magnetic stir bar. An aliquot (20 mL) of the pre-prepared 5.9 mM H₂O₂ solution was added, the vial was capped, and the resulting mixture was stirred at room temperature for 6 h. The MOF

material was separated from the mixture by centrifugation and a portion (200 μL) of the remaining clear solution was diluted with an aliquot (800 μL) of a 7/3 v/v $\text{CH}_3\text{OH}/\text{H}_2\text{O}$ mixture before being combined with an aliquot (1 mL) of 5 mM $\text{Ti}(\text{SO}_4)_2$ indicator solution. The absorption spectrum of the resulting solution was then obtained and the measured absorbance at ~ 405 nm was used to determine the remaining H_2O_2 concentration. Data are listed in Table 2.9.

Reusability and reproducibility of Pd@UiO-66-NH₂ in catalytic H₂O₂ generation.

After being used in our standard 1 h catalytic H_2O_2 generation, the reaction mixture containing the 1.6 wt % Pd@UiO-66-NH₂ catalyst was transferred to a 50 mL centrifuge tube and subjected to centrifugation. The supernatant portion was isolated by careful decanting and the remaining catalyst pellet in the tube was redispersed by sonication in a 7/3 v/v mixture of CH_3OH (14 mL) and DI H_2O (6 mL). This mixture was then transferred to the autoclave to repeat the catalytic H_2O_2 -generation reaction (data are shown in Figure 2.13). As the amount of MOF loss into the supernatant was minimal (Table 2.16, cf. entries 1-3), we assume that the major loss of catalyst was due to adhesion of the MOF microcrystals to the wall of the centrifuge tube. The weight of catalyst used for each cycle was calculated as following.

Weight of catalyst = (Starting weight of catalyst) – (Weight of catalyst adhered to the centrifuge tube)

Weight of catalyst adhered to the centrifuge tube = (Weight of dry centrifuge tube after use) – (Initial weight of tube)

For reproducibility, the aforementioned experiment was repeated twice.

Reusability of Pd/UiO-66-NH₂ in catalytic H₂O₂ generation. This experiment was carried out in a similar manner as described above. The 6.2 wt % Pd/UiO-66-NH₂ materials from a reaction in Table 2.9, entry 3 (see the procedure in the previous section, entitled “Evaluation of H_2O_2 decomposition by MOF materials at room temperature”), was isolated by centrifugation and

redispersed in a 7/3 v/v mixture of CH₃OH (14 mL) and DI H₂O (6 mL). The resulting MOF catalyst dispersion was then transferred to the autoclave to repeat the catalytic H₂O₂ generation reaction. Data are listed in Table 2.10 (entry 4).

Catalytic oxidation of *cis*-cyclooctene. In a 10-20 mL Biotage microwave vial, **UiO-66-sal(Mo)** (15 mg, 2.4 mg or 0.025 mmol of Mo) (or a control, 15 mg of UiO-66-NH₂) was added to a mixture of *cis*-cyclooctene (8 μL, 0.06 mmol) and 10 mM naphthalene in CH₃OH (7 mL, 0.7 mmol, as an internal standard). DI H₂O (3 mL) and hydrogen peroxide (6 μL of a 30 wt % solution in H₂O, 0.06 mmol) were then added. The reaction vial was capped and the combined mixture was stirred at either room temperature or 60 °C for either 6 h or 18 h. At the appropriate time, an aliquot (1.5 mL) of the reaction mixture was removed and filtered through a 0.2 μm PTFE syringe filter (VWR International, North American Cat. No. 28145-495) that was attached to a disposable syringe. The clear filtrate was then analyzed by GC-FID on the HP-5 capillary column (see below). Data are listed in Tables 2.3 and 2.11.

Analysis parameters for the *cis*-cyclooctene substrate were as followed: initial temperature = 60 °C, initial time = 2 min, ramp = 17 °C/min, final temperature = 240 °C, final time = 0 min. Elution times (min) = 3.8 (*cis*-cyclooctene), 4.1 (cyclooctane), 5.4 (salicylaldehyde from the decomposition of the salicylaldehyde ligand), 6.1 (cyclooctene oxide), and 6.8 (naphthalene). The amount of oxidation product was calculated based on calibration curves against naphthalene as an internal standard. Response factors: *cis*-cyclooctene = 0.646, cyclooctane = 0.700, and cyclooctene oxide = 0.650.

Filtration test to determine the activity of the leached Mo from the UiO-66-sal(Mo)-catalyzed oxidation of *cis*-cyclooctene. Two identical reactions were set up following the

procedure described above for the “Catalytic oxidation of *cis*-cyclooctene”. After 2 h, the content of one reaction was subjected to centrifugation and the settled catalyst was separated from the mixture by decantation. The decanted liquid was then filtered through a 0.2 μm PTFE syringe filter to afford a clear yellow solution. This filtrate was transferred to a 10-20 mL Biotage microwave process vial equipped with a magnetic stir bar, allowed to stir, and monitored by GC-FID every hour for four more hours. After a total of 6 h, an aliquot was taken and analyzed for Mo content. As a comparison, the unfiltered reaction was also monitored by GC-FID every hour for four hours after the 2 h time point. Data are listed in Figure 2.14 and Table 2.17.

Catalytic ability of Mo species that leached out of UiO-66-sal(Mo) in the absence of H_2O_2 . In an 8 dram vial, *cis*-cyclooctene (8 μL , 0.06 mmol) was dissolved in 10 mM naphthalene in CH_3OH (7 mL, 0.7 mmol, as an internal standard) and subsequently DI H_2O (3 mL) was added. In a separate 50 mL propylene centrifuge tube, pre-prepared *cis*-cyclooctene solution was added to UiO-66-sal(Mo) (15 mg, 4.8 mg of Mo). After soaking the MOF for 6 h, the aliquot was isolated by centrifugation and transferred to a 10-20 mL Biotage microwave process vial equipped with a stir bar. Hydrogen peroxide (6 μL of a 30 wt % solution in H_2O , 0.06 mmol) was added to the aliquot and the mixture was stirred for 6 h. After that, the aliquot was analyzed by GC-FID following the aforementioned procedure to calculate the oxidation product and by ICP-OES, following the procedure described in the “Analysis of catalyst leaching” section below, to calculate the amount of leached Mo in the reaction solution. Data are listed in Table 2.12 (entry 2).

Catalytic [H_2O_2 generation + Br-COE oxidation] tandem reaction. Prior to the experiment, Br-COE (7 μL , 0.05 mmol) was dissolved in a 5 mM solution of naphthalene in CH_3OH (14 mL, 0.07 mmol as an internal standard) in a 6 dram vial. DI H_2O (6 mL) was

subsequently added to this mixture to generate a clear solution. The same autoclave as mentioned earlier was then charged with catalysts (the amount of catalysts is varied to obtain the loading of NPs and Mo indicated in Tables 2.4 and 2.13) and the just-prepared Br-COE solution. The autoclave was sealed, immersed in a room-temperature water bath, and stirred at 500 rpm. Then the autoclave was filled with 5 vol % H₂/CO₂ (250 psig) and 25 vol % O₂/CO₂ (100 psig) to give a hydrogen-to-oxygen molar ratio of 1:2 at a total pressure of 350 psig. After stirring for 6 h, the autoclave was cooled down to ~10 °C by ice/water bath and vented slowly. The reaction mixture was transferred to a 50 mL centrifuge tube; and ~1.5 mL of this mixture was filtered out using a 0.2 μm PTFE syringe filter (VWR International, North American Cat. No. 28145-495) attached to a disposable syringe. The clear filtrate was analyzed by both GC-MS and GC-FID on HP-5 capillary columns (see below). Data are listed in Tables 2.4 and 2.13.

Analysis parameters for Br-COE substrate were as followed: initial temperature = 70 °C, initial time = 1 min, ramp = 20 °C/min, final temperature = 240 °C, final time = 5 min. Elution times (min) = 4.0 (naphthalene), 4.4 (Br-COE), 4.9 (bromocyclooctane). The elution times (min) of the oxidation products are 6.2 and 7.2 (4-bromo-9-oxabicyclo[6.1.0]nonane or 2-bromo-9-oxabicyclo[3.3.1]nonane, tentatively assigned), and 6.3 and 7.3 (2-bromo-9-oxabicyclo[4.2.1]nonane). The combined amount of all oxidation products was calculated based on calibration curves against naphthalene as an internal standard. As the products are not available in a pure form, an estimated correlation coefficient for the epoxide was used based on extrapolation from the data for the epoxidation of *cis*-cyclooctene. Response factors: Br-COE = 0.553, bromocyclooctane = 0.518, 4-bromo-9-oxabicyclo[6.1.0]nonane = 0.540 (estimated). All other

rearranged products from 4-bromo-9-oxabicyclo[6.1.0]nonane were assumed to have the same response factor as 4-bromo-9-oxabicyclo[6.1.0]nonane.

Critical MS data for each peak of oxidation products:

Peaks at 6.2 min: m/z (%) 206(87), 204(92), 188(4), 186(4), 125(77), 107(34), 80(100)
at 6.3 min: m/z (%) 206(11), 204(11), 125(100), 107(47), 79(71)
at 7.2 min: m/z (%) 206(97), 204(99), 188(6), 186(6), 125(74), 107(46), 80(100)
at 7.3 min: m/z (%) 206(8), 204(8), 125(100), 107(48), 79(58)

Catalytic [H₂O₂ generation + 4-methylstyrene oxidation] tandem reaction. This reaction was conducted following the procedure described above for Br-COE. However, 4-methylstyrene (6.5 μ L, 0.05 mmol) was used instead of Br-COE. In addition, the sample was analyzed by GC-FID on a ZB-624 capillary column (see below). Data are listed in Tables 2.5 and 2.14. Analysis parameters for 4-methylstyrene substrate were as followed: initial temperature = 110 °C, initial time = 2 min, ramp = 10 °C/min, 2nd step temperature = 120 °C, time = 2 min, ramp = 15 °C/min, time = 1 min, final temperature = 240 °C, final time = 3 min. Elution times (min) = 5.9 (4-ethyltoluene), 6.3 (4-methylstyrene), 7.1 (salicylaldehyde from the decomposition of the salicylaldehyde ligand), 7.2 (4-methylacetophenone), 7.4 (4-methylbenzaldehyde), 7.9 (4-methylphenylacetaldehyde), and 8.2 (naphthalene). The amount of products from 4-methylstyrene oxidation was calculated based on calibration curves against naphthalene as an internal standard. Response factor: 4-methylstyrene = 0.915, 4-ethyltoluene = 0.792, 4-methylbenzaldehyde = 0.765, and 4-methylphenylacetaldehyde and 4-methylacetophenone = 0.850 (estimated).

Under our GC analysis conditions, 4-methylstyrene oxide was observed to rearrange to a significant amount of 4-methylphenylacetaldehyde and 4-methylacetophenone. This is a common problem that has been reported in the literature as a function of instrument conditions, injection temperature, catalyst, and media acidity.^{44, 96-97} In addition, 4-methylstyrene oxide is easily

converted into a variety of rearranged products (4-methylphenylacetaldehyde, 4-methylacetophenone, 4-methylbenzaldehyde, and epoxide ring-opening compounds) under our catalytic reaction conditions (see additional experiment in the next section). As such, 4-methylphenylacetaldehyde, 4-methylacetophenone, along with 4-methylbenzaldehyde and the minor epoxide ring-opening products, were included in the total oxidation yield.

Facile rearrangement of 4-methylstyrene oxide under our catalytic reaction conditions. To a 2 dram vial containing a 7/3 v/v CH₃OH/H₂O solvent mixture (~2 mL) and a magnetic stir bar was added a sample of the 4-methylstyrene oxide-rich product mixture (~1.7 mg) that was previously isolated from a separate synthesis. **Pd@UiO-66-sal(Mo)** (~2 mg) and 30 wt % aq H₂O₂ (~2 μ L) were then added and the resulting mixture was stirred for 6 h before being analyzed by both GC-FID and GC-MS on HP-5 capillary columns. All of the epoxide has disappeared and the majority products are 4-methylphenylacetaldehyde, 4-methylphenylacetaldehyde, 4-methylbenzaldehyde, and the epoxide ring-opening compounds. These results are consistent with data reported for the direction epoxidation of styrene with an H₂/O₂ gas mixture in the presence of either a TS-1 catalyst⁴⁴ or with an organic peroxide in the presence of a MCM-41-supported Mo^{II} precatalyst.⁹⁶

Catalytic [H₂O₂ generation + *cis*-cyclooctene oxidation] tandem reaction. This reaction was conducted following the procedure described above for Br-COE. However, *cis*-cyclooctene (16 μ L, 0.12 mmol) and 10 mM solution of naphthalene in CH₃OH (14 mL) were used instead of Br-COE and 5 mM solution of naphthalene in CH₃OH. In addition, samples were analyzed by GC-FID on an HP-5 capillary column. Data are listed in Tables 2.6 and 2.15. Samples for ICP-OES analysis were isolated by centrifuging the remained reaction solution and separating

out the MOF by decantation. The amount of leached metal catalysts was determined following the “Analysis of catalyst leaching” procedure described below.

Analysis parameters for *cis*-cyclooctene substrate were as followed: initial temperature = 60 °C, initial time = 2 min, ramp = 17 °C/min, final temperature = 240 °C, final time = 0 min. Elution times (min) = 3.8 (*cis*-cyclooctene), 4.1 (cyclooctane), 5.4 (salicylaldehyde from the decomposition of the (sal)Mo moiety), 6.1 (cyclooctene oxide), and 6.8 (naphthalene). The concentrations of the oxidation product were calculated based on calibration curves using naphthalene as an internal standard. Response factors: *cis*-cyclooctene = 0.646, cyclooctane = 0.700, and cyclooctene oxide = 0.650.

As mentioned in footnote 72, accurate measurement of the amount of H₂O₂ that remains at the end of the tandem reaction by colorimetric titration with Ti(SO₄) was not possible due to interference by the leached Mo catalyst in the solution. As such, we employed a standard H₂O₂ test strip (VWR Cat. No. EM1.10081.0001), which showed that the [H₂O₂] differed significantly for the **Pd/UiO-66-(sal)Mo** and **Au/UiO-66-(sal)Mo** systems (~0.3 mM for the former and 0.03 mM for the latter). This is consistent with our expectation. In the case of **Pd/UiO-66-(sal)Mo**, the generation of H₂O₂ is a lot faster than can be consumed by the (sal)Mo catalyst, so most of the generated H₂O₂ diffuses into the solution. In contrast, because the Au NPs in **Au/UiO-66-(sal)Mo** generates H₂O₂ at a slower rate, the (sal)Mo moiety can consume a larger portion of the generated H₂O₂; and the result of this combination was a lower overall [H₂O₂] in the reaction media.

Filtration test to determine the activity of the leached Mo from the Pd@UiO-66-(sal)Mo-catalyzed [H₂O₂ generation + *cis*-cyclooctene oxidation] tandem reaction. A reaction was set up following the procedure described above in the “Catalytic [H₂O₂ generation + *cis*-

cyclooctene oxidation] tandem reaction” section. After 2 h, the reaction content was transferred to a 6 dram vial. The vial was gently shaken to release any remaining gas before being subjected to centrifugation. The settled catalyst was separated from the mixture by decantation and the decanted liquid was then filtered through a 0.2 μm PTFE syringe filter to afford a clear yellow solution. This filtrate was transferred to a 10-20 mL Biotage microwave process vial equipped with a magnetic stir bar. H_2O_2 (80 μL of a 30 wt % solution in H_2O , 0.08 mmol, based on the data in Table 2.2, this amount is estimated to be the maximum that will be generated by **Pd@UiO-66-NH₂** after 6 h) was added to the vial and the mixture was set to stir. The mixture was monitored by GC-FID every hour for a total of four hours after the addition of the H_2O_2 (~30 min after the 2 h time point). Data are listed in Figure 2.15 and Table 2.18.

Analysis of catalyst leaching. In an 8 dram vial, a portion (5 mL) of the clear mother liquor collected after catalysis—from the “Catalytic oxidation of *cis*-cyclooctene”, “Catalytic ability of leached Mo catalysts”, and “Catalytic [H_2O_2 generation + *cis*-cyclooctene oxidation] tandem reaction” experiments—was heated at 120 °C for 18 h to evaporate solvent and chemical substrates. Conc. HNO_3 (600 μL) and conc. HCl (600 μL) were added to the vial, which was lightly shaken, capped loosely to prevent the gas build-up, and left at room temperature. After 18 h or until the solution mixture became yellow clear, DI H_2O (18.8 mL) was added slowly. The resulting solution was homogenized and then analyzed by ICP-OES for Au (or Pd), and Mo contents against standard solutions. Data are listed in Tables 2.12 (entry 2) and 2.16.

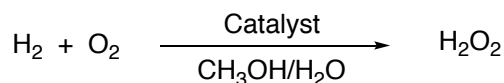
2.9.5 Catalysis data

Table 2.9 Relative comparison of H₂O₂ decomposition in the presence of different MOF materials as measured by the H₂O₂ concentration remained from a standard sample after being stirred for 6 h.

Entry	Catalyst	H ₂ O ₂ remained (mM) ^a
1	-	4.6
2	UiO-66-NH₂ (8 mg)	4.8
3	Pd/UiO-66-NH₂ (9 mg, Pd NPs 0.5 mg)	3.7

Reaction conditions: H₂O₂ (0.12 mmol, starting concentration = 5.9 mM), CH₃OH (14 mL), and H₂O (6 mL). ^aAmount of remained H₂O₂ was determined by colorimetric titration with 5 mM Ti(SO₄)₂ indicator solution.

Table 2.10 H₂O₂ concentration and productivity data for the generation of H₂O₂ from H₂ and O₂ using different catalysts.



Entry	Catalyst	NPs (mg)	Temp. (°C)	Time (h)	H ₂ O ₂ (mM) ^a	H ₂ O ₂ productivity ^a (mol/h/kg _{NP})
1	-	-	8-10	0.5	0	0
2	Au/UiO-66-NH₂	2.0	8-10	1	0.2	2.0
3	Pd/UiO-66-NH₂	0.6	rt	6	2.5	13
4	Pd/UiO-66-NH₂ ^b	0.5	rt	1	5.0	200

Reaction conditions: 5 vol % H₂/CO₂ (250 psig), 25 vol % O₂/CO₂ (100 psig), CH₃OH (14 mL), and H₂O (6 mL). ^aAmount of generated H₂O₂ was determined by colorimetric titration with a 5 mM Ti(SO₄)₂ indicator solution. ^bThis catalyst was reused after being stirred in a 5.9 mM H₂O₂ solution in CH₃OH/H₂O (7/3 v/v) for 6 h (a sample from the reaction in Table 2.9, entry 3).

H₂ selectivity and catalyst efficiency in the generation of H₂O₂. The H₂ selectivity can be classified as either *initial* H₂ selectivity (i.e., at the beginning of the reaction when not very much H₂O₂ has been produced and the only undesirable reaction for H₂ is combustion into H₂O) or *overall* H₂ selectivity. While initial H₂ selectivity is an ideal number to have, it is quite difficult to measure this value unless both H₂ conversion and H₂O₂ production can be accurately sampled at the beginning of the reaction. Thus, researchers often calculate the overall H₂ selectivity for liquid-phase batch reactions by measuring the H₂ conversion and the H₂O₂ production at the end of each reaction.^{15, 25} However, such estimates of the overall H₂ selectivity can be markedly different from the initial H₂ selectivity due to several side reactions of the H₂O₂ product. As shown in Scheme 2.1, the H₂O₂ product can undergo hydrogenation or be decomposed by the catalyst, leading to an overall selectivity number that is much lower than the initial selectivity. For the current study, as our reactions were conducted in a batch reactor without gas-sampling and H₂ analysis capabilities, H₂ conversion could not be obtained and neither of the H₂ selectivity can be made available.

In addition to the reported H₂O₂ productivities (Tables 2.2 and 2.10), the yield of H₂O₂ can be estimated from the initial amount of feeding H₂ gas and the amount of produced H₂O₂ in the reaction after a fixed time.

For **Pd@UiO-66-NH₂** after 1 h:

The initial amount of H₂ gas (250 psig of 5 vol % H₂/CO₂, at 25 °C) = 12.5 psig = 0.7 mmol.

The amount of produced H₂O₂ after 1 h = (7.0 mmol/1000 mL) × 20 mL = 0.14 mmol.

Therefore, the yield of produced H₂O₂ = (0.14 mmol/0.7 mmol) × 100 = 20%.

We note that the aforementioned yield is highly dependent on the pressure and reaction media as H₂O₂ generation occurs in the liquid phase and both H₂ and O₂ are only partially soluble in the solvent mixture.

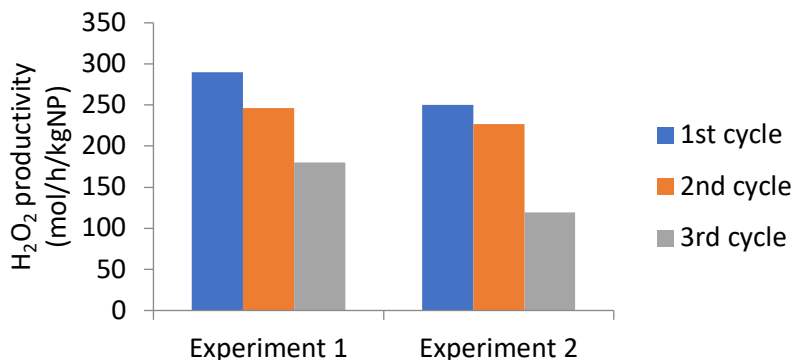
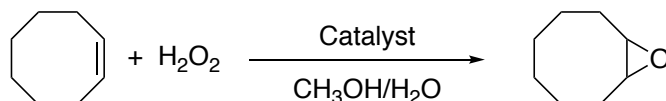


Figure 2.13 Reusability and reproducibility data for **Pd@UiO-66-NH₂** in catalytic H₂O₂ generation. For each cycle, the catalyst is recovered from the previous cycle, taking into account the amount of lost catalyst. The H₂O₂ productivity of the MOF catalyst decreased to 50-60% after the 3rd cycle. This experiment was repeated 2 times (Experiments 1 and 2). Based on the data in Table 2.16, **Pd@UiO-66-NH₂** was selected for these reusability/reproducibility tests due to its lowest tendency to leach Pd.

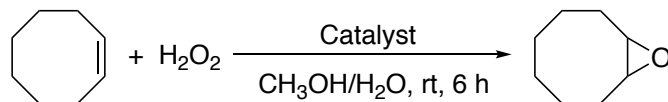
Table 2.11 Yield and oxidation productivity for the oxidation of *cis*-cyclooctene using different catalysts.



Entry	Catalyst	Amount (mg)	Temp (°C)	Time (h)	Conversion ^a (%)	Yield ^b (%)	Oxidation productivity ^b (mmol/h/kg _{cat})
1	-	0	rt	6	~15	0	0
2 ^c	-	0	60	18	~20	0	0
3	UiO-66-sal(Mo)	15	rt	6	~20	4 ± 1	25 ± 2.5
4	UiO-66-sal(Mo)	15	rt	18	~20	7 ± 1	18 ± 2.5
5 ^c	UiO-66-sal(Mo)	15	60	18	~60	15	30

Reaction conditions: *cis*-cyclooctene (0.06 mmol), 30 wt % H₂O₂ (0.06 mmol), CH₃OH (7 mL), and H₂O (3 mL). ^aSome percentage of the *cis*-cyclooctene was lost due to evaporation. ^bYield and oxidation productivity were calculated based on the amount of cyclooctene oxide, determined by GC-FID with an internal standard method. For entries 3 and 4, which show that the conversion remains low over an 18 h period and given that there is significant leaching of the Mo catalyst within a 6 h period (Table 2.16), we attributed most of the decrease in productivity to catalyst leaching. We note, however, that there is a large error in our measurements of the *cis*-cyclooctene amount (footnote a). ^cData from a one-time experiment.

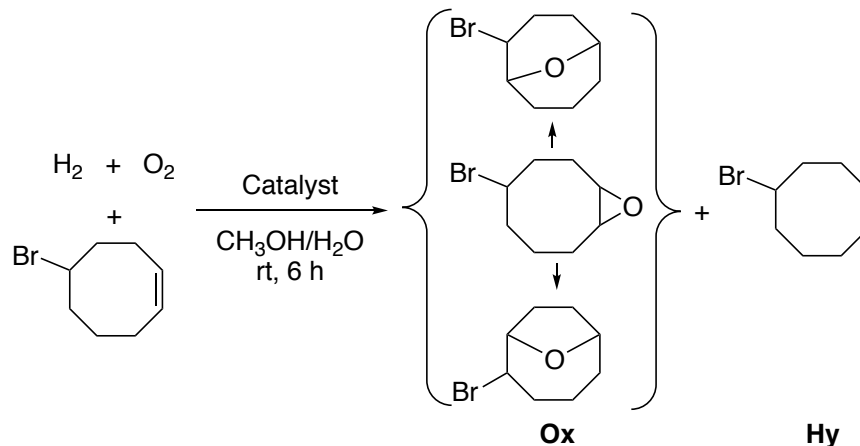
Table 2.12 Yield and oxidation productivity for the oxidation of *cis*-cyclooctene using **UiO-66-sal(Mo)** and the leached Mo.



Entry	Catalyst	Mo (mg)	Yield ^a (%)	Oxidation ^a productivity (mmol/h/kg _{Mo})
1	UiO-66-sal(Mo) (15 mg)	2.4	4 ± 1	156 ± 25
2	Leached Mo from soaking UiO-66-sal(Mo) in solvent for 6 h	0.4 ± 0.2	0.07 ± 0.03	21 ± 4

Reaction conditions: *cis*-cyclooctene (0.06 mmol), 30 wt % H_2O_2 (0.06 mmol), CH_3OH (7 mL), and H_2O (3 mL). ^aYield and oxidation productivity were calculated based on the amount of cyclooctene oxide, determined by GC-FID against an internal standard.

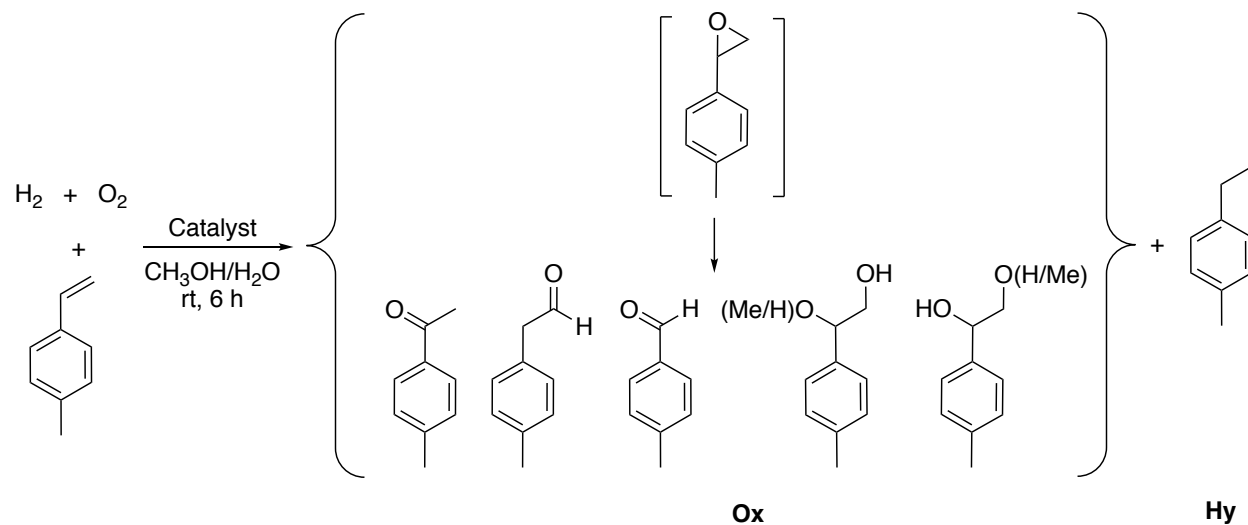
Table 2.13 Concentration of products, **Hy/Ox** ratios, and **Ox** productivities for Br-COE in the presence of different types of MOF catalysts.



Entry	Catalyst	Hy (mM)	Ox ^a (mM)	Hy/Ox ^a ratio ^b	Ox ^a productivity ^c (mmol/h/kg _{NP})
1	Pd@UiO-66-NH₂ + UiO-66-sal(Mo)	0.026 ± 0.015	0.029 ± 0.001	0.91 ± 0.28	191 ± 48
2	Pd-PVP/UiO-66-NH₂ + UiO-66-sal(Mo)	0.178 ± 0.020	0.032 ± 0.007	5.5 ± 1.7	211 ± 48
3	Pd/UiO-66-NH₂ + UiO-66-sal(Mo)	0.026 ± 0.008	0.033 ± 0.003	0.78 ± 0.24	219 ± 48
4	Pd@UiO-66-sal(Mo)	0.030 ± 0.008	0.031 ± 0.015	0.94 ± 0.29	206 ± 48

Reaction conditions: 5 vol % H₂/CO₂ (250 psig), 25 vol % O₂/CO₂ (100 psig), Br-COE (0.05 mmol), CH₃OH (14 mL), and H₂O (6 mL). The catalyst comprises 0.51 mg of NPs and 4.8 mg of Mo by weight. ^aThe oxidation (**Ox**) product comprises epoxide-rearranged compounds and was determined by GC-FID against an internal standard. ^bThe error bar was proportionally calculated as a percentage of the **Hy/Ox** ratio based on the average of the percentage standard deviations from the alkane. ^cThe error bar was calculated based on the average of standard deviations from all runs.

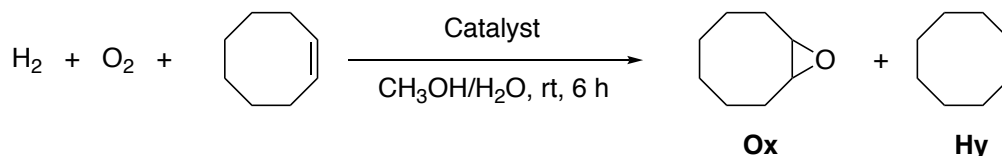
Table 2.14 Concentration of products, **Hy/Ox** ratios, and **Ox** productivities for 4-methylstyrene in the presence of different types of MOF catalysts.



Entry	Catalyst	Hy (mM)	Ox ^a (mM)	Hy/Ox ^a ratio ^b	Ox ^a productivity ^c (mmol/h/kg _{NP})
1	Pd@UiO-66-NH₂ + UiO-66-sal(Mo)	0.690 ± 0.099	0.032 ± 0.003	22 ± 3	156 ± 22
2	Pd-PVP/UiO-66-NH₂ + UiO-66-sal(Mo)	1.07 ± 0.01	0.038 ± 0.011	29 ± 4	184 ± 22
3	Pd@UiO-66-sal(Mo)	0.470 ± 0.042	0.048 ± 0.001	10 ± 1	234 ± 22

Reaction conditions: 5 vol % H₂/CO₂ (250 psig), 25 vol % O₂/CO₂ (100 psig), 4-methylstyrene (0.05 mmol), CH₃OH (14 mL), and H₂O (6 mL). The catalyst comprises 0.68 mg of NPs and 4.8 mg of Mo by weight. ^aThe oxidation (**Ox**) product comprises epoxide-rearranged compounds (4-methylphenylacetaldehyde, 4-methylacetophenone, and minor epoxide ring-opening compounds) as well as other styrene-based oxidation products (4-methylbenzaldehyde) and was determined by GC-FID with an internal standard method. While the epoxide is not directly observed given the protic nature of the solvent mixture, the major rearranged products were verified as derivable from the epoxide by an independent experiment. ^bThe error bar was proportionally calculated as a percentage of the **Hy/Ox** ratio based on the average of the percentage standard deviations from the **Ox** products. ^cThe error bar was calculated based on the average of standard deviations from all runs.

Table 2.15 Concentration of products, **Hy/Ox** ratios, and **Ox** productivity for *cis*-cyclooctene in the presence of different types of MOF catalysts.



Entry	Catalyst	NPs (mg)	Mo (mg)	Hy ^b (mM)	Ox ^a (mM)	Hy/Ox ^a ratio	Ox ^a productivity ^d (mmol/h/kg _{NP})
1	Pd@UiO-66-NH₂	0.5	-	0.025 ± 0.012	0	-	0
2	Pd@UiO-66-NH₂ + UiO-66-sal(Mo)	0.5	4.8	0.006 ± 0.009	0.087 ± 0.014	0.069 ^e	570 ± 64
3	Pd@UiO-66-sal(Mo)	0.5	4.8	0.006 ± 0.008	0.093 ± 0.042	0.061 ^e	828 ± 64
4	Pd/UiO-66-NH₂ ^c	0.5	-	0.011	0	-	0
5	Pd/UiO-66-NH₂ + UiO-66-sal(Mo)	0.7	4.8	0.023 ± 0.022	0.101 ± 0.018	0.23	493 ± 120
6	Pd/UiO-66-sal(Mo)	0.7	4.8	0.021 ± 0.011	0.122 ± 0.031	0.17	599 ± 120
7	Au/UiO-66-NH₂	2.6	-	0.044 ± 0.013	0.002 ± 0	27	2 ± 0.24
8	Au/UiO-66-NH₂ + UiO-66-sal(Mo)	2.6	9.6	0.024 ± 0.002	0.002 ± 0.001	11	2.5 ± 0.24
9	Au/UiO-66-sal(Mo)	2.6	9.6	0.046 ± 0.030	0.020 ± 0	2	26 ± 0.24
10	Pd-PVP/UiO-66-NH₂ + UiO-66-sal(Mo) ^c	0.5	4.8	0.062	0.079	0.78	531
11	Pd-PVP/UiO-66-NH₂ + UiO-66-sal(Mo) ^c	0.4	4.8	0.079	0.063	1.3	420
12	Pd-PVP/UiO-66-sal(Mo)	0.4	4.8	0.134 ± 0.036	0.055 ± 0.013	2.4	424 ± 111

Reaction conditions: 5 vol % H₂/CO₂ (250 psig), 25 vol % O₂/CO₂ (100 psig), *cis*-cyclooctene (0.12 mmol), CH₃OH (14 mL) and H₂O (6 mL). ^aAmount of products and productivity were determined by GC-FID against an internal standard. ^bBecause some cyclooctane, which is a minor component of the reaction mixture, was lost due to evaporation during venting the autoclave after the reaction, the amount of cyclooctane was calculated by conservative estimates assuming a fixed amount of sample remained (72%). ^cData from one experiment. ^dThe error bar was calculated by the average of standard deviations from all runs for each catalyst system. ^eThese low molecular selectivities (**Hy/Ox** ratios) can only be achieved if the majority of the NPs in **Pd@UiO-66-NH₂** (or **Pd@UiO-66-(sal)Mo**) are inside the MOF crystals. They are much lower than that (0.23) for the [**Pd/UiO-66-NH₂** + **UiO-66-sal(Mo)**] combination (entry 5) and that is best explained if the **Pd@UiO-66-NH₂** and **Pd@UiO-66-(sal)Mo** samples have mostly encapsulated Pd NPs.

Table 2.16 Amount of metal leaching from each catalyst after catalysis.

Entry	Reaction	Catalyst	wt % leaching	
			NPs	Mo
1	H ₂ O ₂ generation ^a	Pd@UiO-66-NH₂ , 1 st cycle	0	-
2		2 nd cycle	0.2	-
3		3 rd cycle	0.2	-
4	<i>cis</i> -cyclooctene oxidation ^b	UiO-66-sal(Mo)	-	78
5	Tandem reaction ^c	Pd@UiO-66-NH₂ + UiO-66-sal(Mo)	0.1	49
6		Pd/UiO-66-NH₂ + UiO-66-sal(Mo)	0.4	52
7		Au/UiO-66-NH₂ + UiO-66-sal(Mo)	0	5
8		Pd-PVP/UiO-66-NH₂ + UiO-66-sal(Mo)	0.2	25
9		Pd@UiO-66-sal(Mo)	0.9	53
10		Pd/UiO-66-sal(Mo)	0.1	70
11		Au/UiO-66-sal(Mo)	0.2	41
12		Pd-PVP/UiO-66-sal(Mo)	0.7	32

^aSee reaction conditions in the footnote of Table 2.2. ^bSee reaction conditions in the footnote of Table 2.3, entry 3. ^cSee reaction conditions in the footnote of Table 2.6.

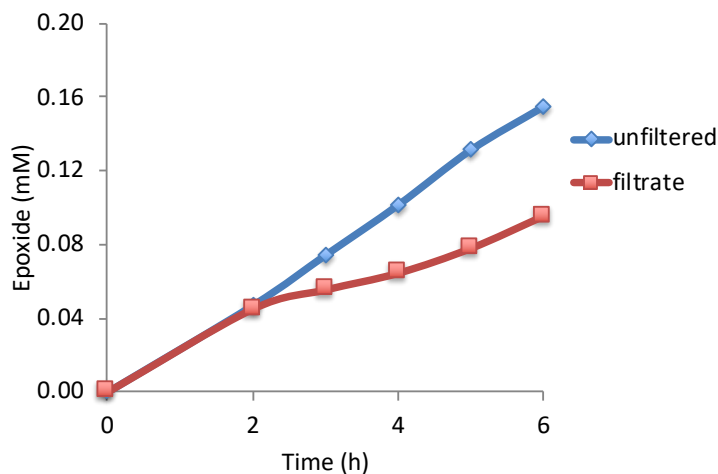


Figure 2.14 Epoxide-formation profiles to assess the activity of the leached Mo from the **UiO-66-sal(Mo)**-catalyzed oxidation of *cis*-cyclooctene using H₂O₂. Two identical experiments were set up where the **UiO-66-sal(Mo)** catalyst was exposed to a reaction media containing a 1:1 molar ratio of substrate and H₂O₂ (mimic our standard benchtop reaction conditions) for 2 h before one was subjected to the filtration test. Epoxide concentrations were monitored for both the unfiltered reaction (blue line) and the filtrate (red line) using GC-FID. The lines are only included as visual guides. See also Table 2.17.

Table 2.17 Amount of Mo catalyst and oxidation productivity in the **UiO-66-sal(Mo)**-catalyzed oxidation of *cis*-cyclooctene using H₂O₂.

Entry	Reaction content	Mo (mg)	Oxidation ^a productivity (mmol/h/kg _{Mo})
1	UiO-66-sal(Mo) under standard benchtop reaction conditions	2.4 ^b	107
2	Reaction in entry 1 after being filtered at 2 h	1.7 ^c	74

Reaction conditions: *cis*-cyclooctene (0.06 mmol), 30 wt % H₂O₂ (0.06 mmol), CH₃OH (7 mL), and H₂O (3 mL). ^aOxidation productivity were calculated at the end of the reaction based on the amount of cyclooctene oxide, determined by GC-FID against an internal standard. ^bAmount of Mo was the total Mo present in the catalyst. ^cAmount of Mo was determined at the end of the 6 h period using ICP-OES.

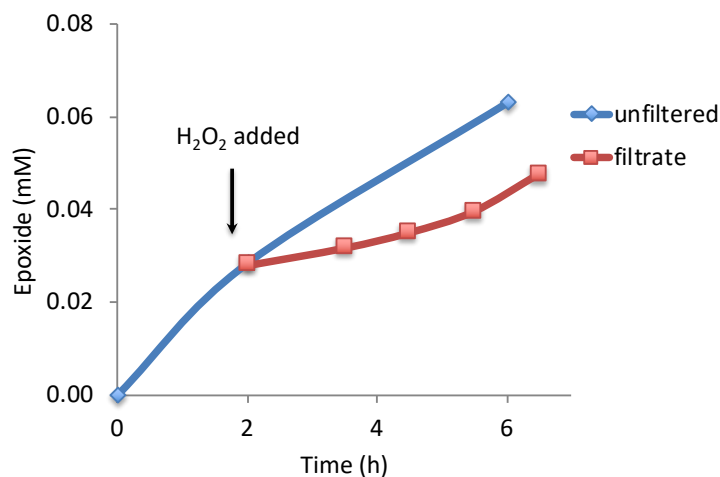


Figure 2.15 Epoxide-formation profiles to assess the activity of the leached Mo from the **Pd@UiO-66-sal(Mo)**-catalyzed [H₂O₂ generation + *cis*-cyclooctene oxidation] tandem reaction. An experiment with the **Pd@UiO-66-sal(Mo)** catalyst were set up under our standard tandem reaction conditions and carried out for 2 h before being stopped and subjected to the filtration test. Additional H₂O₂ was added to the filtrate and the epoxide concentration was monitored using GC-FID. For comparison, epoxide concentration data for the standard (unfiltered) tandem reaction using **Pd@UiO-66-sal(Mo)** were also included (blue line). The lines are only included as visual guides. See also Table 2.18.

Table 2.18 Amount of Mo catalyst and oxidation productivity in the **Pd@UiO-66-sal(Mo)**-catalyzed [H₂O₂ generation + *cis*-cyclooctene oxidation] tandem reaction.

Entry	Reaction content	Mo (mg)	Oxidation ^a productivity (mmol/h/kg _{Mo})
1	Pd@UiO-66-sal(Mo) under standard tandem reaction conditions	3.4 ^b	62
2	Reaction in entry 1 after being filtered at 2 h and combined with more H ₂ O ₂	2.2 ^c	39

Reaction conditions: 5 vol % H₂/CO₂ (250 psig), 25 vol % O₂/CO₂ (100 psig), *cis*-cyclooctene (0.12 mmol), CH₃OH (14 mL), and H₂O (6 mL). The catalyst comprises 0.5 mg of NPs and 3.4 mg of Mo by weight. ^aOxidation productivity were calculated at the end of the reaction based on the amount of cyclooctene oxide, determined by GC-FID against an internal standard. ^bAmount of Mo was the total Mo present in the catalyst. ^cAmount of Mo was determined at the end of the 6.5 h period using ICP-OES.

2.9.6 Molecular dimension estimation

Estimation of the molecular sizes of the substrate was carried out using ChemDraw Professional version 15.0.0.106. The molecules were initially drawn in ChemDraw and imported into Chem3D. The geometry optimizations were then carried out using the MM2 energy minimization protocol. The size of the molecules is estimated based on the smallest dimensions of the optimized structures (Figure 2.16).

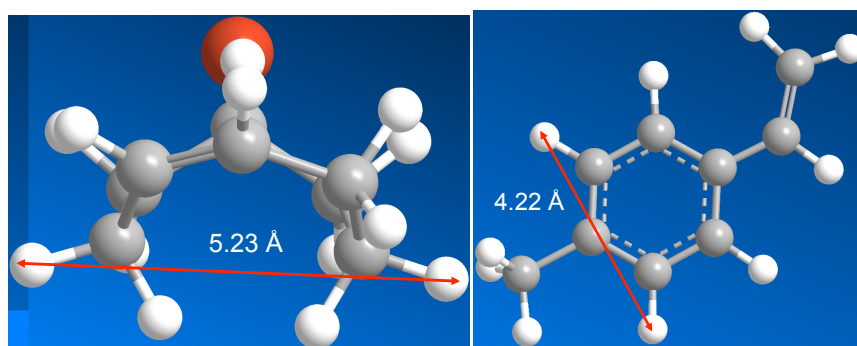


Figure 2.16 Estimated smallest dimension for 5-bromo-1-cyclooctene (5.23 Å, left) and 4-methylstyrene (4.22 Å, right).

2.9.7 Miscellaneous calculations

Justification for the decrease in the wt % of Pd loading. Our **Pd@UiO-66-NH₂** starting materials has a 3.2 wt % NPs loading. Starting with 100 mg of this MOF (assuming that the ideal **UiO-66-NH₂** has a MW of ~1752 g/mol and that there is no modulator on the node), there will be 3.2 mg of Pd and 96.8 mg or ($6 \times 0.055 \text{ mmol} =$) 0.33 mmol of amino group that can be modified with the (sal)Mo moiety. If the modification of the amino group with the salicylaldehyde group and Mo reagent were complete, the resulting **UiO-66-(sal)Mo** will have a MW of 3426 g/mol (assuming a $\text{MoO}(\text{O}_2)_2$ stoichiometry for the (sal)Mo center and complete modification). Thus, the total mass of the **Pd@UiO-66-(sal)Mo** will be $[(0.055 \times 3426) + 3.2 =]$ 191.6 mg and the Pd component is now only 1.67 wt %. As this is the limit for complete modification, the expected final Pd wt % will vary between the 1.67 and 3.2 range.

Chapter 3

**Elucidating the mechanism of the UiO-66-catalyzed sulfide oxidation:
activity and selectivity enhancements through changes in the node coordination
environment and solvent**

Portions of this chapter appear in the following manuscript: Limvorapitux, R.; Chen, H.;
Mendonca, M. L.; Liu, M.; Snurr, R. Q.; Nguyen, S. T., *Catal. Sci. Technol.* **2019**, *9*, 327-335.

3.1 Introduction

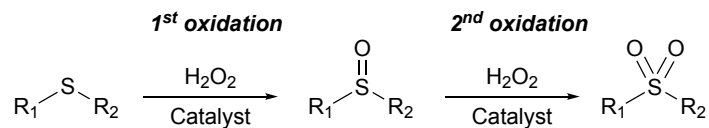
In chapter 2, we demonstrated that dually functionalized MOFs can catalyze the [H₂O₂ generation + alkene oxidation] tandem reaction, resulting in enhancements of the oxidation productivity and suppressions of the side reaction. However, the rate of the oxidation step was slower than that of the H₂O₂-generation step, leading to an inefficient utilization of H₂O₂. To enhance the consumption of H₂O₂, we explored sulfide oxidation as a replacement for the alkene oxidation in this chapter. This was motivated by the fact that sulfide oxidations are generally faster than alkene oxidations as sulfur lone pairs are generally more nucleophilic than carbon-carbon double bonds.⁹⁸ Interestingly, UiO-66 MOF, which was used as the catalyst support in chapter 2, was reported to be catalytically active in the H₂O₂-induced oxidation of the sulfide in aprotic polar solvent such as CH₃CN.⁹⁹⁻¹⁰⁰ However, its mechanism was not fully explained nor was its activity being explored in protic solvents such as the CH₃OH/H₂O mixture, which we employed as a safeguard in our tandem reaction. To this end, we set out to investigate how UiO-66 MOF affects the sulfide-oxidation step in our desired tandem reaction so that we can better implement it in our catalyst design. As will be described below, the combination of kinetics studies and computational modeling enabled us to fully understand the nature of the catalytically active sites on UiO-66 MOF, especially in our protic CH₃OH/H₂O solvent mixture.

3.2 Background and motivation

Zr₆-oxo-hydroxo clusters (Zr₆(μ₃-O)₄(μ₃-OH)₄(OOCR)_x), which can be stabilized by up to 12 carboxylate groups,¹⁰¹⁻¹⁰⁵ have long been used as building blocks for organic-inorganic hybrid materials¹⁰⁶⁻¹⁰⁷ and molecular magnets,¹⁰⁸⁻¹⁰⁹ as well as in catalysis.¹¹⁰ When the carboxylate ligands are multitopic linkers, the Zr₆-oxo-hydroxo clusters can be connected together to form a

broad range of metal-organic frameworks (MOFs),¹¹¹ such as the UiO,^{32, 112-113} PCN,¹¹⁴⁻¹¹⁶ and NU¹¹⁷⁻¹¹⁸ families, among many others.¹¹⁹⁻¹²² Within the UiO MOFs, UiO-66 (linker = 1,4-benzenedicarboxylate, BDC) was found to be catalytically active for the oxidation of sulfides^{99-100, 123-124} and for Lewis-acid-catalyzed reactions such as Friedel-Crafts benzoylation,¹²⁵ aldol condensation,¹²⁶ hydrolysis,¹²⁷⁻¹²⁸ transesterification,¹²⁹ and ring opening.¹³⁰⁻¹³¹ While the catalytically active species in these reactions were assumed to be derived from the coordinatively unsaturated sites on the Zr₆-oxo-hydroxo nodes of the MOF,^{100, 123-124, 131-134} their nature remains ambiguous, particularly for sulfide oxidation where the unsaturated sites, as precatalysts, must be converted into the oxidation-active species.

In the oxidative desulfurization of fuels, where UiO-66 has been studied as a catalyst for the second processing stage¹³⁵ (H₂O₂-induced oxidation of the sulfide, Scheme 3.1), the UiO-66 MOFs that are less crystalline or have more defects^{99-100, 124} are often more active. While this result has been attributed to the increased presence of coordinatively unsaturated node sites^{100, 123-124} and linker deficiencies,^{99-100, 124} previous studies employed widely different MOF preparations^{99-100, 124} that could manifest into large variations on the observed catalytic activities.¹³⁶⁻¹³⁸ Thus, we were interested in the possibility of modulating the catalytic activity of UiO-66 in sulfide oxidation using only materials derived from the same preparation. We hypothesized that increasing the number of missing-linker¹³⁹ sites on the Zr₆-oxo-hydroxo nodes of UiO-66, as well as the accessibility of these sites, should lead to enhancements in catalytic activities. In combination with computational modeling and kinetic studies, this structure-function relationship study will allow us to establish the chemical identity of the active catalyst species in the UiO-66-catalyzed sulfide oxidation and propose a reasonable mechanism for the two steps of Scheme 3.1.

Scheme 3.1 The UiO-66-catalyzed oxidation of sulfide with H₂O₂ oxidant.

Missing-linker sites on the Zr₆-oxo-hydroxo nodes of UiO-66 MOFs are well-known to be naturally capped with modulator-type carboxylate ligands during synthesis.¹⁴⁰ However, the capping is not perfect and the modulator can be lost or removed during modification (Scheme 3.2).^{131, 134} Under these scenarios, the missing-linker sites are assumed to be terminated with a combination of [Zr-μ₁-OH + Zr-μ₁-OH₂]¹⁴¹⁻¹⁴³ (or [Zr-μ₁-Cl + Zr-μ₁-OH₂/neutral solvent]¹⁴⁴⁻¹⁴⁵). Such “open” sites are much more coordinatively labile than the *chelating* carboxylate-capped sites and can become active sites in catalysis.¹⁴⁰ Herein, we report the post-synthesis transformation of a single UiO-66 sample into a family of three UiO-66 materials with the number of open sites readily tuned from ~1 to 5 per node, while preserving the parent particle morphology. These materials were tested for sulfide oxidation in the presence of H₂O₂ (Scheme 3.1), where the MOF with more open sites indeed resulted in higher reaction rates for both sulfide and sulfoxide oxidation. Reactions in different solvents showed a high selectivity for the sulfoxide in CH₃OH, but in CH₃CN and CH₂Cl₂ the selectivity drops rapidly with increasing conversion.

Computational modeling provided support for the formation of a Zr-μ₁-OOH active species, generated from a μ₁-OH site that is capable of oxidizing sulfide to sulfoxide and further oxidation to the sulfone. Together, the experimental and computational results suggested a model where the sulfoxide product can bind to a Zr site adjacent to the active Zr-μ₁-OOH species in CH₃CN and CH₂Cl₂, leading to overoxidation. However, this effect is minimized in CH₃OH,

which can interact strongly with the open sites on the nodes, reduce sulfoxide binding, and thus maintain good sulfoxide selectivity.

3.3 Synthesis and characterization of the UiO-66 derivative

As a prototypical MOF, crystalline UiO-66 nanoparticles have been synthesized under many different conditions, particularly with acid modulators^{134, 146-148} that change the number of missing BDC linkers while maintaining well-defined crystal morphologies.^{146, 148-149} With benzoic acid (BzOH) modulators, the degree of missing-linker sites on the UiO-66 nodes can be readily tuned, with up to ~4 missing-linker sites (or two BDC linkers) per node.¹⁴⁹ These missing-linker sites are presumably capped with the monocarboxylate anions of the acid modulators, which can then be decapped to yield [μ_1 -OH + μ_1 -OH₂]¹⁴¹⁻¹⁴³ open sites. By using a large excess of benzoic acid modulator (BzOH/BDC = ~33)¹⁴⁶ (Scheme 3.2), we synthesized a parent **BzOH-UiO-66** material with ~3 BzOH-capped, 0.3 formic acid (HCOOH)-capped (see further discussion below), and ~1 open sites per node (Table 3.1, entry 2). To increase the number of open sites on the nodes, this **BzOH-UiO-66** was treated with HCl_{aq} in the presence of *n*-butanol to remove BzOH, resulting in **decap-UiO-66**, which had the same BDC linker/node composition as the parent material but with 4.6 times as many open sites (Table 3.1, entry 3).

Scheme 3.2 The synthesis of the three isomorphous UiO-66 materials used in this work (left panel) and a proposal for the conversion of a Zr- μ_1 -OH species in the open sites into active Zr- μ_1 -OOH species (right panel). For simplicity, only one Zr₆-oxo-hydroxo node of each UiO-66 sample is shown here.

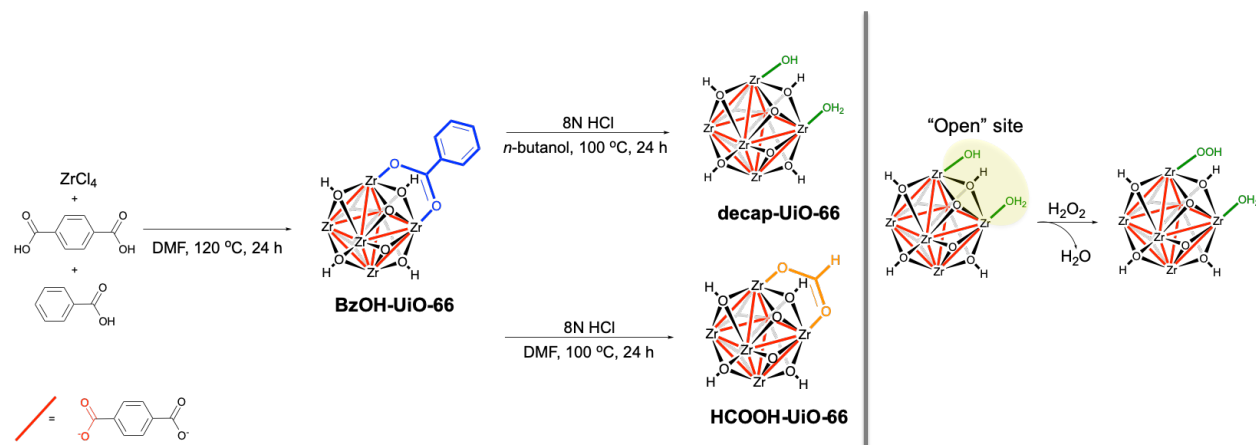


Table 3.1 Composition of the three UiO-66 MOF derivatives and the Zr₆-oxo-hydroxo cluster used in this work.

Entry	MOF	Number per node ^b			Maximum number of open sites ^d
		BDC	BzOH	HCOOH	
1	"Ideal" UiO-66 ^a	6	0	0	0
2	BzOH-UiO-66	3.9	2.9	0.3 ^c	1.0
3	decap-UiO-66	3.7	0	0	4.6
4	HCOOH-UiO-66	3.7	0	3.9	0.7
5	Isolated Zr ₆ -oxo-hydroxo cluster	0	8.7	0	3.3

^aThe "ideal" UiO-66 structure is defined as a structure with the formula Zr₆O₄(OH)₄(BDC)₆, that has exactly 6 BDC linkers/node (i.e., no missing linker and no capping ligand; Table 3.4).

^bDetermined from ¹H NMR analyses of solutions of the digested MOFs. ^cDerived from the hydrolysis of DMF during the MOF synthesis. ^dCalculated by comparing to the "ideal" UiO-66 structure.

When the parent **BzOH-UiO-66** was subjected to the same HCl_{aq} treatment but in the presence of DMF, we obtained a **HCOOH-UiO-66** material with 3.9 HCOOH-capped and 0.7 open sites per node (Table 3.1, entry 4). Presumably, the HCOOH ligands came from the high-

temperature acid-catalyzed hydrolysis of DMF¹⁵⁰ and readily bound to the nodes of UiO-66 to replace the BzOH capping ligands.¹⁴⁷⁻¹⁴⁸ The PXRD patterns (Figure 3.11), BET areas (Table 3.4), and SEM images (Figure 3.13) for **decap-UiO-66** and **HCOOH-UiO-66** are very similar to those of the parent **BzOH-UiO-66** MOF, confirming that the crystallinity, porosity, and morphology are preserved after both modifications. Together with the parent **BzOH-UiO-66**, these materials form a family of isomorphic MOFs with a relatively broad range of open sites (1-5) per node for us to explore in sulfide oxidation catalysis.

3.4 Selection of reaction system

As organic sulfides can be overoxidized to sulfone in the presence of excess H₂O₂, we used only a stoichiometric amount of H₂O₂ oxidant in our catalysis to limit this possibility.^{21, 151-152} We also chose methyl phenyl sulfide as a substrate that is known to give both sulfoxide and sulfone products¹⁵³⁻¹⁵⁴ during the oxidation, allowing us to delineate the activity and selectivity profiles of our catalysts. While dibenzothiophene and its derivatives have been previously used in UiO-66-catalyzed sulfide oxidation experiments,^{99-100, 123-124} sulfoxide products were not observed, presumably because they readily undergo oxidation to the sulfone.¹⁵⁵ Lastly, we employ CH₃OH, CH₃CN, and CH₂Cl₂ as solvents in our study to explore the differences between a solvent that is capable of hydrogen-bond-donating (i.e., CH₃OH) and those that cannot (i.e., CH₃CN, and CH₂Cl₂). As CH₃OH has been shown to bind well to the Zr₆-oxo-hydroxo nodes of UiO-66 through an extensive network of hydrogen bonds,^{129, 141} we hypothesize that it may provide an additional “knob” for tuning the reactivity of these nodes.

3.5 Activity of the catalysts and computational study

As expected, our three UiO-66 derivatives and the isolated Zr₆-oxo-hydroxo cluster^{102, 156} (capped with benzoate ligands, as a positive control¹¹⁰) were all catalytically active for the oxidation of sulfide in CH₃OH (Figure 3.1a). The negative control experiments (i.e., without catalyst or in the presence of bulk ZrO₂) did not show any significant product formation (Figure 3.1a), consistent with previous reports.⁹⁹ Notably, **decap-UiO-66**, the material with the highest number of open sites on the nodes, has better activity than the other two UiO-66 materials (Figure 3.1a, cf. the reaction profiles for **decap-UiO-66** vs **BzOH-UiO-66** and **HCOOH-UiO-66**). As Zr- μ_1 -OH moieties in a Zr^{IV}-containing zeolite¹⁵⁷ have been reported to form a combination of Zr- μ_1 -OOH and Zr(η^2 -O₂) active species in the presence of H₂O₂, it is reasonable to expect that the Zr- μ_1 -OH groups on the open sites of our UiO-66 derivatives could similarly be converted to these groups. The resulting catalytically active species would then promote the oxidation of methyl phenyl sulfide to the corresponding sulfoxide (1st oxidation) and eventually to the sulfone (2nd oxidation), which is observed as a second product in the sulfide oxidation (Figure 3.1b).

Our DFT calculations, carried out with a single Zr₆-oxo-hydroxo cluster possessing *one* open site [μ_1 -OH + μ_1 -OH₂], support the idea that the Zr- μ_1 -OH pre-catalyst moieties on the Zr₆-oxo-hydroxo nodes are preferentially transformed into active Zr- μ_1 -OOH intermediates in the presence of H₂O₂.¹⁵⁸ As shown in Figure 3.2, the free energy barrier for this activation is 74 kJ/mol (blue profile), consistent with a reaction that can take place at room temperature. The DFT calculations additionally confirm that these Zr- μ_1 -OOH active species can catalyze the oxidation of sulfide to sulfoxide and the subsequent overoxidation to sulfone. The free-energy profile of the catalyzed reaction in Figure 3.2 (blue profile) shows that the Zr₆-oxo-hydroxo node catalyst

reduces the barriers for both stages of oxidation compared to the uncatalyzed reaction (black profile).

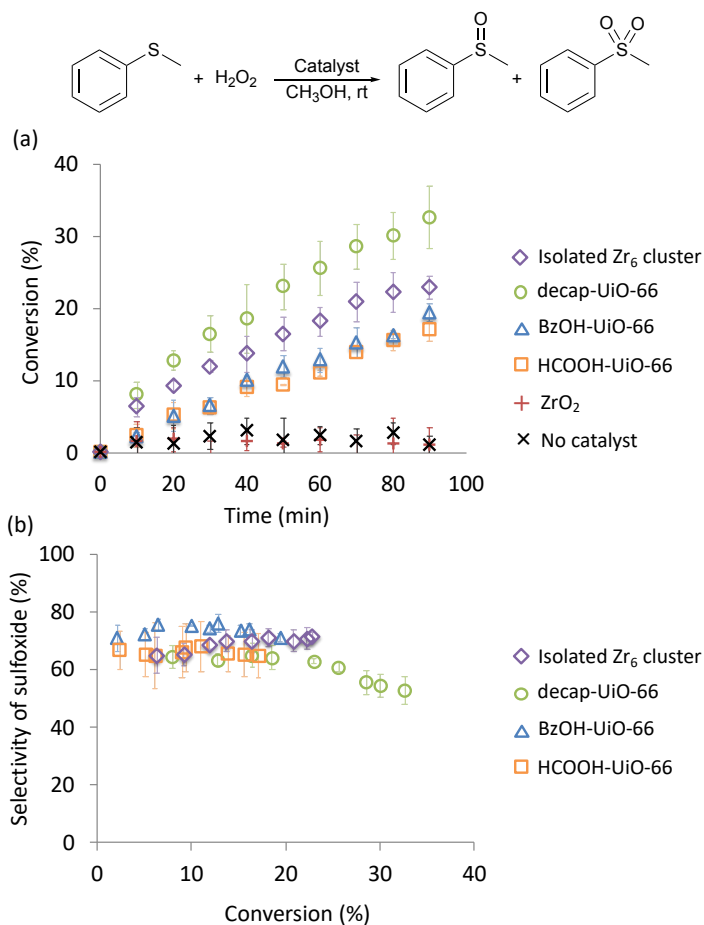


Figure 3.1 The conversion (a) and selectivity (b) profiles in the catalytic oxidation of methyl phenyl sulfide in CH_3OH using H_2O_2 as the oxidant. All reactions were carried out with a 100:100:1 molar ratio of sulfide: H_2O_2 :Zr₆-oxo-hydroxo clusters. See Figures 3.17-3.19 for catalysis data that extend up to 9 h.

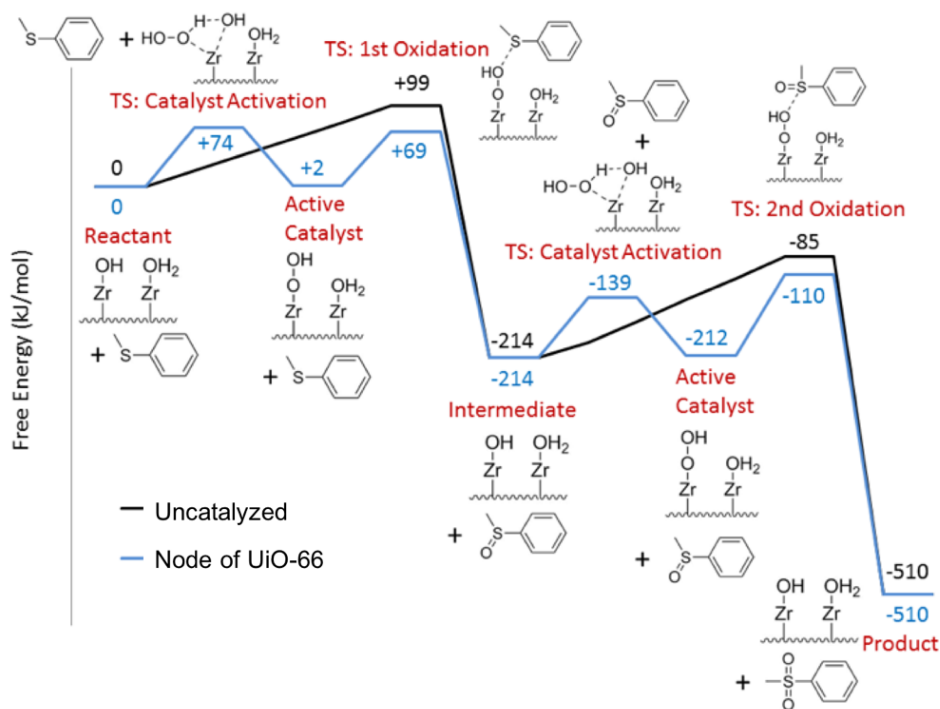


Figure 3.2 The computed free-energy profiles for the catalytic oxidation of methyl phenyl sulfide using H_2O_2 as the oxidant without catalyst (black) and with a Zr_6 -oxo-hydroxo cluster possessing *one* $[\mu_1\text{-OH} + \mu_1\text{-OH}_2]$ open site as a model for an “uncapped” node of UiO-66 (blue). To reduce system size in our node model, the capping acid modulator is HCOOH and all benzene rings in the BDC linker are replaced with hydrogen atoms. The system is essentially a $(\text{Zr}_6(\mu_3\text{-O})_4(\mu_3\text{-OH})_4(\text{OOCH})_{11})$ node. Free energies were calculated at 298 K and are reported in kJ/mol. Results were calculated using the PCM solvation model for CH_3OH for both the uncatalyzed and the catalyzed reactions. In the current figure, only a few selected hydrogen bonds are shown for the transition states to reduce the complexity in the drawings. The reader should note that the simplified depictions of isolated $\mu_1\text{-OH}$ and $\mu_1\text{-OH}_2$ sites are only used in this scheme for clarity. Hydrogen bonds do exist between adjacent $\mu_1\text{-OH}$ and $\mu_1\text{-OH}_2$ sites, as well as with H-bond-capable solvent molecules; thus, isolated μ_1 -species are probably unlikely, as discussed in later sections. For detailed illustrations of the hydrogen-bonded species, see Figure 3.29 as well as the structures shown in Section 3.9.

Similar to the sulfide-oxidation activity trend, **decap-UiO-66** also has the best activity for sulfoxide oxidation among the three MOF catalysts, as shown in Figure 3.3. However, while the observed rates for **decap-UiO-66** in both sulfide and sulfoxide oxidations are noticeably larger than those for **BzOH-UiO-66** (Table 3.2), they are not proportional to the number of open sites that we have engineered into these materials (Table 3.1). Thus, it appears that the steric environment of the MOF places restrictions on the magnitude of the differences in rates among these materials. This is not surprising, as UiO-66 has relatively small pore apertures (~ 6 Å for the “ideal”¹⁵⁹ structure)³² that restrict access for the large sulfide substrate to the open sites around the Zr₆-oxo-hydroxo node. The observed rates are, therefore, influenced by both the number of open sites and differences in steric crowding at the node among **BzOH-UiO-66**, **HCOOH-UiO-66**, and **decap-UiO-66**.

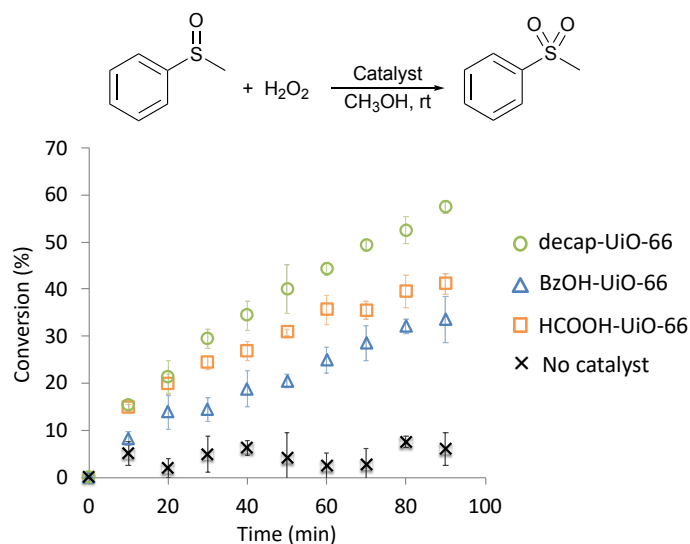


Figure 3.3 The conversion profile in the catalytic oxidation of methyl phenyl sulfoxide in CH₃OH using H₂O₂ as the oxidant. All reactions were carried out with a 100:100:1 molar ratio of methyl phenyl sulfoxide:H₂O₂:Zr₆-oxo-hydroxo node.

Table 3.2 Initial rates for the MOF-catalyzed oxidations of sulfide and sulfoxide in CH₃OH, starting directly with each individual substrate.

Catalyst	Initial rate (M/s)	
	Sulfide oxidation ^a	Sulfoxide oxidation ^b
BzOH-UiO-66	$(8.3 \pm 0.3) \times 10^{-7}$	$(16.8 \pm 1.3) \times 10^{-7}$
HCOOH-UiO-66	$(7.5 \pm 1.0) \times 10^{-7}$	$(26.4 \pm 1.2) \times 10^{-7}$
decap-UiO-66	$(14.7 \pm 3.1) \times 10^{-7}$	$(35.3 \pm 3.5) \times 10^{-7}$

^aCalculated by linearly fitting the conversion profile of methyl phenyl sulfide below the 20% level.
^bCalculated by linearly fitting the conversion profile of methyl phenyl sulfoxide below the 20% level.

The free energy profiles in Figure 3.2 also predict that the 2nd oxidation in the Zr₆-oxo-hydroxo-catalyzed reaction in CH₃OH has a higher barrier than the 1st oxidation (102 vs 67 kJ/mol, respectively), indicating a slower sulfoxide oxidation step and thus a high sulfoxide/sulfone ratio. This appears to be consistent with the experimental data in CH₃OH solvent, where high sulfoxide selectivities were observed (Figure 3.1b). However, when the initial rates for the direct oxidation of sulfoxide (i.e., starting with methyl phenyl sulfoxide as the reactant) were measured, the results (Table 3.2) suggest that the oxidation of sulfoxide is actually faster than the oxidation of sulfide. It is thus possible that the sulfoxide product may have additional interactions with the open sites, which would increase its oxidation rate beyond the relative 2nd oxidation rate given by the free-energy profile shown in Figure 3.2. Supporting this hypothesis is the overall faster oxidation of sulfide catalyzed by **BzOH-UiO-66**¹⁶⁰ in CH₃CN and CH₂Cl₂ (Figure 3.4a), along with lower sulfoxide selectivities (Figure 3.4b), in comparison to those in CH₃OH. As shown in Figure 3.4b, sulfoxide selectivities quickly dropped to 10-15% at 20% conversion, and diminished to almost zero at 30% conversion, suggesting that sulfoxide oxidation in the UiO-66 system is not solely governed by the free-energy landscape shown in Figure 3.2.

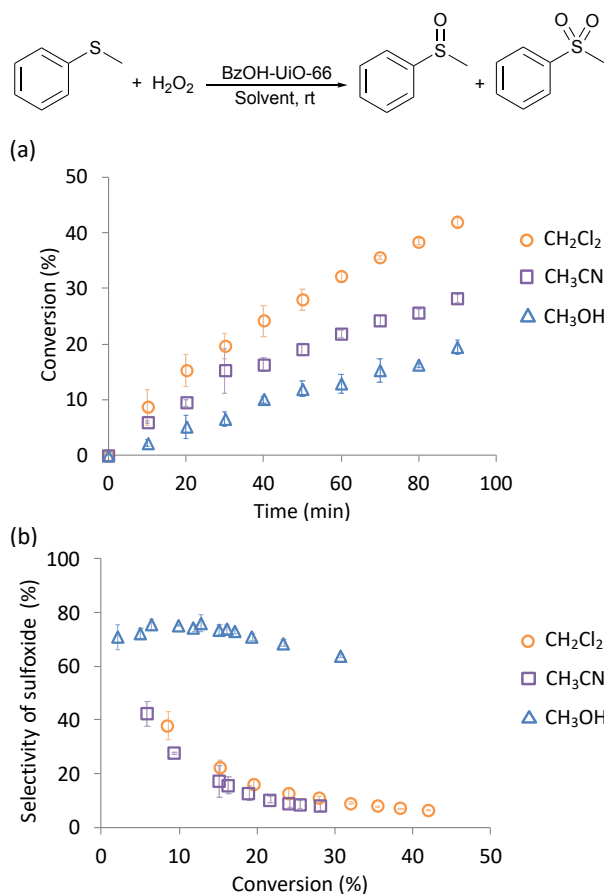


Figure 3.4 The conversion (a) and selectivity (b) profiles in the catalytic oxidation of methyl phenyl sulfide using H₂O₂ as the oxidant and **BzOH-UiO-66** as the catalyst in three different solvents. All reactions were carried out with a 100:100:1 molar ratio of methyl phenyl sulfide:H₂O₂:Zr₆-oxo-hydroxo node.

The low sulfoxide selectivity in CH₃CN and CH₂Cl₂ can be explained by a scenario where the sulfoxide product can associate with the active site and be oxidized more readily than the sulfide, which does not bind to the node. Such a mechanism can be realized in our system if the sulfoxide replaces the OH₂ ligand at the Zr-μ₁-OH₂ site^{129, 161} of the Zr₆-oxo-hydroxo nodes.^{129, 141} The resulting Zr-μ₁-O=S(CH₃)Ph “intermediate” would serve to increase the local concentration of the sulfoxide next to the active Zr-μ₁-OOH catalytic species and lead to faster sulfoxide oxidation (Scheme 3.3). In CH₃OH, the labile OH₂ ligand at the Zr-μ₁-OH₂ site would be replaced

by CH₃OH and the Zr-μ₁-O=S(CH₃)Ph intermediate is less likely to form. In other words, the local concentration of sulfoxide near the active Zr-μ₁-OOH site in CH₃OH will be lower than those in CH₃CN and CH₂Cl₂ and the free-energy profile in CH₃OH solvent is expected to be quite similar to that shown in Figure 3.2 with the Zr-μ₁-OH₂ moiety being replaced by Zr-μ₁-O(CH₃)H species. In such a scenario, the reaction flux would be favored toward the direct reaction of Zr-μ₁-OOH with the sulfide, which has a lower reaction barrier, resulting in higher sulfoxide selectivities.

Indeed, DFT calculations showed that the O atom of the methyl phenyl sulfoxide product can readily bind to the Zr site adjacent to the Zr-μ₁-OH pre-catalyst species to form a stable [Zr-μ₁-OH + Zr-μ₁-O=S(CH₃)Ph] product intermediate (Figure 3.5) that is only about 4.6 kJ/mol higher in energy than the [Zr-μ₁-OH + Zr-μ₁-OH₂] starting species shown in Figure 3.2 (Table 3.3, cf. entries 3 and 2). In contrast, the analogous complex between methyl phenyl sulfide and the node could not be found computationally despite an exhaustive search, presumably due to the weaker Zr-S interaction (in comparison to Zr-O binding). For comparison, the CH₃OH-solvated [Zr-μ₁-OH + Zr-μ₁-O(CH₃)H] species, which should predominate in CH₃OH, is very similar in binding energy to the [Zr-μ₁-OH + Zr-μ₁-OH₂] open site precatalyst, suggesting that it can compete effectively against the formation of the aforementioned [Zr-μ₁-OH + Zr-μ₁-O=S(CH₃)Ph] product intermediate (Table 3.3, cf. entries 3 vs 1 and 2) and prevent overoxidation. As both CH₃CN and CH₂Cl₂ have much weaker interactions with the node than methyl phenyl sulfoxide (Table 3.3, cf. entries 5 and 6 vs 3), the [Zr-μ₁-OH + Zr-μ₁-O=S(CH₃)Ph] product intermediate would dominate, leading to lower sulfoxide selectivity. We note with interest that because sulfoxide has a similar ΔG_{bind} value to that of CH₃OH (Table 3.3, cf. entries 1 and 3), it can compete effectively for

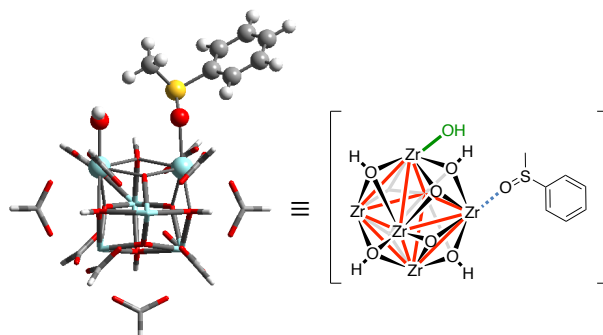


Figure 3.5 Optimized structure of the $[\text{Zr-}\mu_1\text{-OH} + \text{Zr-}\mu_1\text{-O}=\text{S}(\text{CH}_3)\text{Ph}]$ product intermediate. White, grey, red, yellow, and cyan spheres represent H, C, O, S, and Zr atoms, respectively.

Table 3.3 Computed binding free energies at 298 K and equilibrium binding constants of different solvents and reactants to the $\text{Zr}_6\text{-oxo-hydroxo}$ node.

Entry	Solvent/Substrate	ΔG_{bind} (kJ/mol)	K_{bind}
1	CH_3OH	-34.5	1.1×10^6
2	H_2O	-31.2	3.0×10^5
3	Methyl phenyl sulfoxide	-26.6	4.6×10^4
4	Methyl phenyl sulfone	-8.8	3.5×10^1
5	CH_3CN	+8.5	3.2×10^{-2}
6	CH_2Cl_2	+21.3	1.9×10^{-4}

3.6 Inhibition by CH_3OH and the possibility of forming H-bonding networks at the $\text{Zr}_6\text{-oxo-hydroxo}$ nodes

As mentioned earlier, the rate of sulfide oxidation in CH_3OH is slower than in CH_3CN and CH_2Cl_2 (Figure 3.4a), and this indicates an inhibitory effect by CH_3OH . Complementary to the free-energy landscape shown in Figure 3.2, such an effect can be partially attributed to the ability of CH_3OH to interact with the $\text{Zr-}\mu_1\text{-OH}$ moiety via hydrogen bonding, thus competing with H_2O_2 for interactions with the node and preventing the formation of the $\text{Zr-}\mu_1\text{-OOH}$ active catalyst (Scheme 3.3). In addition, the slower rate in CH_3OH may also be a consequence of a more

extensive hydrogen-bonding network, where 2 to 4 CH₃OH molecules interact with both sites in the [Zr- μ_1 -OH + Zr- μ_1 -OH₂] combination (Scheme 3.3), as proposed by Caratelli *et al.*^{129, 161} and recently reviewed by Schubert.¹⁶² Both of these pathways would not exist in CH₃CN and CH₂Cl₂ as these aprotic solvents do not have H-bond-donating capability.

Together, our experimental and computational data support the hypothesis that sulfoxide coordination to the Zr site adjacent to the Zr- μ_1 -OOH species can play an important role in CH₃CN and CH₂Cl₂, resulting in more overoxidation and lower sulfoxide selectivity. They also partly explain why sulfone was always obtained as the major product when the UiO-66-catalyzed oxidations of thiophene and its derivatives were conducted in CH₃CN and under high-oxidant conditions.^{99-100, 123-124} In addition to the sulfoxides of thiophenic substrates being more easily converted to sulfone than our methyl phenyl sulfide substrate,¹⁵⁵ the higher probability for the formation of sulfoxide-node complexes in CH₃CN would also promote overoxidation, especially in the presence of excess oxidant.

We note in passing that the high stability of the [Zr- μ_1 -OH + Zr- μ_1 -O=S(CH₃)Ph] product intermediate (Table 3.3, entry 3) may make it tempting to imagine a Langmuir-Hinshelwood-type mechanism where the bound sulfoxide (Figure 3.5) can interact with the adjacent active Zr- μ_1 -OOH site for conversion to the sulfone. However, our DFT calculations show that the formation of a direct Zr- μ_1 -OOH•S(O)PhMe complex has a much higher barrier (166 kJ/mol, Figure 3.28). Incorporation of H₂O₂ into the precatalyst can lower this barrier (to 147 kJ/mol, Figure 3.28) through the formation of a hydrogen-bonded Zr-OH•(H₂O₂)•S(O)PhMe•Zr intermediate. However, this is still quite high when compared to the direct barrier for sulfoxide oxidation (Figure

3.2), preventing it from playing a significant role. As such, we suspect that a Langmuir-Hinshelwood-type mechanism is unlikely.

3.7 Recyclability of **BzOH-UiO-66** and **decap-UiO-66**

Both **BzOH-UiO-66** and **decap-UiO-66** can be recovered and re-used for several cycles under our chosen reaction conditions. Not surprisingly, their selectivity profiles (Figures 3.22 and 3.24), do not vary significantly over five cycles. Slight decreases in the initial rates of product formation were observed after the 4th cycle (Figures 3.21 and 3.23), due to either small amounts of catalyst losses during the recovery process and/or a slight catalyst degradation. The latter is supported by PXRD data (Figures 3.25-3.26), which indicate that the crystallinities of the catalysts slightly degraded after the first 4 cycles.

The selectivity profiles for both catalysts under repeated recycling closely matched those shown in Figure 3.1 and agreed with our proposed mechanistic scheme. Specifically, the selectivity for the **decap-UiO-66** catalyst slightly drops over the allotted reaction time while remaining relatively constant for the **BzOH-UiO-66** catalyst. The former catalyst, having more open sites, is more active and can achieve faster conversion of the sulfide to produce sulfoxide, which in turn would lead to an observable decrease in sulfoxide selectivity. This can easily be understood when one considers that the rate of sulfoxide oxidation is ~2 times faster than that for sulfide oxidation (Table 3.2): as more sulfoxide is produced, the sulfoxide/sulfide ratio increases and the sulfoxide oxidation will become more dominant, leading to a reduction in the sulfoxide selectivity.

3.8 Conclusion

In this chapter, we reported the post-synthesis modifications of **BzOH-UiO-66** to increase the number of open precatalyst sites (i.e., those that are terminated with $[\text{Zr-}\mu_1\text{-OH} + \text{Zr-}\mu_1\text{-OH}_2]$), achieving a maximum number of up to 5 per node. We observed higher catalytic activities in both sulfide and sulfoxide oxidation with the catalysts possessing higher numbers of open sites. Computational modeling reveals that the $\text{Zr-}\mu_1\text{-OH}$ groups on the open sites are likely to be converted into $\text{Zr-}\mu_1\text{-OOH}$ species that are active in oxidizing the sulfide as well as its sulfoxide product. Notably, reactions carried out in CH_3OH can lead to higher selectivities for the sulfoxide product while overoxidation to sulfone predominates in CH_3CN and CH_2Cl_2 . Kinetic studies and computational evaluations support a model where the sulfoxide product can bind to a site adjacent to the active catalyst species in these latter solvents, resulting in higher degrees of overoxidation through increased local concentration. Such an effect is minimized in CH_3OH , which can interact more competitively with the open sites on the nodes than the sulfoxide and thus maintain good sulfoxide selectivity.

Together, our combined experimental and computational study shows that monocarboxylate-capped missing-linker defects on the $\text{Zr}_6\text{-oxo-hydroxo}$ node of UiO-66 MOFs can be converted into unsaturated coordination sites that serve as catalysts for the oxidation of sulfide. Given the recent surge of interests in the “defect engineering” of MOFs,^{122, 134, 140, 142, 147, 163-167} these insights may enable researchers to design MOF materials with well-defined defects that can be utilized for a broad range of applications. However, for our purpose of increasing the H_2O_2 consumption rate in the $[\text{H}_2\text{O}_2 \text{ generation} + \text{oxidation}]$ tandem reaction, these rates remain low. To further enhance the efficiency of H_2O_2 utilization, we will explore alternative MOFs that

have higher catalytic activities in sulfide oxidation such as metalloporphyrin-functionalized UiO-66 MOFs and metal (acetylacetonate)-functionalized UiO-66 MOFs in chapter 4. In addition, a reactor-based strategy for tuning the rate of H₂O₂ generation will be investigated for a better match with its consumption in sulfide oxidation.

3.9 Experimental

3.9.1 Materials and methods

Unless otherwise stated, all reagents were used as received. Zirconium chloride (ZrCl₄) was purchased from Strem Chemicals, Inc. (Newburyport, MA). Hydrogen peroxide (H₂O₂, 30 wt % in H₂O), naphthalene, benzoic acid (BzOH), zirconium oxide (ZrO₂), zirconium propoxide (Zr(OPr)₃, 70 wt % in *n*-propanol), 1,4-benzenedicarboxylic acid (BDC), methanesulfonic acid, methyl phenyl sulfide, methyl phenyl sulfoxide, methyl phenyl sulfone, maleic acid, and zirconium ICP standards were purchased from Sigma-Aldrich Co., LLC. (St. Louis, MI). Concentrated sulfuric acid was purchased from VWR Scientific, LLC (Chicago, IL). Deuterated dimethylsulfoxide (DMSO-*d*₆, 99%) was purchased from Cambridge Isotope Laboratories, Inc. (Tewksbury, MA). Ultrapure deionized (DI) H₂O (18.2 MΩ•cm resistivity) was obtained from a Millipore Milli-Q Biocel A10 instrument (Millipore Inc., Billerica, MA). Solvents were purchased from either Sigma-Aldrich Co., LLC. (St. Louis, MI) or Fisher Scientific, Inc. (Pittsburg, PA) and used as received.

Powder X-ray diffraction (PXRD) patterns were collected on a STOE's STADI-MP powder diffractometer (STOE & Cie. Ltd., Darmstadt, Germany) equipped with an asymmetric curved Germanium monochromator (Cu K_{α1} radiation, $\lambda = 1.54056 \text{ \AA}$), a one-dimensional silicon strip detector (MYTHEN2 1K from Dectris AG, Baden, Switzerland), and a line-focused Cu X-

ray tube operated at 40 kV and 40 mA. The as-received powder was sandwiched between two acetate foils (polymer substrate with neither Bragg reflections nor broad peaks above 10 degrees) and measured in transmission geometry in a rotating holder. Prior to the measurement, the instrument was calibrated against a NIST Silicon standard (640d). Measurements were made over the range $5^\circ < 2\theta < 53^\circ$ in 4° steps of detector and an exposure time of 10 s per step.

N_2 adsorption and desorption isotherms were measured on a Micromeritics Tristar II 3020 (Micromeritics Instrument Corporation, Norcross, GA) at 77 K. Before each run, samples were activated at 120 °C for 24 h under high vacuum on both a Schlenk line and an ASAP 2020 instrument (Micromeritics Instrument Corporation, Norcross, GA). About 40-100 mg of sample was used in each measurement and the BET area was calculated in the region $P/P_o = 0.005-0.1$.

Inductively coupled plasma optical-emission spectroscopy (ICP-OES) was conducted on a computer-controlled (QTEGRA software v. 2.2) Thermo iCap 7600 Duo ICP-OES (Thermo Fisher Scientific, Waltham, MA) instrument equipped with a SPRINT valve and a CETAC 520ASX autosampler (Teledyne CETAC, Inc., Omaha, NE).

For synthetic work, 1H NMR spectra of products were recorded on a Bruker Avance III 500 MHz (499.4 MHz for 1H) spectrometer (Bruker Biospin Corp., Billerica, MA, USA). 1H chemical shifts are referenced in ppm downfield from tetramethylsilane (TMS, δ scale) using the residual solvent resonances as internal standards.

For obtaining MOF compositions, 1H NMR spectra were recorded on an Agilent DD2 600 MHz spectrometer (Agilent, Santa Clara, CA) equipped with a triple-resonance (HCN) cold probe w/ Z-gradient and a sensitivity of $^1H = 4300$ and $^{13}C = 250$. 1H NMR chemical shifts are referenced

in ppm downfield from tetramethylsilane (TMS, δ scale). Maleic acid was used as an internal standard.

Centrifugation was carried out in an Eppendorf Centrifuge 5804 R, Model AG 22331 (Eppendorf AG, Hamburg, Germany) equipped with an F34-6-38 rotor. All centrifugations were carried out at 5000-6000 rpm (3214-4628 g) for 10-20 minutes.

Scanning electron microscopy (SEM) images were obtained at Northwestern University's EPIC/NUANCE facility on a SU8030 FE-SEM microscope (Hitachi High Technologies America, Inc., Dallas, TX) with an acceleration voltage of 10 kV. Prior to imaging, activated MOF samples were coated with Os (18 nm thickness) using a Filgen Osmium Coater Model OPC-60A (Filgen, Inc., Nagoya, Japan). Size measurements were obtained from sample populations of >100 particles, which were used to construct the standard normal distribution plots (mean \pm 3 standard deviation units) and the histograms.

Gas chromatographic analysis was carried out on an Agilent Technologies 6890N Network GC system (Agilent Technologies, Inc., Santa Clara, CA) equipped with an FID detector. An HP-5 capillary column (30 m \times 320 μ m \times 0.25 μ m film thickness) was used to analyze the substrates. Analysis parameters were as follows: initial temperature = 80 $^{\circ}$ C, initial time = 2 min, ramp = 20 $^{\circ}$ C/min, final temperature = 200 $^{\circ}$ C, final time = 1 min. Elution times (min) = 4.4 (methyl phenyl sulfide), 5.3 (naphthalene), 6.3 (methyl phenyl sulfoxide), and 6.8 (methyl phenyl sulfone). The amount of oxidation product was calculated based on calibration curves against naphthalene as an internal standard. Response factors: methyl phenyl sulfide = 0.723, methyl phenyl sulfoxide = 0.790, and methyl phenyl sulfone = 0.771.

3.9.2 Computational methods (This work was carried out by Dr. Haoyuan Chen and Mr. Matthew Mendonca.)

All electronic structure calculations were carried out using the Gaussian 09 package (revision D.01). The starting structure of the UiO-66 node was adapted from a previous computational work¹⁶⁸ and re-optimized. In the UiO-66 node model, one BzO- linker was replaced by one H₂O and one -OH to saturate the coordination of two Zr atoms and balance the charge, according to the experimental stoichiometry (see Table 3.4). All remaining BzO- linkers were then replaced with HCOO- to reduce the system size and speed up the calculations. All geometry optimizations and transition state searches were performed using density functional theory (DFT) with the B3LYP functional.^{169,170} The def2-SVP basis set¹⁷¹ was used for H, C, N, O, S, and Cl atoms while the LANL2DZ basis sets¹⁷² with effective core potentials were applied to the Zr atoms. The polarizable continuum model (PCM),¹⁷³ with default atomic cavity radii and specific solvents corresponding to experimental conditions, was used to model solvation effects. For example, the results in Figure 3.2 for the uncatalyzed and catalyzed reactions included solvation effects for CH₃OH using the PCM model. Similarly, the free energy for CH₃CN in Table 3.3 was calculated in implicit CH₃CN solvent using the PCM model. Results for methyl phenyl sulfoxide and methyl phenyl sulfone in Table 3.3 are in implicit CH₃OH. Vibrational analysis and thermochemistry calculations were performed for all species at the same level of theory. Single-point energy calculations were also carried out to refine the energies of all species, in which the def2-SVP basis set was replaced by the larger def2-TZVP basis set and the DFT-D3 dispersion correction¹⁷⁴ with Becke-Johnson damping¹⁷⁵ (D3BJ) was applied. The reported Gibbs free energy of each species

was calculated by adding the single-point electronic energy (at B3LYP-D3BJ/def2-TZVP level) and the thermochemistry terms (at B3LYP/def2-SVP level) together.

3.9.3 Synthesis of materials

BzOH-UiO-66 batch 1. This material was made following a previously reported literature procedure with minor modifications.¹⁴⁶ In a 1 L Erlenmeyer flask, BzOH (13.3 g, 108 mmol) was dissolved in DMF (412 mL) by stirring before being combined with ZrCl₄ (0.85 g, 3.6 mmol) and BDC (0.54 g, 3.3 mmol). Additional sonication (~1-5 min) can help with the dissolution of all reagents into a clear solution, which was then partitioned evenly among 8 dram glass vials (25.5 mL each, 16 vials in total). The vials were capped tightly and placed in a preheated oven at 120 °C for 24 h. After being cooled to room temperature, the mixture from each vial was transferred separately into 50 mL centrifuge tubes (16 tubes in total) and the mother liquor was separated from the solid by centrifugation. After decanting the mother liquor, the collected solid was then soaked in fresh DMF (~20 mL/tube) for ~8 h, and pelletized by centrifugation to complete one cycle of washing. This cycle was repeated three times to remove the unreacted starting materials. Half of the crude solid was kept for the synthesis of **HCOOH-UiO-66** (see below), while the rest was redispersed in acetone (~20 mL/tube) to exchange out the DMF, collected by centrifugation, and air-dried overnight. To ensure that no residual DMF remains, the solid was subjected to Soxhlet extraction with acetone for ~12 h. The resulting solid was then dried overnight at 120 °C under vacuum to give a white powder (~400 mg) that is then stored at room temperature in a screw-capped vial. For analytical data, see Table 3.4 (BET area and chemical formula), Figure 3.7a (NMR data), and Figure 3.11 (PXRD data). This material was used for the majority of the catalysis studies except for the recycling data (Figures 3.21-3.22).

BzOH-UiO-66 batch 2. To test the differences in batch-to batch variation, this material was synthesized by Mengtan Liu and worked up by Rungmai Limvorapitux following the same protocol as described above. For analytical data, see Table 3.4 (BET area and formula), Figure 3.7b (NMR data), and Figure 3.11 (PXRD data). From these characterizations, this batch of material is very similar to batch 1. This batch of material was used in the recycling experiments (Figures 3.21-3.22).

HCOOH-UiO-66. This material was made by adapting a literature protocol for HCl-treated UiO-66.⁶¹ Half of the crude **BzOH-UiO-66**, synthesized from the previous experiment, was partitioned evenly into two 100 mL glass vials. DMF (60 mL) was added to each vial and the resulting mixtures were sonicated for 2 min followed by addition of HCl (5 mL of an 8 M aqueous solution). The vials were then capped tightly and swirled briefly before being placed into a preheated oven at 100 °C for 24 h. After being cooled to room temperature, the content of each vial was transferred separately into 50 mL centrifuge tubes and subjected to centrifugation. After decanting the mother liquor, the collected solid was then soaked in fresh DMF (~20 mL/tube) for ~2 h, and pelletized by centrifugation to complete one cycle of washing. This cycle was repeated three times to remove HCl and BzOH. The remaining solid was then redispersed in acetone (~20 mL/tube), collected by centrifugation, and air-dried overnight. To ensure that no residual DMF remains, the solid was subjected to Soxhlet extraction with acetone for ~12 h. The resulting solid was then dried overnight at 120 °C under vacuum to give a white powder (~400 mg) that is then stored at room temperature in a screw-capped vial.

decap-UiO-66 batch 1. This material was made by adapting a literature protocol for HCl-treated UiO-66.⁶¹ In an 8 dram vial, dry **BzOH-UiO-66** (150 mg) was combined with *n*-butanol

(18 mL) and HCl (1.5 mL of an 8 M aqueous solution). The vial was capped tightly and swirled briefly before being placed into a preheated oven at 100 °C for 24 h. After being cooled to room temperature, the mixture was transferred into a 50 mL centrifuge tube and subjected to centrifugation. After decanting the mother liquor, the collected solid was then soaked in fresh *n*-butanol (~20 mL) for ~2 h and pelletized by centrifugation to complete one cycle of washing. This cycle was repeated three times to remove HCl and BzOH. The remaining solid was then redispersed in acetone (~20 mL), collected by centrifugation, and air-dried overnight. To ensure that no residual *n*-butanol remains, the solid was subjected to Soxhlet extraction with acetone for ~12 h. The resulting solid was then dried overnight at 120 °C under vacuum to give a white powder that is then stored at room temperature in a screw-capped vial. For analytical data, see Table 3.4 (BET area and formula), Figure 3.8a (NMR data), and Figure 3.11 (PXRD data). This material was used for the majority of the catalysis studies except for the recycling data (Figures 3.23-3.24).

decap-UiO-66 batch 2. This material was made from **BzOH-UiO-66** batch 2, following the same protocol as described above. For analytical data, see Table 3.4 (BET area and formula), Figure 3.8b (NMR data), and Figure 3.11 (PXRD data). From these characterizations, this batch of material is very similar to batch 1. This batch of material was used in the recycling experiments (Figures 3.23-3.24).

Isolated Zr₆-oxo-hydroxo cluster. This material was made by Dr. Yonghwi Kim following a previously reported literature procedure with a minor modification in the capping agent.^{102, 156} In a 100 mL round-bottom flask equipped with a magnetic stir bar, BzOH (16 g, 130 mmol) was dissolved in *n*-propanol (50 mL) by stirring before being combined with Zr(OPr)₄ (2.1 mL of a 70 wt % solution in *n*-propanol, 5 mmol). The flask was then attached to a water-cooled

reflux condenser and the reaction mixture was brought to reflux for 2 h, during which time precipitate started to form. After cooling down, the precipitate was collected by centrifugation and dried under vacuum overnight to give a white powder that is stored at room temperature in a screw-capped vial.

Perbenzoic acid (BzOOH). This compound was synthesized according to a previously reported literature protocol.¹⁷⁶ In a 100 mL round-bottom flask equipped with a magnetic stir bar, methanesulfonic acid (14.4 g, 150 mmol) was combined with BzOH (3.7 g, 30 mmol). The stirred suspension was warmed up to 40 °C and H₂O₂ (420 μL of a 30 wt % of solution in H₂O, 41 mmol) was then added dropwise over 1-2 min. After 5 h, the reaction mixture was cooled down to room temperature and combined with ice (10 g). The resulting mixture was treated with saturated aqueous (NH₄)₂SO₄ solution (10 mL) before being extracted with CH₂Cl₂ (3 × 10 mL). The combined organic extracts were then washed with saturated aqueous (NH₄)₂SO₄ solution (3 × 10 mL), dried over MgSO₄, and concentrated by rotary evaporation at room temperature. The collected crude-product was further purified via flash-column chromatography on silica gel (3 mm × 15 mm; CH₂Cl₂). Combining the product-containing fractions and removing solvents yielded perbenzoic acid as white solid (27% of benzoic acid impurity).

3.9.4 Compositional analyses of the MOF and cluster materials

Procedure for the quantitative analysis of the Zr content in MOF and cluster materials. Into a 15 mL polypropylene centrifuge tube, conc. H₂SO₄ (1.5 mL), H₂O₂ (30 wt % in H₂O, 250 μL), and HF (250 μL) were added to a small sample (~1 mg) of the material to be analyzed. The resulting mixture was sonicated until the solution became clear (~1 h). The resulting solution was then transferred to a 50 mL polypropylene centrifuge tube, and diluted with

DI H₂O to a final volume of 30 mL. This solution was then analyzed for Zr by ICP-OES ($\lambda = 339.198, 343.823, 327.305, \text{ and } 349.621 \text{ nm}$) against a calibration curve of standards with known [Zr]. Data are listed in Table 3.4.

Caution: HF is very toxic and dangerous to handle without proper safety training. PPE must include Silvershield gloves and goggles. Acid digestions and subsequent dilutions should be carried out in a well-ventilated hood.

Procedure for the quantitative analyses of BDC, BzOH, and HCOOH content in MOF and cluster materials. In a 15 mL polypropylene centrifuge tube, HF (6 μL) and DMSO-*d*₆ (114 μL) were added to a small sample ($\sim 2 \text{ mg}$) of the material to be analyzed. The resulting mixture was sonicated until the solution became clear ($\sim 1 \text{ h}$). Then an aliquot (12 μL , corresponding to $\sim 0.2 \text{ mg}$ of sample) of the resulting solution was transferred to an NMR tube along with an aliquot of 12 mM maleic acid (MA) solution in DMSO-*d*₆ (50 μL), and fresh DMSO-*d*₆ (538 μL). This combined solution was then analyzed by ¹H NMR spectroscopy with a 90° pulse using a 50 s delay between scans, which exceed the T1 relaxation time for BDC (3.7 s), MA (2.8 s), and HCOOH (9.9 s). The amount of each substrate was calculated by comparing the integration against a calibration curve of standards with known concentrations (see Figure 3.6 for calibration curve, and Figures 3.7-3.10 for NMR spectra).

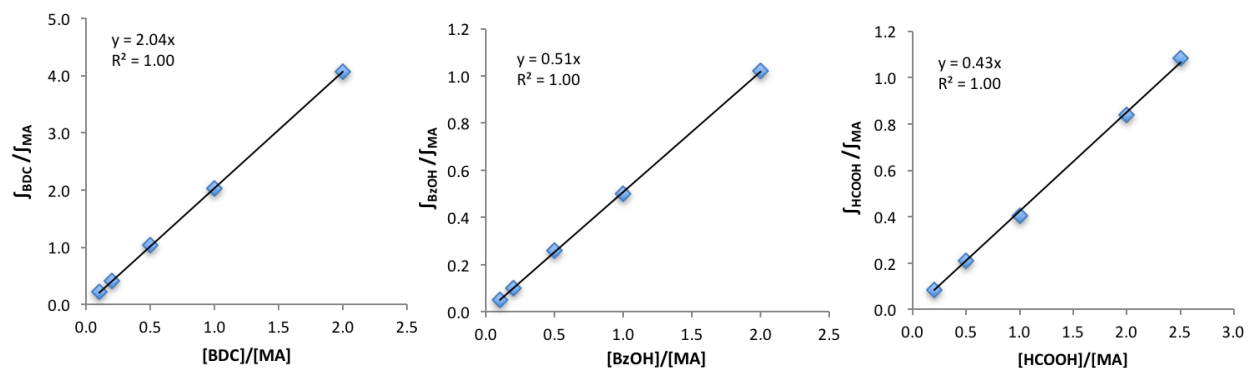


Figure 3.6 Plots of the concentration ratio of BDC, BzOH, and HCOOH to the MA internal standard versus the integration ratio of the signals for the analytes (BDC, BzOH, and HCOOH) to MA.

The ^1H NMR spectra of the digested MOFs can reveal the composition of the organic ligands present in each digested sample. For the **BzOH-UiO-66**, its ^1H NMR spectrum confirms the presence of BDC and BzOH (Figure 3.7), and shows an additional peak for HCOOH, which originates from the decomposition of DMF solvent under the conditions for MOF synthesis. As expected, HCOOH was also found in the **HCOOH-UiO-66** (Figure 3.9) due to the usage of DMF during the HCl-catalyzed thermal removal of BzOH from **BzOH-UiO-66**. Such HCOOH can readily bind to the open sites of the Zr_6 -oxo-hydroxo cluster nodes of UiO-type MOFs, as reported by Lillerud and coworkers.¹⁴⁷⁻¹⁴⁸ When the BzOH was removed in *n*-butanol instead of DMF, the HCOOH peak was no longer observed in the ^1H NMR spectrum of the digested **decap-UiO-66** (Figure 3.8), further supporting that HCOOH indeed comes from the decomposition of DMF. Finally, the absence of the BzOH peaks in both ^1H NMR spectra of **HCOOH-UiO-66** (Figure 3.9) and **decap-UiO-66** (Figure 3.8) confirms the successful removal of BzOH in both materials.

Table 3.4 Formula and BET area of materials.

MOF	Proposed formula ^a	BET area (m ² /g)
Ideal UiO-66	Zr ₆ O ₄ (OH) ₄ (BDC) ₆	1100 ^b
BzOH-UiO-66 batch 1	Zr ₆ O ₄ (OH) ₄ (BDC) _{3.9} (BzOH) _{2.9} (HCOOH) _{0.3} (μ ₁ -OH) ₁ (μ ₁ -OH ₂) ₁	1490
HCOOH-UiO-66	Zr ₆ O ₄ (OH) ₄ (BDC) _{3.7} (HCOOH) _{3.9} (μ ₁ -OH) _{0.7} (μ ₁ -OH ₂) _{0.7}	1640
decap-UiO-66 batch 1	Zr ₆ O ₄ (OH) ₄ (BDC) _{3.7} (μ ₁ -OH) _{4.6} (μ ₁ -OH ₂) _{4.6}	1530 ^c
BzOH-UiO-66 batch 2 ^d	Zr ₆ O ₄ (OH) ₄ (BDC) _{4.1} (BzOH) _{3.1} (HCOOH) _{0.1} (μ ₁ -OH) _{0.6} (μ ₁ -OH ₂) _{0.6}	1510
decap-UiO-66 batch 2 ^d	Zr ₆ O ₄ (OH) ₄ (BDC) _{3.6} (μ ₁ -OH) _{4.8} (μ ₁ -OH ₂) _{4.8}	1440 ^c
Isolated Zr ₆ -oxo-hydroxo cluster ^e	Zr ₆ O ₄ (OH) ₄ (BzOH) _{8.7} (μ ₁ -OH) _{3.3} (μ ₁ -OH ₂) _{3.3}	-

^aThe formula of UiO-66 MOFs are determined from the ¹H NMR spectra and ICP-OES data of digested materials carried out by R.L. The open sites were proposed to be terminated by μ₁-OH and μ₁-OH₂. ^bThis BET area was obtained from a literature report, calculated by fitting simulated N₂ isotherms.¹⁴⁵ For UiO-66 with 8 linkers per node, the calculated BET area was 1400 m²/g.¹⁴⁵

^cThe variation in this data illustrates the differences in materials obtained by the same researcher (R.L.) using the same decapping protocol but from different batches of **BzOH-UiO-66** made by two different experimenters (R.L. and M.L.). In fact, a range of 1440-1720 m²/g has been obtained in our laboratory across three different batches of materials. ^dThis batch of material was used in the recyclability experiment.

^eWhile the literature-reported formula^{102, 156} was Zr₆(OH)₄O₄(BzOH)₁₂(ⁿPrOH)•4BzOH, we did not observe a significant amount of ⁿPrOH and found much less BzOH than expected. We expected that our modified synthesis could have resulted in a loss of BzOH.

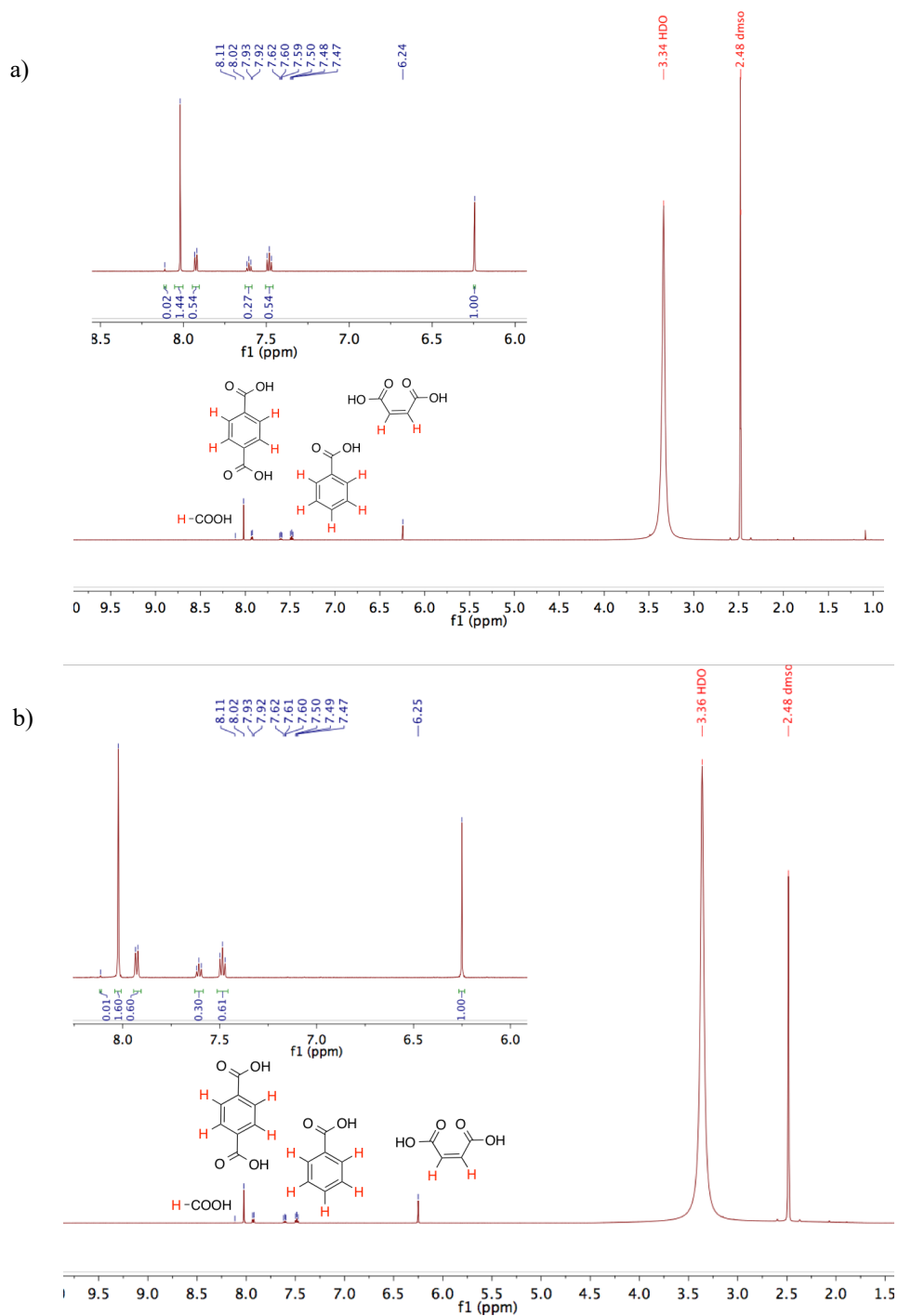


Figure 3.7 The ^1H NMR spectra of: a) digested **BzOH-UiO-66** batch 1 and b) digested **BzOH-UiO-66** batch 2 in $\text{DMSO-}d_6$.

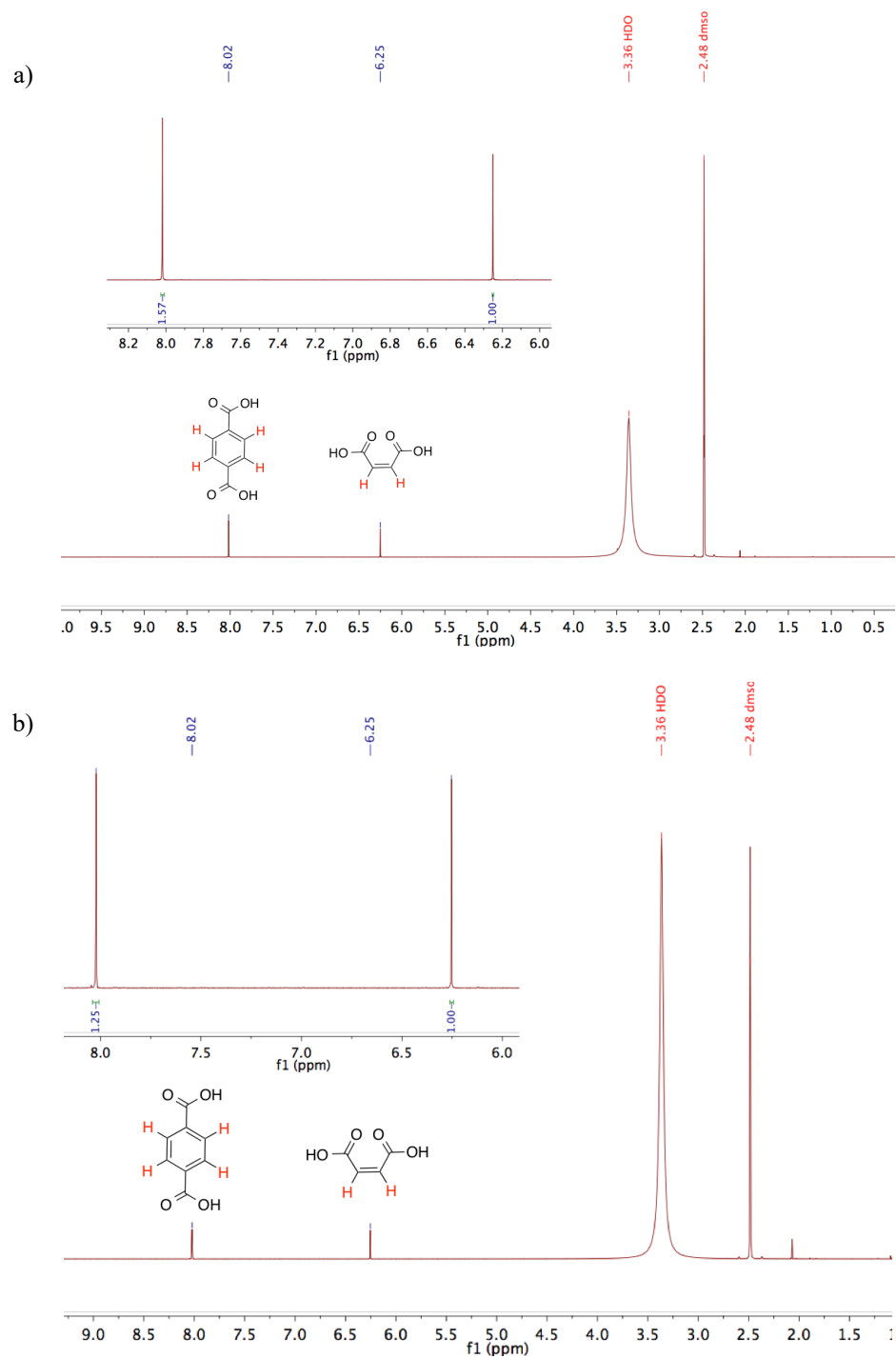


Figure 3.8 The ^1H NMR spectrum of: a) digested **decap-UiO-66** batch 1 and b) digested **decap-UiO-66** batch 2 in $\text{DMSO-}d_6$.

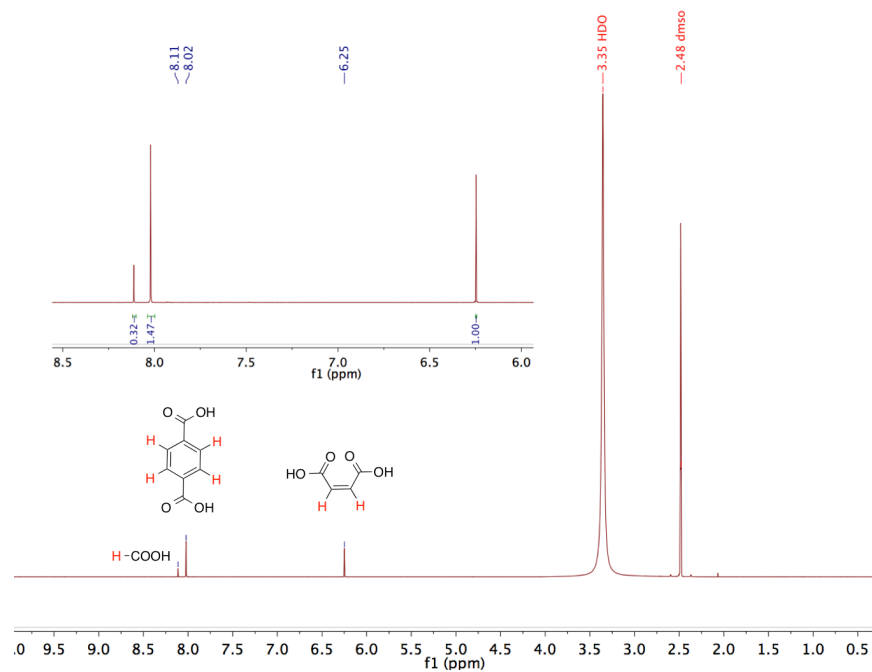


Figure 3.9 The ^1H NMR spectrum of digested HCOOH-UiO-66 in $\text{DMSO-}d_6$.

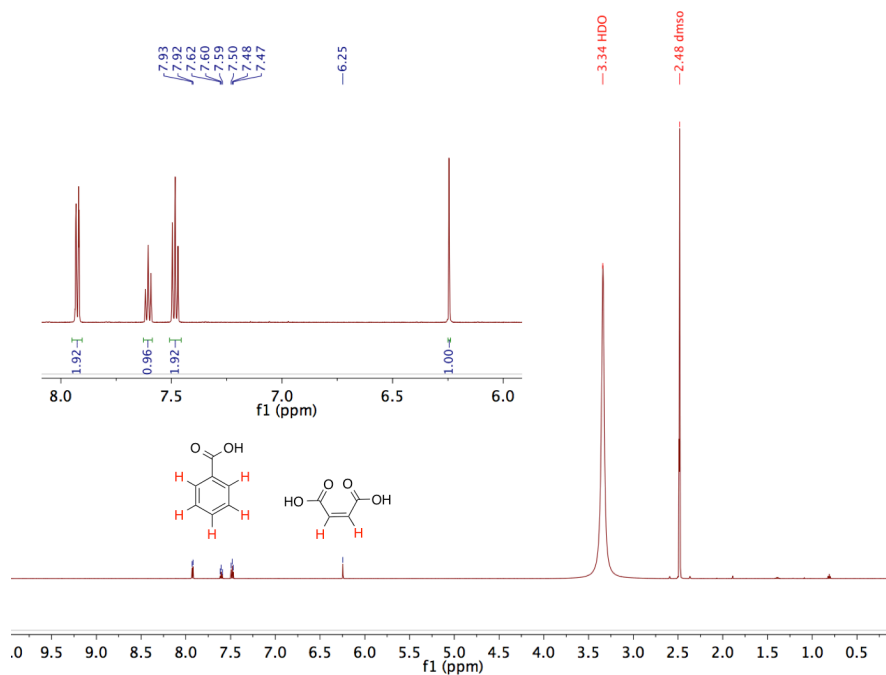


Figure 3.10 The ^1H NMR spectrum of digested isolated Zr_6 -oxo-hydroxo cluster in $\text{DMSO-}d_6$.

3.9.5 Characterization data of the MOF materials

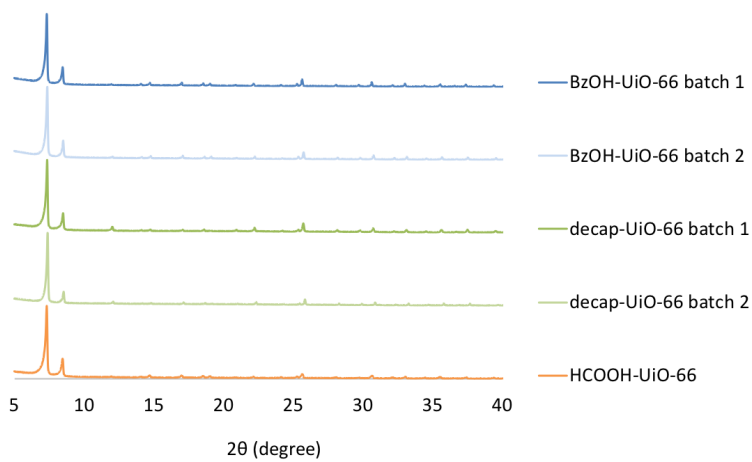


Figure 3.11 PXRD patterns for UiO-66 MOFs used in this study.

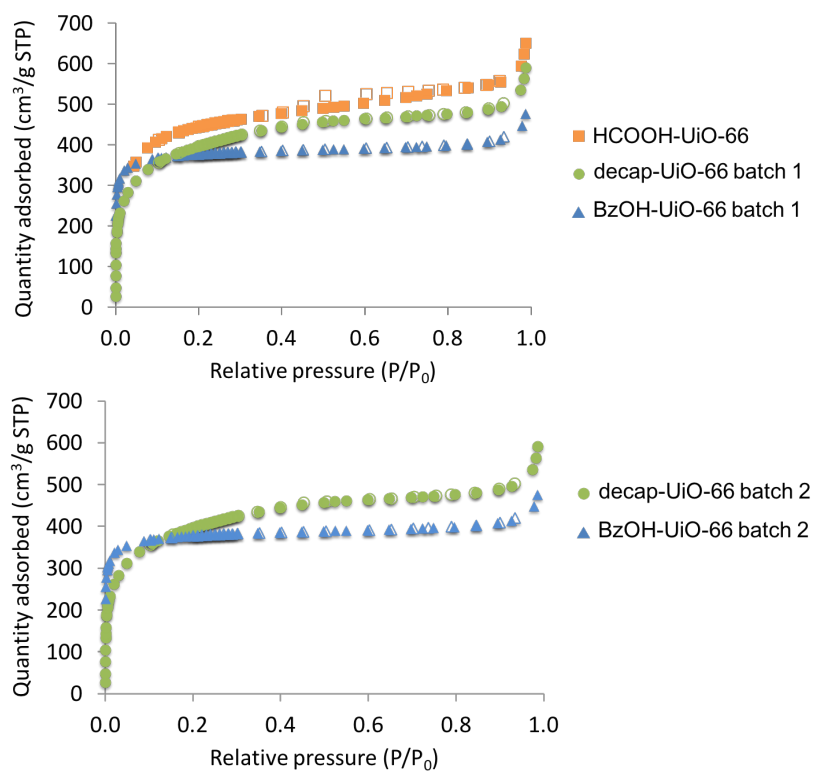


Figure 3.12 N₂ isotherms for UiO-66 MOFs used in this study. Close symbols: adsorption; open symbols: desorption.

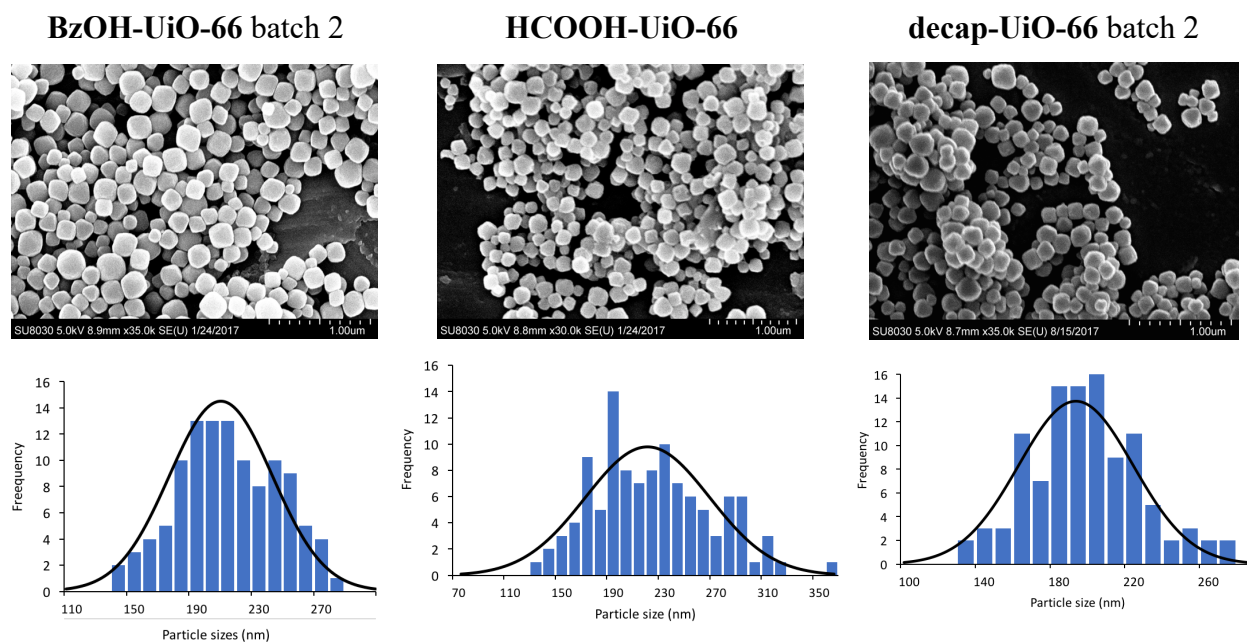


Figure 3.13 Top row: Representative SEM images of three UiO-66 MOFs used in this study. Bottom row: The corresponding SEM-derived particle-size-distribution profile for each of the MOF samples; each profile was constructed based on measurements of >100 particles.

3.9.6 Procedures for the catalysis studies

Stock solution of 20 mM methyl phenyl sulfide or 20 mM methyl phenyl sulfoxide. In a 120 mL jar equipped with a magnetic stir bar, substrate (either methyl phenyl sulfide (240 μL, 2 mmol), or methyl phenyl sulfoxide (280 mg, 2 mmol)), and naphthalene (256 mg, 2 mmol, as an internal standard) were dissolved in a selected solvent (either CH₃OH, CH₃CN, or CH₂Cl₂, 100 mL). This solution was stored at room temperature in a jar until use.

The oxidation of methyl phenyl sulfide with H₂O₂. These experiments were carried out with either **BzOH-UiO-66** batch 1 or **decap-UiO-66** batch 1. In a 6 dram vial equipped with a magnetic stir bar, a catalyst sample (0.012 mmol Zr (see Table 3.5), 6 mol %) was added to an aliquot of the pre-prepared 20 mM methyl phenyl sulfide stock solution (10 mL, 0.2 mmol). H₂O₂

(20 μL of a 30 wt % solution in H_2O , 0.2 mmol) was then added and the mixture was stirred at room temperature. At specific time intervals (10 min or 1 h), an aliquot (0.3 mL) of the reaction mixture was removed and filtered through a 0.2 μm PTFE syringe filter (VWR International, North American Cat. No. 28145-495), that is attached to a disposable syringe. The filter was rinsed with additional reaction solvent (~ 1 mL) and the combined organics was then analyzed by GC-FID. Data are shown in Figure 3.1 and Table 3.2, as well as Figures 3.14 and 3.17-3.19. The error bars are the standard deviations of three trials.

Table 3.5 Catalysts used in the reaction.

Component	Amount of material ^a (mg)
decap-UiO-66	2.8
BzOH-UiO-66	3.4
HCOOH-UiO-66	2.9
Isolated $\text{Zr}_6\text{-oxo-hydroxo}$ cluster	4.1
ZrO_2	1.2

^aCalculated for a stoichiometry of 100 equiv substrate/ $\text{Zr}_6\text{O}_4(\text{OH})_4$ cluster based on the formula shown in Table 3.4.

The oxidation of methyl phenyl sulfoxide with H_2O_2 . This reaction was conducted following the aforementioned procedure and with either **BzOH-UiO-66** batch 1 or **decap-UiO-66** batch 1. However, the pre-prepared 20 mM methyl phenyl sulfoxide stock solution was used as the substrate. Data are shown in Figures 3.3 and 3.15, and Table 3.2. The error bars are the standard deviations of three trials.

Catalyst recycling. These experiments were carried out with either **BzOH-UiO-66** batch 2 or **decap-UiO-66** batch 2. To reduce the proportion of catalyst loss during the recovery process, we carried out this series of experiments using an initial reaction scale that is $10 \times$ larger than our typical catalysis experiment. Into a 250 mL round-bottom flask equipped with a magnetic stir bar,

the appropriate MOF (0.1 mmol Zr, 5 mol %) or was added to a portion of the 20 mM methyl phenyl sulfide stock solution in CH₃OH (100 mL, 2 mmol). H₂O₂ (200 μL of a 30 wt % solution in H₂O, 2 mmol) was then added and the combined mixture was stirred at room temperature. At every 10 min, an aliquot (0.3 mL) of the reaction mixture was removed and filtered through a 0.2 μm PTFE syringe filter (VWR International, North American Cat. No. 28145-495), that is attached to a disposable syringe. The filter was rinsed with additional CH₃OH (~1 mL) and the combined organics was then analyzed by GC-FID. After 90 min, the reaction mixture was subjected to centrifugation and the supernatant portion was isolated by carefully decanting to leave the catalyst behind. The remaining catalyst was immersed in fresh CH₃OH (~15 mL) for ~5 min before being collected by centrifugation and decantation. This immersion and centrifugation process was repeated two more times. New aliquots of substrates and oxidant (same stoichiometry as shown above) were then added to repeat the oxidation of methyl phenyl sulfide. Data are shown in Figures 3.21-3.24. The PXRD of the catalysts after each cycles are shown in Figures 3.25-3.26. The SEM data are shown in Figure 3.27.

To analyze the amount of Zr leaching, a portion (2 mL) of the clear supernatant collected at the end of each cycle was added to an 8 dram vial and heated at 120 °C for 18 h to evaporate solvent and chemical substrates. Conc. H₂SO₄ (750 μL) and H₂O₂ (125 μL) were then added, and the vial was swirled briefly before the mixture was left unstirred at room temperature. After ~2 h (until the mixture became clear), the resulting clear solution was transferred to a 15 mL polypropylene centrifuge tube and diluted with DI H₂O to reach a final volume of 15 mL. The Zr content of this solution was then analyzed by ICP-OES ($\lambda = 339.198, 343.823, 327.305$, and

349.621 nm) comparing against a calibration curve of standards with known [Zr] concentrations.

Data are listed in Table 3.6.

3.9.7 Catalysis data

Unless otherwise noted in the caption, the materials employed in the experiments described below were from **BzOH-UiO-66** batch 1.

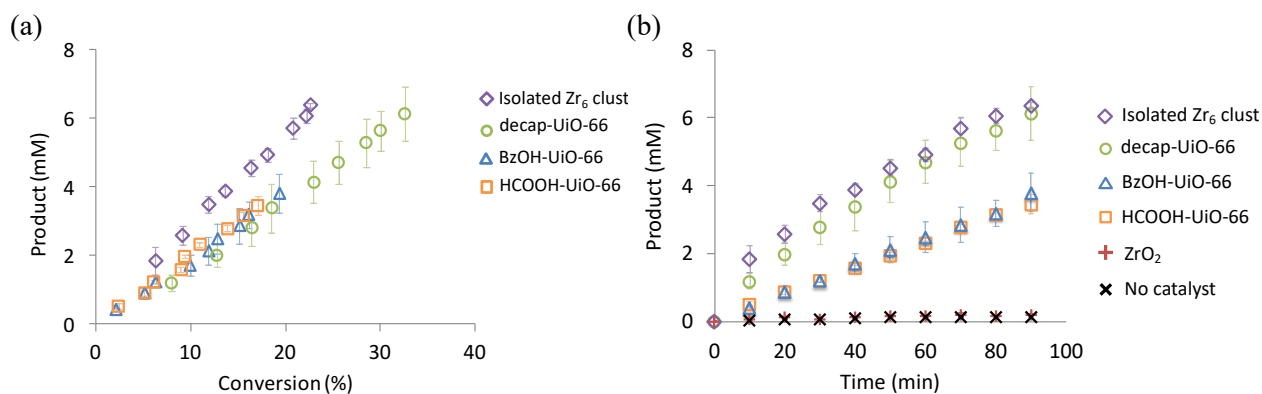


Figure 3.14 Product-formation profiles (product vs conversion (a) and product vs time (b)) in the catalytic oxidation of methyl phenyl sulfide in CH₃OH using H₂O₂ (1 equiv) as the oxidant. For convenience, product = sulfoxide + sulfone.

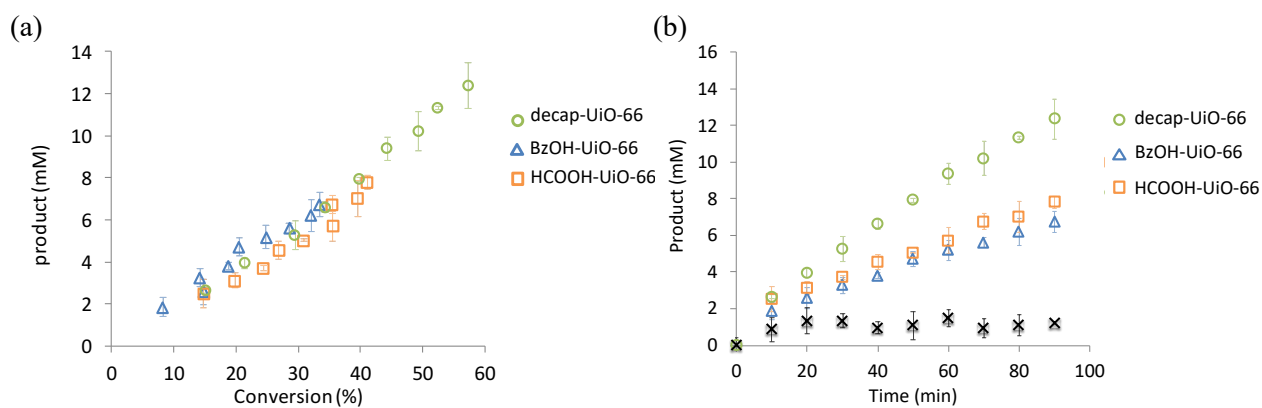


Figure 3.15 Product-formation profiles (product vs conversion (a) and product vs time (b)) in the catalytic oxidation of methyl phenyl sulfoxide in CH₃OH using H₂O₂ (1 equiv) as the oxidant.

Because carboxylic acids can potentially be converted to peracids after treating with H₂O₂ under acidic condition,¹⁷⁶ we initially suspected that BzOOH might form on the Zr₆-oxo-hydroxo cluster nodes of **BzOH-UiO-66**, and provide an additional pathway for oxidizing the sulfide. Thus, we carried out the uncatalyzed oxidation of methyl phenyl sulfide using BzOOH oxidant (Figure 3.16) as a control. However, this experiment does not result in sulfone (~99% selectivity to sulfoxide), which was very different from our observed sulfide reaction in the presence of **BzOH-UiO-66** and H₂O₂, where the sulfoxide selectivity was only ~70% (Figure 3.1b). In addition, DFT calculations reveal a barrier of 164 kJ/mol for the catalyst activation step, which is much higher than all of the barriers in the favored Zr-μ₁-OOH mechanism (Figure 3.2). Together, these data suggest that the formation of BzOOH is less likely to occur under our reaction conditions.

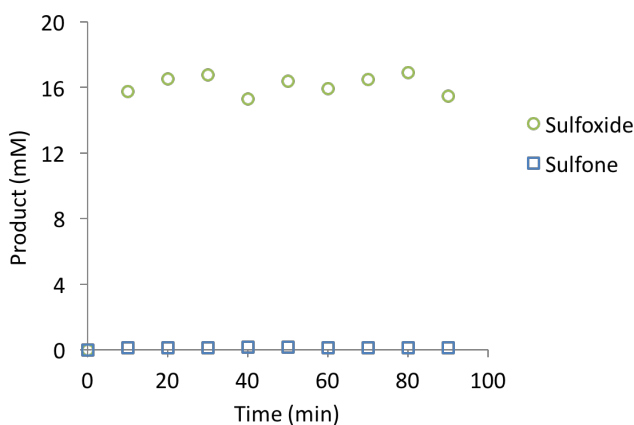


Figure 3.16 Product-formation profiles in the uncatalyzed oxidation of methyl phenyl sulfide in CH₃OH using BzOOH (~0.8 equiv) as an oxidant.

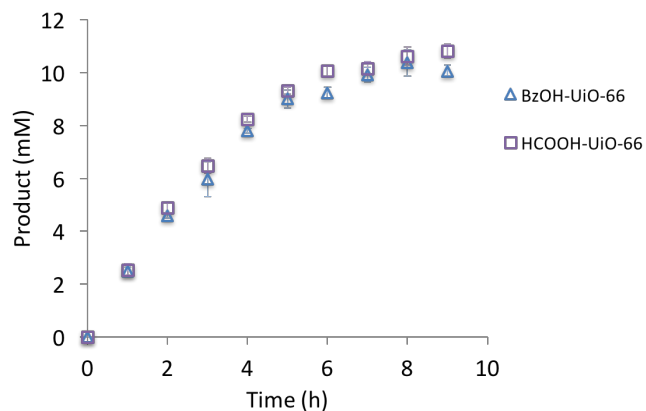


Figure 3.17 Product-formation profiles (9 h, product vs time) in the catalytic oxidation of methyl phenyl sulfide in CH_3OH using H_2O_2 (1 equiv) as the oxidant. For convenience, product = sulfoxide + sulfone.

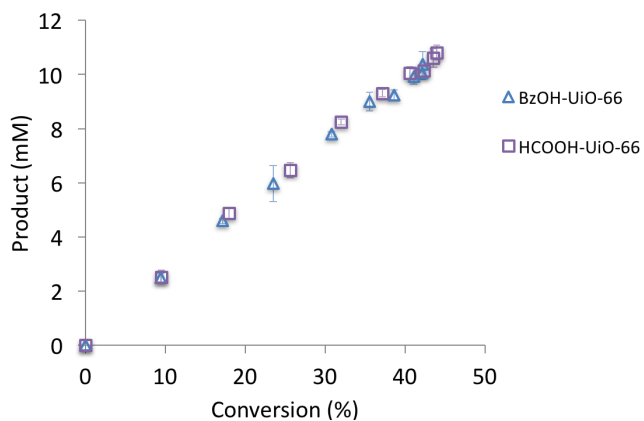


Figure 3.18 Product-formation profiles (9 h, product vs conversion) in the catalytic oxidation of methyl phenyl sulfide in CH_3OH using H_2O_2 (1 equiv) as the oxidant. For convenience, product = sulfoxide + sulfone.

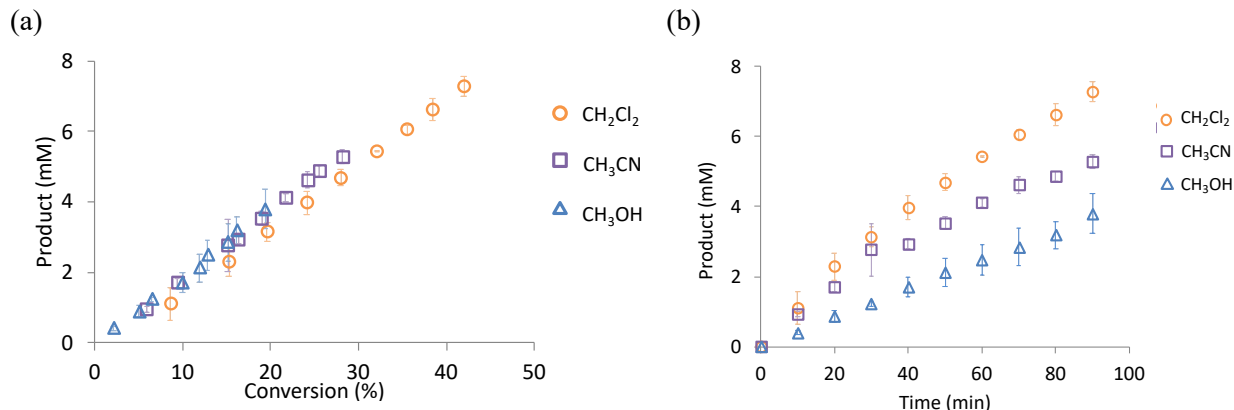


Figure 3.19 Selectivity profiles (9 h) in the catalytic oxidation of methyl phenyl sulfide in CH₃OH using H₂O₂ (1 equiv) as the oxidant.

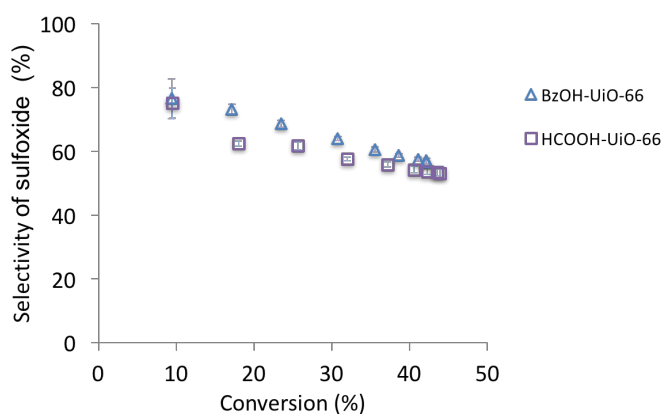


Figure 3.20 Product-formation profiles (product vs conversion (a) and product vs time (b)) in the catalytic oxidation of methyl phenyl sulfide using H₂O₂ as the oxidant and **BzOH-UiO-66** as the catalyst in three different solvents. For convenience, product = sulfoxide + sulfone.

Figures 3.21-3.24 below show the recycling data for **BzOH-UiO-66** batch 2 and **decap-UiO-66** batch 2 in the catalytic oxidation of methyl phenyl sulfide in CH₃OH using H₂O₂ as the oxidant. In comparison to the respective data in Figure 3.1a, the product-formation profiles for these materials are slightly slower. However, the sulfide selectivity trends (cf. Figures 3.22 and 3.24 vs Figure 3.1b) are very similar. In addition, the difference in initial rate of sulfide oxidation

between **BzOH-UiO-66** batch 2 and **decap-UiO-66** batch 2 (6.5×10^{-7} and 10.0×10^{-7} M/s, respectively) follow the same trend as shown in Table 3.2, with the latter material approximately twice as fast as the former. Together with the near-indistinguishable characterization data reported for both batches, these data accentuate a main point of our work in that subtle variations in MOF starting materials can lead to differences in catalysis results; however, a systematic comparison is best made with materials derived from the same source.

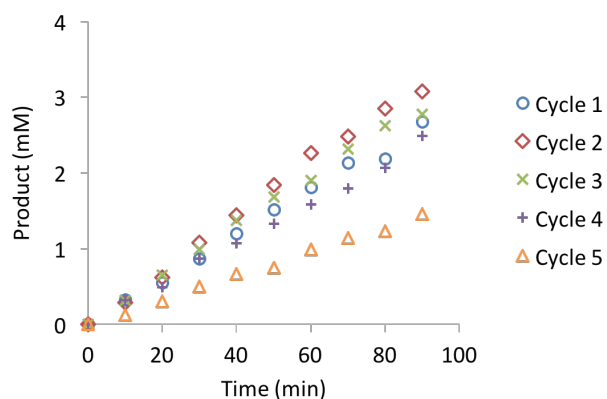


Figure 3.21 Product-formation profiles in the catalytic oxidation of methyl phenyl sulfide in CH_3OH using H_2O_2 (1 equiv) as the oxidant and **BzOH-UiO-66** batch 2 as the catalyst. Five cycles were carried out. For convenience, product = sulfoxide + sulfone.

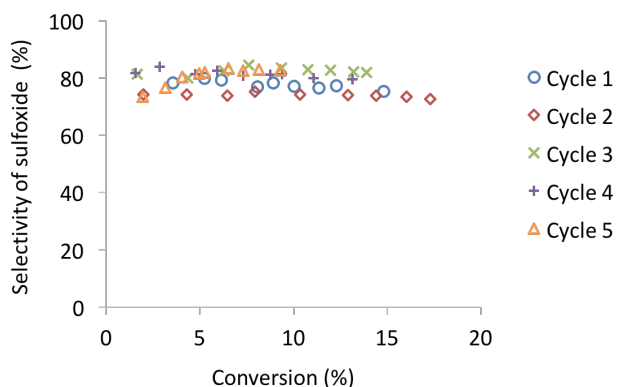


Figure 3.22 Selectivity profiles in the catalytic oxidation of methyl phenyl sulfide in CH_3OH using H_2O_2 (1 equiv) as the oxidant and **BzOH-UiO-66** batch 2 as the catalyst. Five cycles were carried out.

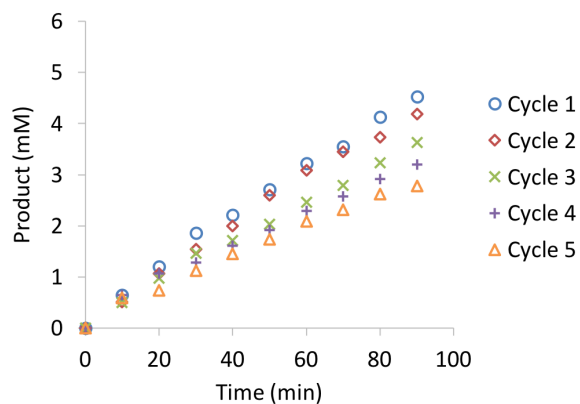


Figure 3.23 Product-formation profiles in the catalytic oxidation of methyl phenyl sulfide in CH_3OH using H_2O_2 (1 equiv) as the oxidant and **decap-UiO-66** as the catalyst. The materials used in this study came from **BzOH-UiO-66** batch 2. Five cycles were carried out. For convenience, product = sulfoxide + sulfone.

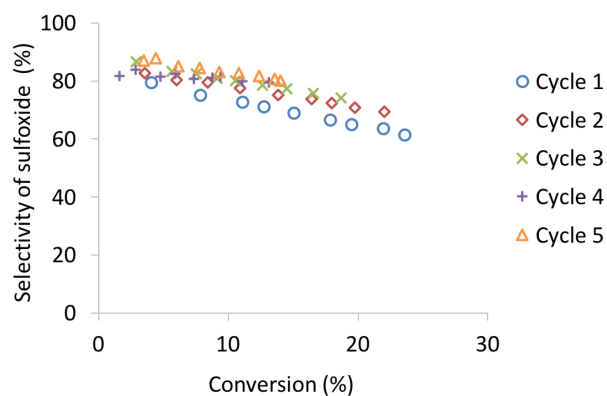


Figure 3.24 Selectivity profiles in the catalytic oxidation of methyl phenyl sulfide in CH_3OH using H_2O_2 (1 equiv) as the oxidant and **decap-UiO-66** as the catalyst. The materials used in this study came from **BzOH-UiO-66** batch 2. Five cycles were carried out.

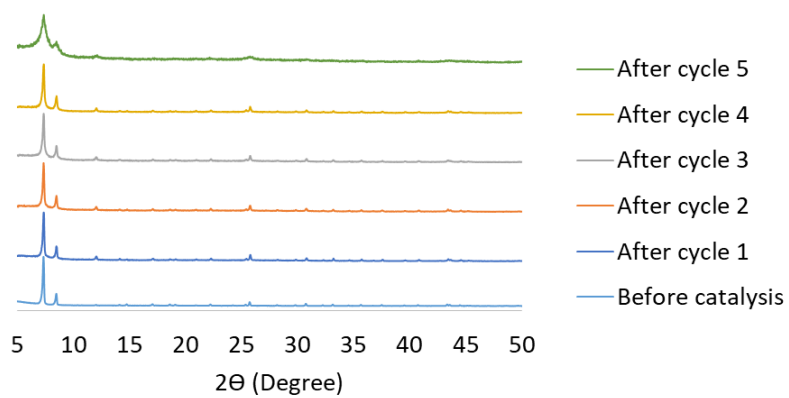


Figure 3.25 PXRD patterns for **BzOH-UiO-66** batch 2 before and after catalysis.

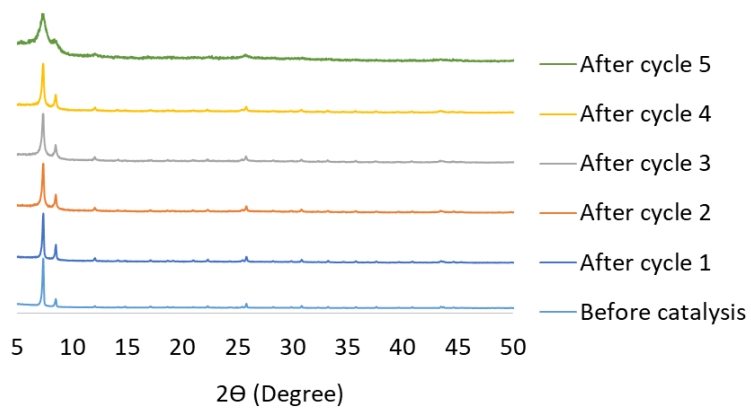


Figure 3.26 PXRD patterns for **decap-UiO-66** batch 2 before and after catalysis.

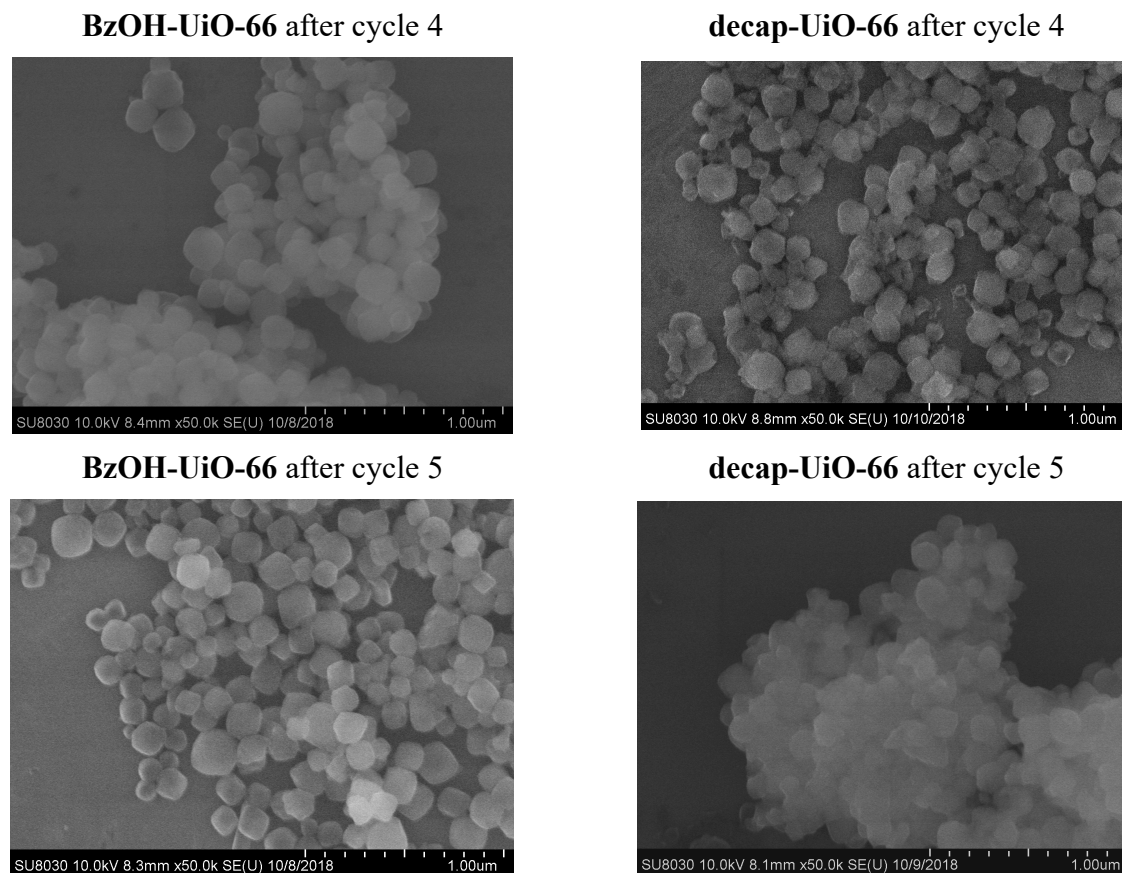


Figure 3.27 SEM images of UiO-66 MOFs after cycles 4 (top panels) and 5 (bottom panels) of catalysis. While there is no visible changes in morphology, the broadening of the PXRD profiles shown in Figures 3.25-3.26 suggest some loss of crystallinity.

Table 3.6 Amount of Zr leached out into solution after each cycle.

Cycle	Amount of Zr in supernatant (mg) ^a	
	decap-UiO-66	BzOH-UiO-66
1	0.010	0.156
2	0.002	0.038
3	0.008	0.013
4	0.013	0.006
5	0.013	0.004

^aThe values reported are calculated from ICP-OES analyses against a calibration curve and are based only one run for each sample. Thus, the number of significant figures should not be taken literally. The total amount of leached Zr after the 5th cycle is less than 1 wt % of the initial catalyst amount.

3.9.8 Additional computational data

Table 3.7 Relative enthalpy values (ΔH , kJ/mol) for the various species in the oxidation of methyl phenyl sulfide without catalyst (corresponding to the “Uncatalyzed” profile in Figure 3.2).

Reactant	TS for the 1 st oxidation	Intermediate	TS for the 2 nd oxidation	Product
0.0	62.7	-214.3	-131.5	-518.8

Table 3.8 Relative enthalpy values (ΔH , kJ/mol) for the various species in the oxidation of methyl phenyl sulfide by the Zr₆-oxo-hydroxo cluster node of UiO-66 (corresponding to the “Node of UiO-66” profile in Figure 3.2).

Reactant	TS for the catalyst activation	Active catalyst	TS for the 1 st oxidation	Intermediate	TS for the catalyst activation	Active catalyst	TS for the 2 nd oxidation	Product
0.0	25.6	-4.0	7.8	-214.3	-188.3	-217.9	-165.8	-518.8

Table 3.9 Binding enthalpies of three different solvents and substrates to the Zr₆-oxo-hydroxo cluster node of UiO-66.

Solvent/substrate	ΔH_{bind} (kJ/mol)
H ₂ O	-88.0
CH ₃ OH	-88.0
CH ₃ CN	-47.5
CH ₂ Cl ₂	-32.8
Methyl phenyl sulfide	No binding
Methyl phenyl sulfoxide	-87.6
Methyl phenyl sulfone	-71.7

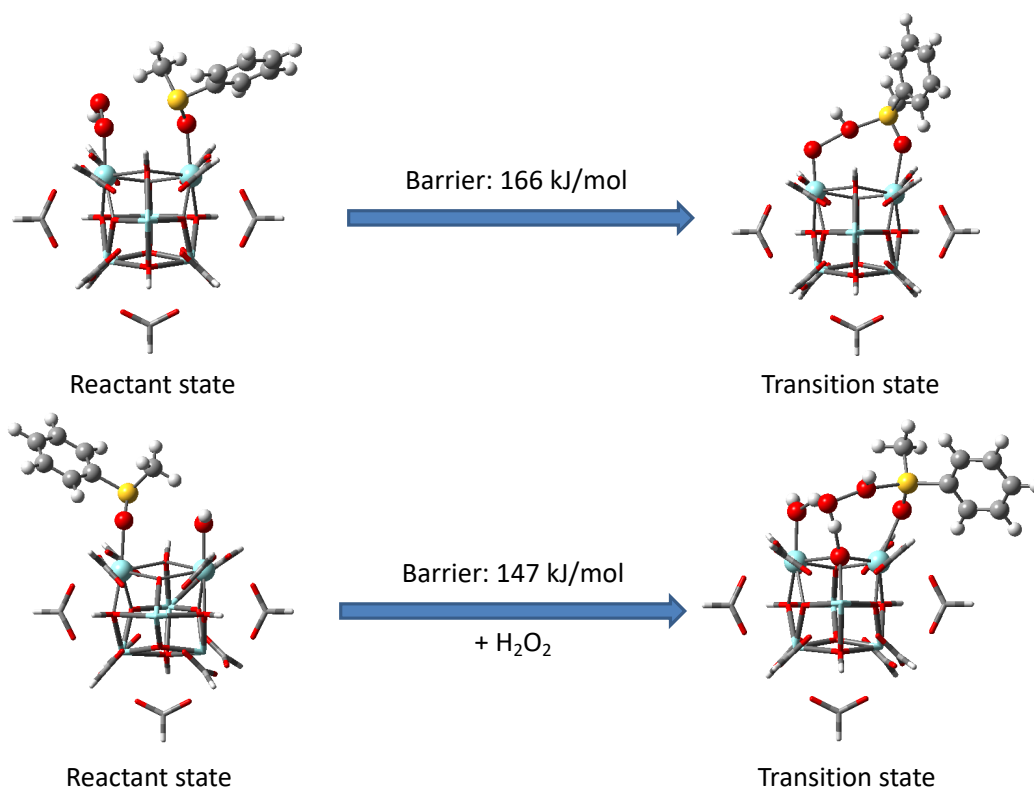


Figure 3.28 Two possible Langmuir-Hinshelwood-type reaction mechanisms of sulfoxide oxidation obtained from DFT calculations.

As discussed in footnote 158, we searched for a $\text{Zr}(\eta^2\text{-O}_2)$ intermediate that was proposed to form in the presence of H_2O_2 .¹¹⁰ However, such a species does not appear to be a stable intermediate: in our DFT calculations, the 3-member $\text{Zr}(\eta^2\text{-O}_2)$ peroxy ring breaks during the optimization and forms a $\text{Zr-}\mu_1\text{-OOH}$ species (Figure 3.29) that is 58 kJ/mol higher in energy than the $\text{Zr-}\mu_1\text{-OOH}$ species shown in Figure 3.2. Thus, we proceeded with the lower-energy structure.

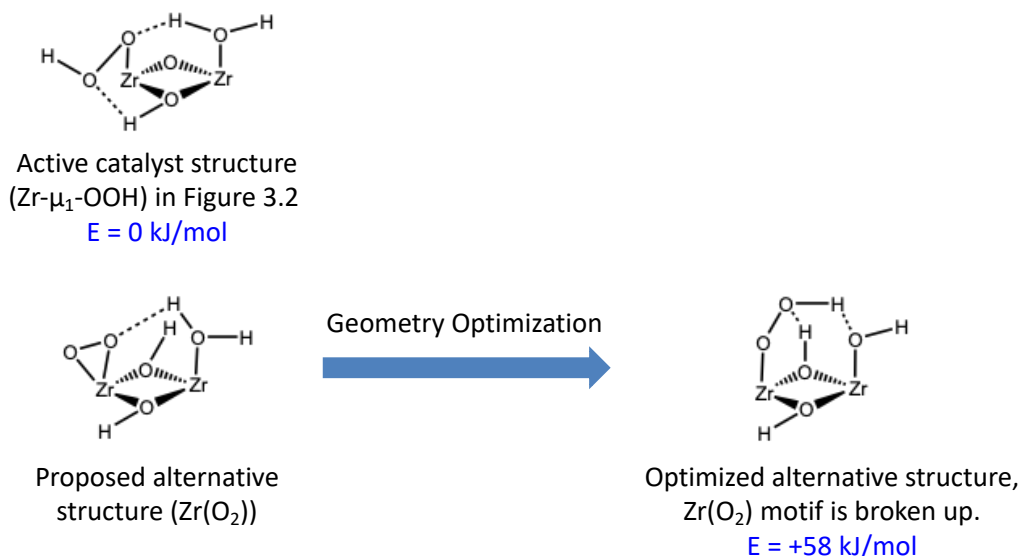
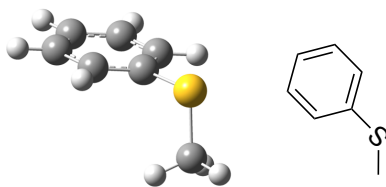


Figure 3.29 Top: A structural drawing of the Zr- μ_1 -OOH species shown in Figure 3.2. Bottom: Outcome of an attempt to carry out geometry optimization of the 3-member Zr(η^2 -O₂) peroxy ring proposed by Faccioli *et al.*¹¹⁰

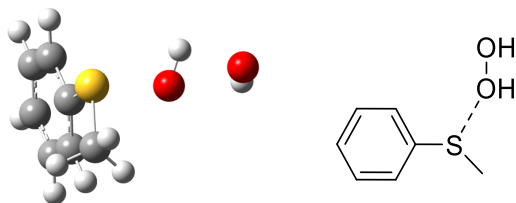
3.9.9 Optimized structures and Cartesian coordinates of key species

For the figures in this section, white, grey, red, yellow, and cyan spheres represent H, C, O, S, and Zr atoms, respectively. Active site and the reagent atoms are shown in the “ball and stick” format while the other atoms are shown in the “tube” format.



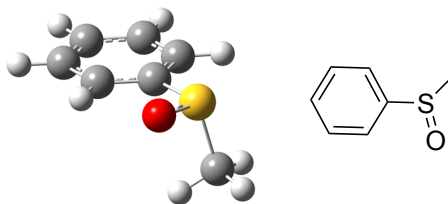
C₆H₅SCH₃

C	1.94711600	-1.21104700	0.10842200	H	0.03071400	2.15643300	-0.25000000
C	0.57149400	-1.21297500	-0.14450600	H	2.48205900	2.15956800	0.20292800
C	-0.12490900	0.00000000	-0.26649900	H	3.71191800	0.00000000	0.42998000
C	0.57149400	1.21297500	-0.14450700	S	-1.88429300	0.00000000	-0.63507100
C	1.94711600	1.21104700	0.10842200	C	-2.59860600	0.00000100	1.05156500
C	2.63649800	0.00000000	0.23510000	H	-2.29945600	0.90065800	1.60643500
H	2.48205900	-2.15956800	0.20292900	H	-3.69107900	-0.00000100	0.92444900
H	0.03071400	-2.15643300	-0.24999900	H	-2.29945600	-0.90065600	1.60643600



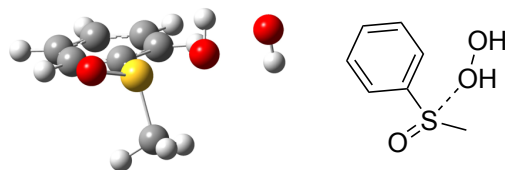
TS for the 1st oxidation $C_6H_5SCH_3 + H_2O_2$

O	-2.20964200	0.52240400	0.10461400	C	1.37328400	0.43524200	-1.21508600
O	-3.40602200	2.06200900	0.58911800	C	1.13521700	-0.55328500	0.99930600
H	-2.42712600	1.22438500	-0.54463100	C	2.63761500	0.91030400	-0.86452100
H	-2.70752000	2.42044000	1.15928000	H	0.97216000	0.62746300	-2.21330500
S	-0.99239000	-0.80529600	-0.81915200	C	2.40629700	-0.07880000	1.33358300
H	-0.77694700	-2.92893100	0.30684200	H	0.56356600	-1.11726300	1.73677000
C	-1.48831100	-2.09338700	0.34205700	C	3.15841800	0.65372200	0.40904800
H	-1.56994000	-1.67099400	1.35144100	H	3.22049800	1.47809900	-1.59350100
H	-2.47818500	-2.42419000	0.00274700	H	2.80863200	-0.28365400	2.32851800
C	0.61879200	-0.29680700	-0.28060900	H	4.15054000	1.02212700	0.67974000



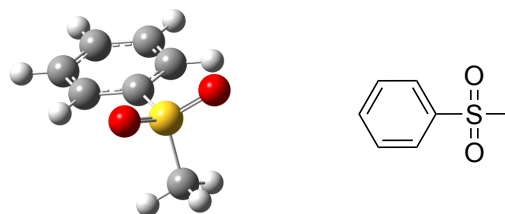
$C_6H_5S(O)CH_3$

C	-2.07130500	1.23746100	0.36331200	H	-2.93678000	-1.98457300	-0.37790800
C	-0.68690400	1.14877500	0.18225100	H	-3.95959100	0.18345000	0.30648000
C	-0.12782400	-0.07561500	-0.18396700	C	2.14220400	-0.95050300	1.10351800
C	-0.92238300	-1.20574300	-0.40371100	H	1.69997900	-1.95542700	1.15233300
C	-2.30465100	-1.10798000	-0.21602600	H	3.23920300	-1.01462600	1.09837000
C	-2.87812400	0.11099700	0.16746000	H	1.79317700	-0.31577900	1.92965800
H	-2.52128600	2.19007300	0.65432700	S	1.67492600	-0.13897500	-0.47286300
H	-0.02802000	2.01043200	0.31339500	O	2.18541800	1.28983000	-0.35872900
H	-0.47491600	-2.15293900	-0.71802900				



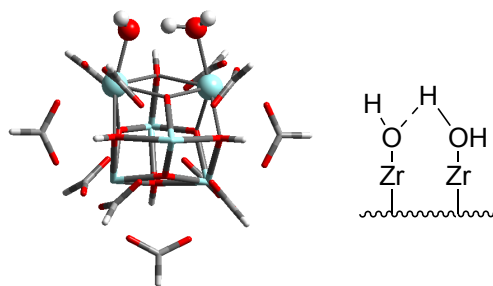
TS for the 2nd oxidation $\text{C}_6\text{H}_5\text{S}(\text{O})\text{CH}_3 + \text{H}_2\text{O}_2$

O	-2.07676200	0.71012400	-0.33444600	C	3.17386000	0.78717200	0.10259500
H	-1.77230100	1.17598700	-1.13503600	H	2.24259100	2.72464000	0.35728600
O	-0.96367300	-2.26269100	-0.84774100	H	3.82640400	-1.25618600	-0.19998300
S	-1.06000300	-0.92420300	-0.18298300	H	4.19002300	1.18334900	0.16660600
C	0.59605800	-0.21420800	-0.05386600	C	-1.58239100	-1.18498800	1.52574900
C	0.77382000	1.16377100	0.13179800	H	-1.50505600	-0.23837500	2.07223700
C	1.67523800	-1.09424400	-0.18862200	H	-2.62367800	-1.53120200	1.47824500
C	2.08044300	1.65389000	0.21368500	H	-0.92933200	-1.95966800	1.94747600
H	-0.08422200	1.83953200	0.18107600	O	-2.41460600	2.69752000	-0.31781300
C	2.97209700	-0.58241700	-0.10277300	H	-2.37428700	2.67262800	0.64994000
H	1.49548100	-2.15693600	-0.36151100				



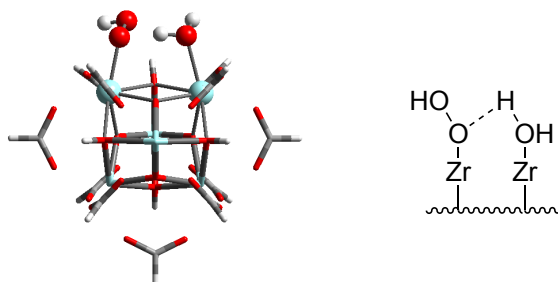
$\text{C}_6\text{H}_5\text{S}(\text{O})_2\text{CH}_3$

C	-2.40436500	1.21464600	0.04047700	H	-2.95055700	-2.16051600	0.06065400
C	-1.00877900	1.22180800	-0.03144800	H	-4.19027900	-0.00004400	0.13234200
C	-0.32896500	0.00000900	-0.05824100	C	2.04685600	-0.00049400	1.53933300
C	-1.00875900	-1.22179700	-0.03153100	H	1.68753900	-0.90790700	2.04064700
C	-2.40434000	-1.21467600	0.04038600	H	3.14386800	-0.00113500	1.47102500
C	-3.09896600	-0.00002400	0.07837200	H	1.68860900	0.90728600	2.04075400
H	-2.95058900	2.16047900	0.06085900	S	1.46803200	0.00004800	-0.16461400
H	-0.45096100	2.15879300	-0.07731500	O	1.88930100	1.27378500	-0.77967700
H	-0.45085000	-2.15873200	-0.07743100	O	1.88927600	-1.27326200	-0.78054800

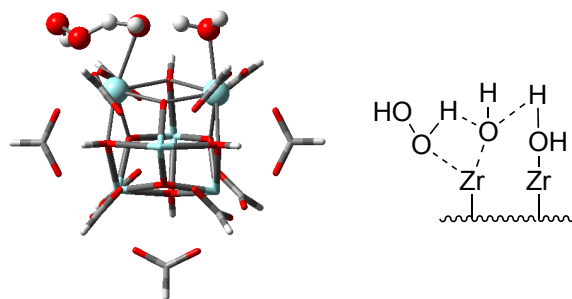


Initial state ($[\text{Zr}_6(\mu_3\text{-O})_4(\mu_3\text{-OH})_4(\mu_1\text{-OH})(\mu_1\text{-OH}_2)(\text{HCOO})_{11}]$)

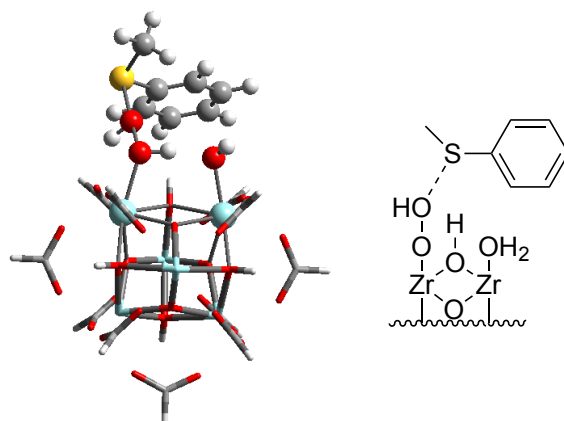
C	1.98712600	3.04378900	-2.68945700	O	-1.35713700	-3.76016900	-1.01202600
C	4.48626600	0.24217400	-0.48905700	O	-1.44607300	3.65527200	1.15762500
C	2.05735300	-3.30982900	-2.32892600	O	-1.69721900	3.41489300	-1.54753700
C	2.40190600	3.43748900	1.61001700	O	1.43758700	3.73595500	0.85909200
C	0.44787900	0.28246900	4.44592900	O	-0.72698900	0.24219800	3.99661100
C	-2.27802500	-3.48779800	-1.82822000	O	-3.82166200	0.05014900	1.48034900
C	-4.50016500	-0.05706600	0.42550300	O	-2.15525300	-1.82112800	2.94068300
C	2.54395900	-2.89138800	2.32664200	O	-2.39811000	2.12639800	2.51562000
C	-2.69562200	2.93196000	-2.15191100	Zr	1.60212500	-0.10311600	-1.97158900
C	-1.80164100	-3.01885700	2.77277900	Zr	-1.98771300	-0.23187200	-1.65505600
C	-2.22479300	3.29629500	2.08070600	Zr	-0.10773300	2.51140800	-0.25786100
O	-1.72153900	-0.39090600	-3.75359800	Zr	1.96476100	0.21873300	1.56857000
O	1.16821000	3.48736600	-1.84141900	Zr	0.10533000	-2.51158400	0.17410200
O	2.26256800	1.83628900	-2.91727100	Zr	-1.59582000	0.10781700	1.91037200
O	2.28690400	-2.12952800	-2.72081800	H	-0.37372600	1.67101400	-3.02218100
O	3.82419600	0.07255200	-1.54541900	H	2.85461700	-1.88483500	-0.15421700
O	2.05072700	-1.34865600	-0.12172900	H	0.20383500	2.21195100	2.56729700
O	-0.26410600	1.19570400	-2.18588900	H	-2.68091900	-2.06181000	0.43035000
O	1.42374300	1.08070000	-0.27120700	O	0.79396800	-0.36367300	-4.10932200
O	-0.10152800	-1.17901900	-1.41299800	H	-0.24418900	-0.40444000	-4.07642400
O	4.03347800	0.28526300	0.68546700	H	5.58467200	0.35733600	-0.60215600
O	1.37876200	-3.66014800	-1.32993100	H	3.13187900	-3.59679900	2.95099800
O	0.14787300	1.58659200	1.83226200	H	0.55793100	0.29137400	5.55068300
O	2.82817900	-1.66862900	2.44420100	H	-2.81678000	4.09844900	2.56938800
O	2.72975100	2.28459300	2.00254000	H	-5.60423000	-0.02056000	0.54044800
O	1.51390600	0.32300200	3.77509000	H	-2.19524900	-3.75826300	3.50165200
O	0.19795800	-0.90603300	1.51501000	H	2.51207800	-4.12320400	-2.93235600
O	-1.92680900	-1.47455400	0.28622800	H	2.51783000	3.79848500	-3.30724600
O	-2.97544000	1.71825200	-2.29514600	H	-2.79546300	-4.35244800	-2.29487900
O	-2.67942500	-2.34286500	-2.16523100	H	3.02844000	4.27884200	1.97371900
O	-4.06011800	-0.21064900	-0.74288600	H	-3.39293200	3.66527900	-2.61006500
O	-1.48988600	0.99265900	0.02175900	H	-2.14927400	-1.17185000	-4.13583300
O	-1.05840400	-3.46943800	1.86106000	H	1.09910100	-1.19041000	-4.51426500
O	1.67425300	-3.39732200	1.57127200				

Active catalyst ($[\text{Zr}_6(\mu_3\text{-O})_4(\mu_3\text{-OH})_4(\mu_1\text{-OOH})(\mu_1\text{-OH}_2)(\text{HCOO})_{11}]$)

C	-2.13731400	3.86465800	0.72967200	O	0.18271500	-2.11385400	-3.51560400
C	2.06687100	3.99858800	-0.43334100	O	-1.48961500	-0.32735900	3.78310000
C	1.04524500	1.41515500	-4.17157100	O	-3.44970200	0.47604700	2.12223300
C	1.02947400	2.61404100	3.52896700	O	-0.16620500	2.23014700	3.43124400
C	3.35972500	-1.34518200	2.73488900	O	2.41252100	-2.15189500	2.54508100
C	-1.03862800	-2.37018700	-3.68129700	O	-0.98614800	-3.77934000	1.23174900
C	-2.07203900	-3.94081500	0.61318100	O	1.78755800	-3.69460400	0.39423500
C	4.37751400	0.02319000	-1.27533000	O	-0.36638000	-2.24769900	3.39812900
C	-4.22818400	-0.28275400	1.48745400	Zr	-0.39501400	2.08089300	-1.33438700
C	2.36789800	-3.78994700	-0.72005000	Zr	-2.09870200	-1.06132600	-0.89531100
C	-1.09865000	-1.48591700	4.08658000	Zr	-1.27484600	0.95518900	1.93283600
O	-3.50697400	-0.02992600	-2.20445200	Zr	2.16665800	1.04218900	0.90055900
O	-2.11503700	3.03913300	1.67870000	Zr	1.34411300	-0.95250200	-1.96186300
O	-1.63331500	3.72008400	-0.41938300	Zr	0.50537100	-2.08780400	1.32816300
O	0.41894900	2.22712700	-3.44006000	H	-3.04056700	1.44412600	-0.36996800
O	1.01268800	3.82464700	-1.10083500	H	2.35681200	1.70761900	-1.85556200
O	1.70669500	1.22285800	-1.32917000	H	1.03895900	-0.06780900	3.25819000
O	-2.14434900	1.09511500	-0.19511400	H	-0.21631300	-3.18890500	-1.19933700
O	0.18468000	1.68240500	0.61544400	O	-2.21635400	2.17593000	-2.77406400
O	-0.49489400	0.04679300	-1.76356300	H	-2.90033500	2.83668500	-2.58350800
O	2.65596100	3.14672400	0.28530500	H	-2.69089700	1.28529700	-2.76110100
O	1.48063800	0.27837500	-3.84296400	H	2.53056700	5.00534700	-0.48935100
O	0.75904300	-0.04816600	2.33292900	H	5.44923400	-0.02483700	-1.56148300
O	4.10408600	0.67275600	-0.23078100	H	4.19808100	-1.70234600	3.36876200
O	1.98981700	2.29144100	2.78241100	H	-1.42781700	-1.87661700	5.07229400
O	3.45536000	-0.16856300	2.28940000	H	-2.61168000	-4.89281400	0.79992700
O	1.64168500	-0.81781500	0.10903800	H	2.98916400	-4.69614900	-0.87901500
O	-0.14964300	-2.28603900	-0.86015800	H	1.24385200	1.73823100	-5.21486300
O	-3.97825300	-0.89440100	0.41525500	H	-2.65958600	4.82564300	0.91934600
O	-1.98277100	-2.11036200	-2.88832700	H	-1.31240900	-2.88851700	-4.62431100
O	-2.60665500	-3.14195300	-0.20180300	H	1.26181700	3.30276300	4.36827500
O	-1.17374800	-0.90056100	0.98694800	H	-5.24574000	-0.41441600	1.91167500
O	2.31234000	-2.97210600	-1.67751600	O	-4.44911400	0.88275800	-1.58118200
O	3.56693400	-0.56932200	-2.03817400	H	-4.99792400	0.26918000	-1.05922300

Catalyst activation TS ($[\text{Zr}_6(\mu_3\text{-O})_4(\mu_3\text{-OH})_4(\mu_1\text{-OH})(\mu_1\text{-OH}_2)(\text{HCOO})_{11}] + \text{H}_2\text{O}_2$)

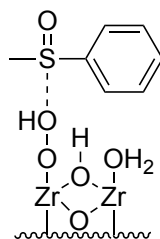
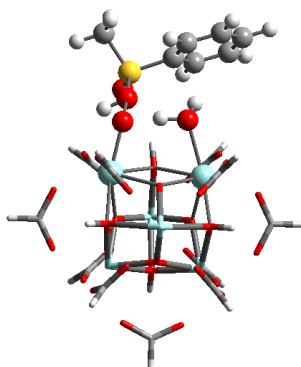
C	-3.29075600	-2.77986300	-1.12473000	O	-0.07034200	-2.59347500	-3.15032100
C	-3.22095400	-0.92316900	2.90305500	O	-0.40516500	-4.05136800	0.49218700
C	-2.55770900	3.50259000	1.07582000	O	3.55641600	-1.10899800	1.96968200
C	-0.49851300	-4.11261200	1.74727300	O	3.80453000	0.23680400	-1.80207300
C	3.07620900	-1.46752400	3.07780700	O	3.89648200	1.36606900	0.87383400
C	0.54145500	4.12778500	-1.78032800	O	3.49489500	-2.22928000	-0.72167000
C	3.48531100	0.70607900	-2.92562500	Zr	-2.47147600	0.32995400	-0.02943100
C	0.39338400	1.72081800	4.13492600	Zr	0.30835500	0.92371800	-2.33508000
C	0.17679500	-1.81342800	-4.11026500	Zr	-0.14232700	-2.32410300	-0.93805100
C	3.62555700	2.50453200	1.34416100	Zr	-0.05141200	-0.94045900	2.33060700
C	2.98120700	-3.26811700	-1.22166600	Zr	0.40065400	2.31638600	0.92813700
O	-1.40067800	1.59778700	-3.73121800	Zr	2.65040400	-0.31346600	0.05702000
O	-2.13104700	-3.19587500	-1.37091900	H	-1.97942000	-0.80093300	-2.65740700
O	-3.59366100	-1.64198700	-0.68535300	H	-1.76001300	1.34250400	2.51824200
O	-3.11535500	2.47661100	0.61755300	H	1.73944500	-2.78898300	1.13266000
O	-3.55951400	-0.39396900	1.81456100	H	2.41885300	2.30680800	-1.05764800
O	-1.24824200	0.95712800	1.79340400	O	-3.30471100	1.69401600	-2.04932300
O	-1.43348600	-0.52332000	-1.90702300	H	-2.26006700	1.62578000	-3.18751300
O	-1.10706300	-1.20987100	0.53517300	H	-4.04130000	-1.19972900	3.59808600
O	-0.74582400	1.48206500	-0.61402400	H	0.53136500	2.13794200	5.15450000
O	-2.04800700	-1.16616200	3.29614800	H	3.80509100	-1.77056400	3.85856100
O	-1.32869300	3.65247800	1.32348600	H	3.68917700	-4.04906700	-1.56974900
O	1.28889900	-1.99691500	0.80970200	H	4.30406300	0.83233800	-3.66416000
O	0.16656200	0.48327700	4.05984300	H	4.48229700	3.09833900	1.72542800
O	-0.38109600	-3.15869600	2.56084800	H	-3.21002500	4.37505100	1.29267500
O	1.85848500	-1.52767700	3.39031300	H	-4.12617100	-3.48302500	-1.32382700
O	1.20025400	0.43896000	1.36671000	H	0.57600900	5.14538800	-2.22234000
O	1.77497000	1.64925800	-0.76125700	H	-0.69784500	-5.11443400	2.18172600
O	0.31789000	-0.56827700	-4.04591300	H	0.26928600	-2.27891800	-5.11383900
O	0.45697400	3.16606700	-2.59576000	H	-1.25963700	2.49987600	-4.06128700
O	2.33282800	1.05664000	-3.29608300	H	-3.28129200	2.61499600	-1.74460700
O	1.11052700	-0.70380600	-1.33194100	O	-4.68119400	0.73064900	-0.47364100
O	2.48925300	3.04040500	1.41659000	H	-4.22550300	1.25209400	-1.53058100
O	0.46905700	2.53375600	3.17779000	O	-5.74175200	-0.22640000	-0.56960000
O	0.59631500	4.05206000	-0.52728900	H	-5.21278800	-1.05375500	-0.62646400
O	1.75632000	-3.51238600	-1.35855600				



TS for the 1st oxidation ($[\text{Zr}_6(\mu_3\text{-O})_4(\mu_3\text{-OH})_4(\mu_1\text{-OOH})(\mu_1\text{-OH}_2)(\text{HCOO})_{11}] + \text{C}_6\text{H}_5\text{SCH}_3$)

C	2.70214900	2.75830700	0.83131200	O	-1.64705200	-3.71511300	1.53704300
C	-0.90218400	3.11037900	3.28624300	O	0.22341200	1.78734300	-3.56377200
C	-0.82545100	-1.43906100	4.30613000	O	2.43525600	0.68770100	-2.48849700
C	-0.79868300	4.42122500	-0.92206400	O	0.12058300	3.74323200	-1.45195100
C	-4.52020100	1.76434300	-1.77801200	O	-4.00439200	0.79930000	-2.40291000
C	-0.68411700	-4.38660500	1.07738200	O	-1.52105500	-2.16867700	-3.40314600
C	-0.55358200	-2.97460300	-3.37317600	O	-3.94847200	-1.86368200	-1.80932300
C	-4.59666300	0.46320400	2.35399100	O	-1.57350100	0.49281900	-3.99398700
C	2.91780500	-0.46459000	-2.58654500	Zr	0.63668900	0.49652000	2.08421200
C	-4.45093200	-2.47591800	-0.82860300	Zr	0.73727800	-1.94101900	-0.57113100
C	-0.63840900	1.27131900	-4.32296400	Zr	0.67562300	1.55516400	-1.35511200
O	2.47585500	-2.47458900	0.71127800	Zr	-2.28848900	1.93944700	0.58388800
O	2.35363500	2.64552400	-0.37984100	Zr	-2.23249400	-1.54846800	1.36871400
O	2.23024500	2.14312200	1.81438600	Zr	-2.17595800	-0.48414400	-2.04355000
O	0.06522200	-0.59818100	4.01802600	H	2.65064100	0.02356300	0.16971200
O	0.00668200	2.24561900	3.38509600	H	-2.02062800	0.67223200	3.11461000
O	-1.66086800	0.48175300	2.23810400	H	-1.92649400	2.33636400	-2.21764100
O	1.68544800	0.05370300	0.08871300	H	-1.83276400	-3.09805800	-0.98725600
O	-0.22966600	1.64539400	0.50910000	O	2.33998700	-0.61663000	2.60211700
O	-0.17245400	-1.25101700	1.17689900	H	2.26742500	-1.01340800	3.48308200
O	-1.80864700	3.16580000	2.41069100	H	2.51078000	-1.84536200	1.49977300
O	-1.73205800	-1.87727700	3.54795800	H	-0.91536900	3.90798500	4.05895900
O	-1.60168700	1.67854900	-1.58848500	H	-5.56968700	0.56992800	2.87872400
O	-4.11729400	1.50896600	1.84150900	H	-5.47326900	2.16366200	-2.18475400
O	-1.74548300	3.99039300	-0.21202100	H	-0.57315400	1.53722600	-5.39935200
O	-4.06853000	2.33173600	-0.74746500	H	-0.46206600	-3.67113400	-4.23306500
O	-2.57920600	-0.03980100	-0.04132500	H	-5.38745300	-3.03932600	-1.02555800
O	-1.53488200	-2.22229900	-0.70702300	H	-0.81758400	-1.83534100	5.34389100
O	2.53763100	-1.50230400	-1.97012200	H	3.52192900	3.47997100	1.03477100
O	0.21736400	-3.98092300	0.30001200	H	-0.63332600	-5.45203500	1.38689700
O	0.31793000	-3.08284800	-2.46874600	H	-0.77676500	5.51600500	-1.10766400
O	-0.12286700	-0.35839700	-1.64213100	H	3.77954000	-0.58918600	-3.27558600
O	-4.00217300	-2.52579600	0.34697400	O	4.14078600	-2.14510800	0.18144700
O	-4.08711300	-0.68833800	2.34379900	H	3.83963000	-2.09685700	-0.75314100

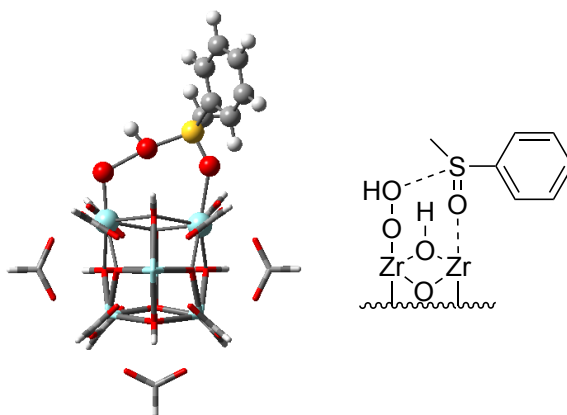
S	6.30320800	-1.82581100	-0.36272200	C	6.75240500	2.08888300	-1.16974600
C	6.74090800	-2.58148600	1.22112800	H	6.55682900	0.23090000	-2.25734600
H	6.64586900	-3.66370400	1.06341100	C	6.75903100	1.91105900	1.24444400
H	7.77723700	-2.33142700	1.48465800	H	6.53900500	-0.06753000	2.06721400
H	6.03953000	-2.26494700	2.00341400	C	6.83215100	2.69617900	0.08899000
C	6.52373300	-0.08030400	-0.10972600	H	6.81564000	2.69323600	-2.07771200
C	6.60272800	0.70506500	-1.27384300	H	6.82373500	2.37828200	2.23003300
C	6.60032900	0.52486800	1.15416000	H	6.95629500	3.77855400	0.16874900



TS for the 2nd oxidation ($[\text{Zr}_6(\mu_3\text{-O})_4(\mu_3\text{-OH})_4(\mu_1\text{-OOH})(\mu_1\text{-OH}_2)(\text{HCOO})_{11}] + \text{C}_6\text{H}_5\text{S}(\text{O})\text{CH}_3$)

C	-2.87487300	1.65258300	1.93071900	O	2.62563300	0.19794000	-0.09482100
C	0.37205900	4.38684100	1.02597900	O	1.73783600	-1.60914400	-1.60057900
C	0.37265800	2.96482700	-3.40792500	O	-2.06378900	-2.97506400	-0.03906000
C	0.86434500	1.53472300	4.24698200	O	-0.09420100	-1.85737400	-3.57679700
C	4.74542600	-0.14424300	2.24501300	O	0.18435100	-3.82883100	-1.38456100
C	0.71218200	-1.27789400	-4.34458900	O	0.42303500	-1.65091300	0.56959400
C	1.17184900	-4.41076800	-0.86887400	O	4.05901800	-0.56084400	-2.49140500
C	4.30161600	2.75316500	-0.96009200	O	3.82898600	2.08456900	-1.91515600
C	-2.38222000	-2.96689800	1.18023100	O	1.59053000	-0.42710200	-4.02836400
C	4.65178500	-1.48286300	-1.87100400	O	0.29557300	-2.19551300	3.42905500
C	1.25565800	-3.00315200	3.31975200	O	-2.00466000	-2.14494900	2.05539900
O	-2.35777800	-1.21198700	-2.23183700	O	0.03150600	0.63273900	3.97310100
O	-2.29158900	0.71935700	2.53853800	O	4.32909100	-1.22617500	1.75625800
O	-2.55458400	2.15793900	0.81912600	O	2.09935400	-3.88841900	-0.18948000
O	-0.48536600	3.01900600	-2.48778400	O	4.26072000	-2.07007700	-0.82757600
O	-0.51494500	3.89260600	0.27946000	O	2.14019400	-3.01741100	2.42207800
O	1.41305800	2.29132300	-0.75677800	Zr	-0.81942600	1.82825500	-0.57860400
O	-1.58517800	-0.23187700	0.12259100	Zr	-0.58310700	-1.67319500	-1.33931400
O	0.18167300	1.24196700	1.15556900	Zr	-0.45432000	-0.53018800	2.07632700
O	0.10927100	0.32185500	-1.66614200	Zr	2.22036300	1.70348900	1.29897900
O	1.40970800	3.81515800	1.45083500	Zr	2.13978500	0.57739900	-2.09274000
O	1.38986900	2.22171700	-3.45829800	Zr	2.49007000	-1.79978000	0.54790400
O	1.81912700	-0.35090600	2.20809700	H	-2.54541100	-0.37114800	0.05122500
O	3.87244600	2.79586700	0.22581700	H	1.63443300	3.18249100	-1.05811700
O	1.73915800	2.02235200	3.47940200	H	2.20408300	-0.50462700	3.08111100
O	4.15753600	0.96946600	2.23473100	H	2.10026600	-2.24899000	-2.22742200

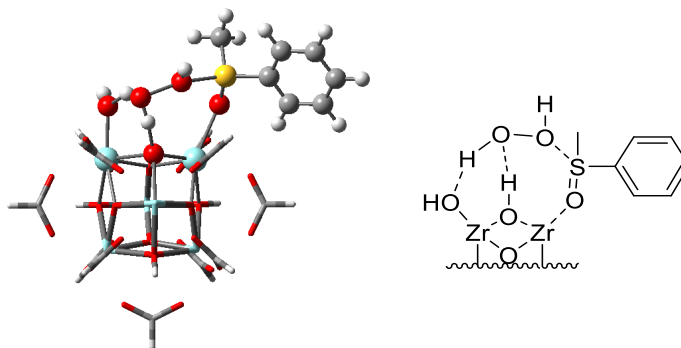
O	-2.58911600	1.27352600	-1.94529300	C	-6.87070500	-2.44392000	-0.89420900
H	-3.47725900	1.44187300	-1.59669700	H	-6.51868700	-3.48364200	-0.86400000
H	-2.54052500	0.23853800	-2.16876600	H	-7.83871400	-2.33304400	-0.38716700
H	0.22487300	5.44296700	1.33637900	H	-6.90125300	-2.06907900	-1.92519500
H	5.18949300	3.38148300	-1.18443600	C	-6.26091500	0.21199800	-0.07234500
H	5.73583000	-0.17581600	2.74752900	C	-6.65416600	0.83064600	1.11713900
H	1.33769000	-3.78389500	4.10568000	C	-6.26783900	0.88394300	-1.30212100
H	1.24534900	-5.50710700	-1.03387600	C	-7.08319000	2.16036200	1.06806900
H	5.62157500	-1.81999300	-2.29495300	H	-6.62439400	0.27571400	2.05634900
H	0.22261900	3.65444500	-4.26574400	C	-6.70122300	2.21201000	-1.33051800
H	-3.77590500	2.07744700	2.42113200	H	-5.95152600	0.38735600	-2.22187300
H	0.65612800	-1.54312100	-5.42245300	C	-7.10539200	2.84811500	-0.14959300
H	0.83391600	1.94267800	5.27961600	H	-7.39980400	2.65839500	1.98714500
H	-3.08857400	-3.75435200	1.51837100	H	-6.72024600	2.75158800	-2.27981000
O	-3.92297100	-1.29730800	-1.14293100	H	-7.43910500	3.88771900	-0.18059500
H	-3.56129600	-2.19085400	-0.95284500	O	-5.64861400	-1.92077700	1.46523600
S	-5.65746800	-1.47342400	0.03734200				



Alternative TS 1 for the 2nd oxidation ($[\text{Zr}_6(\mu_3\text{-O})_4(\mu_3\text{-OH})_4(\mu_1\text{-OOH})(\mu_1\text{-C}_6\text{H}_5\text{S}(\text{O})\text{CH}_3)(\text{HCOO})_{11}]$)

C	2.49481900	-3.16498900	-0.02442400	O	-0.31416700	0.37387100	-2.37617400
C	0.78473900	-1.92886300	-3.80060000	O	1.46510600	-0.54693400	1.09694300
C	1.57432400	2.55521000	-2.90532100	O	-0.06657200	-1.51928400	-0.75768700
C	-1.45942600	-4.38114500	-0.94775000	O	0.52851700	1.37290600	-0.19430000
C	-4.93161900	-1.30594500	-1.04228800	O	-0.44941800	-2.03132500	-3.57381300
C	-0.02103700	4.45183700	0.73033600	O	0.41669100	2.95210800	-2.61688100
C	-2.18764200	1.8005140	3.88940200	O	-2.35893500	-1.86491500	0.23292600
C	-2.71679900	1.12861900	-3.88448700	O	-2.63342400	-0.10673000	-3.64648300
C	0.83899300	-1.27138700	4.06389700	O	-1.85710200	-3.55028800	-1.81155300
C	-4.19998700	2.83881800	-0.18387900	O	-4.03030800	-1.63071500	-1.86657300
C	-2.99863500	-2.51020300	3.03059600	O	-2.27287500	0.40600000	-0.81937200
O	2.17005700	1.88176800	2.54401400	O	-1.64765100	2.01013100	0.99708600
O	1.57023200	-3.31761600	0.81971400	O	0.74856500	-0.04561600	3.87635000
O	2.66722100	-2.18580000	-0.78748900	O	0.32669100	3.70194000	1.66291900
O	2.13684500	1.49455600	-2.52042400	O	-0.97514800	2.01492000	3.63755600
O	1.63391400	-1.29914200	-3.11355300	O	-1.03359100	-0.35031700	1.74099600

O	-3.20684500	3.12567900	-0.90024100	H	-2.57253100	2.20114000	4.85229700
O	-2.24695100	2.06849500	-3.19300800	H	-5.08535500	3.50451100	-0.27457600
O	-0.56520700	4.11018300	-0.36545100	H	2.16821600	3.21053700	-3.57866100
O	-1.89684000	-2.98526200	2.64750300	H	3.24099100	-3.98681100	-0.08731300
O	0.64590900	-2.19307600	3.21116800	H	0.15189400	5.54379400	0.85627300
O	-0.94123400	-4.12752600	0.16830700	H	-1.59081800	-5.45424400	-1.20426400
O	-4.77942400	-0.72970300	0.06248100	H	1.12744800	-1.61659100	5.08194100
O	-3.02315800	1.18980500	3.16862200	S	4.75031200	1.04574100	-0.16269800
O	-4.30109700	1.88428100	0.63376500	C	6.25996400	0.10611800	-0.00789000
O	-3.55865000	-1.45770100	2.62094600	C	7.42748300	0.73076000	0.45470500
Zr	1.48749800	-0.21578900	-1.14025300	C	6.19333400	-1.26993400	-0.26409600
Zr	0.41160500	1.33187200	1.97808300	C	8.57195400	-0.04941400	0.62098700
Zr	-0.31515100	-2.19018100	1.22177200	H	7.46017000	1.79791300	0.68085000
Zr	-1.81081900	-1.30287500	-1.91155900	C	7.35243600	-2.02873300	-0.08736500
Zr	-1.16310200	2.14344100	-1.19735000	H	5.26034000	-1.72369100	-0.60296400
Zr	-2.94616300	0.15150200	1.15495600	C	8.53522200	-1.42297000	0.35069400
H	2.29316900	-0.77183400	1.54437300	H	9.49492100	0.41975800	0.96749900
H	-0.14139000	0.54425200	-3.31166300	H	7.32779500	-3.10047500	-0.29526700
H	-2.99926700	-2.58159700	0.33196200	H	9.43572700	-2.02575900	0.48712900
H	-2.01832600	2.81158800	1.38814900	C	5.12142200	2.50103600	-1.15192000
O	3.77102300	0.17147200	-0.89851500	H	5.84915600	3.11583800	-0.60650700
H	1.16673500	-2.44143600	-4.70874100	H	5.50935500	2.16300500	-2.12217700
H	-3.25683200	1.41610600	-4.81176700	H	4.16507400	3.02759700	-1.25604200
H	-5.97229400	-1.56954400	-1.32949600	O	3.58552900	1.48774900	1.27124200
H	-3.54092000	-3.08613100	3.81054600	H	4.06814200	2.04416500	1.91385200



Alternative TS 2 for the 2nd oxidation ($[\text{Zr}_6(\mu_3\text{-O})_4(\mu_3\text{-OH})_4(\mu_1\text{-OH})(\mu_1\text{-C}_6\text{H}_5\text{S(O)CH}_3)(\text{HCOO})_{11}] + \text{H}_2\text{O}$)

C	-3.05535700	0.30082000	-2.37926900	C	3.07433800	1.21029100	-3.68776800
C	-2.14632200	-3.44787600	-0.22563700	O	-0.92538800	3.64056800	1.31352700
C	-1.38372600	-1.11725500	3.79332100	O	-2.00238900	0.63481200	-2.98243500
C	0.02680300	-2.28802500	-3.81792900	O	-3.15442200	-0.11238400	-1.19961400
C	4.04721100	-2.80763300	-1.49485700	O	-2.07424000	-0.87811800	2.77726300
C	1.36632400	2.16839700	3.91894000	O	-2.57412400	-2.36045400	0.24006500
C	3.72338700	3.39701000	0.07272200	O	-0.13882000	-1.90355000	1.25249800
C	1.86136400	-3.90891600	2.07782100	O	-0.99058500	1.49729600	-0.54489100
C	0.08721100	3.82941000	-2.24776100	O	-0.44188000	-0.94025300	-1.03002500
C	4.70147100	-0.61220900	2.20909800	O	-0.01330300	0.59052800	1.58195400

O	-0.96536300	-3.72187200	-0.57694100	H	4.86095500	-3.49490800	-1.81167000
O	-0.12214600	-1.17172600	3.87089800	H	3.63008200	1.57001800	-4.58104700
O	1.86999900	-0.89122000	-2.02212900	H	4.43087500	4.25401300	0.03616800
O	1.52194000	-4.00179500	0.86736800	H	5.66259900	-0.80429000	2.73285800
O	0.40371000	-2.98661600	-2.83684600	H	-1.93327400	-1.31661100	4.73983700
O	2.90029400	-3.31969900	-1.37688900	H	-4.00030500	0.38074300	-2.96071300
O	2.11571000	-1.19246500	0.44543800	H	1.45083800	2.69770100	4.89333400
O	2.45337000	1.10720100	1.38506500	H	-0.21855500	-2.84517400	-4.74834800
O	0.40335200	3.92853400	-1.04250900	H	-0.01207500	4.77535700	-2.82439600
O	1.05712300	2.86876600	2.92319500	S	-4.98487300	1.04406800	0.80434800
O	2.57471300	3.63550700	0.52123400	C	-6.20966400	-0.10950700	0.17329300
O	1.53421800	1.35081700	-0.95122300	C	-7.43772300	0.38653300	-0.28491000
O	3.65165200	-0.80548900	2.87723500	C	-5.87650100	-1.46667700	0.11200800
O	1.88031300	-2.86872800	2.78436600	C	-8.37615700	-0.52073700	-0.77970800
O	1.60035300	0.92779800	3.94282100	H	-7.67012600	1.45343500	-0.26190800
O	1.82499500	1.14213500	-3.79257900	C	-6.83251100	-2.35508900	-0.38829700
O	-0.13768300	2.76483000	-2.89041300	H	-4.89392400	-1.81441000	0.43453900
O	-0.09213400	-1.03838400	-3.86361100	C	-8.07528700	-1.88736300	-0.82880000
O	4.37008300	-1.60768800	-1.30050700	H	-9.34296200	-0.15589300	-1.13266500
O	4.17684600	2.28945000	-0.33285800	H	-6.59889000	-3.42107300	-0.43553100
O	4.78163900	-0.21776000	1.01680000	H	-8.81316900	-2.59120500	-1.22046300
O	3.77906300	0.90691000	-2.68383500	C	-5.76993000	1.81379100	2.23037000
Zr	-1.61598000	-0.28427300	0.53684500	H	-6.65317200	2.36901100	1.88793800
Zr	0.91978700	-2.47880200	-0.68879500	H	-6.03664200	1.02340400	2.94429300
Zr	1.44720800	-0.67734700	2.36556300	H	-5.01832300	2.49889300	2.64320700
Zr	3.23926200	0.24651900	-0.59047200	H	-0.99376500	3.80812000	2.26325900
H	-1.90476000	2.63684600	-0.78916600	H	-2.04075000	3.76110500	0.23711700
H	-0.54800400	-2.62112600	1.75380400	O	-2.46875000	3.52086700	-0.66661400
H	2.27487400	-1.20902300	-2.83961700	O	-3.87061700	2.51665200	-0.07620100
H	3.10075900	1.57590000	1.92777100	H	-4.48067600	2.96063000	-0.700254
O	-3.80993100	0.25544300	1.34911600	Zr	0.64858500	2.38515800	0.68142000
H	-2.88943300	-4.26770600	-0.33145500	Zr	0.13449700	0.63211200	-2.30076300
H	2.17107300	-4.85262400	2.57603800				

Chapter 4

**Developing metal-organic framework catalysts for the efficient consumption of H₂O₂ in the
[H₂O₂ generation + sulfide oxidation] tandem reaction**

4.1 Introduction

In chapter 3, we explored sulfide oxidation as a potential replacement for alkene oxidation to enhance the rate of the oxidation step in the [H₂O₂ generation + oxidation] tandem reaction. While UiO-66 MOF itself can serve as a catalyst for the H₂O₂-induced sulfide-oxidation step, the rates of oxidation are lower than our target for matching the two component rates in the overall tandem reaction. In this chapter, we aimed to develop new MOF-based catalysts that can oxidize sulfide at higher rates. We also explored a reactor-based strategy to measure the rate of H₂O₂ utilization in sulfide oxidation and adjusted the rate for H₂O₂ generation to match the consumption in our tandem catalyst design (Figure 4.1). In addition, the loading amount of Pd NPs in our UiO-66 MOF was adjusted to encompass a wider range of H₂O₂-generation rate.

Rate of H₂O₂ generation ≈ Rate of sulfide oxidation

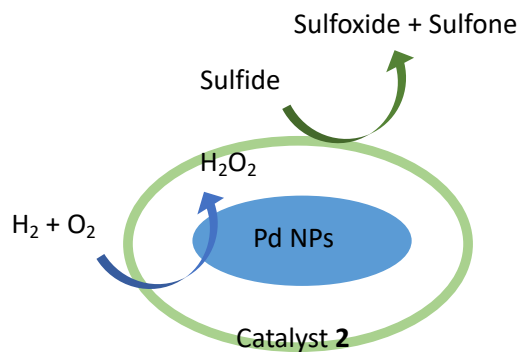


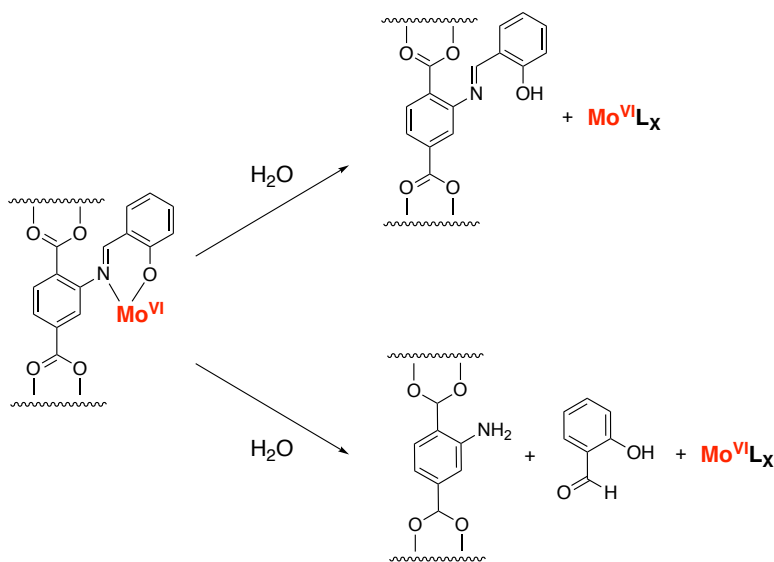
Figure 4.1 Proposed core-shell catalyst for the [H₂O₂ generation + sulfide oxidation] tandem reaction.

4.2 Selection of UiO-66-based catalyst for sulfide oxidation

While the Mo^{VI} moiety in the **UiO-66-sal(Mo)** catalyst used in chapter 2 could also serve as a potential catalyst for sulfide oxidation,¹⁷⁷⁻¹⁷⁹ it was not very stable in the CH₃OH/H₂O solvent mixture (see chapter 2, Table 2.16). The leaching of Mo^{VI} ions could be attributed to the H₂O-

induced disassociation of Mo^{VI} from the salicylidene ligands or the hydrolysis of the imine ligands (Scheme 4.1). Not only did the metal leaching diminish the recyclability of the catalytic materials, it also reduces reaction rates in the tandem reaction. As the usage of $\text{CH}_3\text{OH}/\text{H}_2\text{O}$ solvent mixture is important for the safe and high generation of H_2O_2 ,^{15, 69, 71} we sought alternative UiO-66-based catalysts with ligands that are stable to protic conditions.

Scheme 4.1 Possible paths for Mo^{VI} leaching from **UiO-66-sal(Mo)**. For simplicity, only one organic linker is shown here.



To improve the binding between the metal species and the ligand, we initially anticipated that the porphyrin ligands would be good candidates due to their tetradentate coordination environment. In addition, porphyrin complexes of metal species, such as Fe^{III} ,¹⁸⁰⁻¹⁸² Mn^{III} ,^{151, 181} and V^{IV} ,¹⁸³ have been shown to be active in H_2O_2 -induced oxidations. Thus, we compared activities of three metalloporphyrins (**(por)Fe**, **(por)Mn**, and **(por)V**) in the oxidation of sulfide in $\text{CH}_3\text{OH}/\text{H}_2\text{O}$ solvent mixture (Figure 4.2). While all three complexes were catalytically active, **(por)V** exhibited the lowest conversion. The final conversion by **(por)Fe** was similar to that by **(por)Mn**; however, the former exhibited faster activity at the beginning. As a result, we selected

(por)Fe as our initial test case for sulfide oxidation and set out to incorporate this complex onto the UiO-66 framework.

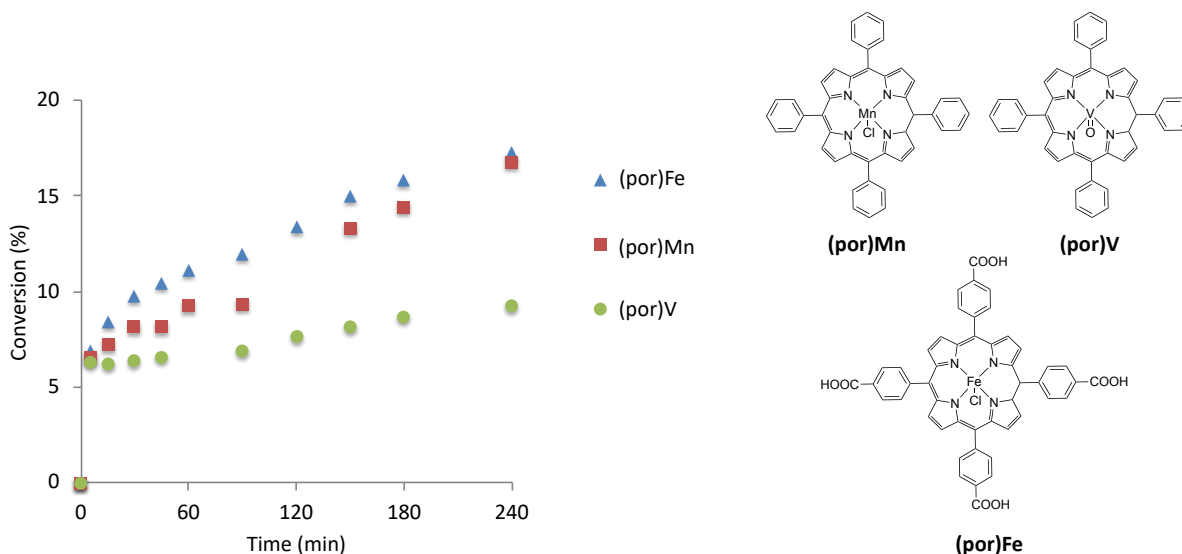


Figure 4.2 The conversion profiles in the catalytic oxidation of methyl phenyl sulfide at room temperature in the CH₃OH/H₂O (7/3 v/v) solvent mixture using H₂O₂ as the oxidant. All reactions were carried out with a 100:100:1 molar ratio of sulfide:H₂O₂:metalloporphyrin.

Generally, carboxylic acids can couple with amines to form amides, which is stable to hydrolysis at pH 5-9.¹⁸⁴ As the selected **(por)Fe** already bears carboxylic acid groups, it was coupled with **UiO-66-NH₂** MOF using Ghosez's reagent¹⁸⁵ (Scheme 4.2). The resulting **UiO-66-por(Fe)** was found to have ~3.4 wt % of Fe based on ICP-OES analysis and exhibited similar activities per Fe in sulfide oxidation as its homogenous **(por)Fe** analogue (Table 4.1). However, a significant portion of the activity in **UiO-66-por(Fe)** could come from the Zr nodes because the nodes can also catalyze sulfide oxidation in the presence of H₂O₂ (see chapter 3). Thus, a control sulfide oxidation was also carried out using **UiO-66-NH₂** MOF to delineate the contribution of the framework. As shown in Table 4.1, **UiO-66-NH₂** appears to be as active as the **UiO-66-por(Fe)**, indicating that the contribution of the **(por)Fe** is not significant enough to eliminate the

contribution of the nodes. We then explored a new strategy of metallation that can eliminate the influence from the nodes to carry out a simple kinetic study as well as to obtain a more active UiO-66-based catalyst.

Scheme 4.2 Synthesis of **UiO-66-por(Fe)**. For simplicity, only one organic linker is shown here.

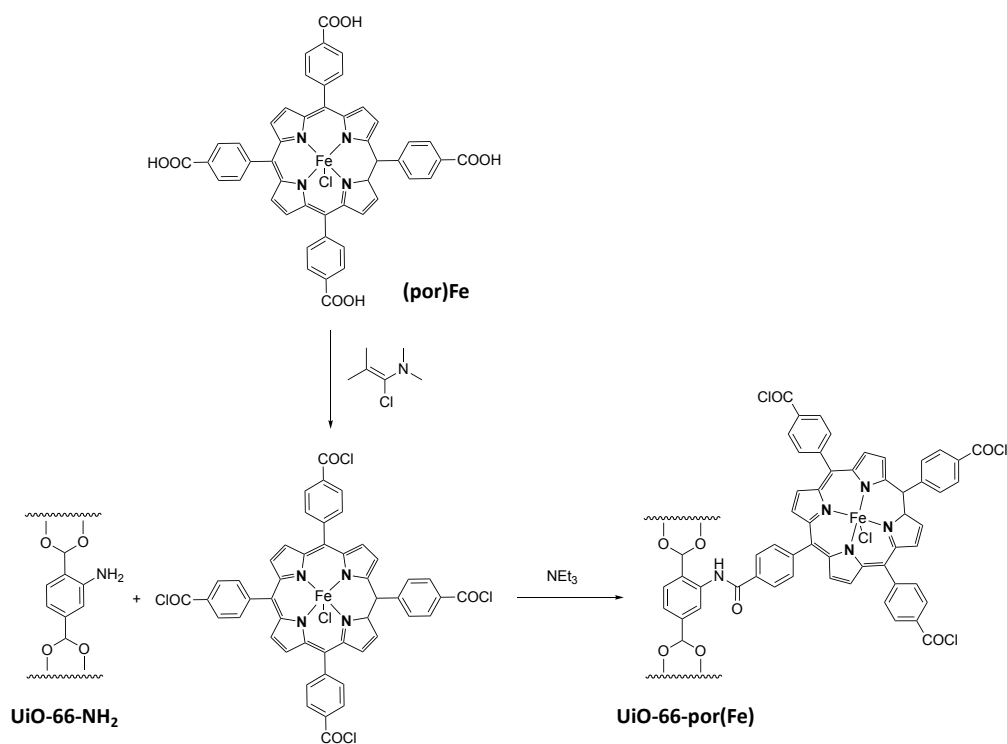


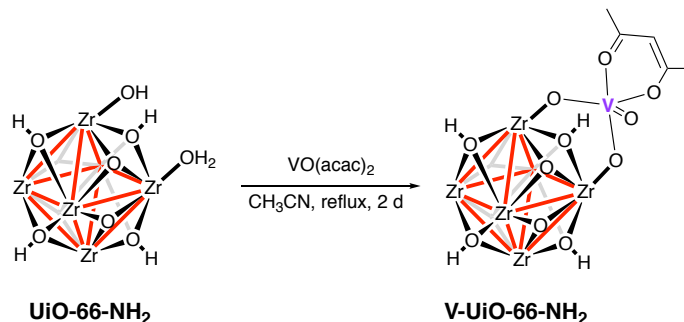
Table 4.1 Catalytic activity of MOF-based catalysts in the oxidation of methyl phenyl sulfide with H₂O₂ in the CH₃OH/H₂O (7/3 v/v) solvent mixture.

Entry	Catalyst	Fe (mmol)	Time (h)	Conversion (%)
1	(por)Fe	0.002	6	14
2			24	19
3	UiO-66-por(Fe)^a	0.005	6	34
4			24	34
5	UiO-66-NH₂^a	-	6	41
6			24	74

Reaction conditions: methyl phenyl sulfide (0.2 mmol), 30 wt % H₂O₂ (0.2 mmol), CH₃OH (7 mL), and H₂O (3 mL). ^a8 mg of the MOF was used.

Previous works from our group have shown that oxidation-active metal species,^{61, 186} such as VO(acac)₂ can bind to the Zr nodes of UiO-66 MOF and the resulting **V-UiO-66** is catalytically active for the oxidative dehydrogenation of cyclohexene.⁶¹ Based on this successful result, we should be able to implement this strategy to create a sulfide-oxidation active MOF catalyst. We additionally hypothesized the added metal complexes can also occupy the defect sites on the nodes (chapter 3) that were primarily responsible for sulfide oxidation, thus eliminating the background activity of the MOF. While the amino groups on the organic linkers are not necessary for this modification, **UiO-66-NH₂** MOF was selected due to the advantage that the BDC-NH₂ ligands exhibited in the encapsulation of Pd NPs as shown in chapter 2.¹⁸⁷ In a test reaction, **UiO-66-NH₂** was successfully modified with VO(acac)₂ to form **V-UiO-66-NH₂** with ~1 wt % of V (Scheme 4.3, see Section 4.7 for details in the synthesis and characterization). Its PXRD pattern, SEM image, and BET area are similar to those for the **UiO-66-NH₂** parent, indicating that the crystallinity, morphology, and porosity of the MOF were maintained after the modification.

Scheme 4.3 Synthesis of **V-UiO-66-NH₂**. For simplicity, only one Zr node is shown here.



As expected, **V-UiO-66-NH₂** was catalytically active for methyl phenyl sulfide oxidation in the presence of H₂O₂ (Figure 4.3). As discussed above, while **UiO-66-NH₂** also exhibited some catalytic activity in sulfide oxidation (Figure 4.3), the defect sites on **V-UiO-66-NH₂** were

presumably occupied with the V^{IV} species and would not contribute significantly to the activity. Indeed, the significantly higher conversion (~ 5 times) from **V-UiO-66-NH₂** suggests that the V^{IV} species are responsible for the majority of the observed activities in this sulfide oxidation. These promising results led us to choose **V-UiO-66-NH₂** as a catalyst for the sulfide oxidation component of our tandem reaction.

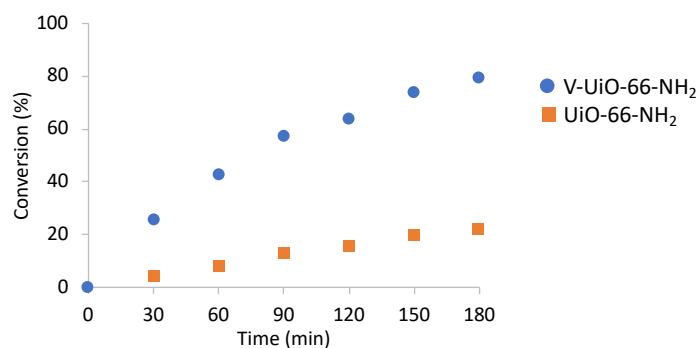


Figure 4.3 Conversion profiles in the oxidation of methyl phenyl sulfide using H_2O_2 in the CH_3OH/H_2O (7/3 v/v) solvent mixture.

4.3 Measurements of H_2O_2 -consumption rate in sulfide oxidation

To quantify the rate of H_2O_2 -consumption by **V-UiO-66-NH₂** catalyst in sulfide oxidation, we employed a circulating packed-bed reactor. Here, a mixture of methyl phenyl sulfide, H_2O_2 , and CH_3OH/H_2O (7/3 v/v) solvent mixture in a reservoir was pumped through a packed-catalyst bed at a controllable flow rate and circulated back into the same system (Figure 4.4). Collecting a series of aliquots over time enabled the reaction progress to be monitored under a low-conversion regime ($<12\%$) due to a low single-pass conversion through the catalyst bed. As the catalyst was also isolated from the reaction mixture, catalyst separation before each analysis was unnecessary and catalyst after the reaction became simple.

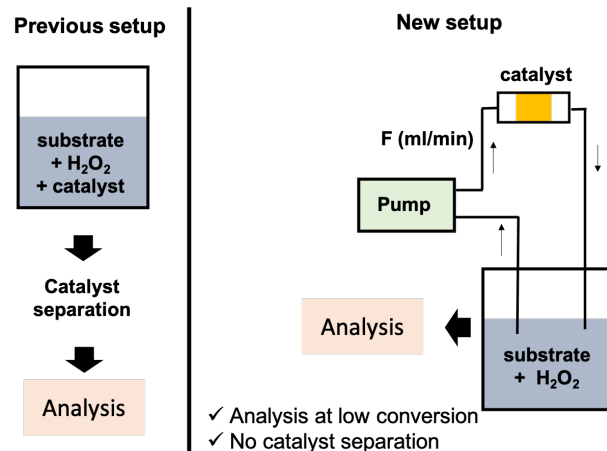


Figure 4.4 Previous and new reaction setups for sulfide oxidation reaction (see Section 4.7 for details and photo of an actual setup).

Our preliminary data indicated that reliable results from the aforementioned reactor could be obtained when 2-10 mM of sulfide and 5-20 mg of catalyst were employed in this reaction. The sulfide oxidation in the presence of H₂O₂ using our **V-UiO-66-NH₂** (5 mg) was then carried out under these conditions and the change in concentration of sulfide was monitored over time. We found that the initial rates were not dependent on the flow rate at > 0.8 mL/min flow (Figure 4.5). This result indicated that the system is not limited by the mass transfer under these conditions.

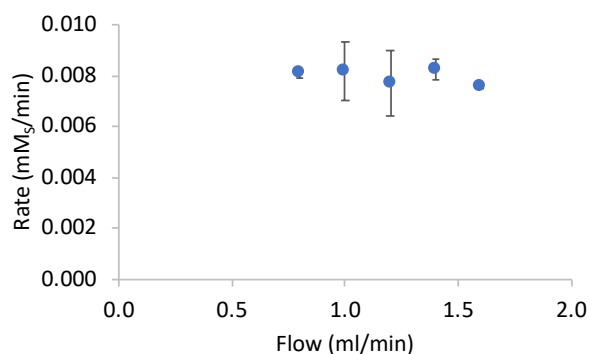


Figure 4.5 The rate profile in the oxidation of methyl phenyl sulfide at different flow rates using **V-UiO-66-NH₂** catalyst (~0.05 mg V).

To identify the maximum activity of our **V-UiO-66-NH₂** catalyst in sulfide oxidation, the initial rates at different concentrations of H₂O₂ were measured, while the concentration of sulfide and the amount of catalysts were kept constant. When 10 mg of **V-UiO-66-NH₂** (~0.1 mg V) was used, the reaction has the highest rate of ~0.035 mM/min (Figure 4.6). This result implied that the rate of H₂O₂ generation that would be coupled with this catalyst in the tandem reaction should not exceed 0.035 mM/min for efficient consumption of the oxidant.

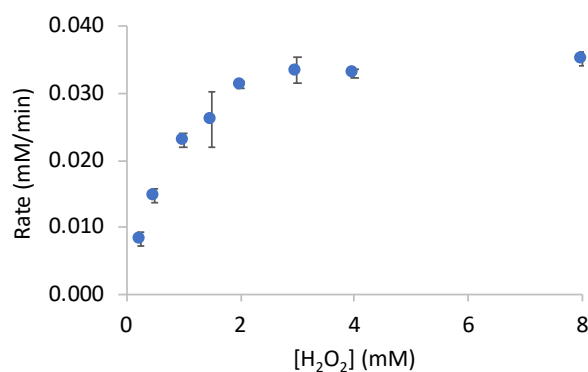


Figure 4.6 The rates of methyl phenyl sulfide oxidation at different concentration of H₂O₂ using **V-UiO-66-NH₂** catalyst (~0.1 mg V).

4.4 Measurements of H₂O₂-generation rate

To measure the rate of H₂O₂ generation, we developed a circulating packed-bed reactor that allows for reactions under moderate pressures of H₂ and O₂ gases (Figure 4.7). With the automatic valve, the collection of aliquots over time was possible, while the pressure inside the vessel was kept constant. The concentration of generated H₂O₂ was then determined by colorimetric titration with the FOX reagent using UV-vis spectroscopy (see Section 4.7 for the synthesis of this reagent and its used in the detection of H₂O₂).

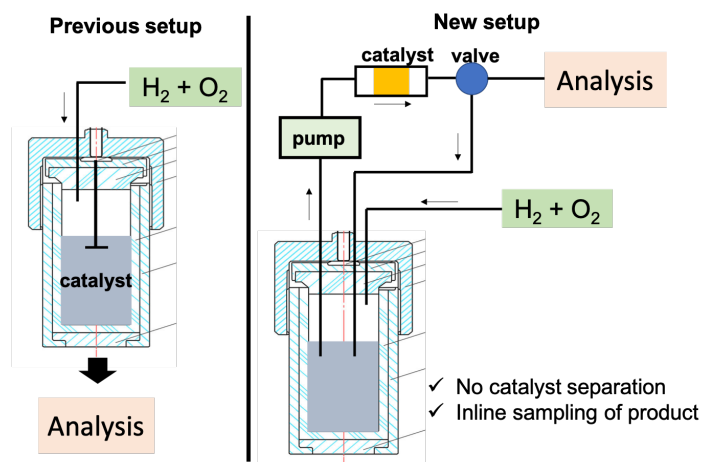


Figure 4.7 Previous and new reaction setups for H_2O_2 generation and [H_2O_2 generation + oxidation] tandem reaction (see Section 4.7 for details and photo of an actual setup).

We carried out the H_2O_2 generation at room temperature using 5 vol % H_2/CO_2 (50 psig) and 25 vol % O_2/CO_2 (20 psig) gas feeds under condition that were safe for our reactor setup. As this pressure was 5 times lower than that used in the work of chapter 2, we anticipated the slowdown in the rate of H_2O_2 generation. After these gasses were charged to the autoclave, the $\text{CH}_3\text{OH}/\text{H}_2\text{O}$ (7/3 v/v) reaction mixture was delivered to a packed **Pd@UiO-66-NH₂** catalyst (~0.3 mg Pd) by the pump and circulated back to the reservoir. The H_2O_2 -containing aliquots collected every 15 min and the concentration of H_2O_2 was found to increase linearly over a period of 60 min (Figure 4.8). Based on this data, the rate of H_2O_2 generation was ~0.0037 mM/min, falling in the target range that could be coupled with our **V-UiO-66-NH₂**-catalyzed sulfide oxidation.

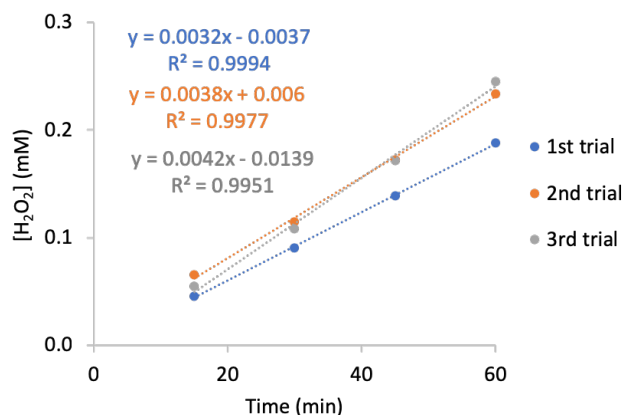


Figure 4.8 The H₂O₂-generation profiles of 3 trials using **Pd@UiO-66-NH₂** catalyst (~0.3 mg Pd).

As the generation of H₂O₂ can be tuned by adjusting the content of Pd NPs in **Pd@UiO-66-NH₂** catalyst (Table 4.3), the rate of H₂O₂ generation can be enhanced to match the maximum rate of sulfide oxidation by **V-UiO-66-NH₂** catalyst (0.035 mM/min). It is worth noting that the local H₂O₂ concentration at the MOF-based V species is likely to be higher than the H₂O₂ concentration that we can observe. This is because the observed concentration is resulted from the measurement of H₂O₂ that diffuses out from the catalysts into a larger volume of reaction mixture. Nevertheless, we can begin to investigate the catalytic activity of our catalysts in tandem reaction and evaluate their efficiency in H₂O₂ utilization by measuring the left-over H₂O₂ after the reaction.

4.5 [H₂O₂ generation + sulfide oxidation] tandem reaction

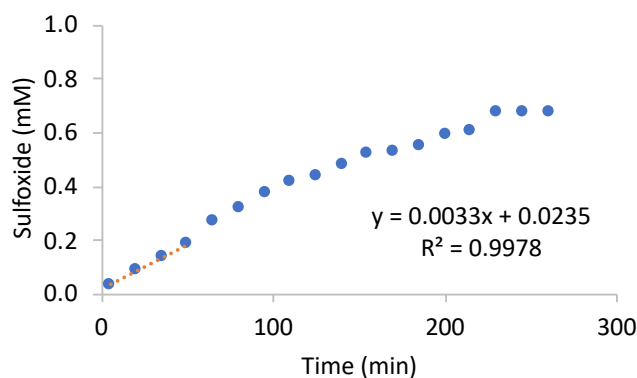


Figure 4.9 The methyl phenyl sulfoxide profile for the [H₂O₂ generation + sulfide oxidation] tandem reaction using a physical mixture of Pd@UiO-66-NH₂ (~0.3 mg Pd) + V-UiO-66-NH₂ (~0.1 mg V) catalysts.

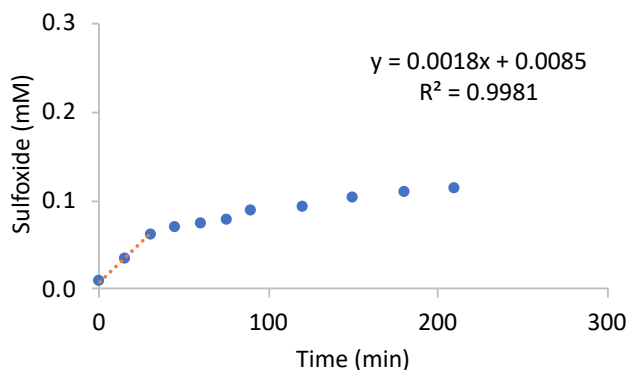


Figure 4.10 The methyl phenyl sulfoxide profile for the [H₂O₂ generation + sulfide oxidation] tandem reaction using a physical mixture of Pd@UiO-66-NH₂ (~0.15 mg Pd) + V-UiO-66-NH₂ (~0.1 mg V) catalysts.

The [H₂O₂ generation + sulfide oxidation] tandem reaction was then carried out using the circulating packed-bed reactor shown in Figure 4.7 but with an additional inline HPLC analysis that allows for methyl phenyl sulfide and its oxidized products to be quantified automatically. When a physical mixture of Pd@UiO-66-NH₂ and V-UiO-66-NH₂ catalysts (~0.3 mg Pd and ~0.1 mg V) was used, the increase of sulfoxide product was observed over ~200 min with an initial rate of ~0.0033 mM/min (Figure 4.9). Based on the H₂O₂ strip test, there was no H₂O₂ left over in the

reaction mixture, suggesting that our **V-UiO-66-NH₂** can consume the majority of the H₂O₂ generated by **Pd@UiO-66-NH₂**. In addition, when the amount of Pd NPs in the catalyst mixture was reduced to half (i.e., ~0.15 mg Pd and ~0.1 mg V), the rate of reaction was also decreased to ~0.0018 mM/min (Figure 4.10), which could be attributed to a slower generation of H₂O₂ by the smaller amount of Pd loading.

Under the same condition as the aforementioned experiments, a dually functionalized **Pd@V-UiO-66-NH₂** MOF (~0.03 mg Pd and ~0.2 mg V) was found to catalyze the [H₂O₂ generation + sulfide oxidation] tandem reaction under the same condition with no detectable H₂O₂ after the reaction (Figure 4.11). The relatively good initial rate (~0.024 mM/min) from this catalyst indicates that a dually functionalized UiO-66 catalyst can indeed be used to efficiently generate H₂O₂ and consume it in our tandem reaction.

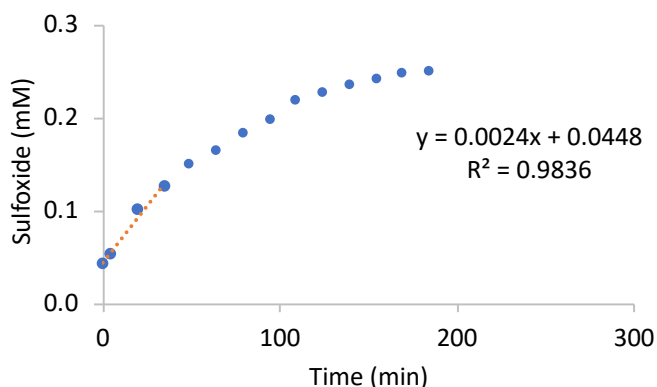


Figure 4.11 The methyl phenyl sulfoxide profile for the [H₂O₂ generation + sulfide oxidation] tandem reaction using a **Pd@V-UiO-66-NH₂** (~0.03 mg Pd and ~0.2 mg V) catalyst.

4.6 Conclusion

We have demonstrated the node modification of UiO-66 MOF using V^{IV} species and the resulting **V-UiO-66-NH₂** catalyst can enhance the H₂O₂ consumption in methyl phenyl sulfide

oxidation. The initial rate of this sulfide oxidation can be measured at low conversion (<12%) using a circulating packed-bed reactor, allowing for the determination of the maximum rate of H₂O₂ consumption. In addition, the initial rate of H₂O₂ generation can be tuned for a good match with a target rate of H₂O₂ consumption by controlling the Pd NPs loading in **Pd@UiO-66-NH₂**. Both the physical mixture of **Pd@UiO-66-NH₂** and **V-UiO-66-NH₂** catalysts and a dually functionalized **Pd@V-UiO-66-NH₂** catalyst were capable of catalysing the [H₂O₂ generation + sulfide oxidation] tandem reaction with efficient consumption of H₂O₂.

4.7 Experimental

4.7.1 Materials and methods

Unless otherwise stated, all reagents were used as received. Zirconium chloride was purchased from Strem Chemicals, Inc. (Newburyport, MA). 2-Aminoterephthalic acid, hydrogen peroxide, thioanisole, methyl phenyl sulfone, naphthalene, vanadyl acetylacetonate, Na₂PdCl₄, (NH₄)₂Fe(SO₄)₂·6H₂O, D-sorbitol, xylenol orange, 5,10,15,20-tetraphenyl-21*H*,23*H*-porphine manganese (III) chloride (**(por)Mn**), 5,10,15,20-tetraphenyl-21*H*,23*H*-porphine vanadium (IV) oxide (**(por)V**), SiO₂ (Davisil, grade 644, 100-200 mesh, 150 Å, Cat. No. 23682-9), and ICP standards (palladium, vanadium, and zirconium) were purchased from Sigma-Aldrich Co., LLC. (St. Louis, MI). 5,10,15,20-tetrakis(4-carboxyphenyl)-21*H*,23*H*-porphine iron (III) chloride (**(por)Fe**) was purchased from Frontier Scientific, Inc. (Logan, UT). Methyl phenyl sulfoxide was purchased from Alfa Aesar (Ward Hill, MA). Concentrated sulfuric acid was purchased from VWR Scientific, LLC (Chicago, IL). Ultrapure deionized (DI) H₂O (18.2 MΩ•cm resistivity) was obtained from a Millipore Milli-Q Biocel A10 instrument (Millipore Inc., Billerica, MA). Solvents

were purchased from either Sigma-Aldrich Co., LLC. (St. Louis, MI) or Fisher Scientific, Inc. (Pittsburg, PA) and used as received.

N₂ gas (Ultra High Purity Grade 5) used for the adsorption and desorption measurements, 5 vol % H₂/CO₂, and 25 vol % O₂/CO₂ were obtained from Airgas Specialty Gases (Chicago, IL).

All powder X-ray diffraction (PXRD) patterns except for **UiO-66-NH₂ (1)** sample were collected on a STOE's STADI-MP powder diffractometer (STOE & Cie. Ltd., Darmstadt, Germany) equipped with an asymmetric curved Germanium monochromator (Cu K_{α1} radiation, $\lambda = 1.54056 \text{ \AA}$), a one-dimensional silicon strip detector (MYTHEN2 1K from Dectris AG, Baden, Switzerland), and a line-focused Cu X-ray tube operated at 40 kV and 40 mA. The sample powder was sandwiched between two acetate foils (polymer substrate with neither Bragg reflections nor broad peaks above 10 degrees) and measured in transmission geometry in a rotating holder. Prior to the measurement, the instrument was calibrated against a NIST silicon standard (640d). Measurements were made over the range $5^\circ < 2\theta < 53^\circ$ in 4° steps of detector and an exposure time of 10 s per step.

Powder X-ray diffraction (PXRD) pattern of **UiO-66-NH₂ (1)** was collected on a ATX-G Rigaku X-ray Diffractometer (Rigaku Americas, The Woodlands, TX) equipped with an 18 kW Cu rotating anode, an MLO monochromator, and a high-count-rate scintillation detector. Measurements were made over the range $2^\circ < 2\theta < 50^\circ$ in 0.05° step width with a $3^\circ/\text{min}$ scanning speed.

N₂ adsorption and desorption isotherms were measured on a Micromeritics Tristar II 3020 (Micromeritics Instrument Corporation, Norcross, GA) at 77 K. Before each run, samples were activated at 120 °C for 24 h under high vacuum on both a Schlenk line and a VacPrep 061

instrument (Micromeritics Instrument Corporation, Norcross, GA). About 40-100 mg of sample was used in each measurement and the BET area was calculated in the region $P/P_0 = 0.005-0.1$.

Inductively coupled plasma optical-emission spectroscopy (ICP-OES) was conducted on a computer-controlled (QTEGRA software v. 2.2) Thermo iCap 7600 Duo ICP-OES (Thermo Fisher Scientific, Waltham, MA) instrument equipped with a SPRINT valve and a CETAC 520ASX autosampler (Teledyne CETAC, Inc., Omaha, NE). MOF samples (~3 mg) were digested in a 15 mL centrifuge tube using a mixture of HNO_3 (150 μL), HCl (150 μL), and HF (10 μL) by sonication. After becoming clear (~30 min), the resulting solution was then diluted with DI H_2O to a final volume of 15 mL. The solution was then analyzed for Pd (324.270 and 340.458 nm), V (310.230, 292.402, and 309.311 nm), and Zr (339.198, 343.823, and 327.305 nm) content as compared to standard solutions.

Scanning electron microscopy (SEM) images were obtained at Northwestern University's EPIC/NUANCE facility on a SU8030 FE-SEM microscope (Hitachi High Technologies America, Inc., Dallas, TX) with an acceleration voltage of 10 kV.

Absorption spectra were recorded on a Varian Cary 300 Bio UV-vis spectrophotometer (Varian, Inc., Palo Alto, CA) using a masked quartz cell (path length = 10 mm, catalog # 29-Q-10, Starna cells Inc., Atascadero, CA).

Centrifugation was carried out in an Eppendorf Centrifuge 5804 R, Model AG 22331 (Eppendorf AG, Hamburg, Germany) equipped with an F34-6-38 rotor. All centrifugations were carried out at 5000-6000 rpm (3214-4628 g) for 10-20 minutes.

Gas chromatographic analysis was carried out on an Agilent Technologies 6890N Network GC system (Agilent Technologies, Inc., Santa Clara, CA) equipped with an FID detector and an

HP-5 capillary column (30 m \times 320 μ m \times 0.25 μ m film thickness). Analysis parameters were as follows: initial temperature = 80 $^{\circ}$ C, initial time = 2 min, ramp = 20 $^{\circ}$ C/min, final temperature = 200 $^{\circ}$ C, final time = 1 min. Elution times (min) = 4.4 (methyl phenyl sulfide), 5.3 (naphthalene), 6.3 (methyl phenyl sulfoxide), and 6.8 (methyl phenyl sulfone). The amount of oxidation product was calculated based on calibration curves against naphthalene as an internal standard. Response factors: methyl phenyl sulfide = 0.723, methyl phenyl sulfoxide = 0.790, and methyl phenyl sulfone = 0.771.

Rate measurement of the sulfide-oxidation step was carried out on a circulating packed-bed reactor that was set up in a fume hood (Figures 4.4 and 4.12). The mixture of catalyst powder (5-10 mg) and SiO₂ (same mass as the catalyst) was packed between quartz wool in a bed (Teflon, O.D. = 1/4", length = 2"). Every component is connected through Teflon tubing (O.D.=1/16"). Liquid mixture in an 8 dram vial was circulated through a catalyst bed at specific flow rates (mL/min) using a dual piston-isocratic pump (series 1500, Chrom Tech, Apple Valley, MN). The reaction started when the reaction mixture contacted with the catalyst in the bed (after turning the pump on for \sim 30 s at flow rate = 1 mL/min).

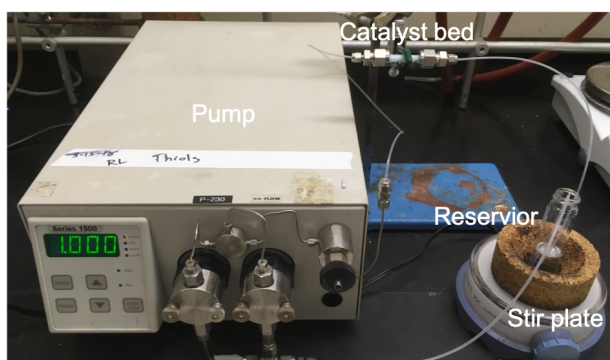


Figure 4.12 Reaction setup for rate measurement of the sulfide oxidation.

Rate measurement of the H_2O_2 -generation step was carried out on a high-pressure circulating packed-bed reactor (Figures 4.7 and 4.13) in the REACT facility at Northwestern University. The catalyst powder (5-10 mg) was packed between quartz wool in a bed (stainless steel, O.D. = 1/4", length = 2"). Inside this reactor, a 100 mL Parr Instruments stainless steel autoclave (series 4790 with modification, maximum working pressure of 3000 psig, Parr Instrument, Inc., Moline, IL) was connected to a magnetic drive gear pump (series GA, Micropump, Vancouver, WA) and a catalyst bed through stainless steel tubing (O.D.=1/16"). The reactor was also equipped with a K type thermocouple, a pressure transducer, a pressure relief valve (80 psig), and sampling valves for temperature monitor, pressure monitor, pressure control, and aliquot samplings, respectively. Liquid mixture ($\text{CH}_3\text{OH}/\text{H}_2\text{O}$, 7/3 v/v, 30 mL) was charged into the autoclave and circulated through the bed at specific flow rates (mL/min).

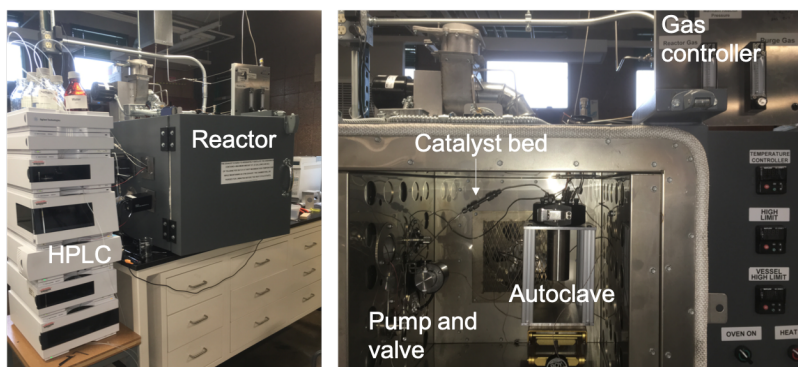


Figure 4.13 Reaction setup to measure the rate of the H_2O_2 generation and the [H_2O_2 generation + sulfide oxidation] tandem reaction.

In the case of H_2O_2 analysis, the collected aliquot (20 μL) was flushed using HPLC pump and $\text{CH}_3\text{OH}/\text{H}_2\text{O}$ (7/3 v/v) mobile phase into a vial with a total volume of ~ 100 μL before being analyzed with FOX reagent.

In the case of organic substrate analysis, the collected aliquot (2 μL) was automatically injected into an Agilent 1200 HPLC system equipped with reverse-phase (Zorbax, 3.0×50 mm, Eclipse Plus 95 \AA /3.5 μm /C18, Agilent 959943-302) column and DAD detector. Samples were eluted using a gradient method with a flow rate of 1 mL/min beginning with a 80/20 v/v $\text{H}_2\text{O}/\text{CH}_3\text{CN}$ mixture for 3 min, increasing to 0/100 v/v $\text{H}_2\text{O}/\text{CH}_3\text{CN}$ over 6 min, and holding there for 2 min. Elution times (min) = 0.59 (methyl phenyl sulfoxide), 0.99 (methyl phenyl sulfone), and 5.50 (methyl phenyl sulfide). The amount of methyl phenyl sulfide and methyl phenyl sulfoxide were calculated by comparing the area of integration against a calibration curves of standards with known concentration (see Figure 4.14 for calibration curves). As methyl phenyl sulfone was not observed as a product in our tandem reaction, its calibration curve was not determined.

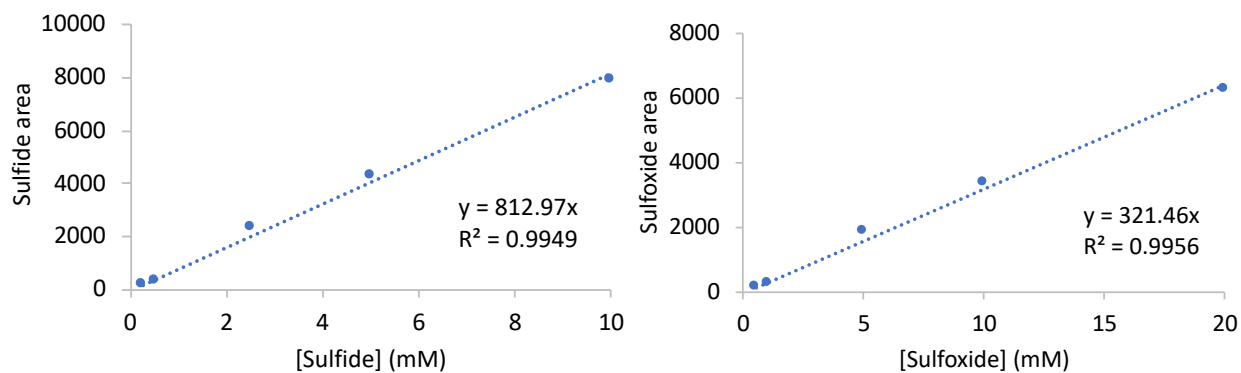


Figure 4.14 Plots of the concentration of methyl phenyl sulfide and methyl phenyl sulfoxide versus their areas of intergration.

4.7.2 Synthesis of UiO-66-NH₂ and its derivatives

UiO-66-NH₂ (1). This material was made following a previously reported procedure in chapter 2 and was then used to synthesize **UiO-66-por(Fe)**. In a 250 mL round-bottom flask, ZrCl_4 (0.4 g, 1.7 mmol) was dissolved in DMF (75 mL) by ultra-sonication at 50-60 $^\circ\text{C}$ before

being combined with glacial acetic acid (2.85 mL, 850 mmol). In a separate 50 mL Erlenmeyer flask, 2-aminoterephthalic acid (0.311 g, 1.7 mmol) was dissolved completely in DMF (25 mL) before being added to the $ZrCl_4$ solution. This combined mixture was homogenized by swirling before a small amount (0.125 mL) of DI H_2O was added. The round-bottom flask was tightly capped, and sonicated at 50-60 °C, and placed in a 120 °C oil bath under static condition for 24 h. After being cooled to room temperature, the precipitate was collected by centrifugation and immersed in DMF (~20 mL) with fresh solvent being exchanged twice each day for two days. The collected materials were then washed and immersed in CH_3OH (~20 mL) three times for one day before being isolated through centrifugation and decantation. This isolated solid was then dried at 120 °C under vacuum to give a light yellow powder that is then stored at room temperature. Three batches of MOFs were combined together for characterization and subsequent experiments.

UiO-66-por(Fe). This material was made by adapting a literature protocol.¹⁸⁵ In a 10-20 mL Biotage microwave vial equipped with a magnetic stir bar, **(por)Fe** (30 mg, 0.1034 mmol) and Ghosez' reagent (23 μ L, 0.17 mmol) was dissolved in anhydrous CH_2Cl_2 (6 mL) under nitrogen. After being stirred for 3 h at room temperature, this mixture was placed under vacuum to remove most of the volatiles. Anhydrous CH_2Cl_2 (~6 mL) was added to the resulting porphyrin acid chloride and the mixture was again placed under vacuum to remove the *N,N*-dimethyl amide byproduct and solvent. This step was then repeated two more times before the resulting porphyrin acid chloride was dissolved in anhydrous CH_2Cl_2 (6 mL) and triethylamine (1 drop) to be used in the next step.

In a separate 10-20 mL Biotage microwave vial equipped with a magnetic stir bar, **UiO-66-NH₂ (1)** (50 mg) was dispersed in a mixture of anhydrous CH_2Cl_2 (6 mL) and triethylamine (1

drop) under nitrogen. The pre-prepared solution of porphyrin acid chloride was added dropwise and the reaction mixture was stirred for 12 h at room temperature. The MOFs was collected by centrifugation and redispersed in CH_2Cl_2 (~20 mL) before being collected by centrifugation. This washing step was repeated 3 times with CH_2Cl_2 (~20 mL) and 3 more times with CH_3OH (~20 mL). The collected solid was then dried at 120 °C under vacuum to give a green powder that is then stored at room temperature.

UiO-66-NH₂ (2). This material was made following a literature procedure⁶⁴ with some modifications and then used to synthesize **V-UiO-66-NH₂**. Two separate stock solutions of 80 mM ZrCl_4 and 80 mM 2-aminoterephthalic acid were prepared by dissolving ZrCl_4 (1.864 g, 0.8 mmol) and 2-aminoterephthalic acid (1.448 g, 0.8 mmol) in DMF (100 mL), respectively. Into 20-mL scintillation vials (26 vials in total), the stock solutions of each (1 mL) were added, following by DMF (6.622 mL) and CH_3COOH (1.378 mL). The vials were capped tightly, and the combined mixture was homogenized by swirling before being placed in a preheated oven (120 °C) under static condition for 24 h. After being cooled to room temperature, the solid was collected by centrifugation and immersed in DMF (~25 mL) with fresh solvent being exchanged twice each day for two days and then immersed in CH_3OH (~25 mL) for ~1 h. After being isolated through centrifugation and decantation, the resulting light-yellow solid was then air-dried overnight, subjected to Soxhlet extraction with CH_3OH for ~12 h, and dried overnight at 120 °C under vacuum. Three batches of MOFs were combined together for characterization and subsequent experiments.

V-UiO-66-NH₂. This material was made following a literature procedure with some modification.⁶¹ In a 250 mL round-bottom flask equipped with a magnetic stir bar, **UiO-66-NH₂**

(2) (1.6 g) was dispersed in CH₃CN (160 mL) by ultra-sonication for ~1 min before being combined with VO(acac)₂ (1.6 g, 6.0 mmol). After being stirred at reflux for 24 h, the mixture was transferred into four 50 mL centrifuge tubes and subjected to centrifugation to separate out the solid product. The mother liquor was decanted and the solid was redispersed and soaked in CH₃CN (~20 mL) for ~3 h before being collected by centrifugation. This CH₃CN-washing step was repeated until the mother liquor after centrifugation became clear. After being isolated through decantation, the greenish yellow solid was then air-dried overnight, subjected to Soxhlet extraction with CH₃OH for ~12 h, and dried overnight at 120 °C under vacuum.

Pd@UiO-66-NH₂. This material was made by Dr. Allison Young and Mr. Victor Lo following a previously reported literature procedure⁶⁵ with some modifications in a manner that is similar to the synthesis of **UiO-66-NH₂**. Briefly, Na₂PdCl₄ (2.35 mg, 0.008 mmol for 3 wt % Pd loading, or 0.24 mg, 0.0008 mmol for 0.19 wt % Pd loading) was first dissolved in the DMF (1 mL) that is going to be used in the **UiO-66-NH₂** synthesis. The synthesis of **Pd@UiO-66-NH₂** was then carried out using this DMF solution as described above. After 24 h at 120 °C, the product was collected by centrifugation, immersed in DMF (~25 mL) with fresh solvent being exchanged twice each day for two days, and immersed in CH₃OH (~25 mL) for three additional days. The isolated solid was then dried at 120 °C under vacuum overnight and stored at room temperature before use.

Pd@V-UiO-66-NH₂. This material can be prepared by following the synthesis of **V-UiO-66-NH₂** by replacing **UiO-66-NH₂** with **Pd@UiO-66-NH₂**. In a 50 mL round-bottom flask equipped with a magnetic stir bar, 0.19 wt % **Pd@UiO-66-NH₂** (150 mg) was dispersed in CH₃CN (20 mL) by ultra-sonication for ~1 min before being combined with VO(acac)₂ (150 mg, 0.56

mmol). After being stirred at reflux for 24 h, the mixture was transferred into a 50 mL centrifuge tube and the solid was collected by centrifugation. The mother liquor was decanted and the solid was redispersed and soaked in CH₃CN (~20 mL) for ~3 h before being collected by centrifugation. This CH₃CN-washing step was repeated until the mother liquor after centrifugation became clear. After being isolated through decantation, the solid was then air-dried overnight, subjected to Soxhlet extraction with CH₃OH for ~12 h, and dried overnight at 120 °C under vacuum.

FOX reagent. This indicator solution was prepared according to a previously reported literature protocol with some modification.¹⁸⁸ In a 50 mL volumetric flask, D-sorbitol (910 mg) and (NH₄)₂Fe(SO₄)₂·6H₂O (5 mg, 0.013 mmol) were dissolved in DI H₂O (20 mL). Concentrated H₂SO₄ (70 μL, 1.3 mmol) and xylenol orange (3.5 mg, 0.005 mmol) were then added before diluted with DI H₂O to obtain 50 mL solution. The resulting reagent was stored in a 4 °C refrigerator under dark condition up to 3 days until being used.

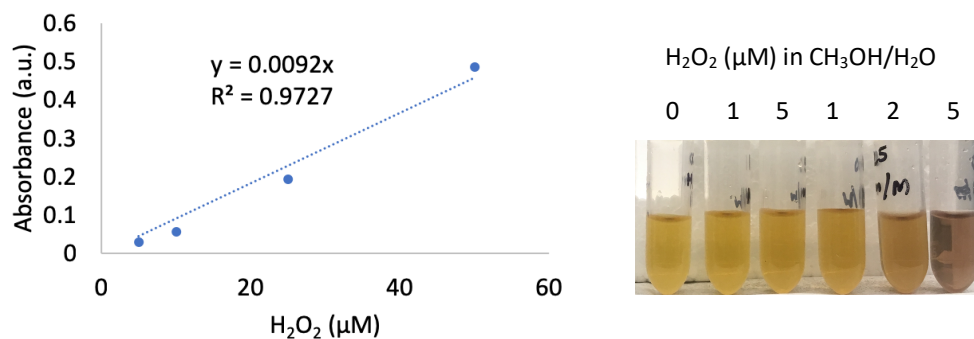


Figure 4.15 Left: A calibration curve for H₂O₂ concentration constructed from titrating against a FOX reagent. Right: Photo of mixtures of FOX reagent (50 μL) and H₂O₂ standard solution (950 μL) at different concentrations.

4.7.3 Characterization data of UiO-66-NH₂ and its derivatives

Table 4.2 Amount of metal loading and BET area of UiO-66-NH₂ and its derivatives.

Entry	MOFs	Fe (wt %)	V (wt %)	Pd NPs (wt %)	BET area (m ² /g)
1	UiO-66-NH ₂ (1)	-	-	-	1410
2	UiO-66-por(Fe)	3.4	-	-	- ^a
3	UiO-66-NH ₂ (2)	-	-	-	1120
4	V-UiO-66-NH ₂	-	1.0	-	1100
5	Pd@UiO-66-NH ₂ ^b	-	-	3.0	1020
6	Pd@UiO-66-NH ₂	-	-	0.19	1000
7	Pd@V-UiO-66-NH ₂	-	1.0	0.16	1040

^aDue to the small amount of material, the BET area of this sample was not quantified. ^bThis material was also used in the work shown in chapter 2.

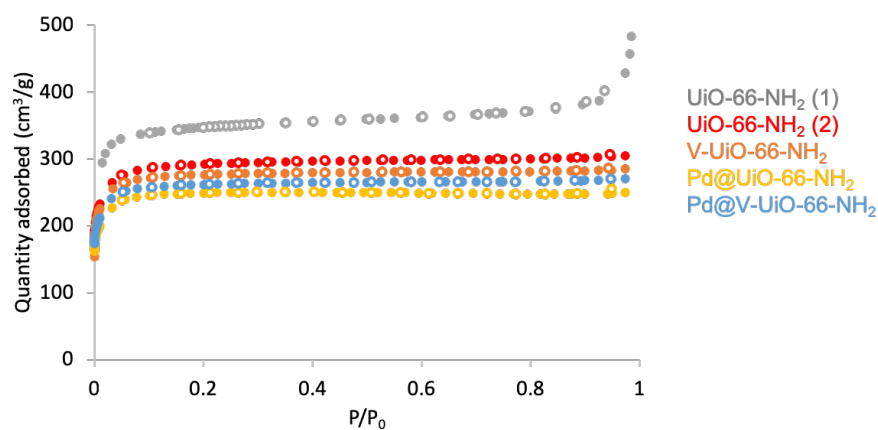


Figure 4.16 N₂ isotherms for UiO-66-NH₂ and its derivatives. Close symbols: adsorption; open symbols: desorption.

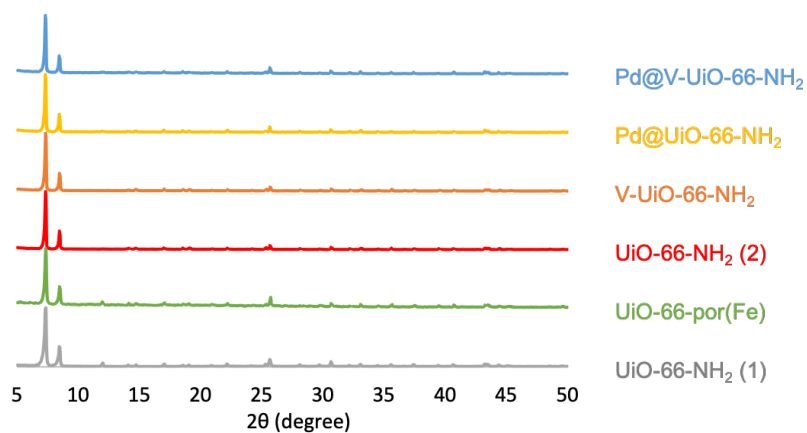


Figure 4.17 PXRD patterns of UiO-66-NH₂ and its derivatives.

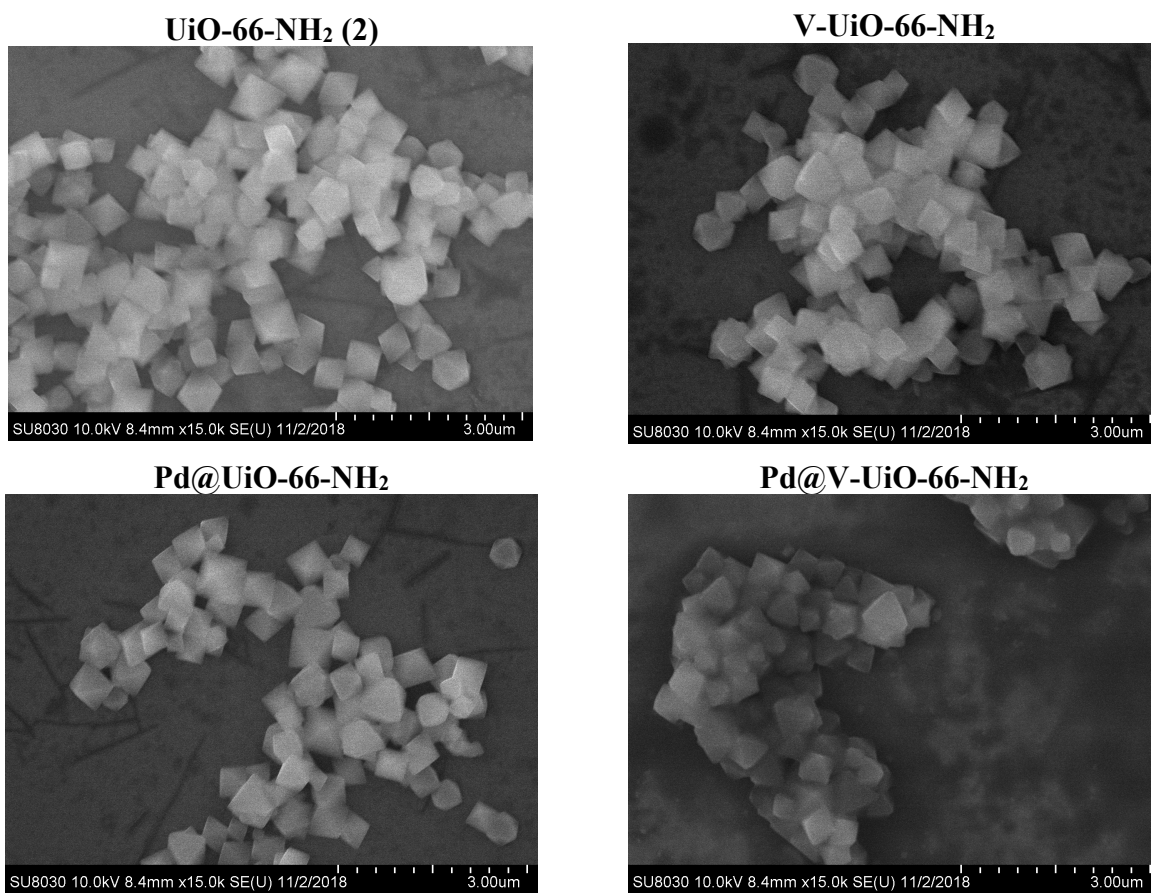


Figure 4.18 SEM images of UiO-66-NH₂ and its derivatives.

4.7.4 Evaluation of catalytic activity

The oxidation of sulfide with metalloporphyrin. In a 10-20 mL Biotage microwave vial, catalyst (1.76 mg of **(por)Fe**, 0.002 mmol of Fe; 1.41 mg of **(por)Mn**, 0.002 mmol of Mn; or 1.36 mg of **(por)V**, 0.002 mmol of V) was added to a solution of 20 mM methyl phenyl sulfide in CH₃OH/H₂O (7/3 v/v, 10 mL with naphthalene (20 mM) as an internal standard). After adding hydrogen peroxide (20 μ L of a 30 wt % solution in H₂O, 0.2 mmol), the combined mixture was stirred at room temperature for 4 h. At the appropriate time, an aliquot (100 μ L) of the reaction mixture was removed and mixed with CH₃OH (900 μ L) before being analyzed by GC-FID. Data are shown in Figure 4.2 and Table 4.1.

The oxidation of sulfide with UiO-66-NH₂ or UiO-66-por(Fe). In a 10-20 mL Biotage microwave vial, **UiO-66-por(Fe)** (8 mg, 0.005 mmol of Fe) (or a control, 8 mg of **UiO-66-NH₂** (1)) was added to a solution of 20 mM methyl phenyl sulfide in CH₃OH/H₂O (7/3 v/v, 10 mL with naphthalene (20 mM) as an internal standard). After adding hydrogen peroxide (20 μ L of a 30 wt % solution in H₂O, 0.2 mmol), the combined mixture was stirred at room temperature for either 6 or 24 h. At the appropriate time, an aliquot (~0.1 mL) of the reaction mixture was removed and filtered through a 0.2 μ m PTFE syringe filter (VWR International, North American Cat. No. 28145-495) that was attached to a disposable syringe. The clear filtrate was then analyzed by GC-FID; data are shown in Table 4.1.

The oxidation of sulfide using UiO-66-NH₂ or V-UiO-66-NH₂. In a 8 dram vial, **V-UiO-66-NH₂** (10 mg, 0.001 mmol of V) (or a control, 10 mg of **UiO-66-NH₂** (2)) was added to a solution of 8 mM methyl phenyl sulfide in CH₃OH/H₂O (7/3 v/v, 10 mL with naphthalene (8 mM) as an internal standard). After adding hydrogen peroxide (8 μ L of a 30 wt % solution in H₂O, 0.08

mmol), the combined mixture was stirred at room temperature for 3 h. At the appropriate time, an aliquot (~0.1 mL) of the reaction mixture was removed and filtered through a 0.2 μm PTFE syringe filter (VWR International, North American Cat. No. 28145-495) that was attached to a disposable syringe. The clear filtrate was then analyzed by GC-FID; data are shown in Figure 4.3.

Measurement of rate in sulfide oxidation at different flow rate. This experiment was carried out on the circulating-packed bed reactor (Figures 4.4 and 4.12). In an 8 dram vial equipped with a stir bar, H_2O_2 (25 μL of a 100 mM solution in H_2O , 0.0025 mmol) was added to a solution of 4 mM methyl phenyl sulfide in $\text{CH}_3\text{OH}/\text{H}_2\text{O}$ (7/3 v/v, 10 mL with naphthalene (4 mM) as an internal standard). While being stirred at room temperature, the mixture was delivered through a catalyst bed packed with a mixture of **V-UiO-66-NH₂** (5 mg, 0.005 mg V) and SiO_2 (5 mg) at a flow rate of 0.8, 1.0, 1.2, 1.4, or 1.6 mL/min. At the appropriate time, an aliquot (50 μL) of the reaction mixture was removed from the vial and mixed with CH_3OH (~450 μL) before being analyzed by GC-FID. Data are shown in Figure 4.5.

Measurement of rate in sulfide oxidation at different H_2O_2 concentration. In an 8 dram vial equipped with a stir bar, H_2O_2 (0.025, 0.05, 0.1, 0.15, 0.2, 0.3, 0.4, or 0.8 mmol) was added to a solution of 8 mM methyl phenyl sulfide in $\text{CH}_3\text{OH}/\text{H}_2\text{O}$ (7/3 v/v, 10 mL with naphthalene (8 mM) as an internal standard). While being stirred at room temperature, the mixture was delivered through a catalyst bed packed with a mixture of **V-UiO-66-NH₂** (10 mg, 0.01 mg V) and SiO_2 (10 mg) at a flow rate of 1.0 mL/min. At the appropriate time, an aliquot (50 μL) of the reaction mixture was removed from the vial and mixed with CH_3OH (~450 μL) before being analyzed by GC-FID. Data are shown in Figure 4.6.

Measurement of rate in H₂O₂ generation. This experiment was carried out on the high-pressure circulating-packed bed reactor shown in Figures 4.7 and 4.13. The autoclave was charged with CH₃OH/H₂O (7/3 v/v, 30 mL) and sealed. The solution was then pumped at a flow rate of ~7-8 mL/min through a catalyst bed packed with a mixture of Pd@UiO-66-NH₂ (10 mg, 0.3 mg Pd) and SiO₂ (10 mg). Then the autoclave was sequentially filled with 5% H₂/CO₂ (50 psig) and 25% O₂/CO₂ (20 psig). At every 15 min time point, an aliquot (20 μL) was drawn into a sample loop, which was then flushed for 30 s with CH₃OH/H₂O (7/3 v/v) using the HPLC pump (~0.25 mL/min) and the combined liquid was collected into a 1 dram vial. The whole vial was then weighted to quantify the amount of collected liquid, which was used to calculate the concentration of H₂O₂. A portion (50 μL) of the aliquot was combined with an aliquot of FOX reagent (950 μL). To analyze the concentration of H₂O₂, the absorbance at ~590 nm of the solution mixture was measured using UV-vis spectroscopy. Data are listed in Figure 4.8.

H₂O₂ generation from MOF samples with different contents of Pd NPs. This experiment was carried out in a similar manner as described in Section 2.9. Pd@UiO-66-NH₂ samples with different contents of Pd NPs were used. The generation of H₂O₂ was carried out in a 50 mL stainless-steel autoclave (model 4590, the maximum working pressure of 3000 psig, Parr Instrument, Inc., Moline, IL) equipped with an overhead mechanical stirrer, and thermocouple and pressure gauge for temperature and pressure measurements. The autoclave was charged with the catalysts (15 mg) and CH₃OH/H₂O (7/3 v/v, 20 mL). The autoclave was sealed and immersed into a room-temperature water bath and the mixture was stirred at 500 rpm. Then the autoclave was sequentially filled with 5% H₂/CO₂ (250 psig) and 25% O₂/CO₂ (100 psig) to give a final hydrogen-to-oxygen ratio of 1:2 at a total pressure of 350 psig. After the experiment has progressed for 1 h,

the autoclave was vented slowly and an aliquot (2 mL) of the reaction mixture was removed and filtered using a 0.2 μm PTFE syringe filter (VWR International, North American Cat. No. 28145-495) that is attached to a disposable syringe. The filtered aliquot (100 μL) was diluted 10 times with $\text{CH}_3\text{OH}/\text{H}_2\text{O}$ (7/3 v/v, 900 μL) before being mixed with an aliquot (1 mL) of 5 mM $\text{Ti}(\text{SO}_4)_2$ solution. (In an experiment where **Pd@UiO-66-NH₂** (0.03 wt % Pd) was used; a portion (1 mL) of the clear filtrate was combined with the aliquot (1 mL) of the 5 mM $\text{Ti}(\text{SO}_4)_2$ solution. To analyze the concentration of H_2O_2 , the absorbance at ~ 405 nm of the solution mixture was measured using a UV-vis spectrometer. Data are listed in Table 4.3.

Table 4.3 H_2O_2 generation at different amount of Pd NPs loading.

Pd NPs loading (wt %)	Pd NPs content (mg) ^a	H_2O_2 generation (mM)
3.0	0.45	5.7
0.3	0.045	4.6
0.03	0.0045	0.5

^aThis number was estimated based on the addition of Pd precursor in the **Pd@UiO-66-NH₂** synthesis. The materials used in these experiments were not listed in Table 4.2.

Catalytic [H_2O_2 generation + sulfide oxidation] tandem reaction. This experiment was carried out on the high-pressure circulating-packed bed reactor (Figures 4.7 and 4.13) equipped with HPLC inline analysis. The autoclave was charged with a solution of 8 mM methyl phenyl sulfide in $\text{CH}_3\text{OH}/\text{H}_2\text{O}$ (7/3 v/v, 30 mL) and sealed. The solution was then pumped at a flow rate of ~ 7 -10 mL/min through a catalyst bed packed with MOFs (see Table 4.4). After ~ 5 min, the autoclave was sequentially filled with 5% H_2/CO_2 (50 psig) and 25% O_2/CO_2 (20 psig). The aliquot from the reaction (2 μL) was collected and automatically injected into the HPLC column every 15 or 30 min for analysis. Data are listed in Figures 4.9-4.11.

Table 4.4 MOFs used in the [H₂O₂ generation + sulfide oxidation] tandem reaction.

Entry	MOFs	Amount of MOF (mg)
1	Pd@UiO-66-NH₂ (3 wt % Pd) + V-UiO-66-NH₂ (1 wt % V)	5 + 10
2	Pd@UiO-66-NH₂ (3 wt % Pd) + V-UiO-66-NH₂ (1 wt % V)	10 + 10
3	Pd@V-UiO-66-NH₂ (0.16 wt % Pd and 1 wt % V)	20

Chapter 5

Epilogue

5.1 General conclusions about the work described in this thesis

This thesis has demonstrated the development of MOF-based catalysts for the [H₂O₂ generation + oxidation] tandem reaction, in which H₂O₂ is generated and used in the same reaction pot as the oxidation, eliminating the need for a separate reaction process. In addition, the *in-situ* production of unstable H₂O₂ allows for fast and efficient utilization in the subsequent oxidation. In chapter 2, we designed and synthesized dually functionalized UiO-66 MOF crystals that contain encapsulated metal NPs and surface-incorporated Mo^{VI} complexes for catalyzing the [H₂O₂ generation + alkene oxidation] tandem reaction. The close proximity of these two catalyst sites resulted in an enhancement of epoxide productivity compared to a physical mixture of two singly functionalized UiO-66 crystals. Our work also demonstrated that the encapsulation of NPs inside the MOF crystals can suppress the alkene-hydrogenation side reaction.

The work in chapter 2 revealed the importance of matching the reaction rates in our tandem reactions for efficient generation and consumption of H₂O₂. In chapter 3, we then attempted to reach this goal through sulfide oxidation, a faster reaction than alkene oxidation, to match the rate of our H₂O₂-generation step. The UiO-66 MOF exhibited catalytic activity for this reaction and the modification of its node to pose higher numbers of open-coordination sites resulted in a catalyst with increased H₂O₂ consumption. In addition, kinetic study and computational modeling allow us to elucidate the nature of these open-coordination sites and their mechanism in catalyzing H₂O₂-induced sulfide oxidation.

As it became crucial to obtain accurate rates for each reaction step for matching, chapter 4 demonstrates how measuring the rates of H₂O₂ generation and sulfide oxidation can be carried out in a circulating flow reaction system. This new strategy allows us to obtain those rate values at

low conversion, where the catalytic activity is best determined. We also developed a UiO-66 catalyst with V^{IV} species on the open-coordination sites to further increase the consumption rate of H₂O₂ in sulfide oxidation. In addition, the loading of encapsulated metal NPs in UiO-66 was also tuned to match the rate of oxidation. Based on these strategies, the desired NPs and V^{IV} species were both incorporated on UiO-66 crystals to catalyze a tandem reaction that would generate and consume H₂O₂ more efficiently than the consumption reported in chapter 2. While this thesis has focused on the modification of UiO-66 MOF as a catalyst for the [H₂O₂ generation + oxidation] tandem reaction in the solution phase, these promising results can lead to possible future work that are outlined below.

5.2 MOFs with larger pore size for better mass transportation and more catalyst loading

In this thesis, we mainly employed the UiO-66 MOF derivative as a model support for our catalyst. Although its small pore ($\sim 6 \text{ \AA}^{189}$) was required to selectively screen out certain substrates (i.e., alkenes from the encapsulated NPs in our previous study), this can limit the accessibility of internal oxidation catalyst sites and result in a low rate. Evidence of this inhibited accessibility was shown in chapter 3, in which not all of the open-coordination sites on the node of UiO-66 could be easily accessed by sulfide, resulting in a smaller increase in the rate of sulfide oxidation than expected. In addition, the small pores of UiO-66 also result in low incorporation of catalyst complexes into either the organic linkers or nodes of UiO-66. To extend this work, MOF supports with larger pore sizes would be a solution for enhancing the mass transportation of substrate and the loading of oxidation catalyst in cases where substrate screening is not required.

The most obvious candidate is robust Zr-based MOFs comprising of organic linkers that are longer than 1,4-dibenzenecarboxylic acids in UiO-66. For example, two other MOFs in the

UiO-6X families, UiO-67 (with 4,4'-biphenyldicarboxylic acid linkers) and UiO-68 (with tetraphenyldicarboxylic acid linkers) (Figure 5.1), have larger pore diameters than that of UiO-66.¹⁴⁵ Their organic linkers can pose functional groups such as aminos and hydroxyls that can be modified to incorporate many metal complexes. Another attractive candidate would be MOFs in PCN families that have the same $[\text{Zr}_6(\text{O})_4(\text{OH})_4]$ nodes but with porphyrin linkers (Figure 5.1).¹⁹⁰⁻
¹⁹¹ As discussed in chapter 4, porphyrin can strongly chelate with various metal species that are catalytically active in oxidation.

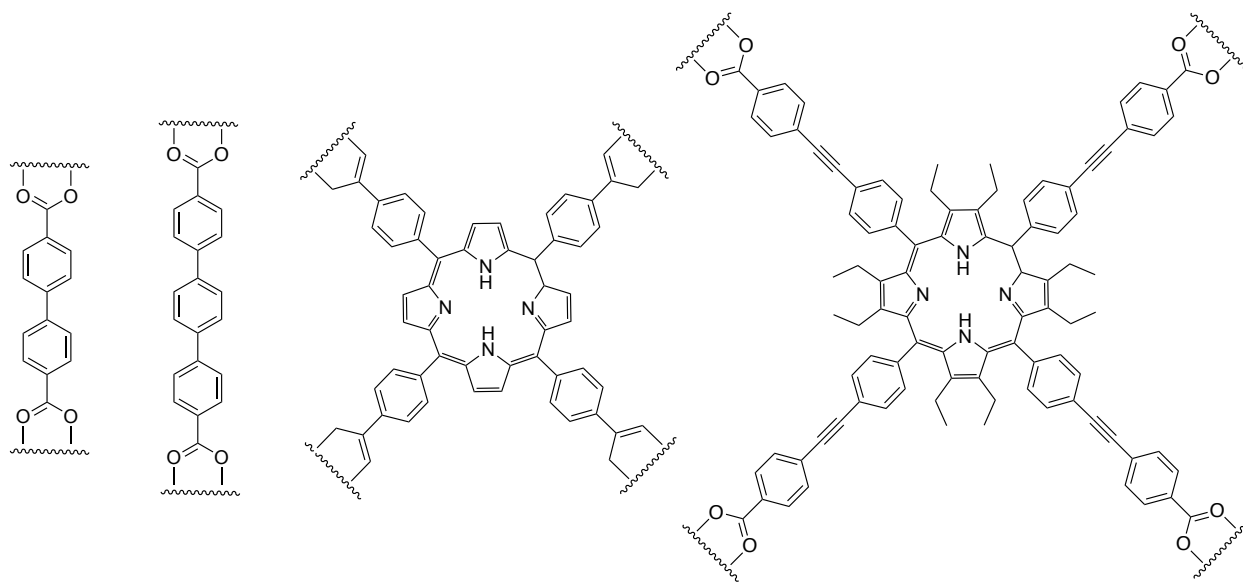


Figure 5.1 The organic linkers (left to right) of UiO-67, UiO-68, PCN-222, and PCN-229 MOFs.

5.3 Tandem reaction in the gas phase to eliminate solvent and simplify separation

In this thesis, we have demonstrated the catalyst design and reaction development using solution-phase tandem reactions. As two of our three starting materials are gaseous, another possible future direction is the extension of the $[\text{H}_2\text{O}_2$ generation + oxidation] tandem reaction to the gas phase. The elimination of solvent could reduce waste, resulting in a simpler and cleaner

process from an environmental perspective. Gas-phase reactions also eliminate low-solubility issues of H_2 gas, O_2 gas, and many organic reagents in the $\text{CH}_3\text{OH}/\text{H}_2\text{O}$ medium that we used, thus enhance the overall reaction rate. Lastly, the temperature in gas-phase reactions can be implemented over a wider range to increase the mobility and collision frequency of molecules, resulting in a faster reaction.

One attractive reaction that appeals to industry is the [H_2O_2 generation + propene epoxidation] tandem reaction to generate propene oxide, an important intermediate for the production of propylene glycol, polyols, and polyurethane (Figure 5.2a).¹⁹ Another potential target would be the [H_2O_2 generation + benzene oxidation] tandem reaction to generate phenol, an intermediate for the production of biphenol A, cyclohexanol, a polycarbonates (Figure 5.2b).

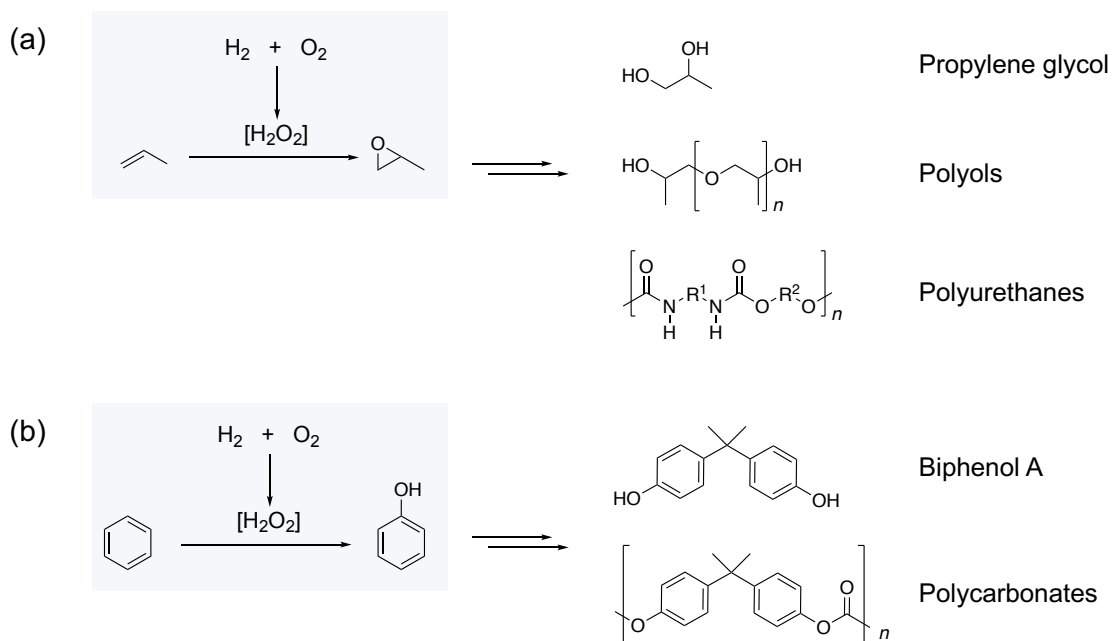


Figure 5.2 Two potential oxidation-focused tandem reactions in the gas phase. (a) [H_2O_2 generation + propene epoxidation] tandem reaction. (b) [H_2O_2 generation + benzene oxidation] tandem reaction.

5.4 Last remarks

Beyond oxidation, there are still many multistep processes that involve intermediates that are unstable, hazardous, or in equilibrium with other species. While most of these are currently unexplored as tandem reactions, we hope that our work would stimulate interest in their development into efficient tandem processes. In addition, we envisioned that the study in this thesis can serve as a model protocol for the design and optimization of efficient tandem reactions. Due to fast advancement in MOF synthesis and modification, there are many attractive materials that can be used as supports for tandem catalysts. We are confident that more examples of utilizing MOFs in tandem reactions will emerge to address challenges in both academia and industry.

REFERENCES

1. Wasilke, J.-C.; Obrey, S. J.; Baker, R. T.; Bazan, G. C., Concurrent tandem catalysis. *Chem. Rev.* **2005**, *105*, 1001-1020.
2. Lohr, T. L.; Marks, T. J., Orthogonal tandem catalysis. *Nat. Chem.* **2015**, *7*, 477-482.
3. Parsons, P. J.; Penkett, C. S.; Shell, A. J., Tandem reactions in organic synthesis: novel strategies for natural product elaboration and the development of new synthetic methodology. *Chem. Rev.* **1996**, *96*, 195-206.
4. Robert, C.; Thomas, C. M., Tandem catalysis: a new approach to polymers. *Chem. Soc. Rev.* **2013**, *42*, 9392-9402.
5. Hayashi, Y., Pot economy and one-pot synthesis. *Chem. Sci.* **2016**, *7*, 866-880.
6. Dydio, P.; Ploeger, M.; Reek, J. N. H., Selective isomerization–hydroformylation sequence: a strategy to valuable α -methyl-branched aldehydes from terminal olefins. *ACS Catal.* **2013**, *3*, 2939-2942.
7. Sebren, L. J.; Devery, J. J.; Stephenson, C. R. J., Catalytic radical domino reactions in organic synthesis. *ACS Catal.* **2014**, *4*, 703-716.
8. Zhou, J., Recent advances in multicatalyst promoted asymmetric tandem reactions. *Chem. Asian J.* **2010**, *5*, 422-434.
9. Jeong, N.; Seo, S. D.; Shin, J. Y., One pot preparation of bicyclopentenones from propargyl malonates (and propargylsulfonamides) and allylic acetates by a tandem action of catalysts. *J. Am. Chem. Soc.* **2000**, *122*, 10220-10221.
10. Climent, M. J.; Corma, A.; Iborra, S.; Sabater, M. J., Heterogeneous catalysis for tandem reactions. *ACS Catal.* **2014**, *4*, 870-891.
11. Huang, H.; Denard, C. A.; Alamillo, R.; Crisci, A. J.; Miao, Y.; Dumesic, J. A.; Scott, S. L.; Zhao, H., Tandem catalytic conversion of glucose to 5-hydroxymethylfurfural with an immobilized enzyme and a solid acid. *ACS Catal.* **2014**, *4*, 2165-2168.
12. Yamada, Y.; Tsung, C.-K.; Huang, W.; Huo, Z.; Habas, S. E.; Soejima, T.; Aliaga, C. E.; Somorjai, G. A.; Yang, P., Nanocrystal bilayer for tandem catalysis. *Nat. Chem.* **2011**, *3*, 372-376.
13. Murzin, D. Y., On spatial control in heterogeneous multifunctional catalysts. *Catal. Lett.* **2017**, *147*, 613-621.

14. Zečević, J.; Vanbutsele, G.; de Jong, K. P.; Martens, J. A., Nanoscale intimacy in bifunctional catalysts for selective conversion of hydrocarbons. *Nature* **2015**, *528*, 245-248.
15. Edwards, J. K.; Solsona, B. E.; Landon, P.; Carley, A. F.; Herzing, A.; Kiely, C. J.; Hutchings, G. J., Direct synthesis of hydrogen peroxide from H₂ and O₂ using TiO₂-supported Au–Pd catalysts. *J. Catal.* **2005**, *236*, 69-79.
16. O’Callaghan, N.; Sullivan, J. A., Towards selective catalytic oxidations using *in situ* generated H₂O₂. *Appl. Catal., B.* **2014**, *146*, 258-266.
17. Campos-Martin, J. M.; Blanco-Brieva, G.; Fierro, J. L. G., Hydrogen peroxide synthesis: An outlook beyond the anthraquinone process. *Angew. Chem., Int. Ed.* **2006**, *45*, 6962-6984.
18. Goti, A.; Cardona, F., *Hydrogen peroxide in green oxidation reactions: Recent catalytic processes*. Springer: Dordrecht, Netherlands, 2008; pp 191-212.
19. Puértolas, B.; Hill, A. K.; García, T.; Solsona, B.; Torrente-Murciano, L., *In-situ* synthesis of hydrogen peroxide in tandem with selective oxidation reactions: a mini-review. *Catal. Today* **2015**, *248*, 115-127.
20. Jones, C. W., *Applications of Hydrogen Peroxide and Derivatives*. Royal Society of Chemistry: Cambridge, UK, 1999; pp 1-35.
21. Doherty, S.; Knight, J. G.; Carroll, M. A.; Ellison, J. R.; Hobson, S. J.; Stevens, S.; Hardacre, C.; Goodrich, P., Efficient and selective hydrogen peroxide-mediated oxidation of sulfides in batch and segmented and continuous flow using a peroxometalate-based polymer immobilised ionic liquid phase catalyst. *Green Chem.* **2015**, *17*, 1559-1571.
22. Freakley, S. J.; Piccinini, M.; Edwards, J. K.; Ntainjua, E. N.; Moulijn, J. A.; Hutchings, G. J., Effect of reaction conditions on the direct synthesis of hydrogen peroxide with a AuPd/TiO₂ catalyst in a flow reactor. *ACS Catal.* **2013**, *3*, 487-501.
23. Yi, Y.; Wang, L.; Li, G.; Guo, H., A review on research progress in the direct synthesis of hydrogen peroxide from hydrogen and oxygen: noble-metal catalytic method, fuel-cell method and plasma method. *Catal. Sci. Technol.* **2016**, *6*, 1593-1610.
24. Edwards, J. K.; Freakley, S. J.; Lewis, R. J.; Pritchard, J. C.; Hutchings, G. J., Advances in the direct synthesis of hydrogen peroxide from hydrogen and oxygen. *Catal. Today* **2015**, *248*, 3-9.
25. Chung, Y.-M.; Lee, Y.-R.; Ahn, W.-S., Direct synthesis of hydrogen peroxide from hydrogen and oxygen over Pd-supported metal-organic framework catalysts. *Bull. Korean Chem. Soc.* **2015**, *36*, 1378-1383.

26. Meunier, B., *Metal-oxo and metal-peroxo species in catalytic oxidations*. Springer Berlin Heidelberg: Berlin, Germany, 2003; pp 1-323.
27. Chen, Y.-Z.; Zhang, R.; Jiao, L.; Jiang, H.-L., Metal-organic framework-derived porous materials for catalysis. *Coord. Chem. Rev.* **2018**, *362*, 1-23.
28. Zhang, Q.; Lee, I.; Joo, J. B.; Zaera, F.; Yin, Y., Core-shell nanostructured catalysts. *Acc. Chem. Res.* **2013**, *46*, 1816-1824.
29. Hu, P.; Morabito, J. V.; Tsung, C.-K., Core-shell catalysts of metal nanoparticle core and metal-organic framework shell. *ACS Catal.* **2014**, *4*, 4409-4419.
30. Lu, G.; Li, S.; Guo, Z.; Farha, O. K.; Hauser, B. G.; Qi, X.; Wang, Y.; Wang, X.; Han, S.; Liu, X.; DuChene, J. S.; Zhang, H.; Zhang, Q.; Chen, X.; Ma, J.; Loo, S. C. J.; Wei, W. D.; Yang, Y.; Hupp, J. T.; Huo, F., Imparting functionality to a metal-organic framework material by controlled nanoparticle encapsulation. *Nat. Chem.* **2012**, *4*, 310-316.
31. Zhao, M.; Deng, K.; He, L.; Liu, Y.; Li, G.; Zhao, H.; Tang, Z., Core-shell palladium nanoparticle@metal-organic frameworks as multifunctional catalysts for cascade reactions. *J. Am. Chem. Soc.* **2014**, *136*, 1738-1741.
32. Cavka, J. H.; Jakobsen, S.; Olsbye, U.; Guillou, N.; Lamberti, C.; Bordiga, S.; Lillerud, K. P., A new zirconium inorganic building brick forming metal organic frameworks with exceptional stability. *J. Am. Chem. Soc.* **2008**, *130*, 13850-13851.
33. Kandiah, M.; Nilsen, M. H.; Usseglio, S.; Jakobsen, S.; Olsbye, U.; Tilset, M.; Larabi, C.; Quadrelli, E. A.; Bonino, F.; Lillerud, K. P., Synthesis and stability of tagged UiO-66 Zr-MOFs. *Chem. Mater.* **2010**, *22*, 6632-6640.
34. Lin, K.-Y. A.; Liu, Y.-T.; Chen, S.-Y., Adsorption of fluoride to UiO-66-NH₂ in water: Stability, kinetic, isotherm and thermodynamic studies. *J. Colloid Interface Sci.* **2016**, *461*, 79-87.
35. Liu, X.; Demir, N. K.; Wu, Z.; Li, K., Highly water-stable zirconium metal-organic framework UiO-66 membranes supported on alumina hollow fibers for desalination. *J. Am. Chem. Soc.* **2015**, *137*, 6999-7002.
36. Grigoropoulou, G.; Clark, J. H.; Elings, J. A., Recent developments on the epoxidation of alkenes using hydrogen peroxide as an oxidant. *Green Chem.* **2003**, *5*, 1-7.
37. Lee, W.-S.; Akatay, M. C.; Stach, E. A.; Ribeiro, F. H.; Delgass, W. N., Enhanced reaction rate for gas-phase epoxidation of propylene using H₂ and O₂ by Cs promotion of Au/TS-1. *J. Catal.* **2013**, *308*, 98-113.

38. Lee, W.-S.; Akatay, M. C.; Stach, E. A.; Ribeiro, F. H.; Delgass, W. N., Gas-phase epoxidation of propylene in the presence of H₂ and O₂ over small gold ensembles in uncalcined TS-1. *J. Catal.* **2014**, *313*, 104-112.
39. Huang, J.; Takei, T.; Akita, T.; Ohashi, H.; Haruta, M., Gold clusters supported on alkaline treated TS-1 for highly efficient propene epoxidation with O₂ and H₂. *Appl. Catal., B.* **2010**, *95*, 430-438.
40. Lee, W.-S.; Lai, L.-C.; Akatay, M. C.; Stach, E. A.; Ribeiro, F. H.; Delgass, W. N., Probing the gold active sites in Au/TS-1 for gas-phase epoxidation of propylene in the presence of hydrogen and oxygen. *J. Catal.* **2012**, *296*, 31-42.
41. Hashmi, A. S. K., Gold-catalyzed organic reactions. *Chem. Rev.* **2007**, *107*, 3180-3211.
42. Singh, U. K.; Vannice, M. A., Kinetics of liquid-phase hydrogenation reactions over supported metal catalysts — a review. *Appl. Catal., A.* **2001**, *213*, 1-24.
43. Kertalli, E.; Schouten, J. C.; Nijhuis, T. A., Direct synthesis of propylene oxide in the liquid phase under mild conditions. *Appl. Catal., A.* **2016**, *524*, 200-205.
44. Laufer, W.; Hoelderich, W. F., Direct oxidation of propylene and other olefins on precious metal containing Ti-catalysts. *Appl. Catal., A.* **2001**, *213*, 163-171.
45. Prieto, A.; Palomino, M.; Díaz, U.; Corma, A., One-pot two-step process for direct propylene oxide production catalyzed by bi-functional Pd(Au)@TS-1 materials. *Appl. Catal., A.* **2016**, *523*, 73-84.
46. Qi, C.; Huang, J.; Bao, S.; Su, H.; Akita, T.; Haruta, M., Switching of reactions between hydrogenation and epoxidation of propene over Au/Ti-based oxides in the presence of H₂ and O₂. *J. Catal.* **2011**, *281*, 12-20.
47. Hikazudani, S.; Mochida, T.; Matsuo, N.; Nagaoka, K.; Ishihara, T.; Kobayashi, H.; Takita, Y., Monoatomically dispersed Pd/TiO₂ catalyst effective for epoxidation of propylene at ambient temperature in the presence of H₂ and O₂. *J. Mol. Catal. A: Chem.* **2012**, *358*, 89-98.
48. Lee, W.-S.; Akatay, M. C.; Stach, E. A.; Ribeiro, F. H.; Delgass, W. N., Reproducible preparation of Au/TS-1 with high reaction rate for gas phase epoxidation of propylene. *J. Catal.* **2012**, *287*, 178-189.
49. Wang, R.; Guo, X.; Wang, X.; Hao, J., Gas-phase epoxidation of propylene over Ag/Ti-containing catalysts. *Catal. Today* **2004**, *93-95*, 217-222.

50. Jiang, H.-L.; Liu, B.; Akita, T.; Haruta, M.; Sakurai, H.; Xu, Q., Au@ZIF-8: CO oxidation over gold nanoparticles deposited to metal–organic framework. *J. Am. Chem. Soc.* **2009**, *131*, 11302-11303.
51. Li, X.; Guo, Z.; Xiao, C.; Goh, T. W.; Tesfagaber, D.; Huang, W., Tandem catalysis by palladium nanoclusters encapsulated in metal–organic frameworks. *ACS Catal.* **2014**, *4*, 3490-3497.
52. Zhao, M.; Yuan, K.; Wang, Y.; Li, G.; Guo, J.; Gu, L.; Hu, W.; Zhao, H.; Tang, Z., Metal–organic frameworks as selectivity regulators for hydrogenation reactions. *Nature* **2016**, *539*, 76-80.
53. Kuo, C.-H.; Tang, Y.; Chou, L.-Y.; Sneed, B. T.; Brodsky, C. N.; Zhao, Z.; Tsung, C.-K., Yolk–shell nanocrystal@ZIF-8 nanostructures for gas-phase heterogeneous catalysis with selectivity control. *J. Am. Chem. Soc.* **2012**, *134*, 14345-14348.
54. Guo, Z.; Xiao, C.; Maligal-Ganesh, R. V.; Zhou, L.; Goh, T. W.; Li, X.; Tesfagaber, D.; Thiel, A.; Huang, W., Pt nanoclusters confined within metal–organic framework cavities for chemoselective cinnamaldehyde hydrogenation. *ACS Catal.* **2014**, *4*, 1340-1348.
55. Song, F.; Wang, C.; Falkowski, J. M.; Ma, L.; Lin, W., Isoreticular chiral metal–organic frameworks for asymmetric alkene epoxidation: tuning catalytic activity by controlling framework catenation and varying open channel sizes. *J. Am. Chem. Soc.* **2010**, *132*, 15390-15398.
56. Shultz, A. M.; Farha, O. K.; Hupp, J. T.; Nguyen, S. T., A catalytically active, permanently microporous MOF with metalloporphyrin struts. *J. Am. Chem. Soc.* **2009**, *131*, 4204-4205.
57. de Silva, N.; Ha, J.-M.; Solovyov, A.; Nigra, M. M.; Ogino, I.; Yeh, S. W.; Durkin, K. A.; Katz, A., A bioinspired approach for controlling accessibility in calix[4]arene-bound metal cluster catalysts. *Nat. Chem.* **2010**, *2*, 1062-1068.
58. Ling, P.; Lei, J.; Jia, L.; Ju, H., Platinum nanoparticles encapsulated metal-organic frameworks for the electrochemical detection of telomerase activity. *Chem. Commun.* **2016**, *52*, 1226-1229.
59. Zhang, W.; Lu, G.; Cui, C.; Liu, Y.; Li, S.; Yan, W.; Xing, C.; Chi, Y. R.; Yang, Y.; Huo, F., A family of metal-organic frameworks exhibiting size-selective catalysis with encapsulated noble-metal nanoparticles. *Adv. Mater.* **2014**, *26*, 4056-4060.
60. Zhu, J.; Wang, P. C.; Lu, M., Selective oxidation of benzyl alcohol under solvent-free condition with gold nanoparticles encapsulated in metal-organic framework. *Appl. Catal., A.* **2014**, *477*, 125-131.

61. Nguyen, H. G. T.; Schweitzer, N. M.; Chang, C.-Y.; Drake, T. L.; So, M. C.; Stair, P. C.; Farha, O. K.; Hupp, J. T.; Nguyen, S. T., Vanadium-node-functionalized UiO-66: A thermally stable MOF-supported catalyst for the gas-phase oxidative dehydrogenation of cyclohexene. *ACS Catal.* **2014**, *4*, 2496-2500.
62. Tang, J.; Dong, W.; Wang, G.; Yao, Y.; Cai, L.; Liu, Y.; Zhao, X.; Xu, J.; Tan, L., Efficient molybdenum(VI) modified Zr-MOF catalysts for epoxidation of olefins. *RSC Adv.* **2014**, *4*, 42977-42982.
63. Kardanpour, R.; Tangestaninejad, S.; Mirkhani, V.; Moghadam, M.; Mohammadpoor-Baltork, I.; Zadehahmadi, F., Anchoring of Cu(II) onto surface of porous metal-organic framework through post-synthesis modification for the synthesis of benzimidazoles and benzothiazoles. *J. Solid State Chem.* **2016**, *235*, 145-153.
64. Pintado-Sierra, M.; Rasero-Almansa, A. M.; Corma, A.; Iglesias, M.; Sánchez, F., Bifunctional iridium-(2-aminoterephthalate)-Zr-MOF chemoselective catalyst for the synthesis of secondary amines by one-pot three-step cascade reaction. *J. Catal.* **2013**, *299*, 137-145.
65. Chen, L.; Chen, H.; Li, Y., One-pot synthesis of Pd@MOF composites without the addition of stabilizing agents. *Chem. Commun.* **2014**, *50*, 14752-14755.
66. Shen, L.; Luo, M.; Huang, L.; Feng, P.; Wu, L., A clean and general strategy to decorate a titanium metal-organic framework with noble-metal nanoparticles for versatile photocatalytic applications. *Inorg. Chem.* **2015**, *54*, 1191-1193.
67. Jin, M.; Liu, H.; Zhang, H.; Xie, Z.; Liu, J.; Xia, Y., Synthesis of Pd nanocrystals enclosed by {100} facets and with sizes <10 nm for application in CO oxidation. *Nano Res.* **2010**, *4*, 83-91.
68. Edwards, J. K.; Pritchard, J.; Lu, L.; Piccinini, M.; Shaw, G.; Carley, A. F.; Morgan, D. J.; Kiely, C. J.; Hutchings, G. J., The direct synthesis of hydrogen peroxide using platinum-promoted gold-palladium catalysts. *Angew. Chem., Int. Ed.* **2014**, *53*, 2381-2384.
69. Ntainjua, E. N.; Piccinini, M.; Freakley, S. J.; Pritchard, J. C.; Edwards, J. K.; Carley, A. F.; Hutchings, G. J., Direct synthesis of hydrogen peroxide using Au-Pd-exchanged and supported heteropolyacid catalysts at ambient temperature using water as solvent. *Green Chem.* **2012**, *14*, 170-181.
70. Landon, P.; Collier, P. J.; Carley, A. F.; Chadwick, D.; Papworth, A. J.; Burrows, A.; Kiely, C. J.; Hutchings, G. J., Direct synthesis of hydrogen peroxide from H₂ and O₂ using Pd and Au catalysts. *Phys. Chem. Chem. Phys.* **2003**, *5*, 1917-1923.

71. Wilson, N. M.; Flaherty, D. W., Mechanism for the direct synthesis of H₂O₂ on Pd clusters: Heterolytic reaction pathways at the liquid–solid interface. *J. Am. Chem. Soc.* **2016**, *138*, 574-586.
72. We note in passing that the activity of **Pd@UiO66-(sal)Mo** in H₂O₂ generation was not evaluated due to interference of the leached Mo species (see Section 2.9) with the colorimetric analysis.
73. Alba-Rubio, A. C.; Plauck, A.; Stangland, E. E.; Mavrikakis, M.; Dumesic, J. A., Direct synthesis of hydrogen peroxide over Au–Pd catalysts prepared by electroless deposition. *Catal. Lett.* **2015**, *145*, 2057-2065.
74. Patil, N. S.; Uphade, B. S.; McCulloh, D. G.; Bhargava, S. K.; Choudhary, V. R., Styrene epoxidation over gold supported on different transition metal oxides prepared by homogeneous deposition–precipitation. *Catal. Commun.* **2004**, *5*, 681-685.
75. Della Pina, C.; Falletta, E.; Prati, L.; Rossi, M., Selective oxidation using gold. *Chem. Soc. Rev.* **2008**, *37*, 2077-2095.
76. Kuwahara, Y.; Ando, T.; Kango, H.; Yamashita, H., Palladium nanoparticles encapsulated in hollow titanosilicate spheres as an ideal nanoreactor for one-pot oxidation. *Chem. Eur. J.* **2017**, *23*, 380-389.
77. Lin, J.-L.; Palomec, L.; Wheeldon, I., Design and analysis of enhanced catalysis in scaffolded multienzyme cascade reactions. *ACS Catal.* **2014**, *4*, 505-511.
78. Ricca, E.; Brucher, B.; Schrittwieser, J. H., Multi-enzymatic cascade reactions: Overview and perspectives. *Adv. Synth. Catal.* **2011**, *353*, 2239-2262.
79. Wheeldon, I.; Minter, S. D.; Banta, S.; Barton, S. C.; Atanassov, P.; Sigman, M., Substrate channelling as an approach to cascade reactions. *Nat. Chem.* **2016**, *8*, 299-309.
80. Lee, L.-C.; Lu, J.; Weck, M.; Jones, C. W., Acid–base bifunctional shell cross-linked micelle nanoreactor for one-pot tandem Reaction. *ACS Catal.* **2016**, *6*, 784-787.
81. <https://www.micromeritics.com/Product-Showcase/MicroActive-Interactive-Data-Analysis-Software/MicroActive-Interactive-Data-Analysis-Reports.aspx> (accessed April 17, 2019).
82. Zabetakis, M. G., *Flammability characteristics of combustible gases and vapors*. U.S. Department of the Interior, Bureau of Mines: Washington, D.C., 1965; Vol. 627, pp 1-121.
83. Dwyer, J. J.; Hansel, J. G.; Philips, T., *Temperature Influence on the Flammability Limits of Heat Treating Atmospheres*. Air Products and Chemicals, Inc.: 2003.

84. Schroeder, V.; Holtappels, K., In *Safety of hydrogen as an energy carrier, Proceedings of the HySafe International Conference on Hydrogen Safety*: Pisa, Italy, 2005.
85. Dong, W.; Feng, C.; Zhang, L.; Shang, N.; Gao, S.; Wang, C.; Wang, Z., Pd@UiO-66: An efficient catalyst for Suzuki–Miyaura coupling reaction at mild condition. *Catal. Lett.* **2016**, *146*, 117-125.
86. Pourkhosravani, M.; Dehghanpour, S.; Farzaneh, F., Palladium nanoparticles supported on zirconium metal organic framework as an efficient heterogeneous catalyst for the Suzuki–Miyaura coupling reaction. *Catal. Lett.* **2016**, *146*, 499-508.
87. Shen, L.; Wu, W.; Liang, R.; Lin, R.; Wu, L., Highly dispersed palladium nanoparticles anchored on UiO-66(NH₂) metal-organic framework as a reusable and dual functional visible-light-driven photocatalyst. *Nanoscale* **2013**, *5*, 9374-9382.
88. Ashby, E. C.; Coleman, D., Evidence for single electron transfer in the reactions of lithium dimethylcuprate with alkyl halides. *J. Org. Chem.* **1987**, *52*, 4554-4565.
89. Limnios, D.; Kokotos, C. G., 2,2,2-Trifluoroacetophenone: An organocatalyst for an environmentally friendly epoxidation of alkenes. *J. Org. Chem.* **2014**, *79*, 4270-4276.
90. Liu, X.; Xia, Q.; Zhang, Y.; Chen, C.; Chen, W., Cu-NHC-TEMPO catalyzed aerobic oxidation of primary alcohols to aldehydes. *J. Org. Chem.* **2013**, *78*, 8531-8536.
91. Chowdhury, A. D.; Ray, R.; Lahiri, G. K., An iron catalyzed regioselective oxidation of terminal alkenes to aldehydes. *Chem. Commun.* **2012**, *48*, 5497-5499.
92. Eisenberg, G., Colorimetric determination of hydrogen peroxide. *Ind. Eng. Chem., Anal. Ed.* **1943**, *15*, 327-328.
93. Mimoun, H. S. d. R., I.; Sajus, L., Covalent peroxide complexes of molybdenum. *Bull. Soc. Chim. Fr.* **1969**, 1481-1492.
94. Weyland, M.; Midgley, P. A.; Thomas, J. M., Electron tomography of nanoparticle catalysts on porous supports: a new technique based on Rutherford scattering. *J. Phys. Chem. B* **2001**, *105*, 7882-7886.
95. Aijaz, A.; Karkamkar, A.; Choi, Y. J.; Tsumori, N.; Rönnebro, E.; Autrey, T.; Shioyama, H.; Xu, Q., Immobilizing highly catalytically active Pt nanoparticles inside the pores of metal–organic framework: a double solvents approach. *J. Am. Chem. Soc.* **2012**, *134*, 13926-13929.
96. Fernandes, C. I.; Rudic, S.; Vaz, P. D.; Nunes, C. D., Looking inside the pores of a MCM-41 based Mo heterogeneous styrene oxidation catalyst: an inelastic neutron scattering study. *Phys. Chem. Chem. Phys.* **2016**, *18*, 17272-17280.

97. Maurya, M. R.; Kumar, M.; Sikarwar, S., Polymer-anchored oxoperoxo complexes of vanadium(V), molybdenum(VI) and tungsten(VI) as catalyst for the oxidation of phenol and styrene using hydrogen peroxide as oxidant. *React. Funct. Polym.* **2006**, *66*, 808-818.
98. Bortolini, O.; Di Furia, F.; Modena, G.; Seraglia, R., Metal catalysis in oxidation by peroxides. Sulfide oxidation and olefin epoxidation by dilute hydrogen peroxide, catalyzed by molybdenum and tungsten derivatives under phase-transfer conditions. *J. Org. Chem.* **1985**, *50*, 2688-2690.
99. Granadeiro, C. M.; Ribeiro, S. O.; Karmaoui, M.; Valenca, R.; Ribeiro, J. C.; de Castro, B.; Cunha-Silva, L.; Balula, S. S., Production of ultra-deep sulfur-free diesels using a sustainable catalytic system based on UiO-66(Zr). *Chem. Commun.* **2015**, *51*, 13818-13821.
100. Ye, G.; Zhang, D.; Li, X.; Leng, K.; Zhang, W.; Ma, J.; Sun, Y.; Xu, W.; Ma, S., Boosting catalytic performance of metal-organic framework by increasing the defects via a facile and green approach. *ACS Appl. Mater. Interfaces* **2017**, *9*, 34937-34943.
101. Artner, C.; Czakler, M.; Schubert, U., New zirconium and zirconium-titanium oxo cluster types by expansion or metal substitution of the octahedral Zr_6O_8 structural motif. *Inorg. Chim. Acta* **2015**, *432*, 208-212.
102. Kickelbick, G.; Wiede, P.; Schubert, U., Variations in capping the $Zr_6O_4(OH)_4$ cluster core: X-ray structure analyses of $[Zr_6(OH)_4O_4(OOC-CH=CH_2)_{10}]_2(\mu-OOC-CH=CH_2)_4$ and $Zr_6(OH)_4O_4(OOCR)_{12}(PrOH)$ (R = Ph, CMe = CH_2). *Inorg. Chim. Acta* **1999**, *284*, 1-7.
103. Piszczek, P.; Radtke, A.; Grodzicki, A.; Wojtczak, A.; Chojnacki, J., The new type of $[Zr_6(\mu_3-O)_4(\mu_3-OH)_4]$ cluster core: crystal structure and spectral characterization of $[Zr_6O_4(OH)_4(OOCR)_{12}]$ (R = Bu^t , $C(CH_3)_2Et$). *Polyhedron* **2007**, *26*, 679-685.
104. Kickelbick, G.; Schubert, U., Oxozirconium methacrylate clusters: $Zr_6(OH)_4O_4(OMc)_{12}$ and $Zr_4O_2(OMc)_{12}$ (OMc = Methacrylate). *Chem. Ber.* **1997**, *130*, 473-478.
105. Kogler, F. R.; Jupa, M.; Puchberger, M.; Schubert, U., Control of the ratio of functional and non-functional ligands in clusters of the type $Zr_6O_4(OH)_4(carboxylate)_{12}$ for their use as building blocks for inorganic-organic hybrid polymers. *J. Mater. Chem.* **2004**, *14*, 3133-3138.
106. Schubert, U., Polymers reinforced by covalently bonded inorganic clusters. *Chem. Mater.* **2001**, *13*, 3487-3494.
107. Schubert, U., Cluster-based inorganic-organic hybrid materials. *Chem. Soc. Rev.* **2011**, *40*, 575-582.

108. Malaestean, I. L.; Speldrich, M.; Ellern, A.; Baca, S. G.; Kogerler, P., Heterometal expansion of oxozirconium carboxylate clusters. *Dalton Trans.* **2011**, *40*, 331-333.
109. Malaestean, I. L.; Kutluca, M.; Speldrich, M.; Ellern, A.; Kögerler, P., Macrocycles based on magnetically functionalized zirconium oxide clusters. *Inorg. Chim. Acta* **2012**, *380*, 72-77.
110. Faccioli, F.; Bauer, M.; Pedron, D.; Sorarù, A.; Carraro, M.; Gross, S., Hydrolytic stability and hydrogen peroxide activation of zirconium-based oxoclusters. *Eur. J. Inorg. Chem.* **2015**, *2015*, 210-225.
111. Bai, Y.; Dou, Y.; Xie, L.-H.; Rutledge, W.; Li, J.-R.; Zhou, H.-C., Zr-based metal-organic frameworks: design, synthesis, structure, and applications. *Chem. Soc. Rev.* **2016**, *45*, 2327-2367.
112. Garibay, S. J.; Cohen, S. M., Isoreticular synthesis and modification of frameworks with the UiO-66 topology. *Chem. Commun.* **2010**, *46*, 7700-7702.
113. Li, L.; Tang, S.; Wang, C.; Lv, X.; Jiang, M.; Wu, H.; Zhao, X., High gas storage capacities and stepwise adsorption in a UiO type metal-organic framework incorporating Lewis basic bipyridyl sites. *Chem. Commun.* **2014**, *50*, 2304-2307.
114. Jiang, H.-L.; Feng, D.; Liu, T.-F.; Li, J.-R.; Zhou, H.-C., Pore surface engineering with controlled loadings of functional groups via Click chemistry in highly stable metal-organic frameworks. *J. Am. Chem. Soc.* **2012**, *134*, 14690-14693.
115. Feng, D.; Gu, Z.-Y.; Chen, Y.-P.; Park, J.; Wei, Z.; Sun, Y.; Bosch, M.; Yuan, S.; Zhou, H.-C., A highly stable porphyrinic zirconium metal-organic framework with shp-a topology. *J. Am. Chem. Soc.* **2014**, *136*, 17714-17717.
116. Feng, D.; Wang, K.; Su, J.; Liu, T. F.; Park, J.; Wei, Z.; Bosch, M.; Yakovenko, A.; Zou, X.; Zhou, H. C., A highly stable zeotype mesoporous zirconium metal-organic framework with ultralarge pores. *Angew. Chem., Int. Ed.* **2015**, *54*, 149-154.
117. Gutov, O. V.; Bury, W.; Gomez-Gualdrón, D. A.; Krungleviciute, V.; Fairen-Jimenez, D.; Mondloch, J. E.; Sarjeant, A. A.; Al-Juaid, S. S.; Snurr, R. Q.; Hupp, J. T.; Yildirim, T.; Farha, O. K., Water-stable zirconium-based metal-organic framework material with high-surface area and gas-storage capacities. *Chem. Eur. J.* **2014**, *20*, 12389-12393.
118. Wang, T. C.; Bury, W.; Gómez-Gualdrón, D. A.; Vermeulen, N. A.; Mondloch, J. E.; Deria, P.; Zhang, K.; Moghadam, P. Z.; Sarjeant, A. A.; Snurr, R. Q.; Stoddart, J. F.; Hupp, J. T.; Farha, O. K., Ultrahigh surface area zirconium MOFs and insights into the applicability of the BET theory. *J. Am. Chem. Soc.* **2015**, *137*, 3585-3591.

119. Furukawa, H.; Gándara, F.; Zhang, Y.-B.; Jiang, J.; Queen, W. L.; Hudson, M. R.; Yaghi, O. M., Water adsorption in porous metal–organic frameworks and related materials. *J. Am. Chem. Soc.* **2014**, *136*, 4369-4381.
120. Morris, W.; Voloskiy, B.; Demir, S.; Gándara, F.; McGrier, P. L.; Furukawa, H.; Cascio, D.; Stoddart, J. F.; Yaghi, O. M., Synthesis, structure, and metalation of two new highly porous zirconium metal–organic frameworks. *Inorg. Chem.* **2012**, *51*, 6443-6445.
121. Choi, K. M.; Jeong, H. M.; Park, J. H.; Zhang, Y.-B.; Kang, J. K.; Yaghi, O. M., Supercapacitors of nanocrystalline metal–organic frameworks. *ACS Nano* **2014**, *8*, 7451-7457.
122. Ardila-Suarez, C.; Perez-Beltran, S.; Ramirez-Caballero, G. E.; Balbuena, P. B., Enhanced acidity of defective MOF-808: effects of the activation process and missing linker defects. *Catal. Sci. Technol.* **2018**, *8*, 847-857.
123. Zhang, X.; Huang, P.; Liu, A.; Zhu, M., A metal–organic framework for oxidative desulfurization: UiO-66(Zr) as a catalyst. *Fuel* **2017**, *209*, 417-423.
124. Ye, G.; Qi, H.; Li, X.; Leng, K.; Sun, Y.; Xu, W., Enhancement of oxidative desulfurization performance over UiO-66(Zr) by titanium ion exchange. *ChemPhysChem* **2017**, *18*, 1903-1908.
125. Doan, T. L. H.; Dao, T. Q.; Tran, H. N.; Tran, P. H.; Le, T. N., An efficient combination of Zr-MOF and microwave irradiation in catalytic Lewis acid Friedel-Crafts benzoylation. *Dalton Trans.* **2016**, *45*, 7875-7880.
126. Vermoortele, F.; Ameloot, R.; Vimont, A.; Serre, C.; De Vos, D., An amino-modified Zr-terephthalate metal-organic framework as an acid-base catalyst for cross-aldol condensation. *Chem. Commun.* **2011**, *47*, 1521-1523.
127. Katz, M. J.; Klet, R. C.; Moon, S.-Y.; Mondloch, J. E.; Hupp, J. T.; Farha, O. K., One step backward is two steps forward: enhancing the hydrolysis rate of UiO-66 by decreasing $[\text{OH}^-]$. *ACS Catal.* **2015**, *5*, 4637-4642.
128. de Koning, M. C.; van Grol, M.; Breijaert, T., Degradation of paraoxon and the chemical warfare agents VX, Tabun, and Soman by the metal–organic frameworks UiO-66-NH₂, MOF-808, NU-1000, and PCN-777. *Inorg. Chem.* **2017**, *56*, 11804-11809.
129. Caratelli, C.; Hajek, J.; Cirujano, F. G.; Waroquier, M.; Llabrés i Xamena, F. X.; Van Speybroeck, V., Nature of active sites on UiO-66 and beneficial influence of water in the catalysis of Fischer esterification. *J. Catal.* **2017**, *352*, 401-414.

130. Blandez, J. F.; Santiago-Portillo, A.; Navalón, S.; Giménez-Marqués, M.; Álvaro, M.; Horcajada, P.; García, H., Influence of functionalization of terephthalate linker on the catalytic activity of UiO-66 for epoxide ring opening. *J. Mol. Catal. A: Chem.* **2016**, *425*, 332-339.
131. Liu, Y.; Klet, R. C.; Hupp, J. T.; Farha, O., Probing the correlations between the defects in metal-organic frameworks and their catalytic activity by an epoxide ring-opening reaction. *Chem. Commun.* **2016**, *52*, 7806-7809.
132. Ling, S.; Slater, B., Dynamic acidity in defective UiO-66. *Chem. Sci.* **2016**, *7*, 4706-4712.
133. Vermoortele, F.; Bueken, B.; Le Bars, G.; Van de Voorde, B.; Vandichel, M.; Houthoofd, K.; Vimont, A.; Daturi, M.; Waroquier, M.; Van Speybroeck, V.; Kirschhock, C.; De Vos, D. E., Synthesis modulation as a tool to increase the catalytic activity of metal-organic frameworks: The unique case of UiO-66(Zr). *J. Am. Chem. Soc.* **2013**, *135*, 11465-11468.
134. Dissegna, S.; Epp, K.; Heinz, W. R.; Kieslich, G.; Fischer, R. A., Defective metal-organic frameworks. *Adv. Mater.* **2018**, *1704501*, 1-23.
135. In typical oxidative desulfurization model study of diesel fuels, the first stage is "extraction" of a large portion of the sulfur-containing component into a good solvent such as CH₃CN that is also miscible with aqueous H₂O₂. The injection of H₂O₂ to induce oxidation is considered a second stage. The oxidized product is much more soluble in CH₃CN than in the diesel fuel mixture and remained in the former phase. See ref. 99
136. Davis, M. E.; Davis, R. J., *Fundamentals of chemical reaction engineering*. McGraw-Hill Higher Education: New York, 2003; pp 184-239.
137. Cao, S.; Tao, F.; Tang, Y.; Li, Y.; Yu, J., Size- and shape-dependent catalytic performances of oxidation and reduction reactions on nanocatalysts. *Chem. Soc. Rev.* **2016**, *45*, 4747-4765.
138. Ye, R.; Hurlburt, T. J.; Sabyrov, K.; Alayoglu, S.; Somorjai, G. A., Molecular catalysis science: Perspective on unifying the fields of catalysis. *Proc. Natl. Acad. Sci. U.S.A* **2016**, *113*, 5159-5166.
139. Wu, H.; Chua, Y. S.; Krungleviciute, V.; Tyagi, M.; Chen, P.; Yildirim, T.; Zhou, W., Unusual and highly tunable missing-linker defects in zirconium metal-organic framework UiO-66 and their important effects on gas adsorption. *J. Am. Chem. Soc.* **2013**, *135*, 10525-10532.
140. Taddei, M., When defects turn into virtues: the curious case of zirconium-based metal-organic frameworks. *Coord. Chem. Rev.* **2017**, *343*, 1-24.

141. Yang, D.; Bernales, V.; Islamoglu, T.; Farha, O. K.; Hupp, J. T.; Cramer, C. J.; Gagliardi, L.; Gates, B. C., Tuning the surface chemistry of metal organic framework nodes: proton topology of the metal-oxide-like Zr₆ nodes of UiO-66 and NU-1000. *J. Am. Chem. Soc.* **2016**, *138*, 15189-15196.
142. Canivet, J.; Vandichel, M.; Farrusseng, D., Origin of highly active metal-organic framework catalysts: defects? Defects! *Dalton Trans.* **2016**, *45*, 4090-4099.
143. Trickett, C. A.; Gagnon, K. J.; Lee, S.; Gándara, F.; Bürgi, H. B.; Yaghi, O. M., Definitive molecular level characterization of defects in UiO-66 crystals. *Angew. Chem., Int. Ed.* **2015**, *54*, 11162-11167.
144. Shearer, G. C.; Chavan, S.; Ethiraj, J.; Vitillo, J. G.; Svelle, S.; Olsbye, U.; Lamberti, C.; Bordiga, S.; Lillerud, K. P., Tuned to perfection: ironing out the defects in metal-organic framework UiO-66. *Chem. Mater.* **2014**, *26*, 4068-4071.
145. Katz, M. J.; Brown, Z. J.; Colon, Y. J.; Siu, P. W.; Scheidt, K. A.; Snurr, R. Q.; Hupp, J. T.; Farha, O. K., A facile synthesis of UiO-66, UiO-67 and their derivatives. *Chem. Commun.* **2013**, *49*, 9449-9451.
146. Schaate, A.; Roy, P.; Godt, A.; Lippke, J.; Waltz, F.; Wiebcke, M.; Behrens, P., Modulated synthesis of Zr-based metal-organic frameworks: from nano to single crystals. *Chem. Eur. J.* **2011**, *17*, 6643-6651.
147. Shearer, G. C.; Chavan, S.; Bordiga, S.; Svelle, S.; Olsbye, U.; Lillerud, K. P., Defect engineering: Tuning the porosity and composition of the metal-organic framework UiO-66 via modulated synthesis. *Chem. Mater.* **2016**, *28*, 3749-3761.
148. Atzori, C.; Shearer, G. C.; Maschio, L.; Civalleri, B.; Bonino, F.; Lamberti, C.; Svelle, S.; Lillerud, K. P.; Bordiga, S., Effect of benzoic acid as a modulator in the structure of UiO-66: An experimental and computational study. *J. Phys. Chem. C.* **2017**, *121*, 9312-9324.
149. Gutov, O. V.; Hevia, M. G.; Escudero-Adán, E. C.; Shafir, A., Metal-organic framework (MOF) defects under control: insights into the missing linker sites and their implication in the reactivity of zirconium-based frameworks. *Inorg. Chem.* **2015**, *54*, 8396-8400.
150. Cottineau, T.; Richard-Plouet, M.; Mevellec, J.-Y.; Brohan, L., Hydrolysis and complexation of *N,N*-dimethylformamide in new nanostructured titanium oxide hybrid organic-inorganic sols and gel. *J. Phys. Chem. C.* **2011**, *115*, 12269-12274.
151. Srour, H.; Jalkh, J.; Le Maux, P.; Chevance, S.; Kobeissi, M.; Simonneaux, G., Asymmetric oxidation of sulfides by hydrogen peroxide catalyzed by chiral manganese porphyrins in water/methanol solution. *J. Mol. Catal. A: Chem.* **2013**, *370*, 75-79.

152. Shaabani, A.; Rezayan, A. H., Silica sulfuric acid promoted selective oxidation of sulfides to sulfoxides or sulfones in the presence of aqueous H₂O₂. *Catal. Commun.* **2007**, *8*, 1112-1116.
153. Cojocariu, A. M.; Mutin, P. H.; Dumitriu, E.; Fajula, F.; Vioux, A.; Hulea, V., Non-hydrolytic synthesis of mesoporous silica-titania catalysts for the mild oxidation of sulfur compounds with hydrogen peroxide. *Chem. Commun.* **2008**, 5357-5359.
154. Hulea, V.; Fajula, F.; Bousquet, J., Mild oxidation with H₂O₂ over Ti-containing molecular sieves—A very efficient method for removing aromatic sulfur compounds from fuels. *J. Catal.* **2001**, *198*, 179-186.
155. Bonchio, M.; Conte, V.; Assunta De Conciliis, M.; Di Furia, F.; Ballistreri, F. P.; Tomaselli, G. A.; Toscano, R. M., The relative reactivity of thioethers and sulfoxides toward oxygen transfer reagents: the oxidation of thianthrene 5-oxide and related compounds by MoO₅HMPT. *J. Org. Chem.* **1995**, *60*, 4475-4480.
156. Thornburg, N. E.; Liu, Y.; Li, P.; Hupp, J. T.; Farha, O. K.; Notestein, J. M., MOFs and their grafted analogues: regioselective epoxide ring-opening with Zr₆ nodes. *Catal. Sci. Technol.* **2016**, *6*, 6480-6484.
157. Bregante, D. T.; Flaherty, D. W., Periodic trends in olefin epoxidation over group IV and V framework-substituted zeolite catalysts: a kinetic and spectroscopic study. *J. Am. Chem. Soc.* **2017**, *139*, 6888-6898.
158. As Zr₆-oxo-hydroxo clusters have been reported to form oxidation-active Zr(η²-O₂) intermediates in the presence of H₂O₂ (see ref. 110), we also searched for this peroxy intermediate computationally. However, such a species does not appear to be a stable intermediate in our DFT calculations. See Section 3.9 for additional discussion.
159. The “ideal” UiO-66 structure is defined as a structure with the formula Zr₆O₄(OH)₄(BDC)₆, that has exactly 6 BDC linker/node (i.e., no missing linker and no capping ligand); see Table 3.4.
160. **BzOH-UiO-66** was selected as the catalyst for this set of studies as it has one open site (Table 3.1) and can be correlated with the computational work, which used a model catalyst possessing one [μ₁-OH + μ₁-OH₂] open site.
161. Caratelli, C.; Hajek, J.; Rogge, S. M. J.; Vandenbrande, S.; Meijer, E. J.; Waroquier, M.; Van Speybroeck, V., Influence of a confined methanol solvent on the reactivity of active sites in UiO-66. *ChemPhysChem* **2018**, *19*, 420-429.
162. Schubert, U., Surface chemistry of carboxylato-substituted metal oxo clusters – Model systems for nanoparticles. *Coord. Chem. Rev.* **2017**, *350*, 61-67.

163. Ghosh, P.; Colón, Y. J.; Snurr, R. Q., Water adsorption in UiO-66: the importance of defects. *Chem. Commun.* **2014**, *50*, 11329-11331.
164. Sholl, D. S.; Lively, R. P., Defects in metal–organic frameworks: challenge or opportunity? *J. Phys. Chem. Lett* **2015**, *6*, 3437-3444.
165. Cheetham, A. K.; Bennett, T. D.; Coudert, F.-X.; Goodwin, A. L., Defects and disorder in metal organic frameworks. *Dalton Trans.* **2016**, *45*, 4113-4126.
166. Fang, Z.; Bueken, B.; De Vos, D. E.; Fischer, R. A., Defect-engineered metal–organic frameworks. *Angew. Chem., Int. Ed.* **2015**, *54*, 7234-7254.
167. Ren, J.; Ledwaba, M.; Musyoka, N. M.; Langmi, H. W.; Mathe, M.; Liao, S.; Pang, W., Structural defects in metal–organic frameworks (MOFs): formation, detection and control towards practices of interests. *Coord. Chem. Rev.* **2017**, *349*, 169-197.
168. Troya, D., Reaction mechanism of nerve-agent decomposition with Zr-based metal organic frameworks. *J. Phys. Chem. C.* **2016**, *120*, 29312-29323.
169. Becke, A. D., Density-functional thermochemistry. III. The role of exact exchange. *J. Chem. Phys.* **1993**, *98*, 5648-5652.
170. Lee, C.; Yang, W.; Parr, R. G., Development of the Colle-Salvetti correlation-energy formula into a functional of the electron density. *Phys. Rev. B* **1988**, *37*, 785-789.
171. Weigend, F.; Ahlrichs, R., Balanced basis sets of split valence, triple zeta valence and quadruple zeta valence quality for H to Rn: design and assessment of accuracy. *Phys. Chem. Chem. Phys.* **2005**, *7*, 3297-3305.
172. Hay, P. J.; Wadt, W. R., Ab initio effective core potentials for molecular calculations. Potentials for the transition metal atoms Sc to Hg. *J. Chem. Phys.* **1985**, *82*, 270-283.
173. Cossi, M.; Barone, V.; Cammi, R.; Tomasi, J., Ab initio study of solvated molecules: a new implementation of the polarizable continuum model. *Chem. Phys. Lett.* **1996**, *255*, 327-335.
174. Grimme, S.; Antony, J.; Ehrlich, S.; Krieg, H., A consistent and accurate ab initio parametrization of density functional dispersion correction (DFT-D) for the 94 elements H-Pu. *J. Chem. Phys.* **2010**, *132*, 154104.
175. Becke, A. D.; Johnson, E. R., A density-functional model of the dispersion interaction. *J. Chem. Phys.* **2005**, *123*, 154101.

176. Harman, D. G.; Ramachandran, A.; Gracanin, M.; Blanksby, S. J., The loss of carbon dioxide from activated perbenzoate anions in the aas phase: unimolecular rearrangement via epoxidation of the benzene ring. *J. Org. Chem.* **2006**, *71*, 7996-8005.
177. Chakravarthy, R. D.; Suresh, K.; Ramkumar, V.; Chand, D. K., New chiral molybdenum complex catalyzed sulfide oxidation with hydrogen peroxide. *Inorg. Chim. Acta* **2011**, *376*, 57-63.
178. Carrasco, C. J.; Montilla, F.; Galindo, A., Molybdenum-catalyzed enantioselective sulfoxidation controlled by a nonclassical hydrogen bond between coordinated chiral imidazolium-based dicarboxylate and peroxido ligands. *Molecules* **2018**, *23*, 1595.
179. Baig, N.; Madduluri, V. K.; Sah, A. K., Selective oxidation of organic sulfides to sulfoxides using sugar derived *cis*-dioxo molybdenum(VI) complexes: kinetic and mechanistic studies. *RSC Adv.* **2016**, *6*, 28015-28022.
180. Le Maux, P.; Simonneaux, G., First enantioselective iron-porphyrin-catalyzed sulfide oxidation with aqueous hydrogen peroxide. *Chem. Commun.* **2011**, *47*, 6957-6959.
181. Marques, A.; Marin, M.; Ruasse, M.-F., Hydrogen peroxide oxidation of mustard-model sulfides catalyzed by iron and manganese tetraarylporphyrines. Oxygen transfer to sulfides versus H₂O₂ dismutation and catalyst breakdown. *J. Org. Chem.* **2001**, *66*, 7588-7595.
182. Zucca, P.; Cocco, G.; Pintus, M.; Rescigno, A.; Sanjust, E., Biomimetic sulfide oxidation by the means of immobilized Fe(III)-5,10,15,20-tetrakis(pentafluorophenyl)porphin under mild experimental conditions. *J. Chem.* **2013**, *2013*, 1-7.
183. Dar, T. A.; Uprety, B.; Sankar, M.; Maurya, M. R., Robust and electron deficient oxidovanadium(IV) porphyrin catalysts for selective epoxidation and oxidative bromination reactions in aqueous media. *Green Chem.* **2019**, *21*, 1757-1768.
184. Smith, R. M.; Hansen, D. E., The pH-rate profile for the hydrolysis of a peptide bond. *J. Am. Chem. Soc.* **1998**, *120*, 8910-8913.
185. Melomedov, J.; Wunsche von Leupoldt, A.; Meister, M.; Laquai, F.; Heinze, K., Porphyrin amino acids-amide coupling, redox and photophysical properties of bis(porphyrin) amides. *Dalton Trans.* **2013**, *42*, 9727-9739.
186. Nguyen, H. G. T.; Mao, L.; Peters, A. W.; Audu, C. O.; Brown, Z. J.; Farha, O. K.; Hupp, J. T.; Nguyen, S. T., Comparative study of titanium-functionalized UiO-66: support effect on the oxidation of cyclohexene using hydrogen peroxide. *Catal. Sci. Technol.* **2015**, *5*, 4444-4451.

187. Limvorapitux, R.; Chou, L.-Y.; Young, A. P.; Tsung, C.-K.; Nguyen, S. T., Coupling molecular and nanoparticle catalysts on single metal–organic framework microcrystals for the tandem reaction of H₂O₂ generation and selective alkene oxidation. *ACS Catal.* **2017**, *7*, 6691-6698.
188. Ou, P.; Wolff, S. P., A discontinuous method for catalase determination at ‘near physiological’ concentrations of H₂O₂ and its application to the study of H₂O₂ fluxes within cells. *J. Biochem. Bioph. Methods* **1996**, *31*, 59-67.
189. Kandiah, M.; Usseglio, S.; Svelle, S.; Olsbye, U.; Lillerud, K. P.; Tilsted, M., Post-synthetic modification of the metal-organic framework compound UiO-66. *J. Mater. Chem.* **2010**, *20*, 9848-9851.
190. Chen, Y.-Z.; Jiang, H.-L., Porphyrinic metal–organic framework catalyzed Heck-reaction: Fluorescence “turn-on” sensing of Cu(II) ion. *Chem. Mater.* **2016**, *28*, 6698-6704.
191. Feng, D.; Gu, Z.-Y.; Li, J.-R.; Jiang, H.-L.; Wei, Z.; Zhou, H.-C., Zirconium-metalloporphyrin PCN-222: mesoporous metal–organic frameworks with ultrahigh stability as biomimetic catalysts. *Angew. Chem., Int. Ed.* **2012**, *51*, 10307-10310.

CURRICULUM VITAE

Rungmai Limvorapitux

Place of Birth: Phuket, Thailand
limvorapitux.rungmai@gmail.com

EDUCATION

- Ph.D. in Chemistry 2014 - 2019
Northwestern University, Evanston, IL
- B.E. Chemical Engineering 2010 - 2014
Tokyo Institute of Technology, Tokyo, Japan

RESEARCH EXPERIENCE

- Graduate Research**, Northwestern University, Evanston, IL 2014 - 2019
- Advisor: Dr. SonBinh T. Nguyen
 - Developed catalytically active metal-organic frameworks for one-pot tandem reactions
- R&D Internship**, Cabot Microelectronics Corporation, Aurora, IL 2018
- Mentor: Dr. Sudeep Kuttiaoor
 - Analyzed structure-property relationships of nanoparticles and additives to develop products for chemical mechanical planarization (CMP) processes in the semiconductor industry
- Undergraduate Research**, Tokyo Institute of Technology, Tokyo, Japan 2013 - 2014
- Advisor: Dr. Koichi Mikami
 - Developed catalytic Michael addition reaction to synthesize CF₃-bearing compounds, potential building blocks in pharmaceuticals and agrochemicals

PUBLICATIONS

- **Limvorapitux, R.**; Chou, L.-Y.; Young, A. P.; Tsung, C.-K.; Nguyen, S. T., *ACS Catal.*, **2017**, *7*, 6691-6698. "Coupling molecular and nanoparticle catalysts on single metal-organic framework microcrystals for the tandem reaction of H₂O₂ generation and selective alkene oxidation".
- **Limvorapitux, R.**; Chen, H.; Mendonca, M. L.; Liu, M.; Snurr, R. Q.; Nguyen, S. T., *Catal. Sci. Technol.*, **2019**, *9*, 327-335. "Elucidating the mechanism of the UiO-66-catalyzed sulfide oxidation: Selectivity and activity enhancements through modifications of the node coordination environment".
- Du, M.; Agrawal, A. M.; Chakraborty, S.; Garibay, S. J.; **Limvorapitux, R.**; Choi, B.; Madrahimov, S. T.; Nguyen, S. T., *ACS Sustain. Chem. Eng.* **2019**, *7*, 8126-8135. "Matching

the activity of homogeneous sulfonic acids: The fructose-to-HMF conversion catalyzed by hierarchically porous sulfonic-acid-functionalized porous organic polymer (POP) catalysts”.

- Agrawal, A. M.; **Limvorapitux, R.**; Chakraborty, S.; Mao, L.; Nguyen, S. T. “A recyclable thiol-functionalized hyper-crosslinked polymer for environmentally friendly Au^I capture”. *Manuscript in preparation.*

PRESENTATIONS

- “Elucidating the mechanism of the UiO-66-catalyzed sulfide oxidation: Selectivity and activity enhancements through modifications of the node coordination environment”, Catalysis Club of Chicago Symposium, April 2019, Naperville, IL. (poster presentation)
- “Enhanced sulfide oxidation activity via tuning coordination environment of Zr₆-oxo-hydroxo nodes in UiO-66 MOFs” ACS National Meeting, March 2018, New Orleans, LA. (oral presentation)
- “Development of a UiO-66 catalyst for tandem reaction of H₂O₂ generation and selective alkene oxidation”, Symposium Commemorating the 150th Birthday of Vladimir Ipatieff, Sept 2017, Evanston, IL. (poster presentation)
- “Developing a UiO-66 catalyst for tandem reaction of H₂O₂ generation and selective alkene oxidation”, NAM25 North American Catalysis Society Meeting, June 2017, Denver, CO. (poster presentation)
- “Coupling molecular and nanoparticle catalysts on single metal-organic framework microcrystals for the tandem reaction of H₂O₂ generation and selective alkene oxidation”, Catalysis Club of Chicago Symposium, May 2017, Naperville, IL. (poster presentation)

AWARDS & HONORS

Member of The American Chemical Society	2018 - 2019
PLU Travel Award from Alpha Gamma Chapter at Northwestern University	2018
Kokes Award from NAM25 North American Catalysis Society Meeting	2017
Graduate School Travel Grant from Northwestern University	2017, 2018
Grants-in-Aid of Research from Sigma Xi Scientific Research Society	2016
MEXT 4-year Undergraduate Student Scholarship from the Japanese Government	2009

LEADERSHIP

Lab safety officer , Nguyen Group	2015 - 2018
Lab Secretary , Nguyen Group	2017 - 2018
Graduate Side-kick , International Office	2017 - 2018
Event Coordinator , Graduate International Student Association	2016 - 2017

TEACHING

Teaching Volunteer , Science In The Classroom, Northwestern University	2016 - 2018
Graduate Teaching Assistant , Organic lab, Northwestern University	2014 - 2016